



Andriy Lyubchyk

Faculdade de Ciencia e Tecnologia
Universidade Nova de Lisboa

**GAS ADSORPTION IN THE MIL-53(AI)
METAL ORGANIC FRAMEWORK.
EXPERIMENTS AND MOLECULAR
SIMULATION**

 **FACULDADE DE
CIÊNCIAS E TECNOLOGIA
UNIVERSIDADE NOVA DE LISBOA**

Novembro 2013

Nº de Arquivo_____

*Copyright*_____



Andriy Lyubchyk

Faculdade de Ciencia e Tecnologia
Universidade Nova de Lisboa

**GAS ADSORPTION IN THE MIL-53(AI)
METAL ORGANIC FRAMEWORK.
EXPERIMENTS AND MOLECULAR
SIMULATION**

Dissertação para obtenção do Grau de Doutor
em Engenharia Química

Orientador: José Paulo Barbosa Mota

Júri:

Presidente: Prof. Doutor Manuel Jose Teixeira Carrondo
Arguente(s): Prof. Doutor Francois Beguin
Prof. Doutor Sergey V. Mikhalovsky

Vogais: Prof. Doutor Esteban Saadjan
Prof. Doutor Jose Paulo Barbosa Mota
Prof. Doutor Gregorie Marie Jean Bonfait
Prof. Doutor Francisco Avelino da Silva Freitas
Prof. Doutor Joaquim Silverio Marques Vital

 **FACULDADE DE
CIÊNCIAS E TECNOLOGIA
UNIVERSIDADE NOVA DE LISBOA**

Novembro 2013

**I would like to dedicate this thesis to my loving family- my son, my wife, parents,
my grandparents, to whom I owe my unconditional love and friendship**

Basic research is like shooting an arrow into the air and, where it lands, painting a target.

Dr. Homer Burton Adkins

Acknowledgements

I would not be able to complete this work without the support and encouragement of a countless number of people over the past four years. Firstly, I would like to express my gratitude towards my supervisor, Prof. Jose Paulo Mota. His leadership, support and friendship have set an example that I hope to match someday.

I would like to acknowledge several national and international program which supported my research and allowed me to accomplish this work:

(1) FCT for PhD Fellowship at Universidade Nova de Lisboa, Department of Chemistry (bolsa N SFRH/BD/45477/2008), which allowed me to accomplish the research on *Gas storage in the metal organic framework MIL-53(AI). Experiment and simulation*;

(2) the FCT Program, project PTDC/AAC-AMB/108849/2008 *Purification and Cleaning of Gaseous Effluents for Environmental Applications by Hybrid Pressure-Assisted Simulated Moving-Bed Processes* carried out at UNL/FCT, REQUIMTE, Departamento de Química;

(3) the NANO_GUARD, Project N°269138, Programme “PEOPLE” – Call ID “FP7-PEOPLE-2010-IRSES”

I also want to acknowledge my colleagues and friends Isabel Esteves, Ricardo Silva, Rui Rodriguez and Fernando Cruz helping me on the laboratory, coffee break discussion and friendship. A special thanks to my colleague and my wife OlenaLygina, who help me a lot with the discussion and writing.

I would like to thank my grandfather Prof. Boris Voevoda from National Technical University of Ukraine, Dr. Leonid Galushko from Institute of Physical Organic and Coal Chemistry, Eng. Igor Lyubchik form Joint Stock Company “Electrod”, who from the beginning accompanied the growth of my research and who are also good friends. Thank you for all the support and words given.

I acknowledge Universidade Nova de Lisboa, Dept. Quimica, associated laboratory REQUIMTE, for the opportunity to train me there.

I gratefully acknowledge Faculdade de Ciências e Tecnologia, UNL for the possibility to present and defend my thesis in Portugal to obtain the Doctor Degree of the Faculdade de Ciências e Tecnologia, Universidade Nova de Lisboa.

I thank my parents, my brother and my grandparents for instilling in me integrity and a willing to always pursue something more. Their endless support, care and friendship are something immeasurable.

Also, I would like to express special thanks to Prof. Svitlana Lyubchyk, who is my mother for her support and professional expertise with this thesis preparation.

To you my son! This work would not be possible without your smiles!

Thank you all for letting me share my life and love with you!

Preface

The PhD work was carried out as a part of Portugal national program FCT project PTDC/AAC-AMB/108849/2008. Research on “*Gas storage in the metal organic framework MIL-53(Al). Theoretical and Experimental*” was done at Universidade Nova de Lisboa, Faculdade de Ciências e Tecnologia, REQUIMTE, Departamento de Química under supervision of Prof. Paulo Mota. The research was carried out in a frame of the FCT PhD Fellowship SFRH/BD/45477/2008 and FCT R&D project PTDC/AAC-AMB/108849/2008.

The thesis is divided in six *CHAPTERS*. *Chapter 1* and *6* correspond to the introduction and conclusions, respectively. The structure of the research, the achievements and the conclusions are divided in three major sections:

- The characterization of the Metal Organic Framework MIL-53Al (*Chapter 2*);
- Thermodynamic studies of gas adsorption on MIL-53(Al) (*Chapters 3-5*);
- The theoretical studies of the MIL-53(Al) as a storage unit for the investigated gases (*Chapters 4, 5*).

The main core of the *Chapters* is based on published 1 book chapter, 1 scientific paper in a refereed journal, and 4 conference presentations, namely:

1. S. B. Lyubchik, A. I. Lyubchik, O. S. Lygina, S. I. Lyubchik and I. M. Fonseca
Comparison of the Thermodynamic Parameters Estimation for the Adsorption Process of the Metals from Liquid Phase on Activated Carbons
Book Thermodynamics – Interaction Studies – Solids, Liquids and Gases ISBN: 978-953-307-563-1; Ed. J. C. Moreno-Piraján Chapter N 4, **2011**, pp. 95 - 122
2. Andriy Lyubchyk, Isabel A. A. C. Esteves, Fernando J. A. L. Cruz, and José P. B. Mota
Experimental and Theoretical Studies of Supercritical Methane Adsorption in the MIL-53(Al) Metal Organic Framework
J. Phys. Chem. C, **2011**, 115 (42), pp 20628–20638
3. Fernando J.A.L. Cruz, Andriy I. Lyubchyk, Isabel A.A.C. Esteves, Jose P.B. Mota
Probing the Adsorptive Behaviour of MIL-53(Al) using light organics (C1-C4)
Computational Molecular Science and Engineering Forum AIChE **2012**, Pittsburgh.
4. Andriy I. Lyubchyk, Isabel A. A. C. Esteves, Fernando J. A. L. Cruz and José P. B. Mota
Simulated and Experimental Adsorption Equilibria of Light Alkanes In MIL-53(Al) Metal-Organic Framework AIChE **2011** Chemical Engineering Conference In Minneapolis
Highlights Energy, Water Sustainability, Bioengineering Advances.
5. A.I. Lyubchyk, I.A.A.C. Esteves, F.J.A.L. Cruz, S. Agnihotri, J.P.B. Mota* ADSORPTION CHARACTERIZATION OF METAL-ORGANIC FRAMEWORKS RIA2010, Portugal
6. A.I. Lyubchyk, I.A.A.C. Esteves, F.J.A.L. Cruz, S. Agnihotri, J.P.B. Mota*, Experimental Adsorption Equilibria of Alkanes C1 - C4 on Metal-Organic Frameworks, DACHEMA MOF2010 - 2nd International Conference on Metal-Organic Frameworks and Open Framework Compounds, **2010** France

Abstract

The main aim of this research was to explore MIL-53(Al) metal organic framework as a selective adsorbent for adsorption of the components of natural gas (CH_4 , C_2H_6 , C_3H_8 , C_4H_{10}) and possible storage unit according to the Department Of Energy (DOE) target.

To achieve this purpose, the research was focused on the following objectives:

1. Treatability studies of the metal organic framework MIL-53(Al) using advanced chemical-physical techniques.
2. Treatability studies of the thermodynamics of the components of natural gas (CH_4 , C_2H_6 , C_3H_8 , C_4H_{10}) adsorption using gravimetric analytical approach in a temperature range 303-353K and pressure 0 - 5 MPa.
3. Molecular simulation of the adsorption process using the Grand Canonical Monte Carlo (GCMC) method.
4. The GCMC calculations of the gas storage on MIL-53(Al) according to the DOE target.

In order to gain some insight into gas adsorption process the MIL-53(Al) material was characterize by elemental analyze, N_2 adsorption, mercury porosimetry, solid state ^{13}C -NMR, X-ray diffraction, FTIR and thermogravimetric analysis.

The gas-adsorption runs were performed using high-pressure magnetic-suspension balance measurements with automated online data acquisition of temperature, pressure, and sample weight. Adsorption experiments were done for C_1 - C_4 alkanes in a wide range of temperature 303-353 K and pressure 0-5 MPa.

The simulation work was done by the GCMC model using United Atom force field which shows good agreement between simulated and the experimental adsorption data.

It was concluded that the MIL-53(Al) must operate with a charge pressure slightly above 10 MPa to deliver the DOE target of 150 volumes of methane per storage volume in an isothermal cycle operating at 298.15 K and depletion pressure of 0.136 MPa.

Keywords: metal organic framework, adsorption, gas, molecular simulation, Grand Canonical Monte Carlo (GCMC).

Resumo

O principal objetivo desta pesquisa foi explorar MIL-53 (Al) quadro orgânico de metal como um adsorvente seletivo para a adsorção dos componentes do gás natural (CH_4 , C_2H_6 , C_3H_8 , C_4H_{10}) e possível unidade de armazenamento de acordo com o Departamento de energia alvo (DOE).

Para alcançar este objetivo, a pesquisa foi focada nos seguintes objetivos:

1. Tratabilidade estudos de estrutura orgânica do metal MIL-53 (Al) através de técnicas físico-química avançada.
2. Estudos de tratabilidade da termodinâmica dos componentes do gás natural (CH_4 , C_2H_6 , C_3H_8 , C_4H_{10}) adsorção usando gravimétrico abordagem analítica em uma ampla gama de temperaturas de 303-353 K e pressão 0-5 MPa.
3. Simulação molecular do processo de adsorção, utilizando o método de Monte Carlo Grande canónica (GCMC).
4. Os cálculos GCMC do armazenamento de gases na MIL-53 (Al) de acordo com a meta DOE.

A fim de ganhar alguma introspecção em processo de adsorção gás-53 MIL (Al) material foi caracterizar por análise elementar, N_2 adsorção, porosimetria de mercúrio, de estado sólido de ^{13}C -RMN, difração de raios-X, FTIR e análise termogravimétrica.

As corridas de gás de adsorção foram realizadas utilizando medições dos balanços de suspensão magnética de alta pressão, com a aquisição automática de dados on-line da temperatura, pressão, e o peso da amostra. Foram realizadas experiências de adsorção para C1-C4 alcanos em uma ampla gama de temperatura de 303-353 K e pressão de 0-5 MPa.

O trabalho de simulação foi feito pelo modelo GCMC usando o campo de força Atom United, que mostra boa concordância entre simulação e os dados experimentais de adsorção.

Concluiu-se que o MIL-53 (Al) deve ser operado a uma pressão ligeiramente acima da carga de 10 MPa para entregar o alvo DOE de 150 volumes de metano por volume de armazenamento de um ciclo de funcionamento isotérmico a 298.15 K e pressão de esgotamento de 0.136 MPa.

Palavras-chave: estrutura metálica orgânicos, adsorção de gás, simulação molecular, o Grand Canonical Monte Carlo (GCMC).

List of Abbreviation and Notations

Abbreviations

Symbol	Description
1, 3, 5-tris (4-carboxyphenyl) benzene	Benzenetribenzoate
AMBER	Assisted Model Building and Energy Refinement
ARE	Average relative error
BDC	Benzenedicarboxylate
BET	Brunauer, Emmett and Teller (Isotherm model)
BIFs	Boron-Imidazolate Frameworks
BKS	Beest, Kramer, Santen (force field)
BPR	Back-pressure regulator
BTB	Benzenetribenzoate
BTC	Benzenetricarboxylate
CHARMM	Chemistry at HARvard Molecular Mechanics
COFs	Covalent Organic frameworks
CSD	Cambridge Structural Database
CVFF	Consistent Valence Forcefield
DFT	Density functional theory
DOE	U.S. Department of Energy
DREIDING	Force field
FSE	Fit standard error
FT-IR	Fourier-transform infrared (spectrum)
GCMC	Grand canonical Monte Carlo
GEMC	Gibbs Ensemble Monte Carlo
GGA	generalized gradient approximation
HKUST-1	Hong Kong University of Science and Technology
IAST	Ideal adsorbed solution theory
IRMOF	Isoreticular Metal Organic Framework
LDA	local-density approximation
LJ	Lenard-Jones
MAS	Magic angle spinning
MC	Monte Carlo
MCM	Mobil Crystalline Material
MD	Molecular dynamics
MFC	Mass-flow meter/controller
MIL	Materials of Institut Lavoisier
MIL-53as	as-synthesized
MIL-53ht	high temperature form

MIL-53lp	MIL-53 large pore form
MIL-53lt	low-temperature form
MIL-53np	MIL-53 narrow pore form
MM2 MM3 MM4	Developed by Norman Allinger, parametrized for a broad range of molecules.
MMFF	Merck Molecular Force Field
MMOFs	Microporous metal organic frameworks
MMOMs	microporous metal coordination materials
MOFs	Metal organic frameworks
MP (2,3,4)	Møller–Plesset perturbation theory (order)
MSB	Magnetic-suspension balance
NG	Natural gas
NMR	Nuclear magnetic resonance
OPLS-AA	Optimized Potentials for Liquid Simulations - all atom
PCFF	Polymer consistent force field
PCN	Porous Coordination Network
QZVPP	Quadrupole zeta valence basis set
RON	Research octane number
RSS	Regression sum of squares
SBU	Secondary building unit
SWNTs	single walled carbon nanotubes
TBUs	tetrahedral building units
TGA	Thermogravimetric Analysis
TIFs	Tetrahedral-Imidazolate Frameworks
TraPPE-UA	Transferable Potentials for Phase Equilibria-United Atom
Tripos	Force Field developed by Clark, M., Cramer III, R. D., van Opdenbosch, N.
TZVPP	Triple zeta valence basis set
UFF	Universal force field
UMCM	University of Michigan Crystalline Material
ZIFs	Zeolitic-Imidazolate Frameworks
ZMOFs	Zeolitelike Metal-Organic Frameworks
ZPH	Zero-potential hypersurface

Variables and Notations

ϵ	the inter-crystal void fraction
$1/n$	constant related to adsorption efficiency (Frendlich isotherm model)
$a_i()$	particle's acceleration
B	second Virial coefficient
b (bar^{-1})	the adsorption affinity
b_0 (bar^{-1})	the adsorption affinity at the reference temperature
C	parameter related to the binding intensity for all layers (BET isotherm model)
d (nm)	isotropic signal

D_p (Å)	Particle diameter
e	error
f (atm; bar, MPa)	the gas fugacity
F_i	force acting on the particle i
G (kJ mol ⁻¹)	Gibbs energy
h_g	molecular enthalpy of the bulk adsorptive
I ()	relative intensity
k_B (J K ⁻¹)	Boltzmann's constant
K_F	constant related to adsorption capacity (Freundlich isotherm model)
K_L	constant of Langmuir isotherm
m (g)	weight, displayed by the balance
m_h (g)	mass of the sample holder
m_i (g)	particle mass
m_s (g)	mass of the adsorbent sample
$\langle N \rangle$	The ensemble average number of molecules in the simulation box
n (mol/kg; mmol/g)	adsorbed amount (absolute adsorption)
n_{ex} (mol/kg; mmol/g)	Excess amount adsorbed
n_m (mol/kg; mmol/g)	saturation adsorbed amount of monolayer
n_{net} (mol/kg; mmol/g)	expressed per unit mass of adsorbent
n_s (mol/kg; mmol/g)	maximum adsorbed amount
P (atm; bar, MPa)	Pressure
Q (kJ mol ⁻¹)	heat of adsorption
q_i and q_j (C)	charges in atoms i and j
Q_{st} (kJ mol ⁻¹)	isosteric heat of adsorption
r (Å)	the distance between the particles
R (cm ³ MPaK ⁻¹ mol ⁻¹)	Universal Gas Constant
t	Constant characterizing the adsorbate adsorbent interaction (Toth isotherm model)
T (°C; K)	Temperature
t_0	Constant characterizing the adsorbate adsorbent interaction at reference temperature
T_0 (K)	Reference temperature
T_c (K)	critical temperature
U (kJ)	Potential energy
U^{bend} (kJ)	the bond bending energy for the angle formed by two successive chemical bonds
U^{bonded} (kJ)	the intramolecular energy within a molecule
$U^{Coulomb}$ (kJ)	the coulombic interaction energy
$U^{non-bonded}$ (kJ)	the intermolecular energy arising between different molecules
$U^{stretching}$ (kJ)	the bond stretching energy
$U^{torsion}$ (kJ)	the torsional energy due to the dihedral angles formed by four successive atoms in a chain

U^{total} (kJ)	total interaction energy
U^{vdW} (kJ)	the van der Waals interaction energy
V (m^3)	Volume
V_{box} (cm^3)	volume of the simulation box
V_c (cm^3/g)	the specific volume of the unit cell of MIL-53
V_h (cm^3/g)	the volume of all moving parts present in the measuring cell
V_p (cm^3/g)	the specific pore volume of the adsorbent
V_s (cm^3/g)	specific adsorbent volume impenetrable to the adsorbate
V_{zs}	specific pore volume renders excess adsorption
W (g)	Weight
W_{exp} (g)	weight reading before correction
Z	the compressibility factor
α	Constant (Sips isotherm model)
β (1/K)	the inverse temperature
Γ (mmol/ m^2)	constant surface concentration
$\gamma = Q/RT_0$	the heat coefficient
ΔS	entropy change
ΔW (g)	weight change
ε (J)	the depth of the potential well
η	Constant characterizing the adsorbate adsorbent interaction (Sips isotherm model)
η (mol)	mole number
η_0	Constant characterizing the adsorbate adsorbent interaction at reference temperature
θ	fractional loading
Λ (nm)	the thermal de Broglie wavelength
μ (kJ mol $^{-1}$)	chemical potential
ν (kJ mol $^{-1}$)	effective chemical potential
ν_{ig}^0 (kJ mol $^{-1}$)	reference effective chemical potential for the ideal gas (noninteracting particles)
ρ_g (g/ cm^3)	density of the bulk gas
ρ_h (g/ cm^3)	density of the sample holder
ρ_{He} (g/ cm^3)	Density of Helium
ρ_s (g/ cm^3)	density of the adsorbent sample
σ (Å)	the finite distance at which the inter-particle potential is zero
σD_p	standard deviation

Table of Content

1.	INTRODUCTION	1
1.1.	METAL ORGANIC FRAMEWORKS (MOFs)	3
1.1.1.	MOFs overview	3
1.1.2.	MOFs applications	10
1.2.	GAS STORAGE/ADSORPTION	14
1.2.1.	Single-component adsorption	14
1.2.2.	Multi-component adsorption	15
1.3.	THERMODYNAMICS of GAS ADSORPTION	20
1.3.1.	Supporting theory	20
1.3.1.1.	Adsorption in microporous solids	20
1.3.1.2.	Adsorption isotherm models	25
1.3.3.	Thermodynamic parameters	28
1.4.	SIMULATION TOOLS	30
1.4.1.	INTERACTION POTENTIAL	30
1.4.2.	MONTE CARLO	32
1.4.2.1.	CANONICAL ENSEMBLE	32
1.4.2.2.	GRAND CANONICAL ENSEMBLE	32
1.4.2.3.	GIBBS ENSEMBLE	34
1.5.	RESEARCH STRATEGY AND OBJECTIVES	36
1.6.	REFERENCES	38
2.	METAL ORGANIC FRAMEWORK MIL-53A1 CHARACTERIZATION	47
2.1.	INTRODUCTION	49
2.2.	EXPERIMENTAL	50
2.2.1.	Investigation techniques	50
2.3.	RESULTS AND DISCUSSION	51
2.3.1.	Elemental Analysis	51
2.3.2.	Mercury porosimetry	51
2.3.3.	Thermogravimetric Analysis	52
2.3.4.	FT-IR	52
2.3.5.	MAS ¹³ C-NMR	54
2.3.6.	X-ray Powder Diffraction	55
2.3.7.	Low Temperature Gas Adsorption	56
2.4.	REFERENCES	58
3.	EQUILIBRIUM ADSORPTION MEASUREMENTS	61
3.1.	INTRODUCTION	63
3.2.	EXPERIMENTAL	64
3.2.1.	Gravimetric Technique for Adsorption Measurements	64

3.2.2. Adsorption Equilibrium Measurements	68
3.4. CONCLUSION	69
3.5. REFERENCES	70
4. EXPERIMENTAL AND THEORETICAL STUDIES OF SUPERCRITICAL METHANE ADSORPTION IN THE MIL-53(AI) METAL ORGANIC FRAMEWORK	73
4.1. INTRODUCTION	75
4.2. EXPERIMENTAL	75
4.2.1. Molecular Model and Simulation Method	75
4.3. RESULTS AND DISCUSSION	79
4.3.1. Adsorption Equilibrium Measurements	79
4.3.2. Data Fitting	87
4.3.3. Isothermic Heat of Adsorption	89
4.3.4. DOE Target Calculations	92
4.4. CONCLUSION	95
4.5. REFERENCES	96
5. EXPERIMENTAL AND THEORETICAL STUDIES OF C₂H₆, C₃H₈, C₄H₁₀ ADSORPTION IN THE METAL ORGANIC FRAMEWORK MIL-53(AI)	99
5.1. INTRODUCTION	101
5.2. EXPERIMENTAL	101
5.2.1. Molecular Model and Simulation Method	101
5.3. RESULTS AND DISCUSSION	102
5.3.1. Adsorption Equilibrium Measurements	102
5.3.1.1. Adsorption isotherms of C ₁ -C ₄ n-alkanes	106
5.3.1.2. Analysis of the experimental adsorption isotherms	112
5.3.2. Data Fitting	119
5.3.3. Evaluation of the MIL 53 (AI) storage capacity towards C ₂ -C ₄ gases	129
5.4. CONCLUSION	136
5.5. REFERENCES	137
6. CONCLUSIONS	141
6.1. METAL ORGANIC FRAMEWORK MIL-53(AI) CHARACTERISTICS	143
6.2. THERMODYNAMICS OF GAS ADSORPTION ON MIL-53(AI)	144
6.3. MOLECULAR SIMULATION OF GAS STORAGE ON MIL-53(AI)	146
6.4. SUGGESTIONS FOR FUTURE RESEARCH	147
6.5. REFERENCES	149
APPENDIX A. Equilibrium adsorption data	151
A.1. Experimental and simulated methane adsorption equilibrium data at 303 K	153
A.2. Experimental and simulated methane adsorption equilibrium data at 323 K	154
A.3. Experimental and simulated methane adsorption equilibrium data at 353 K	155

A.4. Experimental and simulated ethane adsorption equilibrium data at 303 K	156
A.5. Experimental and simulated ethane adsorption equilibrium data at 323 K	157
A.6. Experimental and simulated ethane adsorption equilibrium data at 353 K	158
A.7. Experimental and simulated propane adsorption equilibrium data at 303 K	159
A.8. Experimental and simulated propane adsorption equilibrium data at 323 K	160
A.9. Experimental and simulated propane adsorption equilibrium data at 353 K	161
A.10. Experimental and simulated butane adsorption equilibrium data at 303 K	162
A.11. Experimental and simulated butane adsorption equilibrium data at 323 K	163
A.12. Experimental and simulated butane adsorption equilibrium data at 353 K	164

List of Figures

Figure 1.1.	Schematic representation of metal organic framework structure (IRMOF) and respective pore structure.	4
Figure 1.2.	Series of 16 highly crystalline MOFs from the prototype MOF-5 by functionalizing the organic linkers with different groups	4
Figure 1.3.	Number of MOF structures reported in the Cambridge Structural Database (CSD) from 1978 through 2006.	5
Figure 1.4.	Number of MOFs published per year since 1970 (left) and the change in the percentage of MOFs in the overall CSD since 1970 (right)	5
Figure 1.5.	Schematic presentation of the reticular chemistry	6
Figure 1.6.	Structure of MIL-53ht	7
Figure 1.7.	Structure of COF-1	8
Figure 1.8.	Single-crystal structure of rho-ZMOF (left) and sod-ZMOF (right).	9
Figure 1.9.	Schematic illustrating various reference states for the definition of adsorption	22
Figure 1.10.	Common isotherm measurement systems	24
Figure 1.11.	Schematic representation of GCMC simulation	33
Figure 1.12.	Three types of move attempted in constant pressure-GEMC	35
Figure 2.1.	Atomic structure of MIL-53lp(Al) unit framework	50
Figure 2.2.	Experimental mercury intrusion–extrusion cycle	52
Figure 2.3.	Particle size distribution of MIL-53(Al) powder	53
Figure 2.4.	TGA analysis of hydrated MIL-53(Al) powder	53
Figure 2.5.	FT-IR spectrum of hydrated MIL-53(Al) powder	54
Figure 2.6.	MAS ¹³ C-NMR spectrum of the MIL-53(Al) sample	55
Figure 2.7.	Powder XRD spectrum of MIL-53(Al) sample	56
Figure 2.8.	Adsorption-desorption of N ₂ on MIL-53(Al)	57
Figure. 3.1	Experimental setup for volumetric measurement of pure gas adsorption equilibria	63
Figure. 3.2	Schematic diagram of gravimetric apparatus	64
Figure 3.3	ISOSORP 2000 high-pressure magnetic-suspension balance (MSB) from Rubotherm GmbH (Bochum, Germany).	65
Figure 3.4	Schematic of the experimental set-up used for the adsorpti measurements	66
Figure 4.1	Snapshot of the GCMC simulation box with condensed methane molecules inside MIL-53lp(Al)	81
Figure 4.2	Molecular density field for condensed methane at 152.5 K	82
Figure 4.3.	Absolute (●), excess (○), and net adsorption (■) isotherms of methane in MIL-53lp(Al)	84
Figure 4.4.	Comparison of experimental (filled circles) and simulated (open circles) excess adsorption isotherms of methane in MIL-53lp(Al)	85

Figure 4.5.	Global fitting of the experimental methane adsorption data by the Sips and Toth isotherm models	89
Figure 4.6.	(a) Isosteric heat as a function of loading and (b) adsorption isosteres for the CH ₄ /MIL-53lp(Al) system at 303–353 K	90
Figure 4.7.	Isosteric heats of adsorption derived from the Sips and Toth isotherm models	91
Figure 4.8.	Cubic Hermite interpolation (solid lines) of the GCMC adsorption isotherms (open circles)	95
Figure. 5.1.	Orthographic view of the unit cell along a axis (top-left), b axis (top-right), and c axis (bottom-right).	102
Figure. 5.2	Orthographic view of the unit cell along the a axis (top-left) and identification of the three types of sub-channel: type 1, type 2, and type 3.	102
Figure 5.3	Molecular density profile, $n_a(x)$, along the a-axis of each sub-channel of the unit cell of MIL-53(Al)lp for a loading of one (top) and three (bottom) ethane molecules per unit cell	104
Figure 5.4	Molecular density field, $n_a(x; y)$, at various positions along the a-axis of the unit cell of MIL-53(Al)lp for a loading of one ethane molecule per unit cell	105
Figure 5.5	Molecular density field, $n_a(x; y)$, at various positions along the a-axis of the unit cell of MIL-53(Al)lp for a loading of 6 ethane molecules per unit cell	106
Figure 5.6	Absolute (\diamond), excess (\square), and net (Δ) adsorption isotherms of methane in MIL-53lp(Al) at 303 K (a), 323 K (b) and 353 K (c)	108
Figure 5.7	Absolute (\diamond), excess (\square), and net (Δ) adsorption isotherms of ethane in MIL-53lp(Al) at 303 K (a), 323 K (b) and 353 K (c)	109
Figure 5.8	Absolute (\diamond), excess (\square), and net (Δ) adsorption isotherms of propane in MIL-53lp(Al) at 303 K (a), 323 K (b) and 353 K (c)	110
Figure 5.9	Absolute (\diamond), excess (\square), and net (Δ) adsorption isotherms of butane in MIL-53lp(Al) at 303 K (a), 323 K (b) and 353 K (c)	111
Figure 5.10	Methane (\diamond), ethane (\square), propane (Δ) and butane (\circ) adsorption isotherms on MIL-53(Al) at 303 K expressed here in terms of n_{ex}	112
Figure 5.11	Methane (\diamond), ethane (\square), propane (Δ) and butane (\circ) adsorption isotherms on MIL-53(Al) at 323 K expressed here in terms of n_{ex}	113
Figure 5.12	Methane (\diamond), ethane (\square), propane (Δ) and butane (\circ) adsorption isotherms on MIL-53(Al) at 353 K expressed here in terms of n_{ex}	113
Figure 5.13	Semi-log scale of methane (\diamond), ethane (\square), propane (Δ), and butane (O) adsorption isotherms in MIL-53lp(Al) at 303 K	114
Figure 5.14	Comparison of the experimental isotherms presented in semi-log scale obtained at 303 K (\diamond), 323 K (Δ) and 353 K (\square) during the adsorption of ethane on MIL-53(Al)	114
Figure 5.15	Experimental adsorption isotherms of butane on MIL-53(Al) at 303 K (\diamond) and 323 K (\square) presented in semi-log scale	115
Figure 5.16	Upper panel: adsorption isotherms of CH ₄ (in red) and C ₄ H ₁₀ (in blue) in MIL-53(Cr), in a Langmuir model. Lower panel: difference in osmotic potential between lp and np phases, as a function of pressure	117
Figure 5.17	Existence of guest-induced structural transitions upon gas adsorption as a function of ΔF_{host} , the free energy difference between empty structures, and the ratio of gas affinities, K_1/K_2	118

Figure 5.18	Existence domains of the lp and np phases of MIL-53 upon gas adsorption, with guests of different affinities (K _{lp} and K _{np}).	118
Figure 5.19	Comparison of excess adsorption isotherms of ethane in MIL-53lp(Al): gravimetry (solid symbols) and simulation (open symbols)	119
Figure 5.20	Comparison of excess adsorption isotherms of propane in MIL-53lp(Al): gravimetry and simulation.	120
Figure 5.21	Global fitting of the experimental ethane adsorption data by the Sips and Toth isotherm models	121
Figure 5.22	Global fitting of the experimental propane adsorption data by the Sips and Toth isotherm models	121
Figure 5.23	Global fitting of the experimental butane adsorption data by the Sips and Toth isotherm models	122
Figure 5.24	(a) Isotheric heat as a function of loading and (b) adsorption isosteres for the C ₂ H ₆ /MIL-53lp(Al) system at 303–353 K.	124
Figure 5.25	(a) Isotheric heat as a function of loading and (b) adsorption isosteres for the C ₃ H ₈ /MIL-53lp(Al) system at 303–353 K.	124
Figure 5.26	(a) Isotheric heat as a function of loading and (b) adsorption isosteres for the C ₄ H ₁₀ /MIL-53lp(Al) system at 303–353 K.	125
Figure 5.27	Isotheric heats of adsorption of ethane derived from the Sips and Toth isotherm models	126
Figure 5.28	Isotheric heats of adsorption of propane derived from the Sips and Toth isotherm models	127
Figure 5.29	Isotheric heats of adsorption of ethane derived from the Sips and Toth isotherm models	128
Figure 5.30	Total storage capacity (black), net adsorption (red) and bulk gas compressed (blue) for the CH ₄ adsorption on MIL-53(Al)	130
Figure 5.31	Total storage capacity (black), net adsorption (red) and bulk gas compressed (blue) for the C ₂ H ₆ adsorption on MIL-53(Al)	131
Figure 5.32	Total storage capacity (black), net adsorption (red) and bulk gas compressed (blue) for the C ₃ H ₈ adsorption on MIL-53(Al)	132
Figure 5.33	Total storage capacity (black), net adsorption (red) and bulk gas compressed (blue) for the C ₄ H ₁₀ adsorption on MIL-53(Al)	133
Figure 5.34	Non Cylindrical ANG and Cylindrical CNG, LNG, LPG tanks	135
Figure 5.35	Adsorption (blue rhombs) and desorption (red circled) run for butane in MIL-53(Al) at 323 K	136
Figure 5.36	Adsorption (blue rhombs) and desorption (red circled) run for butane in MIL-53(Al) at 323 K	136

List of Tables

Table 2.1.	Elemental analysis for anhydrous MIL-53(Al) sample	51
Table 2.2.	Crystallographic unit cell parameters obtained for MIL-53(Al).	57
Table 4.1.	Lennard-Jones parameters for dispersive interactions in the CH ₄ /MIL-53lp(Al) system	77
Table 4.2.	Parameters obtained from the data fitting with the Sips and Toth models	88
Table 5.1.	Table 5.1.Lennard-Jones parameters for dispersive interactions in the C ₂ -C ₄ /MIL-53lp(Al)system.	102
Table 5.2.	Predicted Pressures for the lp-np and np-lp Transitions	115
Table 5.3.	Parameters obtained from the data fitting for the C ₁ -C ₄ experimental adsorption with the Sips and Toth models. In every case $r^2 > 0.998$; ARE is the average relative error	122
Table 5.4.	Isosteric Heat of adsorption determined by GCMC simulation method, integrated form of Clapeyron equation and Sips, Toth isotherms models	125
Table 5.5.	Storage capacity of propane and butane under critical pressure	134
Table 6.1.	Results of low temperature N ₂ adsorption	144
Table 6.2.	Maximal adsorption capacity obtained from the data fitting for the C1-C4 experimental adsorption by the Sips and Toth isotherms model	144
Table 6.3.	Isosteric Heat of adsorption determined by GCMC simulation method, integrated form of Clapeyron equation and Sips, Toth isotherms models.	146
Table A.1.	Experimental and simulated methane adsorption equilibrium data at 303K	153
Table A.2.	Experimental and simulated methane adsorption equilibrium data at 323 K	154
Table A.3.	Experimental and simulated methane adsorption equilibrium data at 353 K	155
Table A.4.	Experimental and simulated ethane adsorption equilibrium data at 303 K	156
Table A.5.	Experimental and simulated ethane adsorption equilibrium data at 323 K	157
Table A.6.	Experimental and simulated ethane adsorption equilibrium data at 353 K	158
Table A.7.	Experimental and simulated propane adsorption equilibrium data at 303 K	159
Table A.8.	Experimental and simulated propane adsorption equilibrium data at 323 K	160
Table A.9.	Experimental and simulated propane adsorption equilibrium data at 353 K	161
Table A.10.	Experimental and simulated butane adsorption equilibrium data at 303 K	162
Table A.11.	Experimental and simulated butane adsorption equilibrium data at 323 K	163
Table A.12.	Experimental and simulated butane adsorption equilibrium data at 353 K	164

List of Schemes

Scheme 1.1.	Presentation of a typical adsorption process	20
Scheme 1.2.	Models presentation of the adsorption process	25
Scheme 5.1.	Diagram for the hypothesis of the temperature and chain size effects on “breathing” and “gate opening” phenomena in MIL-53 (Al) upon C1-C4 adsorption.	116
Scheme 6.1.	Diagram for the hypothesis of the temperature and chain size effects on “breathing” phenomena in MIL-53 (Al) upon C1-C4 adsorption	145

INTRODUCTION

1.1.	METAL ORGANIC FRAMEWORKS (MOFS)	3
1.1.1.	MOFs overview	3
1.1.2.	MOFs applications	10
1.2.	GAS STORAGE/ADSORPTION	14
1.2.1.	Single-component adsorption	14
1.2.2.	Multi-component adsorption	18
1.3.	THERMODYNAMICS of GAS ADSORPTION	20
1.3.1.	Supporting theory	20
1.3.1.1.	Adsorption in microporous solids	21
1.3.1.2.	Adsorption isotherm models	25
1.3.3.	Thermodynamic parameters	28
1.4.	SIMULATION TOOLS	30
1.4.1.	INTERACTION POTENTIAL	30
1.4.2.	MONTE CARLO	32
1.4.2.1.	CANONICAL ENSEMBLE	32
1.4.2.2.	GRAND CANONICAL ENSEMBLE	32
1.4.2.3.	GIBBS ENSEMBLE	34
1.5.	RESEARCH STRATEGY AND OBJECTIVES	36
1.6.	REFERENCES	38

1.1. Metal Organic Framework

Porous materials are of scientific and technological interest because of their ability to interact with atoms, ions and molecules not only at their surfaces, but also in bulk. The pores sizes, shapes and volumes govern their ability for desired function in a particular application. The applications of porous materials involve storage, separation, ion exchange, catalysis and etc. Recently, an advanced approach to porous solid materials synthesis has gained renewed interest [1]. It involves coordination of the metal ions to the organic „linker“ moieties, thus yielding open framework structures called the Metal-Organic Frameworks (MOFs).

1.1.1. MOFs overview

A metal-organic framework (MOF) is composed of two major components: a metal ion or cluster of metal ions and an organic molecule called a linker. The organic units are typically mono, di-, tri-, or tetravalent ligands. The combination of the two components of a MOF, the metal ion or cluster and the organic linker, provides endless possibilities (Fig. 1.1 and 1.2).

Since the 1990s, this area of chemistry has experienced almost unparalleled growth, as evidenced by not only the sheer number of research papers published but also the ever-expanding scope of the research [1-3]. The MOF design *via* functionalization or incorporation of various building blocks ensures the unique physicochemical properties of the resulting materials, such as redox potentials, light absorption, magnetic moments, optics, electronic properties and etc. To date, there are tens of thousands of MOFs catalogued in the Cambridge Structural Database (CSD) (Fig. 1.3, 1.4) [4]. Thus, discovered 15 years ago, MOFs represent one of today's hottest fields of research.

The sum of the physical properties of the inorganic and organic components and possible synergistic play between the two provide intriguing properties of MOFs. MOFs are known for their extraordinarily high surface areas, tunable pore size, and adjustable internal surface properties. Compared to other solid-state matters such as zeolites, carbons and oxides, a number of MOFs are known to exhibit high framework flexibility and shrinkage/expansion due to interaction with guest molecules [4]. One of the most striking differences to traditional inorganic materials is ultrahigh porosity (up to 90% free volume) and enormous internal surface areas, extending beyond 6 000 m²/g. Therefore, owing to the increasingly rational approaches for the synthesis, MOFs can combine all the desired possibilities of the classical porous solids and have potentially unlimited pore sizes and surface areas. These properties, together with the extraordinary degree of variability of both the organic and inorganic components of their structures, make MOFs of interest for potential applications in clean energy. Therefore, MOFs are attracting considerable attention among scientists as well as recalling strong commercial interest in their application as storage media for gases such as hydrogen and methane, and as high-capacity adsorbents to meet various separation needs [4-9].

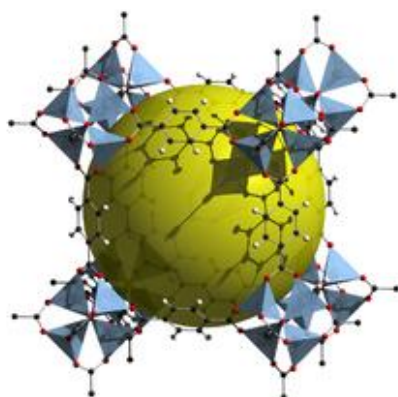


Figure 1.1. The MOF-5 (or IRMOF-1) Structure [http://en.wikipedia.org/wiki/File:IRMOF-1_wiki.png]. Color scheme is as follows: Zn (blue polyhedra), O (red spheres), C (black spheres), Br (green spheres in **2**), amino-groups (blue spheres in **3**). The large yellow spheres represent the largest Van der Waals spheres that would fit in the cavities without touching the frameworks. All hydrogen atoms have been omitted, and only one orientation of disordered atoms is shown for clarity

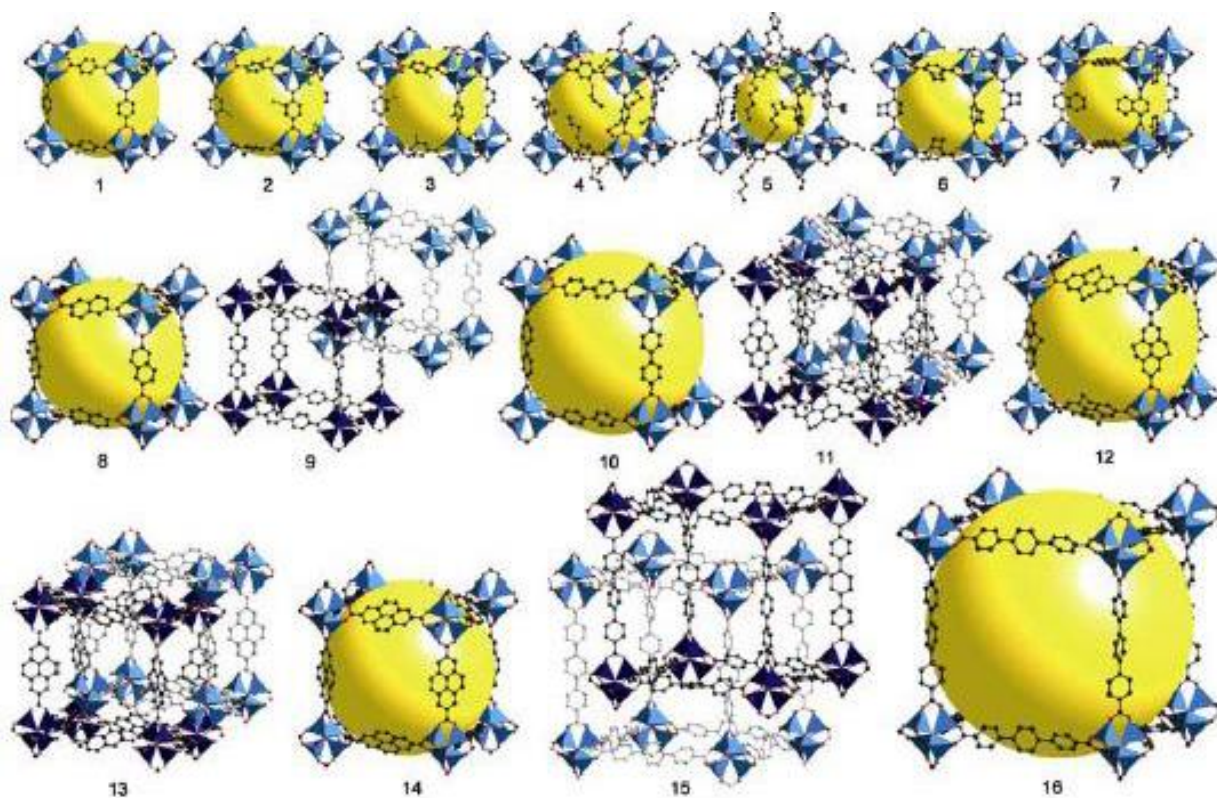


Figure 1.2 Series of 16 highly crystalline MOFs from the prototype MOF-5 by functionalizing the organic linkers with different groups and expanding its pore size by longer linkers. Single crystal x-ray structures of IRMOF-n (n=1 to 16), labeled respectively [2]. Color scheme is the same as in Fig. 1.1.

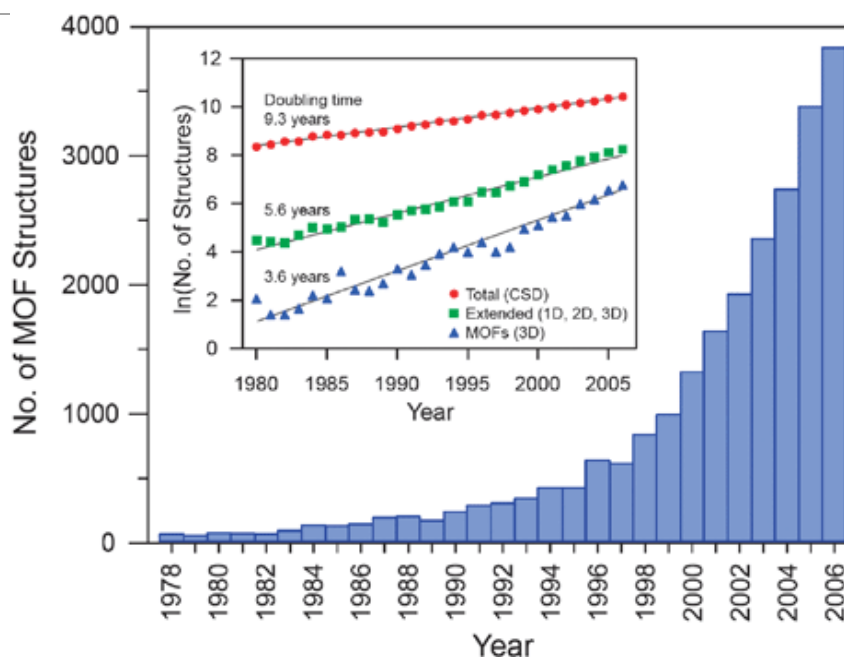


Figure 1.3 Number of MOF structures reported in the Cambridge Structural Database (CSD) from 1978 through 2006. The bar graph illustrates the recent dramatic increase in the number of reports, while the inset shows the natural log of the number of structures as a function of time, indicating the extraordinarily short doubling time for MOF structures compared to the total number of structures archived in the database [10].

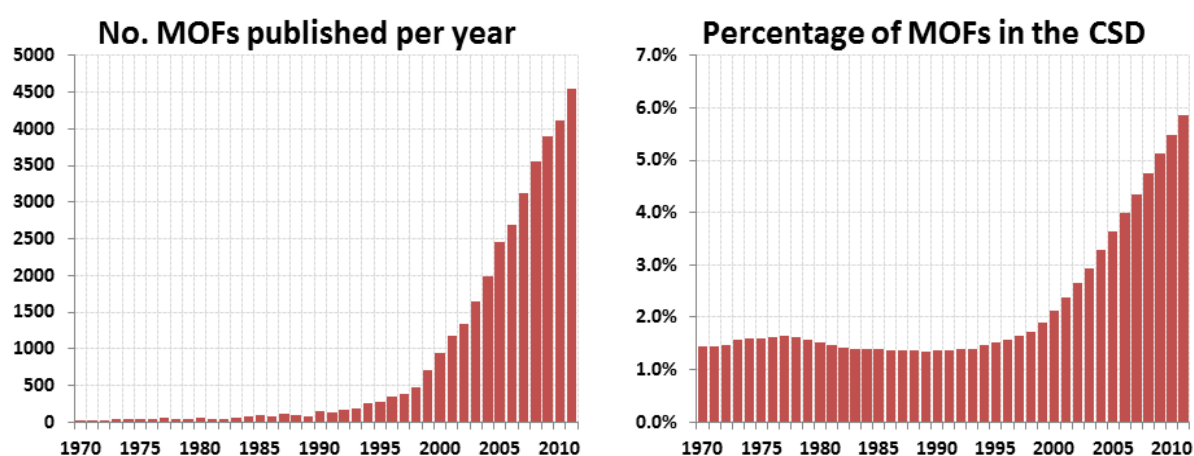


Figure 1.4 Graph of the number of MOFs published per year since 1970 (left) and the change in the percentage of MOFs in the overall CSD since 1970 (right)

The MOFs with predetermined structures, compositions and properties can be conceptually designed using so called “reticular” synthesis [11], when the secondary building units (SBU) such as polygons or polyhedra (Fig. 1.5) are used to direct the ordered frameworks assembly, systematic variation of the pore metrics and materials functionalization. Eddaoudi et al. [12] described the secondary building unit (SBU) as metal complexes and cluster entities, in which the ligand coordination nodes and metal coordination environments could be utilized in a transformation of these fragments into various extended porous networks using polytopic linkers. This led to the design and synthesis of a new class of porous materials with robust structures and high porosity.

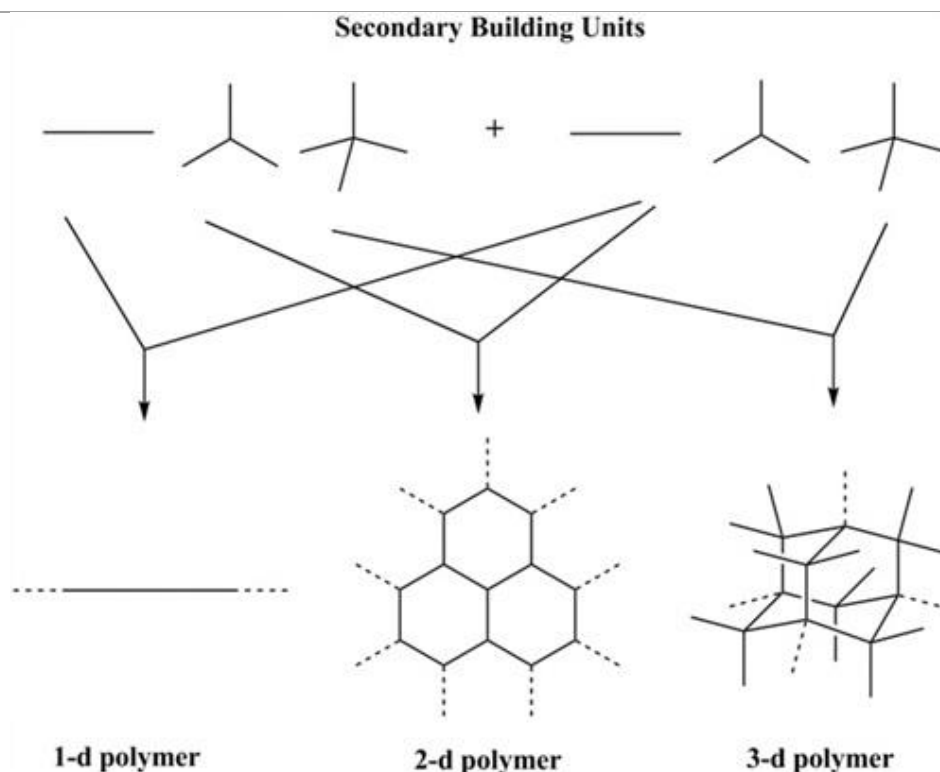


Figure 1.5 Schematic presentation of the reticular chemistry [http://en.wikipedia.org/wiki/File:Reticular_figure!.jpg]

As metal sites play a central role in a vast majority of molecular recognition processes, Chen et al. reported a presence of open metal sites by single-crystal X-ray diffraction analysis in a crystalline MOF [17]. The 3D crystalline MOF named as MOF-11 was formed from copolymerization of inorganic square cluster with an organic adamantane tetrahedral cluster, consisting of 3-D channel filled with guest water molecules. Several chiral porous MOFs were synthesized based on chiral ligands for enantioselective applications. As most of the MOFs contain transition elements, new MOFs were developed based on lanthanide elements due to their high coordination number with specific magnetic and luminescence properties [14-16]. The structure of enclathrated water can be an important parameter in understanding the mechanism of formation of different MOFs. Bharadwaj and co-workers [7-9, 17-22] examined the stable conformation of different isomers of water cluster in various MOFs.

The MOFs can be categorized into rigid and flexible/dynamic frameworks. Rigid MOFs are robust and stable porous frameworks with permanent porosity, similar to zeolites and other inorganic porous materials. In contrast, flexible MOFs possess dynamic frameworks that respond to external stimuli, such as pressure, temperature, and guest molecules [23-26]. Inclusion of guest molecules causes structural transformation in MOFs which is usually not observed in zeolite structure. Structural transformations may include stretching, rotational, breathing and scissoring mechanisms, which induce different effects in the structures. Kitaura et al. [27] observed hysteresis in a 3D pillared layer material, which undergoes contraction and expansion during adsorption, with a 27.9% reduction in a cell volume on contraction. Inclusion of guest molecules in a porous material can cause structural distortion, which is classified into two main categories. One is crystal-to-amorphous transformation which occurs when the framework collapses upon guest removal but

regeneration is possible by guest resorption. The other is crystal-to-crystal transformation where guest exchange or removal causes structural change without loss of crystallinity, i.e., unit cell expansion/contraction or scissoring.

In the MOFs, two processes may occur during adsorption of gas, namely gating and kinetic trapping. Gating occurs when the porous structure changes during adsorption process, going from non-porous to porous at a specific pressure. Physical adsorption of species on many porous materials produces adsorption isotherms that are virtually completely reversible. However, Zhao et al. [28] reported irreversibility in hydrogen uptake in a MOF at 77 K, whereby all or some of the H₂ is retained on pressure reduction referred to as “kinetic trapping”. This is due to a presence of narrow windows, which are considerably smaller than the cavities they connect resulting in a kinetic trapping of the H₂ gas by windows.

Ferey and co-workers first developed a series of 3D rare earth diphosphonates named as MIL-*n* (Materials of the Institute Lavoisier) [29-31]. Later they extended to compounds containing 3D transition metals (M = V, Fe, Ti) and metallic dicarboxylates [32-34]. Ferey et al. [35] used combined targeted chemistry and computational design to create chromium terephthalate based MIL-101 with very large pore sizes of ~ 30-40 Å and surface area of ~ 3900 m²/g. Serre et al. synthesized the first Cr (III) dicarboxylate MIL-53as (as-synthesized) under hydrothermal conditions [36]. MIL-53as exists in two forms, low-temperature form filled with water molecules and high temperature form, the dehydrated solid (Fig. 1.6). The transition between the hydrated form (MIL-53lt) and the anhydrous solid (MIL-53ht) is fully reversible and followed by a very high breathing effect. The pores are clipped in a presence of water molecules (MIL-53lt) and reopened when the channels are empty (MIL-53ht). In addition, MIL-53as and MIL-53lt exhibit antiferromagnetic properties. Similar breathing occurs when they change the Cr atom with other elements such as Al, Fe and Ga and this is due to the presence of the OH groups in one-dimensional channel which strongly interact with water [37-39]. However, no such breathing occurs in vanadium kind of the MIL-47 material, where there are no OH groups in the skeleton [40].

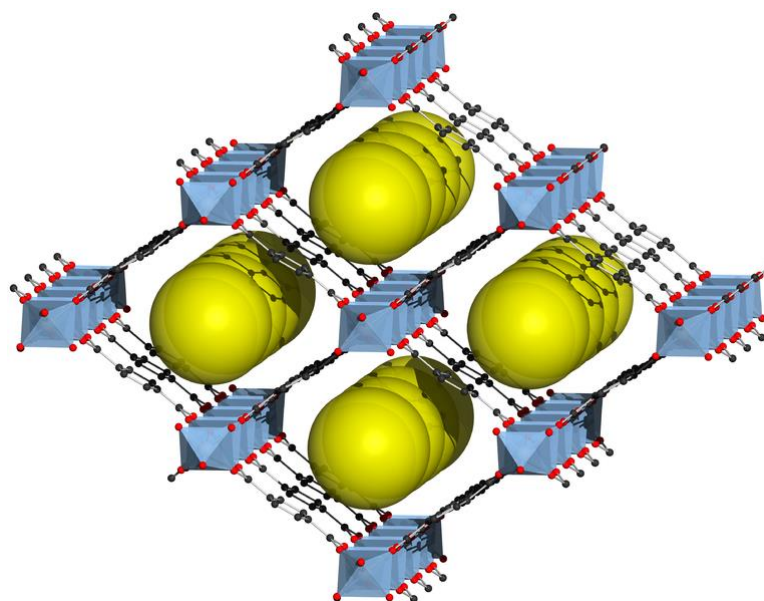


Figure 1.6 Structure MIL-53ht [<http://commons.wikimedia.org/wiki/File:MIL-53ht.png>].

A major breakthrough in the MOFs development is an evolution of the covalent organic frameworks (COFs), which consist of light elements (B, C, N and O) resulting in various 2D and 3D porous framework. Côté et al. [41, 42] and El-Kaderi et al. [43] synthesized the crystalline, porous COFs solely from light elements such as B, C, O and H. Consisting of organic-linkers covalently bonded with boron-oxide clusters, the COF-1 has salient features such as high thermal stability, large surface area and porosity. These boron-oxide clusters can be regarded as analogous to the metal-oxide clusters in MOFs. With the light elements, COFs have even lower density than MOFs. The co-condensation of boric acid with hexa-hydroxytriphenylene results in 2D COF-6, -8 and -10 [42]. These 2D COF structures resemble the layered graphite composed of graphene sheets. The inter-layer distances in the COF-6, -8 and -10 are of 3.399, 3.630 and 3.526 Å, respectively. Alternatively, joining triangular and tetrahedral nodes leads to 3D the COF-102, 103, 105 and 108 [43]. The COF-108 was reported to have the lowest density (as low as 0.17 g/cm³), even lower than the highly porous materials MOF-177 (0.42 g/cm³) and the lowest in any crystalline materials. Similar to carbon nanotube, armchair or zig-zig 1D the COF nanotube (COF_NT) could be constructed by rolling a COF layer in a particular direction. Mazzoni and coworkers [44] tested the stability of COF_NT's by examining the structural and electronic properties using the first principle calculations. Later, Hunt et al. [45] extended this approach by linking organic units with the strong covalent bonds found in the Pyrex (borosilicate glass, B-O and Si-O) to give a porous covalent organic borosilicate framework designated as the COF-202. Uribe-Romo et al. synthesized the first 3D crystalline framework (COF-300) constructed solely from C-C and C-N covalent linkages and demonstrated its permanent porosity by studying Ar adsorption at 87 K [46]. Wan et al. reported the synthesis of a new COF, the TP-COF based on the condensation reaction of triphenylene and pyrene monomers [47]. The TP-COF is highly luminescent, electrically conductive and capable of repetitive on-off current switching at room temperature.

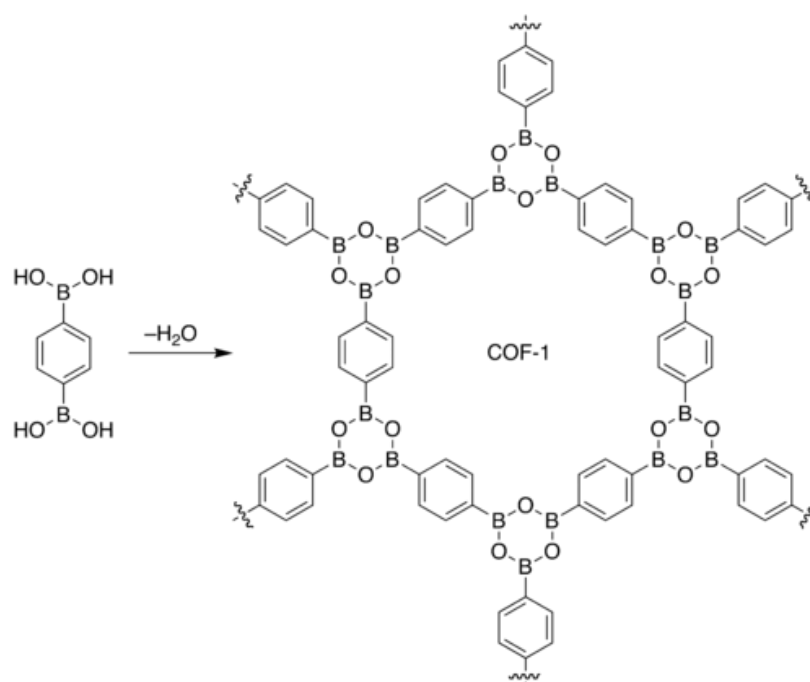


Figure 1.7 Structure COF-1 [http://en.wikipedia.org/wiki/File:boron_condensation.png]

Advanced design of the topological networks of zeolites (inorganic tetrahedral building units) resulted in a new generation of highly porous MOFs, such as the Zeolitic-Imidazolate Frameworks (ZIFs), Tetrahedral-Imidazolate Frameworks (TIFs), Boron-Imidazolate Frameworks (BIFs) and Zeolite like Metal-Organic Frameworks (ZMOFs). Those exhibit unique properties of extra-large cavities, chemical stability and ion-exchange capability. Tian et al. [48] reported a novel MOF with large pores and diamond-like topology from tetrahedral building block (TX₄) with four connections, where T-X-T angle is of 145°, T is Co(II) and X is imidazole linker. Similarly, Tian et al. [49-52] synthesized several MOFs based on the Co (II) and Zn imidazoles with zeolite-like topology. Huang et al. [53] established a new strategy to develop the zeolite-type MOFs with large pores by using a simple imidazolate ligand with a smaller substituent such as a methyl or ethyl group at the 2-position resulting in SOD and ANA topologies [54, 55]. Park et al. [56] synthesized a series of the ZIFs by copolymerization of either the Zn (II) or Co (II) with imidazolate-type linkers. Hayashi et al. [57] reported the ZIF-20, ZIF-21 and ZIF-22 based on the FAU or LTA topologies. Banerjee et al. [58] developed 25 different ZIFs structures, 10 of which have two different links and 5 of topology not yet observed in zeolites and ZIF-68, -69 and -70 are of high thermal and chemical stability in organic and aqueous media. Wang et al. [59] reported the ZIF-95 and ZIF-100 with topology non-observed for the zeolites. Zhang et al. [60] demonstrated a new synthetic method based on the cross-linking of various pre-synthesized boron imidazolate complexes (BIFs). Wu et al. [61] synthesized five 4-connected zeolitic metal imidazolate frameworks (TIFs). Liu et al. [62] reported the 4-connected MOF (*rho*-ZMOF) which is anionic in nature with topology of *rho*-zeolite (Fig. 1.8). Similarly, Sava et al. [63] used the approach based on rigid and directional single-metal-ion tetrahedral building units (TBUs) to synthesize the pyridine - carboxylate ZMOFs.

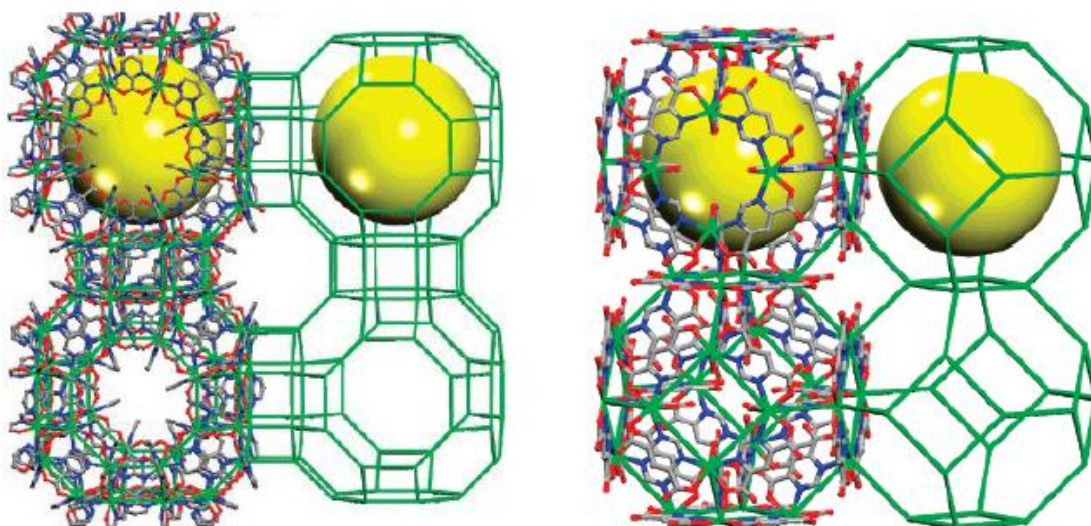


Figure 1.8 Single-crystal structure of *rho*-ZMOF (left) and sod-ZMOF (right). Hydrogen atoms and guest molecules are omitted for clarity. In - green, C - gray, N - blue, O - red. The yellow sphere represents the largest sphere that can be fit inside the cage, considering the van der Waals radii [63].

Post-synthetic modification of MOFs opens up another dimension of structural possibilities that might not be achieved by conventional synthesis. A critical review on post-synthetic modification of the MOFs is given by Wang et al. [64].

1.1.2. MOFs applications

The MOFs have been explored for their interesting properties including optical [62, 65-67], magnetic [68-70] and electronic properties [71-74], as well as their potential applications such as in catalysis [75-78], ion-exchange [62, 63, 79-81], gas storage and separation [82-84], sensing [85-87], polymerization [88, 89] and drug-delivery [90-92]. A brief discussion on the application of MOFs, particularly in gas adsorption, separation and catalysis is summarized below.

Gas Storage

Metal Organic Frameworks (MOFs) attract attention as materials for adsorptive gas storage because of their exceptionally high specific surface areas and chemically tunable structures. MOFs can be considered as a three-dimensional grid. Gas molecules are stored in a MOF by adsorbing to its surface without space-blocking by non-accessible volume. Also, MOFs have a fully reversible uptake-and-release behavior: since the storage mechanism is based primarily on physisorption, there are no large activation barriers to be overcome when liberating the adsorbed gases.

Over past few years, numerous studies have been reported in MOFs toward the H₂ storage for vehicular applications. Rowsell et al. [93] observed that the adsorption capacity in MOFs can be further increased by altering a chemical nature of the organic component. Chen et al. [94] highlighted the H₂ adsorption in the MOF-505 based on NbO topology with two pores types, open metal sites, permanent porosity. Ferey et al. [95] studied the H₂ storage capacity of the MIL-53 (nanoporous metal-benzenedicarboxylate containing trivalent Cr or Al) and found it is of 3.8 wt% and 3.1 wt%, respectively, at 77 K and 1.6 MPa.

Pan et al. [96] explored a new type of microporous metal coordination materials (MMOMs) with pore dimensions comparable to the molecular diameter of H₂. The open channels in MMOMs are perfectly ordered, allowing the effective access of H₂ to interior space. The structures of these materials, including the metal building unit, pore dimension, shape, size and volume, can be systematically tuned for modifying and improving H₂ uptake and adsorption/desorption properties.

Rowsell and Yaghi [97] reported comprehensive study on the strategies that enhance the H₂ storage in MOFs, included the optimization of pore size and adsorption energy by linker modification, impregnation, catenation, and inclusion of open metal sites and lighter metals. Following this, numerous experimental studies have been reported on the effect of catenation and inclusion of open metal sites on the H₂ uptake [98-101]. Wang et al. [102] reported a new porous coordination network, the PCN-12 exhibiting the H₂ uptake of 3.05 wt % at 77 K and 1 bar. Vitillo et al. [103] reported a MOF (CPO-27-Ni) with the highest heat of adsorption of -13.5 kJ/mol.

Li and Yang [104] suggested a new technique, dissociation/spillover to enhance H₂ storage in MOFs. By using this technique, they found an increase in H₂ storage capacity in the IRMOF-8 to 1.8 wt% at 298 K and 10 MPa with enhancement factor of 3.1, and totally reversible. The storage capacity of the IRMOF-8 was found to be 4 wt% at 298 K and 10 MPa, which is 8 times more than that of pure IRMOF-8 under the same conditions [105]. To date, the highest excess H₂ uptake were found in the MOF-5 (7.1 wt %) [121], MOF-177 (7.0 wt %) [113], and NOTT-102 (7.1 wt%) [106] at 77 K. Long and co-workers [107] reported a critical review on the H₂ uptake in MOFs.

Eddaoudi et al. [2] synthesized various MOFs and studied gas storage, particularly the CH₄ storage. They proposed a strategy based on reticulating metal ions and organic carboxylate links into extended networks in which pore size and functionality could be varied systematically. As a prototype of MOFs, the MOF-5 was constructed from Zn₄O clusters and benzene links. The three-dimensional structure of the MOF-5 can be functionalized with the groups -Br, -NH₂, -OC₃H₇, -OC₅H₁₁, -C₂H₄, -C₄H₄ and the pore size can be expanded with long molecular struts biphenyl, tetrahydropyrene, pyrene and tetraphenyl. They synthesized an isorecticular series of 16 highly crystalline materials with open space up to 91.1% of the crystal volume and pore size from 3.8 to 28.8 Å. One member of this series exhibited a high capacity for the CH₄ storage of 240 cm³(STP)/g at 36 atm and ambient temperature. A correlation between efficient CH₄ adsorption and large surface area, high free volume, low framework density was proven [108]. Ma et al. [109] reported a microporous MOF, PCN-14, based on anthracene derivative consisting of nanoscopic cages. High pressure CH₄ adsorption study showed that PCN-14 exhibits an absolute CH₄-adsorption capacity of 230 v/v, which is 28% higher than the DOE target of 180 v/v [110] at ambient temperature.

Gas Removal

In addition to gas storage for energy application, removal of gases from environment is also important. Yaghi and Millward [84] tested the storage capacity for CO₂ at room temperature in nine MOFs, representing a cross section of framework characteristics such as square channels (MOF-2), pores decorated with open metal sites (MOF-505 and Cu₃(BTC)₂), hexagonally packed cylindrical channels (MOF-74), interpenetration (the IRMOF-11), amino- and alkyl-functionalized pores (IRMOFs-3 and -6), and the extra-high porosity frameworks (IRMOF-1 and MOF-177). Llewellyn and Chowdhury et al. [111, 112] reported high uptake of the CO₂, CH₄, CO₂, CH₄, C₃H₈, SF₆ and Ar in chromium-based MIL-101. For all gases considered in their study, the enthalpy of adsorption was found to be lower than those in purely siliceous zeolites such as silicalite indicating a weaker interaction between the adsorbates and MIL-101 framework. Furukawa and Yaghi [83] measured the CO₂ storage capacity in various 1D, 2D and 3D structures of covalent organic frameworks (COFs) [42, 43] and showed that 3D COF structures outperform 1D and 2D COFs. For instance, CO₂ uptake in COF-102 and COF-103 is around 1010 mg/g and 1200 mg/g at 55 bar and 298 K and comparable to that in MOF-177 (1490 mg/g at 40 bar and 298 K) [84] and MIL-101(Cr) (1760 mg/g at 50 bar and 298 K) [111].

Medical applications

Xiao et al. [113] and Mickinlay et al. [114] showed an exceptionally high adsorption capacity and water-triggered delivery of biologically important gas NO in two porous MOFs. The MOFs are also tested for the storage and delivery of drug, for example MIL-101 exhibited a remarkably high dosage capacity of ibuprofen up to of 1.38 g/g MIL-101 [92], larger than that reported in MCM-41 [90]. The sorption and *in vitro* delivery of ibuprofen were also examined in MIL-53 with loading of 0.22 g/g MIL-53 independently of a metal type (Cr, Fe) [91].

Gas Separation

Some MOFs have been demonstrated being potentially useful in gas separation. Chen et al. [115] designed the MOF-508 with pores that can be tuned to match alkane molecular sizes and found highly selective chromatographic separation of alkanes in this MOF. Separation of linear and branched isomers of pentane and hexane were examined in detail, because of their availability and industrial relevance in petroleum refining. Pan et al. [116] studied the separation of hydrocarbons in microporous MOFs (MMOFs). Compared to zeolites, the MMOF structures are typically composed of aromatic rings and other organic moieties. Their pore structures can be designed and modified to yield the desired shape, size, and surface characteristics. They designed and synthesized a group of MMOFs that have 3D or 2D structures built upon paddle-wheel metal clusters (nodes) and a V-shaped dicarboxylate ligand. These structures contain irregular-shaped micro channels with alternating large cages (or chambers) and small entrances (or necks) that connect these cages. One of the MMOFs developed has unique property to separate normal C₂, C₃ and *n*-C₄ olefins and alkanes from all branched alkanes and all normal hydrocarbons above C₄. Dybtsev et al. [117] reported a new MMOF from manganese formate with permanent porosity, high thermal stability and high selective gas sorption properties. It selectively adsorbs H₂ and CO₂ but not the gases of larger kinetic diameters due to a smaller aperture of the channels. The selective adsorption of H₂ over N₂ was also reported on PCN-13 [118], Mg₃(ndc)₃ [119] and Cu (F-pymo)₂ [120].

The adsorption properties of different gases have been studied for the first robust MOFs, the Cu-BTC with a microporous structure [121, 122]. Ma et al. [123] reported a coordinatively linked interpenetrated MOF, the PCN-17, which has the porous structure containing large cages linked by relatively small apertures and retains its porosity at temperatures >480°C. It selectively adsorbs H₂ and O₂ over N₂ and CO aiming at fuel-cell applications.

Taking into account the guest-surface interaction, it is worth noting that the selectivity is related to adsorbate properties such as polarity, quadrupole moment and H-bonding. Matsuda et al. [124] reported the selective adsorption of C₂H₂ over CO₂ at low pressures and room temperature in Cu₂(pzdc)₂(pyz), where pzdc is pyrazine-2,3-dicarboxylate and pyz is pyrazine. Selective adsorption based on the hydrophobic/hydrophilic properties of pores was observed in the Zn (tbip) [125], (tbip-5-tert-butyl isophthalic acid), Zn(bdc)(ted)_{0.5} [126], (bdc -1,4 benzene dicarboxylate, ted-triethylenediamine) and CID-1 [127], (CID-coordination polymer with interdigitated structure). These MOFs selectively adsorb MeOH, EtOH and dimethyl ether over H₂O. Several MOFs selectively adsorb CO₂ over CH₄ because CO₂ has a large quadrupole moment whereas CH₄ has none. For example, Mn(ndc) (naphthalenedicarboxylate) [128] is a 3D microporous MOF with 1D channels which contain unsaturated metal sites. The adsorption measurements show that CO₂ is more adsorbed than CH₄ at ambient temperature. Similarly, Bae et al. [129] reported selective adsorption of CO₂ over CH₄ in a carborane based-MOF with coordinatively unsaturated metal sites. Recently, Mu et al. [130] synthesized a new 2D interpenetrating MOF with unsaturated metal sites and uncoordinated carboxylic group, exhibiting a high selectivity (~13) for CO₂ over CH₄.

In recently developed ZIFs, high storage capacity for CO₂ and selective adsorption of CO₂ over CO were identified in ZIF-68, ZIF-69 and ZIF-70 [58]. In ZIF-95 and ZIF-100 with large cavities and

highly constricted pores, a higher affinity was found for CO₂ over CH₄, CO and N₂ [131]. A high selectivity for CO₂ is due to the combined effects of the aperture sizes, strong quadrupolar interactions of CO₂ with the N surface atoms and higher condensability of CO₂ than other gases.

Catalytic applications

MOFs have large potential in numerous catalytic applications. The study of MOFs as catalysts has only recently begun with the majority of the work achieved during the last few years. The mild synthetic conditions typically employed for MOF synthesis allow direct incorporation of a variety of delicate functionalities into the framework structures. The high surface area, tunable porosity, diversity in metal and functional groups of MOFs makes them especially suited for use as catalysts. Furthermore, the set geometry of the MOFs internal framework allows for their use as size selective catalysts.

Fujita et al. first reported a MOF-based catalyst in a 2D square network material for the cyanosilylation of aldehydes and imines [131]. Evans et al. reported the catalytic properties of set of the homochiral porous lamellar lanthanide biphosphonates [132]. Seo et al. reported the homochiral MOF as the catalysis of trans-esterification in enantioselective manner [133]. Enantiopure chiral ligands or their metal complexes can be incorporated directly into the frameworks of MOFs to lead to efficient asymmetric catalysts. Wu et al. reported the synthesis of a highly porous homochiral MOF and its application in heterogeneous asymmetric catalysis and stereo selectivity rivaling its homogeneous counterparts [134]. Ravon et al. studied the Friedel-Crafts tert-butylation of both toluene and biphenyl in the cubic compound MOF-5 [135]. They found that the MOF-5 catalytic activity is attributed to the encapsulated zinc-hydroxide clusters or to the hydrolytically degraded form of the parent materials. Kaskel and co-workers [136, 137] showed that the Lewis acid sites in HKUST-1 can catalyze cyanosilylation of benzaldehyde or acetone. They also found that MIL-101 is much more active than HKUST-1 as a catalyst for the cyanosilylation of benzaldehyde due to the greater Lewis acidity of Cr (III) vs Cu (II). Alaerts et al. [138] investigated behavior of HKUST-1 as acid catalyst. Eddaoudi and coworkers [139] encapsulated cationic porphyrins in the rho-ZMOF during synthesis and achieved more than 60% loading. They demonstrated that encapsulated free-base porphyrin could be metallated with the Mn, Co, Zn or Cu ions and showed a catalytic activity towards oxidation of cyclohexane in Mn-metallated porphyrin. Hasegawa et al. [140] synthesized a catalytic MOF which consists of the identical pairs of networks and two single cadmium ions, octahedrally ligated by pyridyl nitrogen. They found that the MOF is capable of base-catalyzing the Knoevenagel condensation of the benzaldehyde with malononitrile. Ferey and co-workers [141] modified interior of MIL-101 via Cr(III) coordination with the N atoms of ethylenediamine molecules. They tested the catalytic activity of MIL-101 for the Knoevenagel condensation of benzaldehyde with nitriles. According to the theoretical calculation MOFs might be also use in photocatalysis [141].

1.2. Gas Storage/Adsorption

1.2.1. Single-component adsorption

H₂ Storage

Considerable interest has been shown in the development of non-petroleum energy carriers for use in transportation. Hydrogen is an attractive option because it has a high energy content (120 MJ/kg compared to 44 MJ/kg for gasoline), produces clean exhaust product (water vapor without CO₂ or NO_x), and can be derived from a variety of primary energy sources. A key issue for a practical utilization of H₂ is development of safe and high-capacity systems for the H₂ storage. The U.S. Department of Energy (DOE) has set the targets for on-board H₂ storage as of 6.0 wt% and 45 g/L by 2010, and 9.0 wt% and 81 g/L by 2015 [142]. Considerable research has been undertaken over the past two to three decades to determine the H₂ storage capacity in different carbon nanostructures such as activated carbon, graphite, carbon nanofibres, carbon nanotubes, fullerenes and also in zeolites, metal hydrides and MOFs. Several techniques such as the Monte Carlo, molecular dynamics and first-principle approaches have been employed to examine the H₂ adsorption in different classes of materials and in turn guide to rational design of adsorbent materials that can meet storage targets.

Ab initio calculations have been reported to investigate an interaction of H₂ with MOFs and COFs. Hüber et al. [143] studied H₂ interaction with MOFs using approximate resolution of the identity Møller-Plesset (MP2) [144-146] calculations and triple zeta valence basis set (TZVPP) [163]. They estimated the binding energies between H₂ and various substituted benzenes such as C₆H₆, C₆H₅F, C₆H₅OH, C₆H₅NH₂, C₆H₅CH₃ and C₆H₅CN. The binding energies of H₂ to benzene and naphthalene are of 3.91 and 4.28 kJ/mol, respectively, indicating that enlarging the aromatic systems increases the interaction energy. Sagara et al. [147,148] calculated the binding energy of H₂ with organic linker and metal-oxide part in IRMOF-1 using MP2 with the quadrupole zeta QZVPP [149] basis set. In addition, they calculated H₂ interaction with organic linkers in various MOFs (the IRMOF-1, IRMOF-3, IRMOF-1-4NH₂, IRMOF-6, IRMOF-8, IRMOF-12, IRMOF-14, IRMOF-18 and IRMOF-993) and found that the larger linkers bind more H₂ molecules and addition of NH₂ or CH₃ group to each linker increases a binding energy by up to 33%. Han et al. [166] performed the MP2/QZVPP calculation to find a binding energy of the H₂ with different metal oxides and found that the substitution of metal sites from the Zn to Mg and Be does not change the configuration, with the Mg cluster showing the higher binding energy.

The Grand Canonical Monte Carlo (GCMC) simulations are commonly used to predict gas adsorption in confined space. Sagara et al. [150] studied the uptake of H₂ in MOF-5 using GCMC simulation and found that the experimental data are underestimated predicted results. Yang and Zhong [151] simulated the H₂ adsorption isotherm in IRMOF-1, IRMOF-8 and IRMOF-18 by refitting the parameters using the OPLS-AA force field [152] and obtained better agreement with experimental results. Similarly, Yang and Zhong [153] simulated H₂ isotherm in the IRMOF-1 and Cu-BTC at 298 K up to 70 bar and extended their simulations to MOF-508 with open metal sites.

The presence of open metal sites was found to have a favorable impact on the H₂ uptake, but an uptake was still low at room temperature. Garberoglio et al. [154] predicted the H₂ adsorption isotherms in various MOFs namely, the MOF-2, MOF-3, IRMOF-1, IRMOF-5, IRMOF-8 and IRMOF-14 using the UFF [155] and the DREIDING force fields [156]. The simulation results agreed better with experiments considering the quantum effects, and without the quantum effects they are overestimated in the IRMOF-1 and underestimated in the IRMOF-8 at 1 bar and 77 K. Frost et al. [157] used the GCMC simulations to predict the adsorption isotherm of H₂ in ten different non-interpenetrating MOFs. The calculated results reveal existence of three different adsorption regimes: at low pressures, the H₂ uptake correlates with the heat of adsorption; at intermediate and higher pressures, correlates with the uptake, the surface area and free volume. Jung et al. [158] studied the effect of catenation on the H₂ adsorption in catenated MOFs using the GCMC and found that the small pores generated by catenation play a significant role in densely confining H₂ molecules; therefore, the capacity in catenated frameworks is higher than that of the non-catenated counterparts. Similarly, Ryan et al. [159] reported the effect of catenation on the H₂ uptake in MOFs and found that catenation can be beneficial for improving the H₂ storage in MOFs at a cryogenic temperature and low pressures, however not necessarily at a room temperature.

To improve the H₂ storage capacity in MOFs, Zhang et al. [160] designed new hypothetical MOFs by exchanging the organic linker in MOF-5 with oxalate and introducing –F, –Cl, –CF₃ and –CCl₃ to tune the electronegativity of the linkers. They simulated H₂ adsorption isotherm up to 1 bar and 77 K and found that the proposed MOFs show high H₂ uptake at low pressures. Frost and Snurr [161] investigated how to improve H₂ storage to meet the current DoE targets. They artificially increased H₂–MOF Lennard-Jones attraction and found that the gravimetric H₂ uptake of 6 wt % could be achieved in a MOF with a free volume between 1.6 and 2.4 cm³/g. In MOFs with free volumes less than 1.5 cm³/g the isosteric heat larger than 20 kJ/mol is required to achieve 6 wt%. Garberoglio [162] simulated H₂ uptake in different COFs consisting of lighter elements such as C, B, Si, O and H. The H₂ adsorption isotherm in 3-dimensional COFs (COF-102, COF-10, COF-105 and COF-108) at 77 and 298 K showed a higher capacity in COF-105 at 77 K and the COF-108 at 298 K. Similar work was reported by Klontzas et al. [163] showing a gravimetric H₂ uptake of 21 wt% at 77 K and 100 bar in COF-108 and 4.5 wt % at room temperature and 100 bar. Most GCMC studies have used empirical force fields such as the UFF [155], the DREIDING [156] and the OPLS-AA [152] to predict the H₂ adsorption in different MOFs and COFs. Goddard et al. [164-166] considered non-bonded interactions between H₂ and MOFs (or COFs) and H₂–H₂ using high level *ab initio* calculations. Based on the *ab initio* force field, accurate H₂ adsorption isotherms in the IRMOF-1 and MOF-177 and 2D- and 3D-COFs were shown. Namely, the IRMOF-1 simulation indicated the H₂ adsorption of 1.28 wt % at 77 K and 1 bar, 4.17 wt % and 4.89 wt % at pressures of 20 and 50 bar, which are comparable with experimental results under the same conditions. In COF-5 the simulation data are also in good agreement with the experimental results. As none of the studies reported for the H₂ adsorption in MOFs and COFs meet the DOE targets, several strategies were proposed to improve the storage capacity of H₂ in MOFs and COFs.

Rowsell and Yaghi [97] discussed six strategies for high H₂ adsorption in MOFs, such as high porosity with appropriate pore size, impregnation, catenation, open metalsites, light metals and functionalized linkers. Using the GCMC simulation based on *ab initio* force field, Han et al. [166] found a large heat of adsorption for H₂ of 8.8 kJ/mol in COF-1 due to appropriate pore size, showing a high uptake of 1.7 wt % at 0.1 bar which is higher than in other COFs, such as COF-5, COF-102, COF-103, COF-105 and COF-108. However, at 300 K COF-1 shows a low H₂ storage of 0.78 wt % at 100 bar. Yaghi and co-workers [97] suggested insertion another adsorbate molecule in large-pore MOFs to create appropriate pore size for high H₂ adsorption. Using this approach, Han et al. [156] obtained the C₆₀ loaded MOF-177 by the GCMC simulation at 300 and 1 bar and the standard DRIEDING force field. They found that at low pressures the H₂ uptake increases by an inclusion of C₆₀ into MOF-177 at 77 K and 300 K. However, at high pressures it decreases due to a reduction in pore volume. Another way to reducing MOFs pore size is a framework catenation. Jung et al. and Ryan et al. proved that catenation increases the H₂ adsorption at 77 K, but not at 300 K [167].

Open metal sites can also be used to enhance the H₂ binding energy (up to 10-50 kJ/mol) by using different transition metals in the MOF systems [167-169]. Doping alkali elements on the organic linker parts of MOFs and COFs was considered as another strategy to improve the H₂ uptake [170-175]. Recently, Cao et al. [176] simulated the H₂ adsorption in Li-doped COFs using *ab initio* based force field and the GCMC simulations and reported exceptionally high uptake of H₂ at 298 K and 100 bar in COF-105 (6.84 wt %) and COF-108 (6.73 wt %).

CH₄ Storage

Natural gas, which consists mainly of the CH₄, is considered as an alternative fuel to traditional fossil fuels. The U.S. DOE has set a storage target of 180 v/v (the volume of gas adsorbed at standard temperature and pressure per volume of the storage vessel) at 35 bar [110]. Düren et al. investigated the CH₄ storage in several IRMOFs, zeolites, MCM-41 and carbon nanotubes [108]. They found a correlation between the CH₄ adsorption at 35 bar and 298 K and the surface area and suggested that an ideal adsorbent for the CH₄ storage should have a large surface area, high free volume, low framework density and strong adsorbent-adsorbate interactions. Based on these criteria, they proposed a hypothetical structure with different linkers showing high uptake of CH₄ [108]. Wang simulated the CH₄ adsorption in a series of IRMOFs namely IRMOF-1, -6, -8, -10 and -14, Cu-BTC, CPL-28, CPL-522 and Cu(AF₆)(bpy)₂. Similar to Düren et al., conclusions the surface area was found to play a dominant role in CH₄ adsorption at room temperature and moderate pressure. The heat of adsorption correlated well with a pore size at low loadings and with surface area and free volume at high loadings [177]. Jhon et al. [178] studied the CH₄ adsorption in alkoxy-functionalized variations of IRMOF-1. It was found that the pores constricted by the alkoxy-functionalized linkers promoted the CH₄ adsorption at low to moderate pressures along with decrease of the saturation capacities. The propoxy-functionalized IRMOF-1 showed the largest volumetric adsorption at low to moderate pressures due to a combination of long linkers and small pores.

CO₂ Storage

Kawakami et al. [179] simulated the CO₂ adsorption in Zn₃(bdc)₃ at 78 K using *ab initio*. They found that the framework charge has a substantial effect on the CO₂ saturation capacity. Walton et al. [180] calculated the CO₂ adsorption isotherms in IRMOF-1 at different temperatures which match qualitatively with experimental results. They showed that an inclusion of electrostatic interaction between the CO₂ molecules is required to capture an inflection in the adsorption isotherms. In addition, Walton et al. [180] predicted the CO₂ adsorption isotherms in IRMOF-3 and MOF-177 at 298 K and found good agreement with experiments. It was concluded that inclusion of framework charges has negligible effect on the CO₂ adsorption in different MOFs.

Yang et al. [181] predicted the CO₂ adsorption isotherms in various MOFs (Cu-BTC, IRMOF-1, -8, -10, -11, -14, -16, MOF-177 and Mn-MOF) by fitting parameters to match experimental data. At moderate pressure of 30 bar, the CO₂ uptake is related to both free volume and surface area. They also found that electrostatic interaction between CO₂ and framework atoms enhances the adsorption by ~ 20-30 % at low pressures and decreases to ~ 3 % at high pressures compared with the neutral framework. Ramasahye et al. [182-184] calculated CO₂ adsorption in MIL-53 (Al) and MIL-53 (V). They used the charges computed by the DFT method and a three site model for CO₂. They predicted the adsorption isotherms and enthalpies of the adsorption in two different structures of MIL-53 (Al), namely narrow-pore MIL-53np (Al) and large-pore MIL-53lp (Al) forms, having the same chemical identity but different pore widths of 8.3 and 13.8 Å, respectively. The simulated enthalpy in MIL-53np (Al) matches the experimental results at low pressures, while the enthalpy in MIL-53lp (Al) agrees with the experimental data at high pressures. This finding is consistent with a structural transition from narrow-pore form to large-pore form in MIL-53(Al) during the CO₂ adsorption. They also calculated the CO₂ adsorption isotherms at 303 K for pressure up to 30 bar in the two MIL-53(Al) structural forms and concluded that the μ₂-OH groups in MIL-53(Al) is the main factor for structural transition. The calculated adsorption isotherm for CO₂ in MIL-53(V) overestimates responsible experimental results probably due to a presence of incomplete solvent molecules in the experimental samples. In addition, Ramasahye et al. [185] used the DFT to probe different adsorption sites for the CO₂ adsorption in MIL-53 (Al, Cr) and MIL-53 (V).

Other Gases

Kawakami et al. [179] simulated the N₂, O₂ and Ar adsorption in Zn₃(bdc)₃ and compared predicted N₂ adsorption with experimental data up to 1 atm. They found that the predictions were of 1.7 -fold higher than the experimental data. They also observed the O₂ magnetic chain formation due to a confinement of the O₂ position and orientation by the Zn₃(bdc)₃ pores. Vishnyakov et al. [186] investigated the Ar adsorption in Cu-BTC using the GCMC simulations and experimental measurements at 87 K. The simulated isotherms using UFF [155] agree well with experiments over most loadings but over-predicted the saturation loading. The preferential adsorption sites were identified, first in the side pockets and followed by condensation in the main channels. Dubbeldam et al. [187] studied adsorption isotherms for Ar and N₂ in IRMOF-1 at 78 K. They scaled down the simulated adsorption isotherms by a factor of 0.725 to match the experimental data and identified

the adsorption sites for Ar and N₂ in IRMOF-1. The positions and occupations of the adsorption sites match well with experiments. The molecules are localized around their crystallographic sites at 30 K, however, at 300 K they are quite dispersed inside the pore. Preferential adsorption sites were also identified for many gases such as Ar, N₂, CO₂, CH₄, H₂, C₂H₆ and C₃H₈, which are near to the ZnO₄ cluster with the organic linkers pointing outward.

Walton et al. [188] calculated the BET surface areas in various IRMOFs, IRMOF-1, -6, -10, -14, -16 and -18, using the N₂ adsorption isotherms and found good agreement with the accessible surface areas estimated from crystal structures. They concluded that by careful choosing of pressure range, the BET method can be used to obtain the surface areas of MOF materials. Yang et al. [189] simulated the adsorption isotherms of N₂ and O₂ in the Cu-BTC and adjusted the potential parameters to match experimental adsorption isotherms at 295 K and pressure up to 1 bar. Later they used these potentials to study multicomponent adsorption. Garberoglio et al. [154] predicted the Ar adsorption isotherms in Cu-BTC at 87 K and in manganese formate at 78 K. The simulated result agrees well with experiment at low pressure. However, it is overestimated at high pressure by a factor of ~ 30 % and ~ 50 %, respectively. Since the experiment was conducted at temperature lower than the triple point of Ar (83.8 K), a discrepancy may arise due to a formation of bulk, like the Ar clusters on the adsorbent surface. Similarly, Garberoglio et al. [162] simulated the Ar adsorption in the COF-102 and COF-103 at 87 K using the UFF and DRIEDING force fields and compared with experiments. The predicted adsorption overestimated experiments by ~ 25 % upon saturation and was worse at low pressures. The author mentioned that this discrepancy might be due to a number of effects, including the defects in a crystal structure, inaccurate solid-fluid interaction potentials and structure change upon adsorption at high loadings.

1.2.2. Multi-component adsorption

The potential of MOFs for separations of variety of gas mixtures such as CO₂/N₂, CO₂/CH₄, CO₂/CO, CO₂/C₂H₄, C₂H₆/C₂H₄, and hydrocarbons has been investigated both experimentally [190–198] and using molecular simulations [199–205].

Düren and Snurr [206] reported the CH₄/n-C₄H₁₀ multicomponent adsorption in the IRMOFs-1, -8, -10, -14 and -16 at room temperature and pressure up to 40 bar. They simulated pure CH₄, C₄H₁₀ and their multicomponent adsorption in MOFs aiming at investigation of the linker's effects on the adsorption process. The CH₄ shows a type-I isotherm, whereas the C₄H₁₀ isotherm is more complex and shows sharp jumps. Selectivity of the n-C₄H₁₀ adsorption over the CH₄ increases upon pore size reduction and increase of carbon atom number in a linker. Based on these results, the authors proposed a hypothetical structure with the 9,10-anthracenedicarboxylate linker and named it IRMOF-993. The predicted selectivity in this structure is as high as 2500. Jiang et al. [207] examined multicomponent adsorption of the C₁-n-C₅ linear alkanes and C₅ isomers in IRMOF-1, silicalite and (10,10) carbon nanotubes. They found that an enthalpy effect dominates at low pressures, favoring long alkanes over short alkane and linear alkanes over branched alkanes,

while at high pressures entropy effects become important, favoring adsorption of short alkanes, explain.

Yang et al. [189] predicted adsorption separation of CO₂ from CO₂/N₂/O₂ mixtures, a representative of the flue gas in Cu-BTC. They reported selectivity of 20 at room temperature and a total pressure of 5 MPa. Similarly, Wang et al. [208] performed simulation in Cu-BTC for separation of CO₂ from CO and olefins from their mixtures with paraffins. For an equimolar mixture, a selectivity of CO₂ over CO is of ~ 25 at a pressure of 5 MPa, whereas a selectivity of C₂H₄ from CO₂ is ~ of 2 under the same conditions. Wang et al. [209] predicted mixture selectivity of the CO₂/CH₄/C₂H₆ mixture in the manganese-formate MOFs. They found that a selectivity of the CO₂/CH₄ mixture is higher than that in the IRMOF-1 and Cu-BTC materials [210]. Martin-Calvo et al. [216] studied the adsorption and separation of natural gases considering two- and five-component mixtures, in IRMOF-1 and Cu-BTC. They found that the adsorption capacity is higher in IRMOF-1 and the adsorption selectivity of CO₂ over CH₄ and N₂ is higher in Cu-BTC. Yang and Zhong [153] performed the GCMC simulations to investigate the separation features of Cu-BTC and IRMOF-1 for mixtures of CO₂, CH₄ and H₂. Adsorption selectivity varies on the structure topology and interaction strength of framework with adsorbates. Selectivity of CH₄ over H₂ in an equimolar mixture at room temperature and pressure of 5 MPa was found to be ~ 6 and ~ 12 in IRMOF-1 and Cu-BTC, respectively. In IRMOF-1, selectivity of CH₄ over H₂ is nearly independent of pressure. On the other hand, selectivity of CO₂ over H₂ shows a different trend in Cu-BTC, which initially decreases and then increases, reaching a maximum and finally decreases at high pressures. At a pressure of 5 MPa, the selectivity of CO₂/H₂ is around 40 and 110 in IRMOF-1 and Cu-BTC. The ideal adsorbed solution theory (IAST) has been tested to compare multicomponent selectivity with simulation results. For the CH₄/H₂ mixture, IAST predicts the multicomponent selectivity quite accurately upon comparing with the simulation. However, for the CO₂/H₂ mixture a prediction from IAST is poor. This discrepancy can be attributed to a difference in size and interaction strength of adsorbates with the MOFs.

The siting and segregation of complex alkane mixtures were simulated in MOFs. Suggested possibilities were new for the design of highly selective adsorption sites in MOF-1 towards separation of the alkanes according to their degree of branching and research octane number (RON) from mixed stream [211]. The alkanes in Cu-BTC were studied by infrared microscopy combined with molecular simulation. Both experiments and simulations show strong inflection characteristics due to the adsorption preference within, and in the regions close to the mouths of tetrahedral pockets [212]. Liu et al. [213] performed simulation to study the interpenetration effect on a mixture separation in MOFs. They chose different MOFs with and without interpenetration (IRMOFs -10, -12, -14 and IRMOFs -9, -11 and -13) to compare the adsorption selectivity of the CH₄/H₂ mixtures separation at room temperature. The results showed that the permeation selectivity in the interpenetrated frameworks is much higher than those in their non-interpenetrated counterparts due to the larger adsorption selectivity in the former. Recently, Liu et al. [214] performed a systematic simulation study to compare a separation of the CO₂/N₂ and CH₄/N₂ mixtures in two classes of nanoporous materials, zeolites and MOFs.

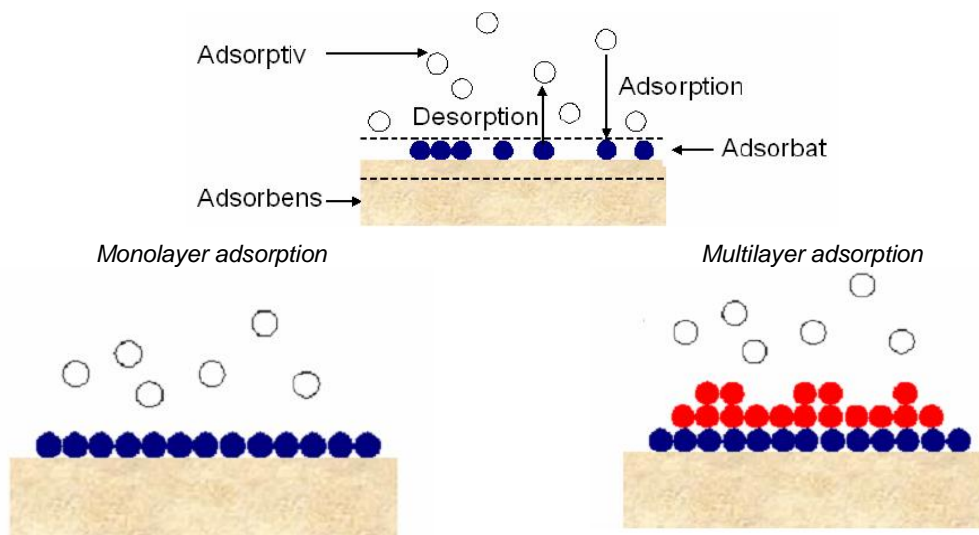
1.3. THERMODYNAMICS of GAS ADSORPTION

1.3.1. Supporting theory

When the adsorbent and adsorptive are in contact, the equilibrium is established between the amounts of adsorptive adsorbed on the adsorbate surface and the amount of free adsorptive in the volume. The equilibrium relationship is described by isotherms.

The adsorption isotherm for a pure gas is the relation between the specific amount adsorbed n (moles of gas per gram of solid) and P , the external pressure in the gas phase.

In a typical adsorption process, species/materials in gaseous or liquid form (the adsorptive) become attached to a solid or liquid surface (the adsorbent) and form the adsorbate [Scheme 1.1].



The heat of adsorption of the first monolayer is much stronger than the heat of adsorption of the second and all following layers. Typical for *Chemisorption* case

The heat of adsorption of the first layer is comparable to the heat of condensation of the subsequent layers. Often observed during *Physisorption*

Scheme 1.1. Presentation of a typical adsorption process (after [215]). Since the adsorptive and the adsorbent often undergo a chemical reactions, the chemical and physical properties of the adsorbate are not always just the sum of the individual properties of the adsorptive and the adsorbent, and often represent a phase with new properties ([215] Christmann, 2010).

Knowledge of the adsorption equilibrium and heat of adsorption is essential for proper design and operation of any gas phase adsorption process. The latter is usually estimated from the temperature dependence of the adsorption isotherm. Therefore, correlations that capture the correct temperature dependence over a relatively wide range are essential for designing and operating gas-phase adsorption processes. However, the assumption of a constant heat of adsorption, over a relatively large temperature interval, introduces in practice only small errors in the pressure and loading estimations. This is why the assumption of a temperature-invariant heat of adsorption is frequently adopted.

1.3.1.1. Adsorption in microporous solids

The thermodynamic treatment of adsorption phenomena is based on the Gibbs dividing surface, which is conceptually clear for a flat surface. On a flat surface, the primary extensive property is the area of the solid. As applications became more significant, necessitating microporous solids, early researchers such as McBain and Coolidge [216-218] implemented the Gibbs definition by invoking a reference state for microporous solids. The mass of solid is used as a primary extensive property because surface area loses its physical meaning for microporous solids. A reference state is used to fix the hypothetical hyperdividing surface typically using helium as a probe molecule, resulting in the commonly used excess adsorption (n_{ex}) [219]; experimentalists measure this reference state for each new sample. Molecular simulations, however, provide absolute adsorption (n). Theoreticians perform helium simulations to convert absolute to excess adsorption, mimicking experiments for comparison. This current structure of adsorption thermodynamics is rigorous (if the conditions for reference state helium measurements are completely disclosed) but laborious. In addition, many studies show that helium, or any other probe molecule for that matter, does adsorb, albeit to a small extent.

An adsorbed phase cannot exist autonomously; it exists only at the interface between two bulk phases, a solid phase and a fluid phase. Therefore, any thermodynamic property (amount adsorbed, enthalpy, entropy, etc.) of an adsorbed phase is measured as its value for the two-phase system relative to its value in some reference state.

Consider a nanoporous solid adsorbent in equilibrium with a bulk gas of density ρ_g at some T and P as shown in Fig. 1.9a. The container represented by the outer box in the Fig. 1.9 encloses the gas in the bulk phase along with the solid adsorbent and adsorbed gas molecules. The total volume of the container is V . The solid adsorbent is represented by small shaded squares (with a total volume of V_s for all squares); the pores are represented as channels between squares (with a total volume of V_p). The gas molecules are indicated by black dots. The density is higher in the channels (more black dots) than in the bulk phase away from the solid. Away from the solid, the gas occupies a volume of V_g . Although such a schematic simplifies the geometry of the nanoporous adsorbent, it correctly depicts the essential features. The known container volume is conceptually partitioned into three regions.

$$V = V_s + V_p + V_g \quad (1.1)$$

Only the container volume, V , can be measured without any ambiguity. The reference state choice fixing the Gibbs dividing surface determines the partitioning among the three regions (i.e., V_s , V_p , and V_g).

The following three definitions for reference states, which essentially differ in their definitions of the bulk phase volume, provide meaningful descriptions of the adsorption process [217]. These definitions are depicted in Fig 1.9 (b-d)

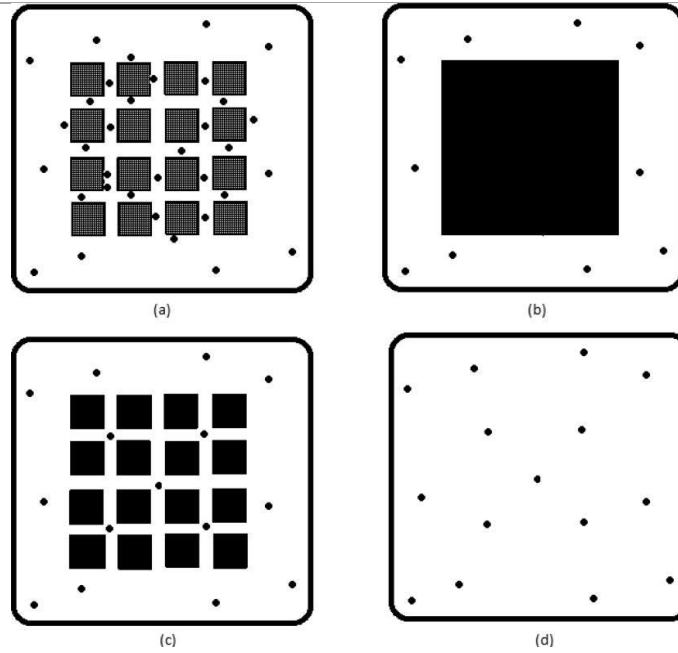


Figure 1.9. Schematic illustrating various reference states for the definition of adsorption. (a) A typical scenario at equilibrium between a gas and a porous solid. (b-d) Reference states for absolute, excess, and net adsorption, respectively.

The regions shaded black in this Fig. 1.9 refer to the volume that is not available to the bulk gas (impenetrable solid volume) and are considered to be on the “solid” side of the Gibbs dividing surface with $\rho(x)=0$. The gas occupies whatever is left over, the region defined as the bulk phase volume, at a density equivalent to its bulk density at the given T and P ; $\rho(x)=\rho_g$ by the Gibbs definition. The region shaded black in Fig. 1.9b is the volume occupied by the adsorbent, including its pores. The difference of the amount of gas present in parts (a) and (b) of Fig. 1.9 is equal to the amount of fluid present within the pores of the adsorbent as a result of adsorption, the so-called absolute adsorption. This definition (*reference state A*) fixes the Gibbs dividing surface at the “outer” surface of the adsorbent; the bulk phase extends only until this surface whereas the solid phase includes all of the pores. The reference volume for the gas to be experimentally measured for absolute adsorption is:

$$V_g = V - V_s - V_p \quad (1.2)$$

The region shaded black in Fig. 1.9c is the so-called impenetrable solid volume of the adsorbent. The difference in the amount of gas present in parts (a) and (c) of Fig. 1.9 is equal to the so-called Gibbs surface excess adsorption in the literature. Note that the channels in Fig. 1.9c are occupied by gas molecules at a density equivalent to the bulk gas density, which in reality is not an achievable condition in experiments. This definition (*reference state B*) fixes the dividing surface at the “inner” surface of the adsorbent, but pores are included in the bulk phase. The reference volume for the gas to be experimentally measured for excess adsorption is:

$$V_g = V - V_s \quad (1.3)$$

A third definition (*reference state C*) of the Gibbs dividing surface extends the bulk phase all the way into the impenetrable solid as indicated in Fig. 1.9d. This definition of the reference state involves the amount of gas present in the empty container (i.e., with no adsorbent present in the container), as called the net adsorption (n_{net}). The net amount adsorbed is equal to the difference in the amount of gas present in parts (a) and (d) of Fig. 1.9. The reference volume for net adsorption does not need any additional experimental measurement; it is simply the volume of the container.

$$V_g = V \quad (1.4)$$

From a thermodynamic perspective, any reference state is acceptable as long as it is easily measurable without ambiguity. It is possible to convert and compare data based on different states through rigorous thermodynamic relations. Coolidge's work [217] only identifies and highlights the differences in using various reference states and concludes that the choice of a reference state may be based on the "purpose at hand".

Later developments in this area were biased toward *reference state B*, excess adsorption. This development in history may be due to the proximity of the excess adsorption to adsorption on flat solid surfaces. Adsorption in micropores based on excess adsorption can readily be used with models (i.e., Langmuir and BET) developed for flat surfaces. However, some works advocate the use of absolute adsorption [220] on the basis of *reference state A* because it can be directly compared to simulation results. To the best of our knowledge, *reference state C* defining net adsorption was not investigated after the Coolidge works. Before elaborating on net adsorption, the following issues highlight difficulties in experimentally and theoretically determining the reference states for absolute and excess adsorption (*reference states A and B*), which require ambiguous measurements of the pore volume and the impenetrable solid volume.

At low pressure, specific properties such as the amounts adsorbed according to the three definitions are essentially equivalent whereas differential properties such as the Henry constants differ substantially. At high pressure, the differences in all properties are profound. The absolute adsorption increases monotonously with pressure whereas excess and net adsorption exhibit maxima. The maximum in the amount adsorbed occurs at a pressure where the rates of change in density (with pressure) for both the adsorbed and the gas phases are equal.

There are two of the most common methods used for measuring adsorption *viz.* the volumetric and gravimetric techniques [221]. A simple volumetric setup for the measurement of pure-gas adsorption equilibrium is shown in Fig. 1.10a. Initially, the solid adsorbent contained in the adsorption column is activated (to remove previously adsorbed species) under appropriate conditions, and the column is sealed under vacuum. Both the column and reservoir are maintained at the desired temperature T . The reservoir is then charged with gas to a predetermined pressure ρ_0 . The valve between the reservoir and column is opened, and adsorption equilibrium is

established between the solid and the gas; the final equilibrium pressure p_g is noted. The contents of the column (in both adsorbed and bulk phases) at equilibrium are equal to the moles exchanged between the reservoir and the column, ΔN ,

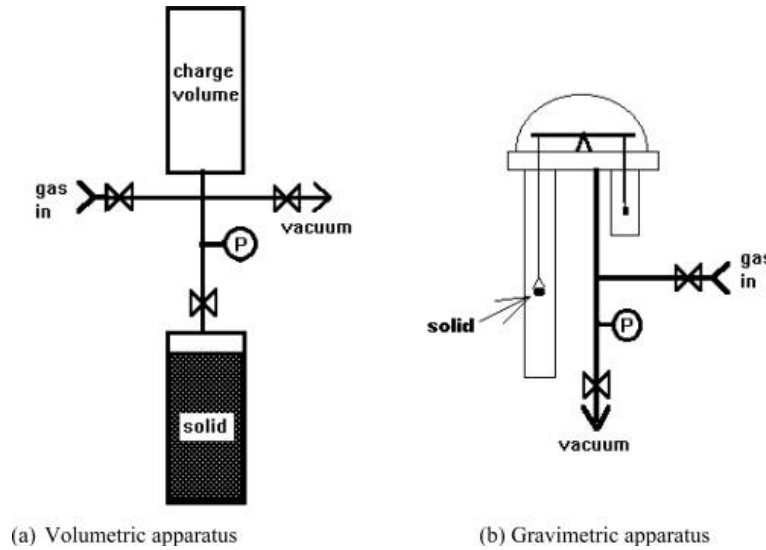


Figure 1.10. Common isotherm measurement systems

$$\Delta N = V_0(\rho_0 - \rho_g) \quad (1.5)$$

where V_0 is the volume of the charge reservoir and ρ_0 and ρ_g are the molar densities in the charge reservoir before and after the valve is opened. In general, the amount adsorbed n^{ads} per unit adsorbent mass m_s is given by (1.6):

$$n^{ads} = \frac{\Delta N - V^{ref} \rho_g}{m_s} \quad (1.6)$$

where V^{ref} is the volume assigned to the bulk phase on the basis of the chosen reference state.

Apart from V^{ref} , an experimental determination of adsorption requires independent knowledge of the reservoir volume V_0 and sample mass m_s , irrespective of the chosen reference state. As explained earlier, V^{ref} for net, excess, and absolute adsorption are (V_{col}) , $(V_{col} - V_s)$ and $(V_{col} - V_s - V_p)$, respectively. In addition to other advantages of net adsorption outlined earlier, from a purely experimental perspective one needs to determine, V^{ref} ($=V_{col}$) only once because it is fixed for a given experimental apparatus. Subsequent changes in the sample do not necessitate additional measurements. In contrast, reference states for both absolute and excess adsorption involve the solid adsorbent, and V^{ref} needs to be measured every time the adsorbent sample is changed (using helium as the probe gas).

A simple gravimetric setup is shown in Fig. 1.10b. Initially, the adsorbent is placed in a bucket, activated under appropriate conditions, and sealed. The signal from the microbalance under vacuum m_0 is due to the mass of the sample (m_s) and the bucket (m_{bucket}). The sample is then allowed to equilibrate with the gas of interest at equilibrium pressure P_g and temperature T (at a gas molar density of ρ_g). The signal from the microbalance m_t is recorded under equilibrium

conditions. The change in the microbalance signal Δm is a result of adsorption occurring on the solid surface and the total buoyancy force. In general, the adsorbed amount per unit solid mass is given by (1.7):

$$n^{ads} = \frac{1}{m} \left(\frac{\Delta m}{MW_g} + V^{ref} \rho_g \right) \quad (1.7)$$

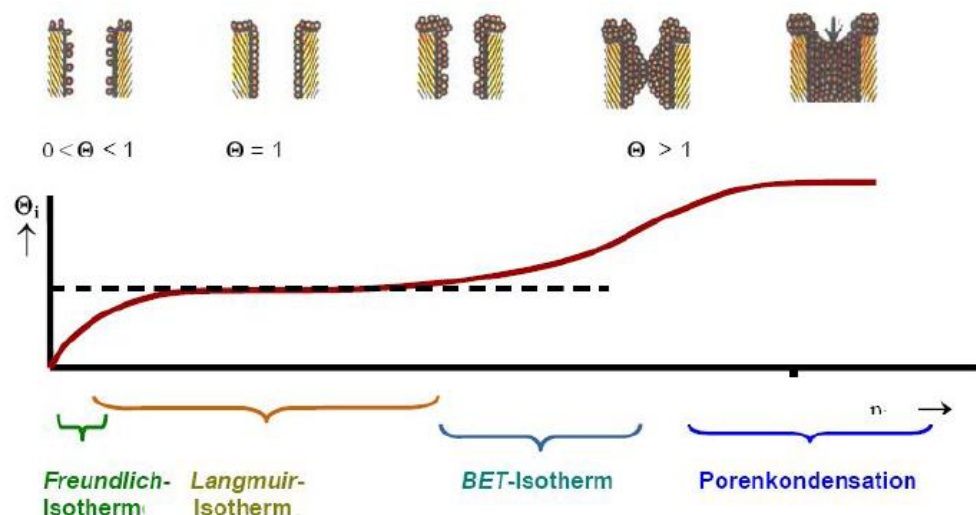
where MW_g is the molar mass of the gas and V^{ref} is the volume experiencing the buoyancy force. To determine the adsorbed amount in addition to V^{ref} , knowledge of the mass of the clean adsorbent in vacuo (i.e., m_s) is necessary.

The buoyancy volume V^{ref} is fixed on the basis of the reference state. In the case of net adsorption, the buoyancy correction is needed only for forces acting on the bucket. For excess adsorption, the buoyancy correction for the impenetrable solid volume is also needed. Finally, for absolute adsorption, yet another correction for the buoyancy acting on the pore volume is also necessary. Thus, (V^{ref}) is (V_{bucket}), ($V_{bucket}+V_s$), and ($V_{bucket}+V_s+V_p$) for net, excess, and absolute adsorption, respectively.

The reference state correction for net adsorption depends only on the bucket volume V_{bucket} . It needs to be determined only once for the given experimental system, similar to the determination for the volumetric apparatus. However, the reference states for both excess and absolute adsorption involve the sample; separate measurements for each sample are necessary.

1.3.1.2. Adsorption isotherm models

The experimental data are analyzed using certain adsorption models (Scheme 1.2).



Scheme 1.2. Models presentation of the adsorption process (after [215]), where symbol (θ) is the fraction of the surface sites occupied.

Whether the adsorption isotherm has been determined experimentally or theoretically, the data points must be fitted with analytical equations for interpolation, extrapolation, and for the calculation of thermodynamic properties by numerical integration or differentiation.

Langmuir isotherm model.

A model assumes monolayer coverage and constant binding energy between surface and adsorbate (1.8):

$$n = n_s \frac{K_L P}{1 + K_L P} \quad (1.8)$$

where n_s is the maximum adsorption capacity (monolayer coverage), i.e. mmol of the adsorbate per (g) of adsorbent; K_L is the constant of Langmuir isotherm if the enthalpy of adsorption is independent of coverage.

As with all equilibrium constants, K_L and, hence, the position of adsorption - desorption equilibrium, will depend on (i) the relative stabilities of the adsorbed and gas phase species involved, (ii) on the temperature of the system, and (iii) on the pressure of the gas above the surface. Factors (ii) and (iii) exert opposite effects on the concentration of adsorbed species - that is to say that the surface coverage may be increased by raising the gas pressure but will be reduced if - at constant pressure - the surface temperature is raised [215].

If the desorption energy is equal to the energy of adsorption, then the first-order processes have been assumed both for the adsorption and the desorption reaction. Whether the deviation exists, the second-order processes should be considered, when adsorption/desorption reactions involve rate-limiting dissociation. From the initial slope of a $\log - \log$ plot of a Langmuir adsorption isotherm the order of adsorption can be easily determined: if a slope is of 1, that is 1st order adsorption; if a slope is of 0.5, that is 2nd order adsorption process [215].

BET (Brunauer, Emmett and Teller) isotherm model.

This is a more general, multi-layer model. It assumes that a Langmuir isotherm applies to each layer and that no transmigration occurs between layers. It also assumes that there is equal energy of adsorption for each layer except for the first layer (1.9):

$$\frac{P}{n(P_s - P)} = \frac{1}{n_m C} + \left[\frac{C-1}{n_m C} \right] \frac{P}{P_s} \quad (1.9)$$

where n is saturation adsorbed amount (in mmol/l) n_m is saturation adsorbed amount of monolayer (in mmol/l) and C is a parameter related to the binding intensity for all layers; P and P_s are pressure and saturated pressure of the gas, respectively.

Two limiting cases can be distinguished: (i) when $C \ll 1$ and $P_s \gg P$, the BET isotherm approaches Langmuir isotherm; (ii) when the constant $C \gg 1$, the heat of adsorption of the very first monolayer is large compared to the condensation enthalpy; and adsorption into the second layer only occurs once the first layer is completely filled. Conversely, if C is small, then a multilayer adsorption already occurs while the first layer is still incomplete [215].

Freundlich isotherm model.

For the special case of heterogeneous surface energies in which the energy term (K_F) varies as a function of surface coverage the Freundlich model is used (1.10):

$$n = K_F \times P^{1/\eta} \quad (1.10)$$

where K_F and $1/\eta$ are Freundlich constants related to adsorption capacity and adsorption efficiency, respectively.

To determine which model describes the particular adsorbate/adsorbent systems better, the models linearization are used: for Freundlich isotherm - log-log plot (1.11); for the Langmuir model - the plot of $1/q_{eq}$ vs $1/C_{eq}$ (1.12); For the BET model - Eq (1.13):

$$\log n = \log K_F + \frac{1}{\eta} \log P \quad (1.11)$$

$$\frac{1}{n} = \frac{1}{K_L n_{\max}} \frac{1}{P} + \frac{1}{n_{\max}} \quad (1.12)$$

$$\frac{P}{n(P_s - P)} = \frac{1}{n_m C} + \left[\frac{C-1}{n_m C} \right] \frac{P}{P_s} \quad (1.13)$$

Sips and Toth isotherm models.

When only a subset of the adsorption data is correlated for later use in a specific gas separation application, without the need for extrapolation to other adsorbates or to a substantially different temperature range, it is more appropriate to obtain a less general but more accurate representation of the adsorption equilibria. The Sips and Toth isotherm models [222] are used here for that purpose.

The Sips isotherm can be written as (1.14, 1.15):

$$n = \frac{n_s (bP)^{1/\eta}}{1 + (bP)^{1/\eta}}, \quad b = b_0 \exp \left[\frac{Q}{RT_0} \left(\frac{T_0}{T} - 1 \right) \right] \quad (1.14)$$

$$\frac{1}{\eta} = \frac{1}{\eta_0} + \alpha \left(1 - \frac{T_0}{T} \right) \quad (1.15)$$

where n_s is the maximum adsorbed amount, $\gamma = Q/RT_0$ is the heat coefficient, η_0 and α are parameters, and Q is the isosteric heat of adsorption at half loading; η characterizes the adsorbate adsorbent, interaction it is usually greater than one, and its magnitude increases with the heterogeneity of the system, b and b_0 are empirical parameters.

The Toth isotherm is given by (1.16):

$$n = \frac{n_s b P}{[1 + b P^{1/n}]^{1/t}}, \quad t = t_0 + \alpha \left(1 - \frac{T_0}{T} \right) \quad (1.16)$$

with b defined in the same way as for the Sips model.

1.3.2. Thermodynamic parameters

Fundamental Gibbs equation

Thermodynamics describes the behavior of matter as a function of state variables (P , T , chemical composition etc.). However, since it is just a continuum description of the chemical state of systems, it is unable to describe or predict microscopic details or elementary processes on the atomic scale, nor is it capable of predicting activation energies and, hence, provides hardly any information about kinetics (time dependences) of chemical reactions.

Consider the differential change of Free Gibbs Energy (dG), the thermodynamic state of the system could be presented as:

$$\begin{aligned}
 dG &= \left(\frac{\partial G}{\partial P}\right)_{T,A} dP + \left(\frac{\partial G}{\partial T}\right)_{P,A} dT + \left(\frac{\partial G}{\partial A}\right)_{P,T} dA + \left(\frac{\partial G}{\partial n_i}\right)_{T,P,A} dn_i & \left(\frac{\partial G}{\partial P}\right)_{T,A} &= +V \\
 dG &= VdP - SdT + \sigma dA + \sum_i \mu_i dn_i & \left(\frac{\partial G}{\partial T}\right)_{P,A} &= -S \\
 & & \left(\frac{\partial G}{\partial A}\right)_{P,T} &= \sigma
 \end{aligned} \quad (1.17)$$

with P = pressure, T = temperature, A = surface area, σ = surface tension, V = system volume, μ = chemical potential and S = entropy. The third term becomes decisive, when the surface area is large in relation to the bulk volume (high degree of dispersion).

The surface tension [N/m] is entirely equivalent to the surface energy (σ) [Nm/m²], which is the driving force for all surface phenomena.

Chemical equilibrium between adsorbate and adsorptive leads to a constant surface concentration (Γ) [mmol/m²]. Constant (Γ) is maintained when the fluxes of adsorbing and desorbing particles are equal, thus the pressure and temperature dependence of this phase equilibrium are considered [215].

A common procedure is to equate the chemical potentials and their derivatives of the phases involved, where the chemical potential (μ) is the derivative of the Gibbs energy (dG) with respect to the mole number (n_i):

$$\mu_i = \left(\frac{dG}{dn_i}\right)_{P,T \text{ other mole numbers}} \quad (1.18)$$

In the (dynamic) phase equilibrium, the chemical potentials μ_{ad} and μ_{gas} are equal and remain equal ("persisting" or "ongoing" equilibrium):

$$\begin{aligned}
 \mu_{ad} = \mu_{gas} \quad \text{and} \quad d\mu_{ad} = d\mu_{gas}; \quad \Gamma = n_{ad} / A \\
 d\mu_{ad+OF} = -s_{ad+OF}dT + v_{ad+OF}dP + \left(\frac{\partial \mu_{ad+OF}}{\partial \Gamma}\right)_{p,T} d\Gamma = d\mu_{gas} = -S_gdT + V_gdP
 \end{aligned} \quad (1.19)$$

(*small letters denote partial molar quantities)

Rearranging and considering that the term of

$$\left(\frac{\partial \mu_{ad+OF}}{\partial \Gamma} \right)_{p,T} d\Gamma$$

gets zero for constant coverage ($d\Gamma=0$) yields the well-known Clausius - Clapeyron equation for the “ongoing” phase equilibrium between gas phase and adsorbate phase(s) is (1.20):

$$\left(\frac{dP}{dT} \right)_{\Gamma} = \frac{s_g - s_{ad+OF}}{V_g - V_{ad+OF}} = \frac{\Delta S}{\Delta V} \quad (1.20)$$

Setting $V_{ad+OF} \ll V_g$ and applying the ideal gas equation, i.e., $V_g=RT/P$ yields the relation (1.21):

$$\frac{1}{P} \left(\frac{dP}{dT} \right)_{\Gamma} = \frac{s_g - s_{ad+OF}}{RT} \quad (1.21)$$

Recalling that the entropy is the “reduced” heat finally leads to the expression (1.22):

$$\frac{1}{P} \left(\frac{dP}{dT} \right)_{\Gamma} = \frac{H_g - H_{ad+OF}}{RT} = \left(\frac{d \ln P}{dT} \right)_{\Gamma} = \frac{Q_{st}}{RT^2} \quad (1.22)$$

Isosteric heat of adsorption

The decisive quantities when studying the adsorption process are the heat of adsorption and its coverage dependence on lateral particle–particle interactions, as well as the kind and number of binding states [215]. The most relevant thermodynamic variable to describe the heat effects during the adsorption process is the differential isosteric heat of adsorption Q_{st} , (kJ mol^{-1}), that represents the energy difference between the state of the system before and after the adsorption of a differential amount of adsorbate on the adsorbent surface [215]. The physical basis is the Clausius-Clapeyron equation (1.23):

$$Q_{st} = RT^2 \left(\frac{\partial \ln P}{\partial T} \right)_q \quad (1.23)$$

Applying Eq. (1.18) to the Sips isotherm model, defined by Eq. (1.14), gives:

$$Q_{st} = Q - \alpha n RT_0 \ln(bP) = Q - \alpha n^2 RT \ln \frac{\theta}{1-\theta} \quad (1.24)$$

where $\theta = n/n_s$ is the fractional loading. The heat of adsorption, Q , equals Q_{st} when n/n_s is 0.5.

The isosteric heat of adsorption for the temperature-dependent form of the Toth isotherm model, given by Eq. (1.16), is

$$Q_{st} = Q - \frac{\alpha RT_0}{t} \left[\ln \frac{\theta}{(1-\theta)^{1/t}} - \frac{\ln \theta}{(1-\theta)^t} \right] \quad (1.25)$$

in which the parameter Q equals Q_{st} when the fractional loading is zero.

Knowledge of the heats of sorption is very important for the characterization and optimization of an adsorption process [223–230]. The magnitude of (Q_{st}) value gives information about the adsorption mechanism as chemical ion-exchange or physical sorption: for physical adsorption, (Q_{st}) should be below 80 kJmol^{-1} and for chemical adsorption it ranges between 80 and 400 kJmol^{-1} . It also gives some indication about the adsorbent surface heterogeneity.

1.4. SIMULATION TOOLS

1.4.1. Interaction Potential

Interaction potential plays a central role in molecular simulations; therefore, it should be accurately modeled. In a simulation system, the total interaction energy U^{total} can be decomposed into two contributions,

$$U^{total} = U^{bonded} + U^{non-bonded} \quad (1.26)$$

where U^{bonded} is the intramolecular energy within a molecule and $U^{non-bonded}$ is the intermolecular energy arising between different molecules.

The non-bonded intermolecular energy usually consists of three terms,

$$U^{non-bonded} = U^{vdw} + U^{Coulomb} \quad (1.27)$$

where U^{vdw} is the Van der Waals interaction energy and $U^{Coulomb}$ is the coulombic interaction energy.

The bonded intramolecular energy is sum of the following terms, *bonded stretching*

$$U^{bonded} = U^{stretching} + U^{bend} + U^{torsion} \quad (1.28)$$

where $U^{stretching}$ is the bond stretching energy, U^{bend} is the bond bending energy for the angle formed by two successive chemical bonds, and $U^{torsion}$ is the torsional energy due to the dihedral angles formed by four successive atoms in a chain.

The Van der Waals interaction is usually mimicked by Lennard-Jones (LJ) potential,

$$U_{LJ}(r) = 4\epsilon \left[\left(\frac{\sigma}{r} \right)^{12} - \left(\frac{\sigma}{r} \right)^6 \right] \quad (1.29)$$

where σ is the collision diameter and ϵ is the well depth.

For a system composed of different types of atoms, the total Lennard-Jones interaction energy is:

$$U_{LJ}(r) = \sum_{\substack{i,j \\ i < j}} 4\varepsilon_{ij} \left[\left(\frac{\sigma_{ij}}{r} \right)^{12} - \left(\frac{\sigma_{ij}}{r} \right)^6 \right] \quad (1.30)$$

where ε_{ij} and σ_{ij} depend on the pair of atoms considered and are generally derived from ε_i and σ_i of pure components by appropriate combining rules, for instance, the most widely used Lorentz-Berthelot rules

$$\sigma_{ij} = \frac{\sigma_i + \sigma_j}{2} \quad (1.31)$$

$$\varepsilon_{ij} = \sqrt{\varepsilon_i \varepsilon_j} \quad (1.32)$$

The coulombic interaction is modeled by the Coulomb's law,

$$U^{coulomb} = \sum_{\substack{i,j \\ i < j}} \frac{1}{4\pi\varepsilon_0} \frac{q_i q_j}{r_{ij}} \quad (1.33)$$

where q_i and q_j are the charges in atoms i and j . The atomic charges are usually estimated by quantum chemical methods.

On the basis of different functional forms and various resources used to optimize potential parameters, numerous force fields have been developed over the years suitable for a particular class of molecules, e.g., the Universal Force Field [155] (for organics, main group elements and organometallic systems) the Dreiding II [156] (for organics, biological compounds, main group elements, and polymers), the CVFF class II force fields [231] (for proteins and organics), PCFF [231] (for polymers and materials science applications), Burchart and BKS [232] (for zeolites) and specialty force fields for sorption [233]. Other newly developed force fields include MM2 [234], MM3 [235-238], MM4 [239-241], AMBER [242], CHARMM [243], Tripos [244]. A general force field should be able to cover a broad range of elements in the periodic table and used for various compounds. The UFF is one such a force field designed for simulating molecules containing any combination of elements. The parameters were defined by combining atomic parameters and empirical rules. They expected to yield reasonable predictions of molecular structures, whereas predicting other molecular properties such as vibration frequencies and conformation properties are limited. Many well parameterized force fields such as MM3, MM4, CHARMM, AMBER and MMFF (Merck Molecular Force Field) were designed primarily for biologically interesting molecules. However, these force fields give very poor results for adsorption in nanoporous materials.

No matter which interaction potential and force field are used, simulation is always performed on a finite system. To minimize the subsequent surface or heterogeneous effect, periodic boundary conditions are commonly exerted. The minimum-image convention is used to calculate the interaction energy during simulation, with potential truncated at a cutoff distance smaller than half of the box length. For system where coulombic interaction is present, the potential decays with distance, the interaction is handled using Ewald summation in which the interactions from infinite periodic array of simulation cells are summed with the aid of Fourier transformation.

1.4.2 Monte Carlo

The basic principles of Monte Carlo (MC) simulations used are presented in the thesis. The more in depth details are given in several books [245-247].

1.4.2.1 Canonical Ensemble

Canonical ensemble or NVT ensemble is an assembly of systems, in which the number of particles, temperature and the volume are constant. Each system in the ensemble can share its energy with a heat reservoir or heat bath. The system is allowed to exchange energy with the reservoir, and the heat capacity of the reservoir is assumed to be so large as to maintain a fixed temperature for the coupled system.

For MC simulation in canonical ensemble, sample distribution is performed according to the Metropolis scheme. The algorithm generates random trial moves from old state (o) to a new state (n). If $P_B(o)$ and $P_B(n)$ denote the probability of finding the system in the state (o) and (n), respectively, and $\alpha(o \rightarrow n)$ and $\alpha(n \rightarrow o)$ denotes the conditional probability to perform a trial move from ($o \rightarrow n$) and ($n \rightarrow o$), respectively, then the probability $P_{acc}(o \rightarrow n)$ is related to $P_{acc}(n \rightarrow o)$ by

$$P_B(o)\alpha(o \rightarrow n)P_{acc}(o \rightarrow n) = P_B(n)\alpha(n \rightarrow o)P_{acc}(n \rightarrow o) \quad (1.34)$$

The probability of generating a particular configuration is constant and independent of the conformation of the system.

$$\alpha(o \rightarrow n) = \alpha(n \rightarrow o) = \alpha \quad (1.35)$$

Introducing this condition in the detailed balance, Eq. (1.34) gives the acceptance rule as

$$P_{acc}(o \rightarrow n) = \min \left[1, \frac{P_B(n)}{P_B(o)} \right] \quad (1.36)$$

In adsorption studies, MC simulations are particularly convenient for computing equilibrium thermodynamic quantities such as the isosteric heat and Henry's constant. In addition, MC simulations provide detailed structural information, in particular, the location and distribution of adsorbed molecules in the pores. Adsorption quantities are usually computed in the grand canonical ensemble as described below.

1.4.2.2 Grand Canonical Ensemble

In Grand Canonical Monte Carlo (GCMC) simulation, the chemical potential (μ), volume (V), and temperature (T) are fixed. At equilibrium, the chemical potentials of adsorbate in the bulk phase and adsorbed phase are equal. The pressure in the bulk phase can be calculated from an equation of state and it is thus directly related to the chemical potential in the adsorbed phase. The ensemble average number of molecules in the nanoporous material $\langle N \rangle$ is computed directly from

the simulation. By performing simulations at various chemical potentials, one obtains the adsorption isotherm at a given temperature. Experimental adsorption isotherm yields the excess number of molecules adsorbed in the porous media which is not, in principle, directly comparable to $\langle N \rangle$.

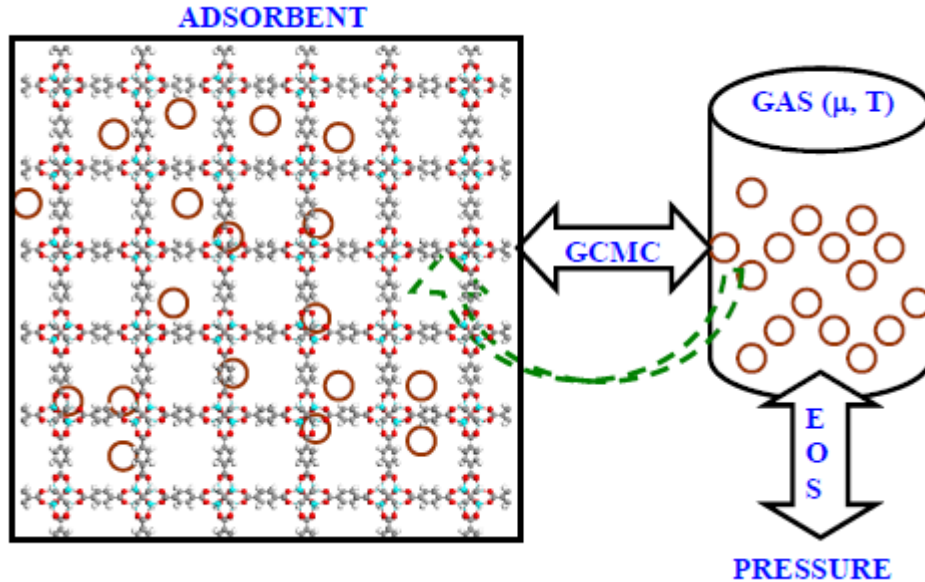


Figure 1.11. Schematic representation of GCMC simulation. Adsorbent in contact with a reservoir that imposes constant chemical potential and temperature by exchanging particles and energy. Equation of state is used to calculate the pressure of gas.

A schematic representation of GCMC simulation is illustrated in Figure 1.11. Three types of moves are usually performed. The first is a displacement and/or rotation, in which the new move is accepted with a probability

$$P_{acc}(o \rightarrow n) = \min\left(1, \exp\{-\beta[U(n) - U(o)]\}\right) \quad (1.37)$$

where β is inverse temperature, $1/k_B T$ k_B is Boltzmann's constant. U is the potential energy, and 'o' refers to old state and 'n' refers to a new state. In the second type, a new molecule is inserted into the system at a randomly chosen position. The new configuration is accepted with a probability

$$P_{acc}(N \rightarrow N+1) = \min\left[1, \frac{fV\beta}{(N+1)} \exp\{-\beta[U(N+1) - U(N)]\}\right] \quad (1.38)$$

where f is the gas fugacity, V is the volume of the simulation box, N is the number of molecules present before the attempted insertion.

In the third type, a molecule is randomly chosen to be deleted with a probability

$$P_{acc}(N \rightarrow N-1) = \min\left[1, \frac{N}{fV\beta} \exp\{-\beta[U(N-1) - U(N)]\}\right] \quad (1.39)$$

In normal GCMC, insertions are attempted throughout an entire volume of the simulation box. Nevertheless, part of the volume is occupied by adsorbent atoms and inaccessible to adsorbate molecules. Therefore a preferred region exists where the sorbate molecules could be inserted energetically favorable with increased acceptance rate. In this case, the acceptance rules for insertions and deletions must be altered to ensure that microscopic reversibility is satisfied and that the grand canonical ensemble is still correctly sampled. For the adsorption of long-chain molecules in a porous material, the configurational-bias (CB) scheme [248] is often used based upon the Rosenbluth sampling scheme [249]. The chain molecule is inserted bead by bead into the pore. First, a number of candidate positions are generated for the atom to be inserted. One of these positions is then selected according to the energy contributions from the external degrees of freedom of the molecule. When the molecule is constructed, a Rosenbluth weight is accumulated and used in the acceptance rule. This procedure was shown by Smit [250, 251] for the adsorption of united-atom (UA) linear alkanes and later extended to branched alkanes [252, 253] and to all-atom (AA) alkanes [254]. The CB-GCMC scheme is primarily for flexible chain molecules, and other bias has to be used in the case of rigid molecules. For aromatic molecules, different biased schemes such as cavity-bias [255, 256], energy-bias, energy/cavity bias [257] and orientational-bias [256-264] GCMC schemes have been used.

1.4.2.3. Gibbs Ensemble

Gibbs Ensemble Monte Carlo (GEMC) method was first introduced for the simulations of phase equilibria in bulk systems by Panagiotopoulos [265]. Considering a macroscopic system with two phases co-existing at equilibrium, Gibbs ensemble simulation is performed in two microscopic regions without the interface. The thermodynamic requirements for phase coexistence require the equality of temperature, pressure, chemical potentials of all components in the two phases. Temperature of the system is specified in advance in GEMC simulation. Three types of MC moves are performed in order to satisfy three conditions mentioned. Namely, the displacement of particle within each region to satisfy internal equilibrium, the coupled volume change to satisfy equality of pressures, and the swap particles between regions to satisfy equality of chemical potential. The acceptance criteria for GEMC were originally derived from fluctuation theory. Detailed statistical mechanical definition of the ensemble can be found in Smit et al. [266] and Smit and Frenkel work [246]. GEMC methods were modified to study the equilibrium properties of adsorbed fluid in nanospace. The method includes the pore-bulk GEMC [267], the pore-pore GEMC [268], the constant pressure pore-bulk GEMC method [268] and the gauge cell method [269, 270].

In constant-pressure GEMC, two simulation cells are used one for the adsorbent and the other for bulk fluid. The total number of the particles, volume of the adsorbent and temperature are fixed. Rather than fixing the volume of the bulk fluid, the pressure is fixed. A schematic representation of constant-pressure GEMC simulation is illustrated in Fig. 1.12. Three types of trial moves are implemented randomly, namely the displacement in each phase, the swap between two phases, and the volume change of the bulk phase.

For displacement, the number of particle in each phase is fixed and the trial move is accepted using the Metropolis scheme:

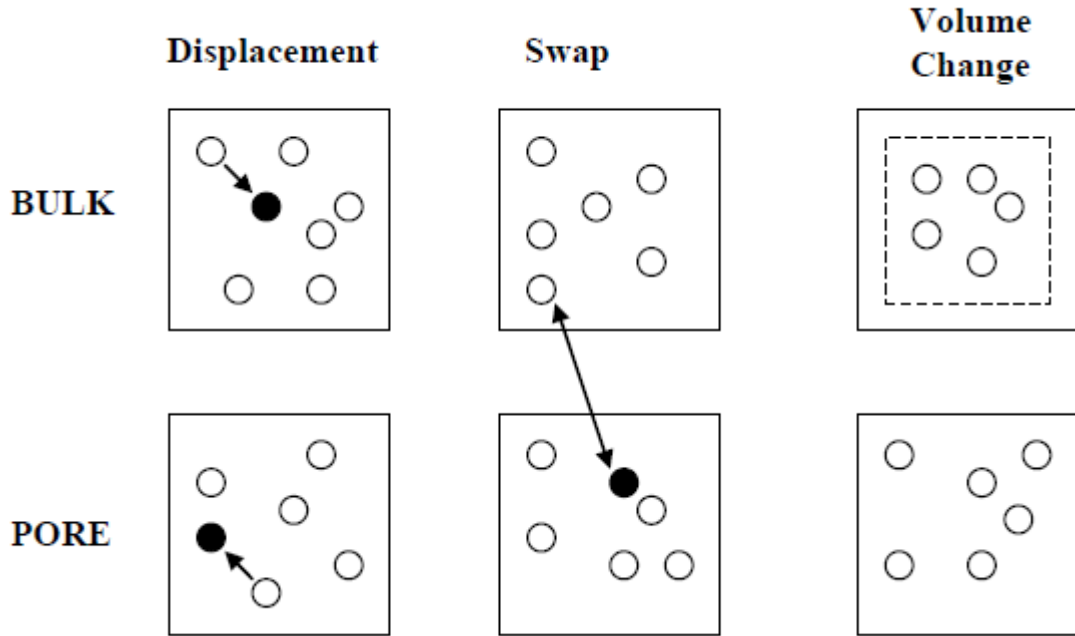


Figure 1.12. Three types of move attempted in constant pressure-GEMC. Volume changes only in the cell representing the bulk fluid.

Creation of a particle in the adsorbed phase (A), corresponding to deletion in the bulk (B) phase, is accepted with a probability of:

$$P = \min \left\{ 1, \exp \left[-\beta (\Delta U_A + \Delta U_B) \right] N_B N_A / (N_A + 1) V_B \right\} \quad (1.40)$$

where $\beta = 1/k_b T$, N_A , N_B refers to the number of particles in the adsorbed and bulk phase, V_A , and V_B refers to the volume of the adsorbent and bulk phase.

Similarly, the probability of acceptance for deletion of a particle in the adsorbed phase and its creation in bulk phase is:

$$P = \min \left\{ 1, \exp \left[-\beta (\Delta U_A + \Delta U_B) \right] N_A N_B / (N_B + 1) V_A \right\} \quad (1.41)$$

The acceptance probability for the trial volume change in the bulk phase is:

$$P = \min \left\{ 1, \exp \left[-\beta \Delta U_B + \beta P \Delta V_B + N_B \ln(1 + \Delta V_B / V_B) \right] \right\} \quad (1.42)$$

1.5. RESEARCH STRATEGY & OBJECTIVES

After analysis of the provided literature sources, a research strategy and the work objectives are elaborated. Namely, from analysis of the literature it can be concluded that:

1. Porous metal organic framework materials (MOFs) have found increasing interest since the past few years in potential applications such as separation and storage.
2. Encouraging results have been obtained recently in terms of hydrogen storage, adsorption of greenhouse gases, liquid phase separation and drug delivery.
3. Increase of the demands to follow the DOE targets recommendations leads to enhance of the research interest for the MOF material screening.
4. For gas storage application, current research interest is focused on MOFs that can demonstrate along with the rigid frameworks a significant structural distortion upon adsorption /desorption of guest molecules.
5. An extreme aspect of this type of distortion is the “breathing” effect that is typically associated with a large change of the internal pore volume and has recently attracted significant research interest.
6. For the gas storage application, investigations are based on a combination of experimental tools completed by a computational approach to deep analysis of the adsorption phenomena for the short linear alkanes, hydrogen and CO₂ on flexible MOFs.

Therefore, the overall research idea of the present work is aimed at studying of the flexible MIL-53(Al) metal organic framework as a selective adsorbent and possible storage unit for the natural gas components according to the target of the Department Of Energy (DOE). The major part of the work is aimed at treatability studies of the adsorption processes of CH₄, C₂H₆, C₃H₈ and C₄H₁₀, on MIL-53(Al) accomplished by the GCMC molecular simulation.

To achieve this purpose, the research is focused on the following objectives:

1. Treatability studies of the metal organic framework MIL-53(Al) using advanced chemical-physical background: *Elemental Analyze, Mercury Porosimetry, Thermogravimetry, X-ray Powder Diffraction, Solid State Nuclear Magnetic Resonance, Fourier Transformation Infrared Spectroscopy and Gas Adsorption techniques.*
2. Treatability studies of the thermodynamics of the components of natural gas (CH₄, C₂H₆, C₃H₈, C₄H₁₀) adsorption using gravimetric analytical approach in a wide range of temperatures 303-353K and pressure 0 - 5 MPa.
3. Molecular simulation of the adsorption process using the Grand Canonical Monte Carlo (GCMC) method.
4. Theoretical calculations of the gas storage on MIL-53(Al) according to the DOE target.

To achieve these objectives the work is planned as a combination of two different types of activities:

1. Experimental work. Studies of MIL-53(Al) aiming at its structural/properties characterization and analysis of the adsorption thermodynamics of the natural gas components.
2. Theoretical work. Studies of the adsorption process using the Grand Canonical Monte Carlo (GCMC) approach and the MIL-53(Al) storage capacity evaluation.

The thesis structure is given by six *CHAPTERS*. *Chapter 1* and *6* correspond to the introduction and conclusions, respectively. The research, achievements and conclusions are divided in three major sections:

- Characterization of the Metal Organic Framework MIL-53Al (*Chapter 2*);
- Experimental studies of the thermodynamics of gas adsorption on MIL-53(Al) (*Chapter 3*);
- Theoretical studies of MIL-53(Al) as the adsorption/storage unit for the investigated gases (*Chapters 4 and 5*).

The detailed characterization of the MIL-53(Al) material using advanced physical-chemicals methods (such as elemental analysis, N₂ adsorption, mercury porosimetry, solid state ¹³C-NMR, X-ray diffraction, FTIR and thermogravimetric analysis) constituted the starting points of the research.

In order to gain insight into the adsorption processes of C₁-C₄ alkanes on MIL-53(Al); the gas-adsorption experiment run were using high-pressure magnetic-suspension balance measurements with automated online of data acquisition of temperature, pressure, and sample weight in a wide range of temperatures 303-353 K and pressure 0-5 MPa.

Aimed at analysis of the experimental adsorption isotherms several reference states (as called thermodynamic framework); net adsorption (n_{net}); excess adsorption (n_{ex}) and absolute adsorption (n), and their reproduction in graphic mode are used. The experimental data obtained are fitted by the Sips and Toth semi-empirical isotherm models. The isosteric heat of adsorption is also calculated using the Clayperon equation and evaluated from statistical mechanical considerations.

Evaluation of the agreement between simulated and the experimental adsorption data (i.e. without needs for the re-parameterization of the cross-terms for the Lennard-Johnes solid–fluid interaction potential) was done by GCMC model using United Atom (UA) force field

At a final stage of the work it was planned to provide an estimation of the MIL-53(Al) net storage capacity in an isothermal cycle operating conditions (such a pressure, temperature) to fulfill the demands of the Department Of Energy (DOE) for the methane. Also the analysis of the net adsorption parameters of MIL-53(Al) together with data on bulk gases compressed under identical conditions aiming at estimation of the total storage capacity, and a rough estimation of the MIL-53(Al) role in storage capacity enhancement above simple gas compression for the C₂-C₄ gases was planned to perform using obtained experimental and theoretical results.

1.6. REFERENCES

- [1] M. E. Davis, *Nature*, **2002**, 417, 813.
- [2] M. Eddaoudi, J. Kim, N. Rosi, D. Vodak, J. Wachter, M. O'Keeffe, and O. M. Yaghi, *Science*, **2002**, 295, 469.
- [3] H. Li, M. Eddaoudi, M. O'Keeffe, and O. M. Yaghi, *Nature*, **1999**, 402, 276.
- [4] S. Kitagawa, R. Kitaura, and S. Noro, *Angew. Chem. Inter. Ed.*, **2004**, 43, 2334.
- [5] J. L. C. Rowsell and O. M. Yaghi, *Microporous Mesoporous Mater.*, **2004**, 73, 3.
- [6] T. J. Barton, L. M. Bull, W. G. Klemperer, D. A. Loy, B. McEnaney, M. Misono, P. A. Monson, G. Pez, G. W. Scherer, J. C. Vartuli, and O. M. Yaghi, *Chem. Mater.*, **1999**, 11, 2633.
- [7] S. K. Ghosh and P. K. Bharadwaj, *Eur. J. Inorg. Chem.*, **2005**, 4880.
- [8] S. K. Ghosh and P. K. Bharadwaj, *Eur. J. Inorg. Chem.*, **2005**, 4886.
- [9] S. K. Ghosh and P. K. Bharadwaj, *Inorg. Chem.*, **2005**, 44, 5553.
- [10] J. R. Long and O. M. Yaghi, *Chem. Soc. Rev.*, **2009**, 38, 1213.
- [11] O. M. Yaghi, M. O'Keeffe, N. W. Ockwig, H. K. Chae, M. Eddaoudi, and J. Kim, *Nature*, **2003**, 423, 705.
- [12] M. Eddaoudi, D. B. Moler, H. L. Li, B. L. Chen, T. M. Reineke, M. O'Keeffe, and O. M. Yaghi, *Acc. Chem. Res.*, **2001**, 34, 319.
- [13] B. L. Chen, M. Eddaoudi, T. M. Reineke, J. W. Kampf, M. O'Keeffe, and O. M. Yaghi, *J. Am. Chem. Soc.*, **2000**, 122, 11559.
- [14] J. C. G. Bunzli and C. Piguet, *Chem. Rev.*, **2002**, 102, 1897.
- [15] L. Pan, X. Y. Huang, J. Li, Y. G. Wu, and N. W. Zheng, *Angew. Chem. Inter. Ed.*, **2000**, 39, 527.
- [16] C. D. Wu, C. Z. Lu, H. H. Zhuang, and J. S. Huang, *J. Am. Chem. Soc.*, **2002**, 124, 3836.
- [17] S. Neogi and P. K. Bharadwaj, *Polyhedron*, **2006**, 25, 1491.
- [18] S. Neogi and P. K. Bharadwaj, *Cryst. Growth Des.*, **2006**, 6, 433.
- [19] S. Neogi and P. K. Bharadwaj, *Synthesis and Reactivity in Inorganic Metal-Organic and Nano-Metal Chemistry*, **2008**, 38, 40.
- [20] S. K. Ghosh and P. K. Bharadwaj, *Inorg. Chem.*, **2004**, 43, 6887.
- [21] S. K. Ghosh and P. K. Bharadwaj, *Inorg. Chem.*, **2003**, 42, 8250.
- [22] S. K. Ghosh and P. K. Bharadwaj, *Inorg. Chem.*, **2004**, 43, 5180.
- [23] O. M. Yaghi, H. L. Li, C. Davis, D. Richardson, and T. L. Groy, *Acc. Chem. Res.*, **1998**, 31, 474.
- [24] S. Kitagawa and K. Uemura, *Chem. Soc. Rev.*, **2005**, 34, 109.
- [25] S. Kitagawa and M. Kondo, *Bulletin of the Chemical Society of Japan*, **1998**, 71, 1739.
- [26] A. J. Fletcher, K. M. Thomas, and M. J. Rosseinsky, *J. Solid State Chem.*, **2005**, 178, 2491.
- [27] R. Kitaura, K. Fujimoto, S. Noro, M. Kondo, and S. Kitagawa, *Angew. Chem. Inter. Ed.*, **2002**, 41, 133.
- [28] X. B. Zhao, B. Xiao, A. J. Fletcher, K. M. Thomas, D. Bradshaw, and M. J. Rosseinsky, *Science*, **2004**, 306, 1012.
- [29] D. Riou and G. Ferey, *J. Mater. Chem.*, **1998**, 8, 2733.
- [30] D. Riou, O. Roubeau, and G. Ferey, *Microporous Mesoporous Mater.*, **1998**, 23, 23.
- [31] D. Riou, C. Serre, and G. Ferey, *J. Solid State Chem.*, **1998**, 141, 89.
- [32] F. Serpaggi and G. Ferey, *J. Mater. Chem.*, **1998**, 8, 2737.
- [33] F. Serpaggi and G. Ferey, *J. Mater. Chem.*, **1998**, 8, 2749.
- [34] F. Serpaggi and G. Ferey, *Microporous Mesoporous Mater.*, **1999**, 32, 311.
- [35] G. Ferey, C. Serre, C. Mellot-Draznieks, F. Millange, S. Surble, J. Dutour, and I. Margiolaki, *Angew. Chem. Inter. Ed.*, **2004**, 43, 6296.
- [36] C. Serre, F. Millange, C. Thouvenot, M. Nogues, G. Marsolier, D. Louer, and G. Ferey, *J. Am. Chem. Soc.*, **2002**, 124, 13519.
- [37] T. Loiseau, C. Serre, C. Huguenard, G. Fink, F. Taulelle, M. Henry, T. Bataille, and G. Ferey, *Chem.-Eur. J.*, **2004**, 10, 1373.
- [38] F. Millange, N. Guillou, R. I. Walton, J. M. Greneche, I. Margiolaki, and G. Ferey, *Chem. Commun.*, **2008**, 4732.
- [39] C. Volkringer, T. Loiseau, N. Guillou, G. Ferey, E. Elkaim, and A. Vimont, *Dalton Transactions*, **2009**, 2241.
- [40] K. Barthelet, J. Marrot, D. Riou, and G. Ferey, *Angew. Chem. Inter. Ed.*, **2002**, 41, 281.
- [41] A. P. Cote, A. I. Benin, N. W. Ockwig, M. O'Keeffe, A. J. Matzger, and O. M. Yaghi, *Science*, **2005**, 310, 1166.

- [42] A. P. Cote, H. M. El-Kaderi, H. Furukawa, J. R. Hunt, and O. M. Yaghi, *J. Am. Chem. Soc.*, **2007**, 129, 12914.
- [43] H. M. El-Kaderi, J. R. Hunt, J. L. Mendoza-Cortes, A. P. Cote, R. E. Taylor, M. O'Keeffe, and O. M. Yaghi, *Science*, **2007**, 316, 268.
- [44] M. A. Lino, A. A. Lino, and M. S. C. Mazzoni, *Chem. Phys. Lett.*, **2007**, 449, 171.
- [45] J. R. Hunt, C. J. Doonan, J. D. LeVangie, A. P. Cote, and O. M. Yaghi, *J. Am. Chem. Soc.*, **2008**, 130, 11872.
- [46] F. J. Uribe-Romo, J. R. Hunt, H. Furukawa, C. Klock, M. O'Keeffe, and O. M. Yaghi, *J. Am. Chem. Soc.*, **2009**, 131, 4570.
- [47] S. Wan, J. Guo, J. Kim, H. Ihee, and D. L. Jiang, *Angew. Chem. Inter. Ed.*, **2008**, 47, 8826.
- [48] Y. Q. Tian, C. X. Cai, Y. Ji, X. Z. You, S. M. Peng, and G. H. Lee, *Angew. Chem. Inter. Ed.*, **2002**, 41, 1384.
- [49] Y. Q. Tian, C. X. Cai, X. M. Ren, C. Y. Duan, Y. Xu, S. Gao, and X. Z. You, *Chem.- Eur. J.*, **2003**, 9, 5673.
- [50] Y. Q. Tian, Z. X. Chen, L. H. Weng, H. B. Guo, S. Gao, and D. Y. Zhao, *Inorg. Chem.*, **2004**, 43, 4631.
- [51] Y. Q. Tian, H. J. Xu, L. H. Weng, Z. X. Chen, D. Y. Zhao, and X. Z. You, *Eur. J. Inorg. Chem.*, **2004**, 1813.
- [52] Y. Q. Tian, Y. M. Zhao, Z. X. Chen, G. N. Zhang, L. H. Weng, and D. Y. Zhao, *Chem.- Eur. J.*, **2007**, 13, 4146.
- [53] X. C. Huang, Y. Y. Lin, J. P. Zhang, and X. M. Chen, *Angew. Chem. Inter. Ed.*, **2006**, 45, 1557.
- [54] D. W. Breck, *Zeolite Molecular Sieves*, Wiley, New York, 1974.
- [55] X. C. Huang, J. P. Zhang, and X. M. Chen, *Chinese Science Bulletin*, **2003**, 48, 1531.
- [56] K. S. Park, Z. Ni, A. P. Cote, J. Y. Choi, R. D. Huang, F. J. Uribe-Romo, H. K. Chae, M. O'Keeffe, and O. M. Yaghi, *Proc. Nat. Acad. Sci. U.S.A.*, **2006**, 103, 10186.
- [57] H. Hayashi, A. P. Cote, H. Furukawa, M. O'Keeffe, and O. M. Yaghi, *Nature Materials*, **2007**, 6, 501.
- [58] R. Banerjee, A. Phan, B. Wang, C. Knobler, H. Furukawa, M. O'Keeffe, and O. M. Yaghi, *Science*, **2008**, 319, 939.
- [59] B. Wang, A. P. Cote, H. Furukawa, M. O'Keeffe, and O. M. Yaghi, *Nature*, **2008**, 453, 207.
- [60] H. Zhang, T. Wu, C. Zhou, S. M. Chen, P. Y. Feng, and X. H. Bu, *Angew. Chem. Inter. Ed.*, **2009**, 48, 2542.
- [61] T. Wu, X. H. Bu, J. Zhang, and P. Y. Feng, *Chem. Mater.*, **2008**, 20, 7377.
- [62] Y. L. Liu, V. C. Kravtsov, R. Larsen, and M. Eddaoudi, *Chem. Commu.*, **2006**, 14, 1488.
- [63] D. F. Sava, V. C. Kravtsov, F. Nouar, L. Wojtas, J. F. Eubank, and M. Eddaoudi, *J. Am. Chem. Soc.*, **2008**, 130, 3768.
- [64] Z. Q. Wang and S. M. Cohen, *Chem. Soc. Rev.*, **2009**, 38, 1315.
- [65] B. D. Chandler, D. T. Cramb, and G. K. H. Shimizu, *J. Am. Chem. Soc.*, **2006**, 128, 10403.
- [66] E. Y. Lee, S. Y. Jang, and M. P. Suh, *J. Am. Chem. Soc.*, **2005**, 127, 6374.
- [67] J. R. Li, Y. Tao, Q. Yu, and X. H. Bu, *Chem. Commu.*, **2007**, 1527.
- [68] G. J. Halder, C. J. Kepert, B. Moubaraki, K. S. Murray, and J. D. Cashion, *Science*, **2002**, 298, 1762.
- [69] P. D. C. Dietzel, Y. Morita, R. Blom, and H. Fjellvag, *Angew. Chem. Inter. Ed.*, **2005**, 44, 6354.
- [70] Z. M. Wang, Y. J. Zhang, T. Liu, M. Kurmoo, and S. Gao, *Adv. Funct. Mater.*, **2007**, 17, 1523.
- [71] M. Alvaro, E. Carbonell, B. Ferrer, F. Xamena, and H. Garcia, *Chem.- Eur. J.*, **2007**, 13, 5106.
- [72] A. Kuc, A. Enyashin, and G. Seifert, *J. Phys. Chem. B.*, **2007**, 111, 8179.
- [73] Q. Ye, Y. M. Song, G. X. Wang, K. Chen, D. W. Fu, P. W. H. Chan, J. S. Zhu, S. D. Huang, and R. G. Xiong, *J. Am. Chem. Soc.*, **2006**, 128, 6554.
- [74] T. Okubo, R. Kawajiri, T. Mitani, and T. Shimoda, *J. Am. Chem. Soc.*, **2005**, 127, 17598.
- [75] S. Horike, M. Dinca, K. Tamaki, and J. R. Long, *J. Am. Chem. Soc.*, **2008**, 130, 5854.
- [76] T. Mueller, M. M. Schubert, and A. O. Yazaydin, in *Handbook of Heterogeneous catalysis*, Weinheim, 2008.
- [77] F. Xamena, O. Casanova, R. G. Tailleux, H. Garcia, and A. Corma, *J. Catal.*, **2008**, 255, 220.
- [78] R. Q. Zou, H. Sakurai, S. Han, R. Q. Zhong, and Q. Xu, *J. Am. Chem. Soc.*, **2007**, 129, 8402.
- [79] B. F. Hoskins and R. Robson, *J. Am. Chem. Soc.*, **1990**, 112, 1546.
- [80] G. B. Gardner, D. Venkataraman, J. S. Moore, and S. Lee, *Nature*, **1995**, 374, 792.
- [81] E. Lee, J. Kim, J. Heo, D. Whang, and K. Kim, *Angew. Chem. Inter. Ed.*, **2001**, 40, 399.
- [82] J. R. Li, R. J. Kuppler, and H. C. Zhou, *Chem. Soc. Rev.*, **2009**, 38, 1477.
- [83] H. Furukawa and O. M. Yaghi, *J. Am. Chem. Soc.*, **2009**, 131, 25, 8875.
- [84] A. R. Millward and O. M. Yaghi, *J. Am. Chem. Soc.*, **2005**, 127, 17998.

- [85] B. L. Chen, L. B. Wang, F. Zapata, G. D. Qian, and E. B. Lobkovsky, *J. Am. Chem. Soc.*, **2008**, 130, 6718.
- [86] B. L. Chen, Y. Yang, F. Zapata, G. N. Lin, G. D. Qian, and E. B. Lobkovsky, *Advan. Mater.*, **2007**, 19, 1693.
- [87] B. V. Harbuzaru, A. Corma, F. Rey, P. Atienzar, J. L. Jorda, H. Garcia, D. Ananias, L. D. Carlos, and J. Rocha, *Angew. Chem. Inter. Ed.*, **2008**, 47, 1080.
- [88] T. Uemura, D. Hiramatsu, Y. Kubota, M. Takata, and S. Kitagawa, *Angew. Chem. Inter. Ed.*, **2007**, 46, 4987.
- [89] T. Uemura, R. Kitaura, Y. Ohta, M. Nagaoka, and S. Kitagawa, *Angew. Chem. Inter. Ed.*, **2006**, 45, 4112.
- [90] M. Vallet-Regi, F. Balas, and D. Arcos, *Angew. Chem. Inter. Ed.*, **2007**, 46, 7548.
- [91] P. Horcajada, C. Serre, G. Maurin, N. A. Ramsahye, F. Balas, M. Vallet-Regi, M. Sebban, F. Taulelle, and G. Ferey, *J. Am. Chem. Soc.*, **2008**, 130, 6774.
- [92] P. Horcajada, C. Serre, M. Vallet-Regi, M. Sebban, F. Taulelle, and G. Ferey, *Angew. Chem. Inter. Ed.*, **2006**, 45, 5974.
- [93] J. L. C. Rowsell, A. R. Millward, K. S. Park, and O. M. Yaghi, *J. Am. Chem. Soc.*, **2004**, 126, 5666.
- [94] B. L. Chen, N. W. Ockwig, A. R. Millward, D. S. Contreras, and O. M. Yaghi, *Angew. Chem. Inter. Ed.*, **2005**, 44, 4745.
- [95] G. Ferey, M. Latroche, C. Serre, F. Millange, T. Loiseau, and A. Percheron-Guegan, *Chem. Commun.*, **2003**, 2976.
- [96] L. Pan, M. B. Sander, X. Y. Huang, J. Li, M. Smith, E. Bittner, B. Bockrath, and J. K. Johnson, *J. Am. Chem. Soc.*, **2004**, 126, 1308.
- [97] J. L. C. Rowsell and O. M. Yaghi, *Angew. Chem. Int. Ed.*, **2005**, 44, 4670.
- [98] A. G. Wong-Foy, A. J. Matzger, and O. M. Yaghi, *J. Am. Chem. Soc.*, **2006**, 128, 3494.
- [99] M. Dinca, A. Dailly, Y. Liu, C. M. Brown, D. A. Neumann, and J. R. Long, *J. Am. Chem. Soc.*, **2006**, 128, 16876.
- [100] M. Dinca and J. R. Long, *J. Am. Chem. Soc.*, **2007**, 129, 11172.
- [101] M. Dinca and J. R. Long, *Angew. Chem. Inter. Ed.*, **2008**, 47, 6766.
- [102] X. S. Wang, S. Q. Ma, P. M. Forster, D. Q. Yuan, J. Eckert, J. J. Lopez, B. J. Murphy, J. B. Parise, and H. C. Zhou, *Angew. Chem. Inter. Ed.*, **2008**, 47, 7263.
- [103] J. G. Vitillo, L. Regli, S. Chavan, G. Ricchiardi, G. Spoto, P. D. C. Dietzel, S. Bordiga, and A. Zecchina, *J. Am. Chem. Soc.*, **2008**, 130, 8386.
- [104] Y. W. Li and R. T. Yang, *J. Am. Chem. Soc.*, **2006**, 128, 726.
- [105] Y. W. Li and R. T. Yang, *J. Am. Chem. Soc.*, **2006**, 128, 8136.
- [106] S. H. Yang, X. Lin, A. Dailly, A. J. Blake, P. Hubberstey, N. R. Champness, and M. Schroder, *Chem.-Eur. J.*, **2009**, 15, 4829.
- [107] L. J. Murray, M. Dinca, and J. R. Long, *Chem. Soc. Rev.*, **2009**, 38, 1294.
- [108] T. Duren, L. Sarkisov, O. M. Yaghi, and R. Q. Snurr, *Langmuir*, **2004**, 20, 2683.
- [109] S. Q. Ma, D. F. Sun, J. M. Simmons, C. D. Collier, D. Q. Yuan, and H. C. Zhou, *J. Am. Chem. Soc.*, **2008**, 130, 1012.
- [110] T. Burchell and M. Rogers, *SAE Tech. Pap. Ser.*, **2000**, 2000-01-2205.
- [111] P. L. Llewellyn, S. Bourrelly, C. Serre, A. Vimont, M. Daturi, L. Hamon, G. De Weireld, J. S. Chang, D. Y. Hong, Y. K. Hwang, S. H. Jung, and G. Ferey, *Langmuir*, **2008**, 24, 7245.
- [112] P. Chowdhury, C. Bikkina, and S. Gumma, *J. Phys. Chem. C.*, **2009**, 113, 6616.
- [113] B. Xiao, P. S. Wheatley, X. B. Zhao, A. J. Fletcher, S. Fox, A. G. Rossi, I. L. Megson, S. Bordiga, L. Regli, K. M. Thomas, and R. E. Morris, *J. Am. Chem. Soc.*, **2007**, 129, 1203.
- [114] A. C. McKinlay, B. Xiao, D. S. Wragg, P. S. Wheatley, I. L. Megson, and R. E. Morris, *J. Am. Chem. Soc.*, **2008**, 130, 10440.
- [115] B. L. Chen, C. D. Liang, J. Yang, D. S. Contreras, Y. L. Clancy, E. B. Lobkovsky, O. M. Yaghi, and S. Dai, *Angew. Chem. Inter. Ed.*, **2006**, 45, 1390.
- [116] L. Pan, D. H. Olson, L. R. Ciemnomolonski, R. Heddy, and J. Li, *Angew. Chem. Inter. Ed.*, **2006**, 45, 616.
- [117] D. N. Dybtsev, H. Chun, S. H. Yoon, D. Kim, and K. Kim, *J. Am. Chem. Soc.*, **2004**, 126, 32.
- [118] S. Q. Ma, X. S. Wang, C. D. Collier, E. S. Manis, and H. C. Zhou, *Inorg. Chem.*, **2007**, 46, 8499.
- [119] M. Dinca and J. R. Long, *J. Am. Chem. Soc.*, **2005**, 127, 9376.
- [120] J. A. R. Navarro, E. Barea, A. Rodriguez-Dieguez, J. M. Salas, C. O. Ania, J. B. Parra, N. Masciocchi, S. Galli, and A. Sironi, *J. Am. Chem. Soc.*, **2008**, 130, 3978.

- [121] S. S. Y. Chui, S. M. F. Lo, J. P. H. Charmant, A. G. Orpen, and I. D. Williams, *Science*, **1999**, 283, 1148.
- [122] Q. M. Wang, D. M. Shen, M. Bulow, M. L. Lau, S. G. Deng, F. R. Fitch, N. O. Lemcoff, and J. Semancin, *Microporous Mesoporous Mater.*, **2002**, 55, 217.
- [123] S. Q. Ma, X. S. Wang, D. Q. Yuan, and H. C. Zhou, *Angew. Chem. Inter. Ed.*, **2008**, 47, 4130.
- [124] R. Matsuda, R. Kitaura, S. Kitagawa, Y. Kubota, R. V. Belosludov, T. C. Kobayashi, H. Sakamoto, T. Chiba, M. Takata, Y. Kawazoe, and Y. Mita, *Nature*, **2005**, 436, 238.
- [125] L. Pan, B. Parker, X. Y. Huang, D. H. Olson, J. Lee, and J. Li, *J. Am. Chem. Soc.*, **2006**, 128, 4180.
- [126] J. Y. Lee, D. H. Olson, L. Pan, T. J. Emge, and J. Li, *Adv. Funct. Mater.*, **2007**, 17, 1255.
- [127] S. Horike, D. Tanaka, K. Nakagawa, and S. Kitagawa, *Chem. Commu.*, **2007**, 3395.
- [128] H. R. Moon, N. Kobayashi, and M. P. Suh, *Inorg. Chem.*, **2006**, 45, 8672.
- [129] Y. S. Bae, O. K. Farha, A. M. Spokoyny, C. A. Mirkin, J. T. Hupp, and R. Q. Snurr, *Chem. Commun.*, **2008**, 4135.
- [130] B. Mu, F. Li, and K. S. Walton, *Chem. Commu.*, **2009**, 2493.
- [131] M. Fujita, Y. J. Kwon, S. Washizu, and K. Ogura, *J. Am. Chem. Soc.*, **1994**, 116, 1151.
- [132] O. R. Evans, H. L. Ngo, and W. B. Lin, *J. Am. Chem. Soc.*, **2001**, 123, 10395.
- [133] J. S. Seo, D. Whang, H. Lee, S. I. Jun, J. Oh, Y. J. Jeon, and K. Kim, *Nature*, **2000**, 404, 982.
- [134] C. D. Wu, A. Hu, L. Zhang, and W. B. Lin, *J. Am. Chem. Soc.*, **2005**, 127, 8940.
- [135] U. Ravon, M. E. Domine, C. Gaudillere, A. Desmartin-Chomel, and D. Farrusseng, *New J. Chem.*, **2008**, 32, 937.
- [136] A. Henschel, K. Gedrich, R. Kraehnert, and S. Kaskel, *Chem. Commu.*, **2008**, 4192.
- [137] K. Schlichte, T. Kratzke, and S. Kaskel, *Microporous Mesoporous Mater.*, **2004**, 73, 81.
- [138] L. Alaerts, E. Seguin, H. Poelman, F. Thibault-Starzyk, P. A. Jacobs, and D. E. De Vos, *Chem.-Eur. J.*, **2006**, 12, 7353.
- [139] M. H. Alkordi, Y. L. Liu, R. W. Larsen, J. F. Eubank, and M. Eddaoudi, *J. Am. Chem. Soc.*, **2008**, 130, 12639.
- [140] S. Hasegawa, S. Horike, R. Matsuda, S. Furukawa, K. Mochizuki, Y. Kinoshita, and S. Kitagawa, *J. Am. Chem. Soc.*, **2007**, 129, 2607.
- [141] Y. K. Hwang, D. Y. Hong, J. S. Chang, S. H. Jung, Y. K. Seo, J. Kim, A. Vimont, M. Daturi, C. Serre, and G. Ferey, *Angew. Chem. Inter. Ed.*, **2008**, 47, 4144.
- [142] 'Hydrogen, Fuel Cells and Infrastructure Technologies Program: Multi-year Research, Development and Demonstration Plan', U.S. Department of Energy, 2005.
- [143] O. Hubner, A. Gloss, M. Fichtner, and W. Klopfer, *J. Phys. Chem. A*, **2004**, 108, 3019.
- [144] R. Ahlrichs, M. Bar, M. Haser, H. Horn, and C. Kolmel, *Chem. Phys. Lett.*, **1989**, 162, 165.
- [145] F. Weigend and M. Haser, *Theor. Chem. Acct.*, **1997**, 97, 331.
- [146] F. Weigend, M. Haser, H. Patzelt, and R. Ahlrichs, *Chem. Phys. Lett.*, **1998**, 294, 143.
- [147] T. Sagara, J. Klassen, J. Ortony, and E. Ganz, *J. Chem. Phys.*, **2005**, 123.
- [148] T. Sagara, J. Ortony, and E. Ganz, *J. Chem. Phys.*, **2005**, 123.
- [149] A. Schafer, C. Huber, and R. Ahlrichs, *J. Chem. Phys.*, **1994**, 100, 5829.
- [150] T. Sagara, J. Klassen, and E. Ganz, *J. Chem. Phys.*, **2004**, 121, 12543.
- [151] Q. Y. Yang and C. L. Zhong, *J. Phys. Chem. B*, **2005**, 109, 11862.
- [152] W. L. Jorgensen, D. S. Maxwell, and J. TiradoRives, *J. Am. Chem. Soc.*, **1996**, 118, 11225.
- [153] Q. Y. Yang and C. L. Zhong, *J. Phys. Chem. B*, **2006**, 110, 17776.
- [154] G. Garberoglio, A. I. Skoulidas, and J. K. Johnson, *J. Phys. Chem. B*, **2005**, 109, 13094.
- [155] A. K. Rappe, C. J. Casewit, K. S. Colwell, W. A. Goddard, and W. M. Skiff, *J. Am. Chem. Soc.*, **1992**, 114, 10024.
- [156] S. L. Mayo, B. D. Olafson, and W. A. Goddard, *J. Phys. Chem.*, **1990**, 94, 8897.
- [157] H. Frost, T. Duren, and R. Q. Snurr, *J. Phys. Chem. B*, **2006**, 110, 9565.
- [158] D. H. Jung, D. Kim, T. B. Lee, S. B. Choi, J. H. Yoon, J. Kim, K. Choi, and S. H. Choi, *J. Phys. Chem. B*, **2006**, 110, 22987.
- [159] P. Ryan, L. J. Broadbelt, and R. Q. Snurr, *Chem. Commun.*, **2008**, 4132.
- [160] L. Zhang, Q. Wang, and Y. C. Liu, *J. Phys. Chem. B*, **2007**, 111, 4291.
- [161] H. Frost and R. Q. Snurr, *J. Phys. Chem. C*, **2007**, 111, 18794.
- [162] G. Garberoglio, *Langmuir*, **2007**, 23, 12154.
- [163] E. Klontzas, E. Tylianakis, and G. E. Froudakis, *J. Phys. Chem. C*, **2008**, 112, 9095.
- [164] W. Q. Deng, X. Xu, and W. A. Goddard, *Phys. Rev. Lett.*, **2004**, 92.
- [165] S. S. Han and W. A. Goddard, *J. Phys. Chem. C*, **2008**, 112, 13431.
- [166] S. S. Han, H. Furukawa, O. M. Yaghi, and W. A. Goddard, *J. Am. Chem. Soc.*, **2008**, 130, 11580.

- [167] M. Kosa, M. Krack, A. K. Cheetham, and M. Parrinello, *J. Phys. Chem. C*, **2008**, 112, 16171.
- [168] Y. Y. Sun, Y. H. Kim, and S. B. Zhang, *J. Am. Chem. Soc.*, **2007**, 129, 12606.
- [169] Q. Y. Yang and C. L. Zhong, *J. Phys. Chem. B*, **2006**, 110, 655.
- [170] S. S. Han and W. A. Goddard, *J. Am. Chem. Soc.*, **2007**, 129, 8422.
- [171] A. Blomqvist, C. M. Araujo, P. Srepusharawoot, and R. Ahuja, *Proc. Natl. Acad. Sci. U.S.A.*, **2007**, 104, 20173.
- [172] A. Mavrandonakis, E. Tylianakis, A. K. Stubos, and G. E. Froudakis, *J. Phys. Chem. C*, **2008**, 112, 7290.
- [173] P. Dalach, H. Frost, R. Q. Snurr, and D. E. Ellis, *J. Phys. Chem. C*, **2008**, 112, 9278.
- [174] E. Klontzas, A. Mavrandonakis, E. Tylianakis, and G. E. Froudakis, *Nano Letters*, **2008**, 8, 1572.
- [175] Y. J. Choi, J. W. Lee, J. H. Choi, and J. K. Kang, *Appl. Phys. Lett.*, **2008**, 92.
- [176] D. P. Cao, J. H. Lan, W. C. Wang, and B. Smit, *Ang. Chem. Inter. Ed.*, **2009**, 48, 4730.
- [177] S. Y. Wang, *Energy & Fuels*, **2007**, 21, 953.
- [178] Y. H. Jhon, M. Cho, H. R. Jeon, I. Park, R. Chang, J. L. C. Rowsell, and J. Kim, *J. Phys. Chem. C*, **2007**, 111, 16618.
- [179] T. Kawakami, S. Takamizawa, Y. Kitagawa, T. Maruta, W. Mori, and K. Yamaguchi, *Polyhedron*, **2001**, 20, 1197.
- [180] K. S. Walton, A. R. Millward, D. Dubbeldam, H. Frost, J. J. Low, O. M. Yaghi, and R. Q. Snurr, *J. Am. Chem. Soc.*, **2008**, 130, 406.
- [181] Q. Y. Yang, C. L. Zhong, and J. F. Chen, *J. Phys. Chem. C*, **2008**, 112, 1562.
- [182] N. A. Ramsahye, G. Maurin, S. Bourrelly, P. Llewellyn, T. Loiseau, and G. Ferey, *Phys. Chem. Chem. Phys.*, **2007**, 9, 1059.
- [183] N. A. Ramsahye, G. Maurin, S. Bourrelly, P. L. Llewellyn, T. Devic, C. Serre, T. Loiseau, and G. Ferey, *Adsorption*, **2007**, 13, 461.
- [184] N. A. Ramsahye, G. Maurin, S. Bourrelly, P. L. Llewellyn, T. Loiseau, C. Serre, and G. Ferey, *Chem. Commu.*, **2007**, 3261.
- [185] N. A. Ramsahye, G. Maurin, S. Bourrelly, P. L. Llewellyn, C. Serre, T. Loiseau, T. Devic, and G. Ferey, *J. Phys. Chem. C*, **2008**, 112, 514.
- [186] A. Vishnyakov, P. I. Ravikovitch, A. V. Neimark, M. Bulow, and Q. M. Wang, *Nano Letters*, **2003**, 3, 713.
- [187] D. Dubbeldam, H. Frost, K. S. Walton, and R. Q. Snurr, *Fluid. Phase. Equilib*, **2007**, 261, 152.
- [188] K. S. Walton and R. Q. Snurr, *J. Am. Chem. Soc.*, **2007**, 129, 8552.
- [189] Q. Y. Yang, C. Y. Xue, C. L. Zhong, and J. F. Chen, *AIChE J.*, **2007**, 53, 2832.
- [190] A.I. Skoulidas, D.S. Sholl, *J. Phys. Chem. B* 106 **2002** 5058-5067.
- [191] O. Talu, A.L. Myers, *Colloids Surf., A* 187-188 **2001** 83-93.
- [192] A.V.A. Kumar, H. Jobic, S.K. Bhatia, *J. Phys. Chem. B* 110 **2006** 16666-16671.
- [193] A.K. Rappé, C.J. Casewit, K.S. Colwel, W.A. Goddard, W.M. Skiff, UFF, *J. Am. Chem. Soc.* 114 **1992** 10024-10035.
- [194] S.L. Mayo, B.D. Olafson, W.A. Goddard, *J. Phys. Chem.* 94 **1990** 8897-8909.
- [195] D. Frenkel, B. Smit, *Academic Press, 2nd Edition*, San Diego, **2002**.
- [196] T.J.H. Vlught, R. Krishna, B. Smit, *J. Phys. Chem. B* 103 **1999** 1102-1118.
- [197] D. Dubbeldam, S. Calero, T.J.H. Vlught, R. Krishna, T.L.M. Maesen, E. Beerdsen, B. Smit, *Phys. Rev. Lett.* 93 **2004** 088302.
- [198] T.J.H. Vlught, BIGMAC, University of Amsterdam, <http://molsim.chem.uva.nl/bigmac/>, 1 November **2000**.
- [199] H. Chen, D.S. Sholl, *Langmuir* 22 **2006** 709-716.
- [200] R. Krishna, J.M. van Baten, *Chem. Eng. J.* 133 **2007** 121-131.
- [201] R. Krishna, J.M. van Baten, *Chem. Phys. Lett.* 420 **2006** 545-549.
- [202] H. Jobic, C. Laloué, C. Laroche, J.M. van Baten, R. Krishna, *J. Phys. Chem. B* 110 **2006** 2195-2201.
- [203] F. Karavias, A.L. Myers, *Langmuir* 7 **1991** 3118-3126.
- [204] W. Smith, T.R. Forester, I.T. Todorov, Warrington, England, http://www.cse.clrc.ac.uk/msi/software/DL_POLY/index.shtml, March 2006.
- [205] SARA, Computing & Networking Services, Amsterdam, <https://subtrac.sara.nl/userdoc/wiki/lisa/description>, 16 January 2008.
- [206] T. Duren and R. Q. Snurr, *J. Phys. Chem. B*, **2004**, 108, 15703.
- [207] J. W. Jiang and S. I. Sandler, *Langmuir*, **2006**, 22, 5702.
- [208] S. Y. Wang, Q. Y. Yang, and C. L. Zhong, *Sep. Purif. Tech.*, **2008**, 60, 30.
- [209] S. Y. Wang, Q. Y. Yang, and C. L. Zhong, *J. Phys. Chem. B*, **2006**, 110, 20526.

- [210] Q. Y. Yang and C. L. Zhong, *ChemPhysChem*, **2006**, 7, 1417.
- [211] D. Dubbeldam, C. J. Galvin, K. S. Walton, D. E. Ellis, and R. Q. Snurr, *J. Am. Chem. Soc.*, **2008**, 130, 10884.
- [212] C. Chmelik, J. Karger, M. Wiebckw, J. Caro, J. M. van Baten, and R. Krishna, *Microporous Mesoporous Mater.*, **2009**, 117, 22.
- [213] B. Liu, Q. Yang, C. Xue, C. Zhong, B. Chen, and B. Smit, *J. Phys. Chem. C*, **2008**, 112, 9854.
- [214] B. Liu and B. Smit, *Langmuir*, **2009**, 25, 5918.
- [215] Klaus Christmann, *Lecture Series 2010/2011*: 'Modern Methods in Heterogeneous Catalysis Research', Institut für Chemie und Biochemie, Freie Universität Berlin
- [216] McBain, J. W.; Britton, G. T. *J. Am. Chem. Soc.* **1930**, 52, 2198–2222.
- [217] Coolidge, A. S. *J. Am. Chem. Soc.* **1934**, 56, 554–561.
- [218] Coolidge, A. S.; Fornwalt, H. J. *J. Am. Chem. Soc.* **1934**, 56, 561–568.
- [219] Sasidhar Gumma† and Orhan Talu *Langmuir* **2010**, 26(22), 17013–17023
- [220] Salem, M. M. K.; Braeuer, P.; Szombathely, M.v.; Heuchel, M.; Harting, P.; Quitzs, K. *Langmuir* **1998**, 14, 3376–3389.
- [221] Talu, O. *Adv. Colloid Interface Sci.* **1998**, 76-77, 227–269.
- [222] D.D. Do, Adsorption Analysis: Equilibria and Kinetics, Series in Chem.Eng., *Imperial College Press*, **1998**.
- [223] J.J. HacsKaylo, M.D. LeVan, *Langmuir* **1985** 97.
- [224] J.J. Mahle, L.C. Buettner, D.K. Friday, *Ind. Eng. Chem. Res.* 33 **1994** 346.
- [225] S.M. Taqvi, M.D. LeVan, *Ind. Eng. Chem. Res.* 36 **1997** 419.
- [226] S.A. Al-Muhtaseb, J.A. Ritter, *Ind. Eng. Chem. Res.* 37 **1998** 684.
- [227] S.A. Al-Muhtaseb, J.A. Ritter, *Langmuir* 14 **1998** 5317.
- [228] N. Sundaram, R.T. Yang, *J. Colloids Interface Sci.* 198 **1998** 378.
- [229] D. Shen, M. Bilow, F.R. Siperstein, M. Engelhard, A.L. Myers, *Adsorption* 6 **2000** 275.
- [230] S. Sircar, D.V. Cao, Heat of adsorption, *Chem. Eng. Technol.* 25 **2002**
- [231] H. Sun, S. J. Mumby, J. R. Maple, and A. T. Hagler, *J. Am. Chem. Soc.*, **1994**, 116, 2978.
- [232] E. de Vos Burchart, V. A. Verheij, and H. van Bekkum, *Zeolites*, **1989**, 9, 432.
- [233] F. A. Momany, L. M. Carruthers, R. F. McGuire, and H. A. Scheraga, *J. Phys. Chem.*, **1974**, 78, 1595.
- [234] N. L. Allinger, *J. Am. Chem. Soc.*, **1977**, 99, 8127.
- [235] J. H. Lii and N. L. Allinger, *J. Am. Chem. Soc.*, **1989**, 111, 8566.
- [236] J. H. Lii and N. L. Allinger, *J. Am. Chem. Soc.*, **1989**, 111, 8576.
- [237] J. H. Lii and N. L. Allinger, *J. Comp. Chem.*, **1991**, 12, 186.
- [238] N. L. Allinger, Y. H. Yuh, and J. H. Lii, *J. Am. Chem. Soc.*, 1989, 111, 8551.
- [239] N. Nevins and N. L. Allinger, *J. Comp. Chem.*, **1996**, 17, 730.
- [240] N. Nevins, K. S. Chen, and N. L. Allinger, *J. Comp. Chem.*, **1996**, 17, 669.
- [241] N. Nevins, J. H. Lii, and N. L. Allinger, *J. Comp. Chem.*, **1996**, 17, 695.
- [242] P. K. Weiner and P. A. Kollman, *J. Comp. Chem.*, **1981**, 2, 287.
- [243] A. D. MacKerell, D. Bashford, M. Bellott, R. L. Dunbrack, J. D. Evanseck, M. J. Field, S. Fischer, J. Gao, H. Guo, S. Ha, D. Joseph-McCarthy, L. Kuchnir, K. Kuczera, F. T. K. Lau, C. Mattos, S. Michnick, T. Ngo, D. T. Nguyen, B. Prodhom, W. E. Reiher, B. Roux, M. Schlenkrich, J. C. Smith, R. Stote, J. Straub, M. Watanabe, J. Wiorkiewicz-Kuczera, D. Yin, and M. Karplus, *J. Phys. Chem. B.*, **1998**, 102, 3586.
- [244] M. Clark, R. D. Cramer, and N. Vanopdenbosch, *J. Comp. Chem.*, **1989**, 10, 982.
- [245] M. P. Allen and D. J. Tildesley, Computer Simulation of Liquids, *Oxford University Press*, Oxford, **1987**.
- [246] D. Frenkel and B. Smit, Understanding Molecular Simulations: From algorithms to applications, *Academic Press*, **2002**.
- [247] T. J. H. Vlugt, J. P. J. M. van der Eerden, M. Dijkstra, B. Smit, and D. Frenkel, Introduction to Molecular Simulation and Statistical Thermodynamics, **2008**.
- [248] G. Mooij, D. Frenkel, and B. Smit, *J. Phys.-Condensed Matter*, **1992**, 4, L255.
- [249] M. N. Rosenbluth and A. W. Rosenbluth, *J. Chem. Phys.*, **1956**, 23, 356.
- [250] B. Smit, *J. Phys. Chem.*, **1995**, 99, 5597.
- [251] B. Smit, *Mol. Phys.*, **1995**, 85, 153.
- [252] T. J. H. Vlugt, R. Krishna, and B. Smit, *J. Phys. Chem. B*, **1999**, 103, 1102.
- [253] M. D. Macedonia and E. J. Maginn, *Mol. Phys.*, **1999**, 96, 1375.
- [254] M. Mezei, *Mol. Phys.*, **1980**, 40, 901.
- [255] M. Mezei, *Mol. Phys.*, **1987**, 61, 565.
- [256] R. Q. Snurr, A. T. Bell, and D. N. Theodorou, *J. Phys. Chem.*, **1993**, 97, 13742.

-
- [257] S. Chempath, R. Q. Snurr, and J. J. Low, *AIChE J.*, **2004**, 50, 463.
[258] Y. P. Zeng, S. G. Ju, W. H. Xing, and C. L. Chen, *Sep. Purif. Technol.*, **2007**, 55, 82.
[259] V. Lachet, A. Boutin, R. J. M. Pellenq, D. Nicholson, and A. H. Fuchs, *J. Phys. Chem.*, **1996**, 100, 9006.
[260] V. Lachet, A. Boutin, B. Tavitian, and A. H. Fuchs, *Faraday Discussions*, **1997**, 307.
[261] V. Lachet, A. Boutin, B. Tavitian, and A. H. Fuchs, *J. Phys. Chem. B*, **1998**, 102, 9224.
[262] V. Lachet, S. Buttefey, A. Boutin, and A. H. Fuchs, *Phys. Chem. Chem. Phys.*, **2001**, 3, 80.
[263] S. M. P. Lucena, C. L. Cavalcante, and J. Pereira, *Adsorption*, **2006**, 12, 423.
[264] S. M. P. Lucena, J. Pereira, and C. L. Cavalcante, *Microporous Mesoporous Mater.*, **2006**, 88, 135.
[265] A. Z. Panagiotopoulos, *Mol. Phys.*, **1987**, 61, 813.
[266] B. Smit, P. Desmedt, and D. Frenkel, *Mol. Phys.*, **1989**, 68, 931.
[267] A. Z. Panagiotopoulos, *Mol. Phys.*, **1987**, 62, 701.
[268] S. C. McGrother and K. E. Gubbins, *Mol. Phys.*, **1999**, 97, 955.
[269] A. V. Neimark and A. Vishnyakov, *Phys. Rev. E*, **2000**, 62, 4611.
[270] A. V. Neimark and A. Vishnyakov, *J. Chem. Phys.*, **2005**, 122.

CHAPTER 2

METAL ORGANIC FRAMEWORK MIL-53A1 CHARACTERIZATION

2.1.	INTRODUCTION	49
2.2.	EXPERIMENTAL	50
	2.2.1. Investigation techniques	50
2.3.	RESULTS AND DISCUSSION	51
	2.3.1. Elemental Analysis	51
	2.3.2. Mercury porosimetry	51
	2.3.3. Thermogravimetric Analysis	52
	2.3.4. FT-IR	52
	2.3.5. MAS ^{13}C -NMR	54
	2.3.6. X-ray Powder Diffraction	55
	2.3.7. Low Temperature Gas Adsorption	56
2.4.	REFERENCES	58

2.1. INTRODUCTION

Over the past decade, a large number of hybrid organic–inorganic porous solids belonging to a new class of structured nanoporous materials — metal organic frameworks (MOFs) have been synthesized and structurally characterized [1, 2]. Due to their high porosity, high adsorption capacity, and thermal stability, these materials have shown great potential for applications in gas storage, gas separation, catalysis, and allied fields [3-7]. Some MOF materials are already produced at industrial scale.

Ferey and co-workers first developed a series of 3D rare earth diphosphonates named as MIL (Materials of Institut Lavoisier) [8-10]. Later they extended to compounds containing 3D transition metals ($M = V, Fe, Ti$) and metallic dicarboxylates [11-13]. Serre et al. synthesized the first Cr (III) dicarboxylate MIL-53as (as-synthesized) under hydrothermal conditions [14]. MIL-53as exists in two forms, the low-temperature form filled with water molecules and the high temperature form, a dehydrated solid. The transition between the hydrated form (MIL-53lt) and the anhydrous solid (MIL-53ht) is fully reversible and followed by a very high breathing effect. The pores are clipped in the presence of water molecules (MIL-53lt) and reopened when the channels are empty (MIL-53ht). In addition, MIL-53as and MIL-53lt exhibit antiferromagnetic properties.

Several isotopic (e.g., chromium, [15] aluminium, [16] and vanadium [17]) porous terephthalates (MIL-53), of which the aluminium analogue [MIL-53(Al)] is the primary focus of this work, form a very interesting class of MOF materials, because not only they adsorb large amounts of gases, such as H_2 , [18] CO_2 , [19] and light alkanes, [20, 21] but they also exhibit exceptional flexibility by undergoing a reversible structural transformation (or “breathing”) between two distinct conformations - a large-pore (lp) and a narrow-pore (np) structure that have a remarkable difference in unit cell volume of up to 40%.

The MIL-53(Al) framework is built up by the interconnection of infinite *trans* chains of corner-sharing (via OH groups) $AlO_4(OH)_2$ octahedra by 1,4-benzenedicarboxylate (BCD) ligands, giving rise to one-dimensional, diamond-shaped channels with pores of free diameter close to 0.85 nm, which are wide enough to accommodate small guest molecules [3, 16, 20, 22]. The dehydrated structure of MIL-53(Al) is stable up to 773 K, which is remarkable since such a high decomposition temperature is unusual for this class of solids; in fact the chromium [8, 22] or vanadium [23, 24] analogues are only stable up to 623 K.

The conditions at which the breathing of MIL-53 happens have been widely studied before, and it was shown that the structural transformation is triggered by adsorption of some gases (e.g., H_2O and CO_2) and fluid mixtures at room temperature, [3, 8, 25, 26], by mechanical compression, [12, 19], and by changes in temperature [18]. When the structural breathing is triggered by host–guest interactions, the hydroxyl group of MIL-53 plays a major role during the structural transition [27, 28]. The reversible structural transitions triggered by changes in mechanical pressure or temperature are due to the intrinsic properties of MIL-53 without the aid of any guest molecules [29, 30, 31]; in these cases, the structural breathing shows an exceptionally large hysteresis behavior.

The crystallographic unit framework of MIL-53lp(Al) is depicted in Figure 2.1., where, for clarity, the hydrogen atoms are not shown; the unit framework consists of six different types of pseudo-atoms: Al, O(1), O(2), C(1), C(2), and C(3).

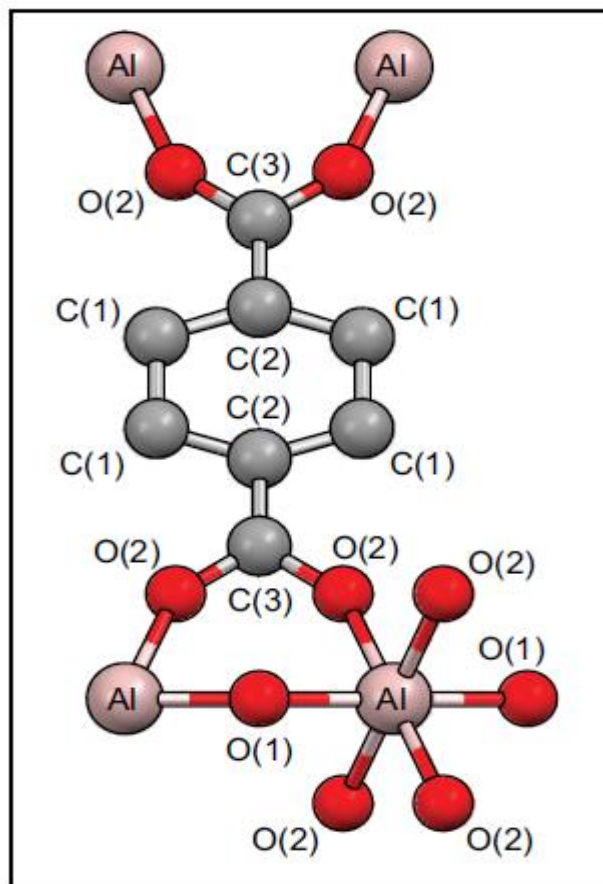


Figure 2.1: Atomic structure of MIL-53lp(Al) unit framework (hydrogens not shown).

2.2. EXPERIMENTAL

MIL-53(Al) crystals synthesized by BASF (Sommerst, NJ) under the trademark Basolite™ A100 were purchased through Sigma-Aldrich (product no. 688738-10G).

2.2.1. Investigation techniques

The following methods were used to characterize MIL-53(Al): elemental analysis (Elemental Analyser 1112, ThermoFinnigan), mercury porosimetry (Autopore IV 9500 porosimeter, Micromeritics, Norcross, Georgia), thermogravimetric analysis (model Q50 V6.7 Build 203, TA Instruments), X-ray powder diffraction (MiniFlex+ X-ray diffractometer, Rigaku, Japan), solid state nuclear magnetic resonance (Bruker MSL 300 P spectrometer), Fourier transform infrared spectroscopy (Perkin Elmer FT-IR spectrometer) and gas adsorption was done on Quantachrome Physi-Chemisorption instrument.

The MIL-53(Al) powder sample was degassed and activated at 473 K over night in a muffle (Nabertherm B170 GmbH),

2.3. RESULTS AND DISCUSSION

2.3.1. Elemental Analysis

The elemental analysis helped to ascertain the structure and purity of the adsorbent material. Before the analysis the MIL-53(AI) was pre-activated for sample purification. The analysis was replicated and averaged results are given (Table. 2.1).

Table 2.1. Elemental analysis for anhydrous MIL-53(AI) sample

	C	N	H	O	Al (wt-%)
Predicted	46.17	–	2.42	38.44	12.97
Experimental	43.38	0.31	2.25	–	–

2.3.2. Mercury porosimetry

The MIL-53(AI) powder was subjected to an experimental mercury intrusion–extrusion cycle in an Autopore IV 9500 porosimeter ((Micromeritics, Norcross, Georgia). The experimental curves are shown in Figure 2.2. The hysteretic behavior of our results is in qualitative agreement with the experimental mercury intrusion–extrusion cycles reported by Neimark et al. [18].

The particle size distribution of the MIL-53(AI) crystals was estimated using the conventional method of Mayer and Stowe [32] applied to low-pressure (0.2–10 MPa) mercury intrusion data. The Mayer–Stowe equation, $P = k\gamma/D_p$, postulates an inverse relation between the intrusion pressure, P , and the particle diameter, D_p , with scaling constant $k\gamma$, where γ is the surface tension of mercury (taken as 0.485 N/m); the Mayer-Stowe constant k , which typically varies in the range 6-13, was taken as 10 [33].

The particle size distribution is well fitted by a log-normal distribution with mean diameter $D_p = 30.0 \mu\text{m}$ and standard deviation $\sigma D_p = 1.7 \mu\text{m}$ (Figure. 2.3); our estimate of D_p is in good agreement with the mean value of $32 \mu\text{m}$ value reported by the manufacturer.

The particle size of our MIL-53(AI) sample is larger than the 2–3 μm size range reported by other authors [25-27] for different batches of MIL-53(AI) particles synthesized by their own groups.

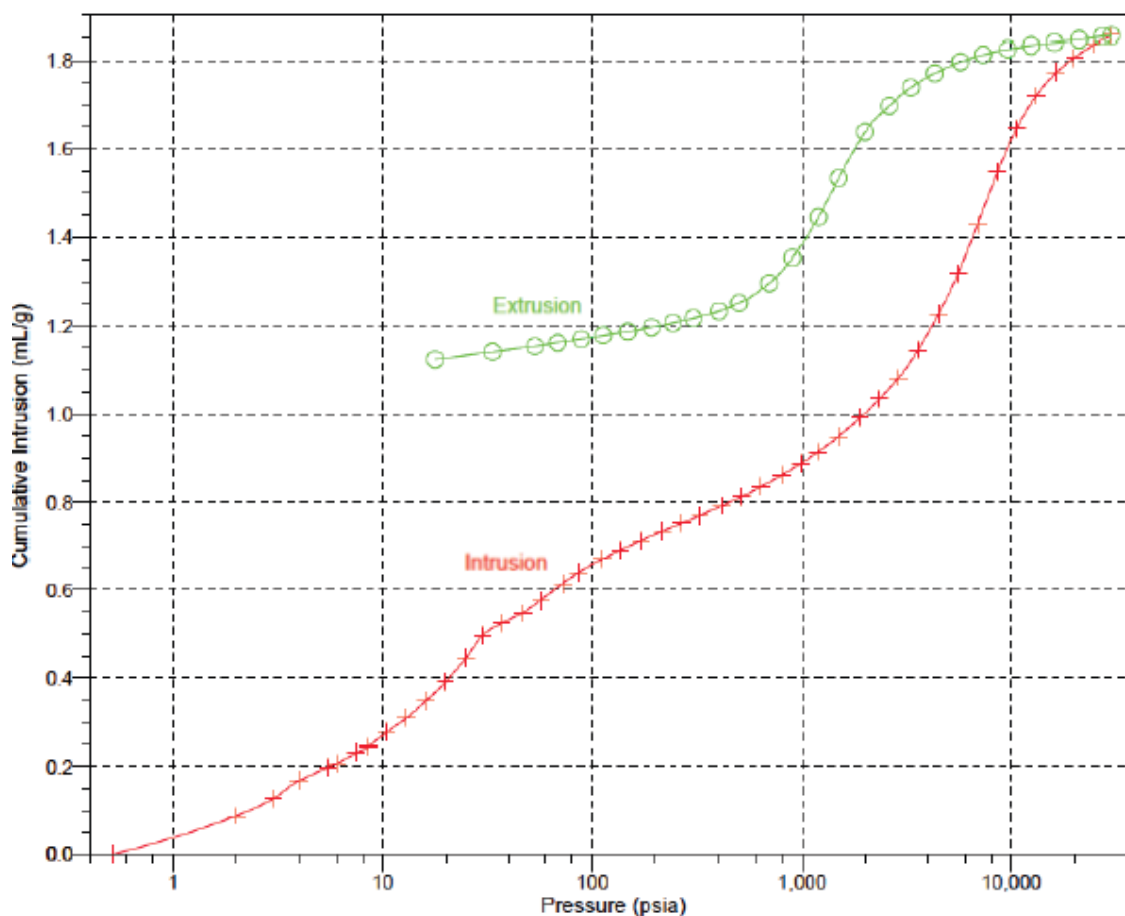


Figure 2.2: Experimental mercury intrusion–extrusion cycle. The curves give the volume of mercury (mL Hg/g of sample) penetrated at a given external pressure P into the measuring cell. The red curve (—+—+—) depicts the intrusion curve obtained by raising P from 0 to 138 MPa; the green curve (—o—o—) shows the extrusion curve, obtained by reverting the process at $P = 138$ MPa and reducing P to 0.14 MPa.

2.3.3. Thermogravimetric Analysis

The hydrated sample of MIL-53(Al) was analyzed by TGA (model Q50 V6.7 Build 203, TA Instruments) to determine the temperature interval over which the sample decomposes; this is done by recording the weight loss as a function of increasing temperature. The analysis was done under a nitrogen atmosphere at a heating rate of 5 deg/min. The experimental TGA profile reproduced in Figure 2.4. shows that the structure is stable up to ca. 773 K, after which it starts to collapse; the profile is in complete agreement with similar TGA results obtained in the literature for this material [16].

2.3.4. FT-IR

Figure 2.5 shows the Fourier-transform infrared spectrum (FT-IR) of the hydrated MIL-53(Al) powder, obtained using a KBr (spectroscopic grade) pellet.

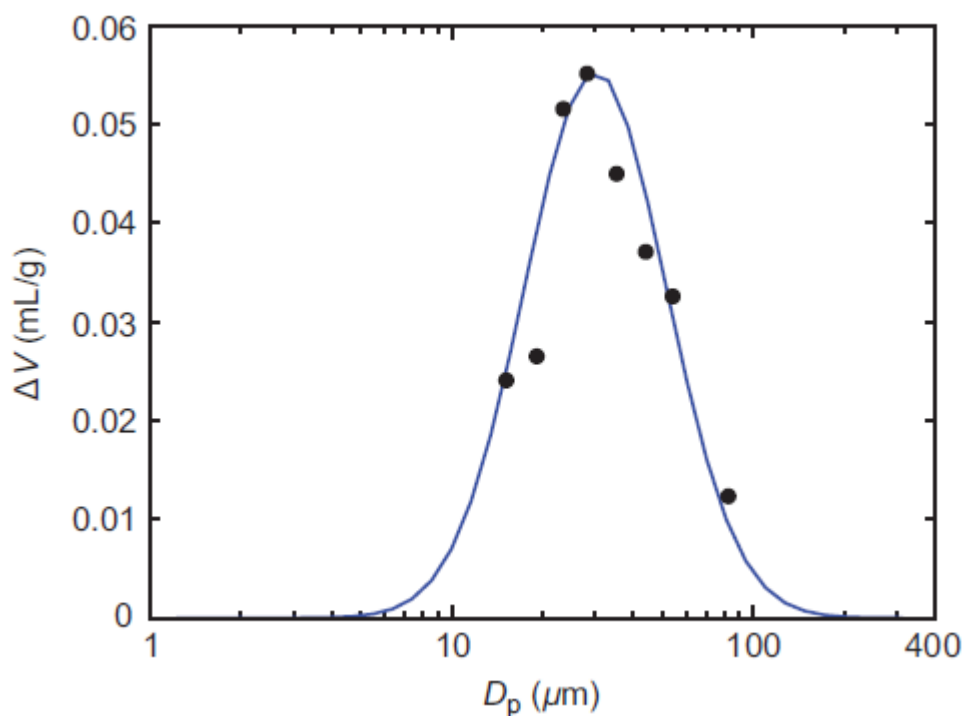


Figure 2.3. Particle size distribution of MIL-53(Al) powder (symbols) and fitting to a lognormal distribution (line) with mean $D_p = 30.0 \mu\text{m}$ and standard deviation $\sigma D_p = 1.7 \mu\text{m}$.

The IR spectrum was recorded on a Perkin Elmer FT-IR spectrometer with single beam, at room temperature, and over the wavelength range of $600\text{--}4000 \text{ cm}^{-1}$.

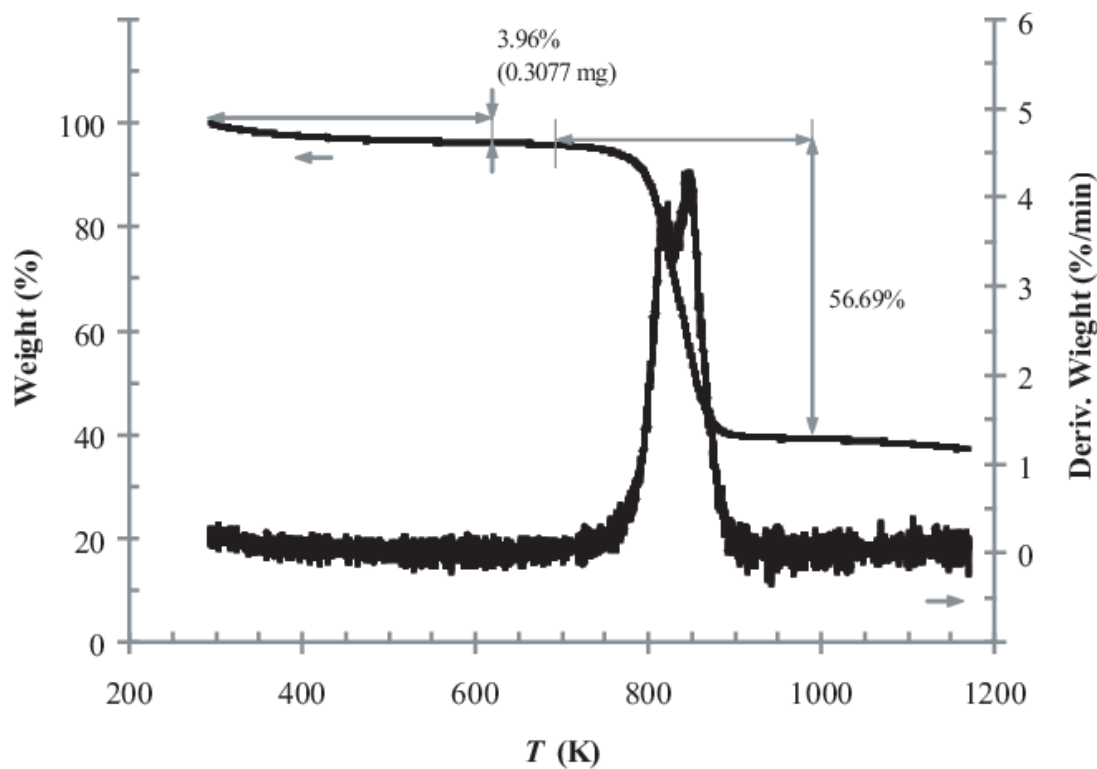


Figure 2.4. Representative TGA analysis of hydrated MIL-53(Al) powder.

Overall, three main groups of signals can be identified [16, 34], corresponding to: (i) H₂O molecules and OH⁻ ions (3400–3600 cm⁻¹); (ii) out of plane bendings of the C–H bonds belonging to the aromatic rings (700–900 cm⁻¹); and (iii) carboxylate functionalities as indicated by several signals in the range 1400–1700 cm⁻¹. In spite of the rather broad H₂O shoulder, the “free” OH⁻ ion stretching, bridging the aluminium ions, can still be observed at ~3610 cm⁻¹. The two observed vibrational bands at 1416 cm⁻¹ and 1446 cm⁻¹ can be assigned to the –CO₂ groups symmetric stretchings, whilst the peaks at 1508 cm⁻¹ and 1578 cm⁻¹ mark the corresponding asymmetric vibrations; these four signals are consistent with –CO₂ groups coordinated to aluminium.

The small shoulder at 1698 cm⁻¹ is ubiquitous. Loiseau et al. [16] identified a well-resolved and intense signal at 1669 cm⁻¹ as corresponding to free protonated benzenedicarboxylate (BDC) molecules trapped in the pores. A direct comparison with our own data is not straightforward, for our peak at 1698 cm⁻¹ is shifted to the red by ca. 30 cm⁻¹. It is interesting to observe the rather weak signals at 2543 cm⁻¹ and 2650 cm⁻¹, which may indicate stretching modes of O–H bonds belonging to a minor amount of protonated carboxylic acids.

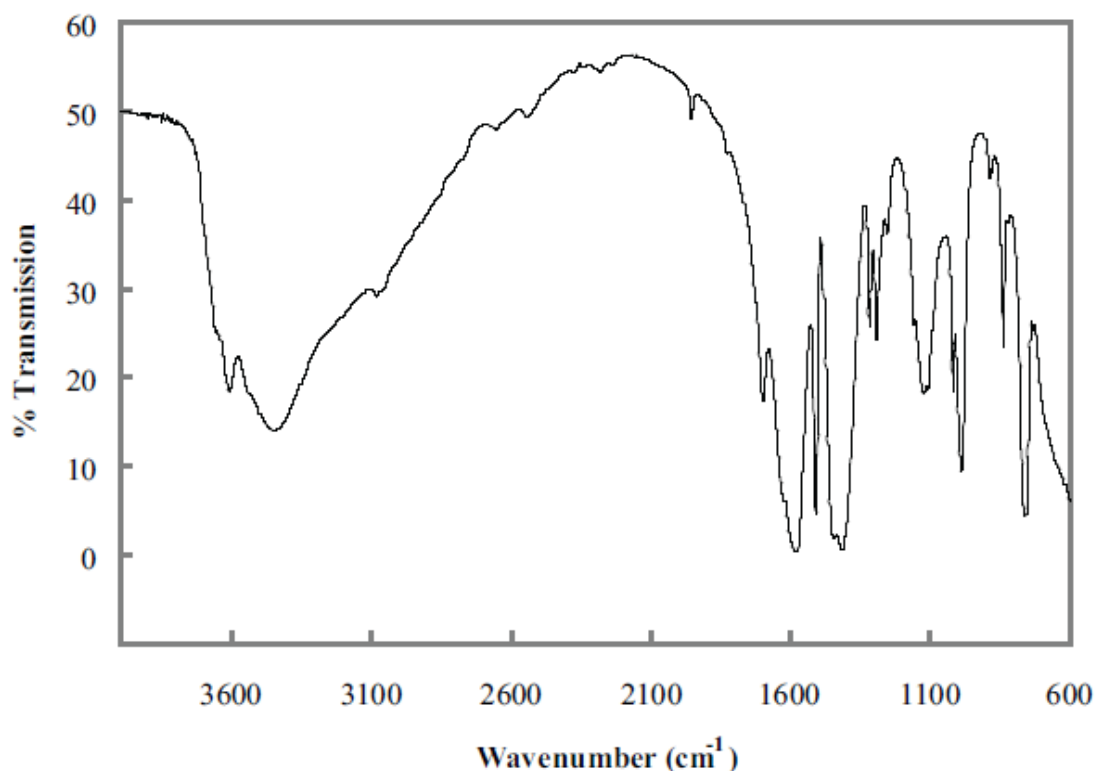


Figure 2.5. FT-IR spectrum of hydrated MIL-53(Al) powder.

2.3.5. MAS ¹³C-NMR

The solid state ¹³C-NMR spectrum was obtained at 75.47 MHz, in a Bruker MSL 300 P spectrometer under magic angle spinning (MAS) mode at a spinning rate of 3.5 kHz, using the conventional cross-polarization/proton decoupling RF pulse sequence with 1 ms contact time and

3s relaxation delay. Prior to analysis, the sample was dried in a vacuum/ N_2 line at 423 K for at least 6 h, then transferred and sealed in zirconia rotors of 3 mm diameter under a controlled atmosphere ($P < 1$ mbar, $[H_2O] < 100$ ppm), after which it was immediately introduced into the spectrometer. The obtained spectrum is reproduced in Fig. 2.6, along with the corresponding chemical shifts. Overall, the ^{13}C -NMR spectrum recorded in Fig. 2.6 agrees satisfactorily with the large pore form of MIL-53(Al) reported by Loiseau et al. [16], namely in the presence of two magnetically distinct carbon atoms in the aromatic ring, as evidenced by the two isotropic signals at $\delta = 136.8$ ppm and $\delta = 128.9$ ppm. The peak at $\delta = 170.7$ ppm, corresponding to the carboxylate group bridging the organic moiety with the inorganic octahedra, is split into a second and less intense contribution at 174.9 ppm, due to the existence of protonated and unprotonated carboxylate functionalities. The signal at $\delta = 182.6$ ppm could not be unmistakably attributed.

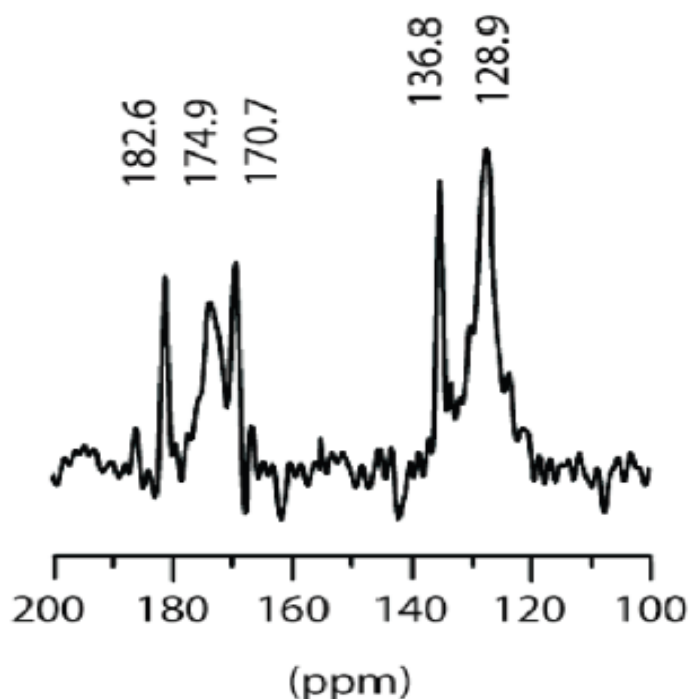


Figure 2.6 MAS ^{13}C -NMR spectrum of the MIL-53(Al) sample.

2.3.6. X-ray Powder Diffraction

The powder X-ray diffraction spectrum of the hydrated MIL-53(Al) powder is shown on Fig. 2.7. The spectrum was obtained in a MiniFlex⁺ X-ray diffractometer (Rigaku, Japan) operating at room temperature, and using the Cu $K\alpha$ line as radiation source ($\lambda = 1.5418$ Å). A continuous scan at 0.5° (2θ) per minute over the range $5^\circ \leq 2\theta \leq 50^\circ$ was performed, using a step size of 0.02° (2θ). For comparison purposes, the diffraction pattern [16] of the narrow pore form of MIL-53(Al) is also recorded in Fig. 2.7. From the inspection of the former, one can essentially identify nine major contributions to the overall diffractogram, and all of them are remarkably consistent with the

narrow-pore form of MIL-53(Al). Considering the two most intense peaks recorded in Figure 2.7 ($2\theta_1 = 8.56^\circ$ and $2\theta_2 = 17.28^\circ$), a relative intensity of $I_2/I_1 \approx 0.38$ is obtained, in good agreement with the corresponding result of Loiseau et al. [16] of $I_2/I_1 \approx 0.32$.

The X-ray powder diffraction pattern was indexed as monoclinic, space group *Cc*, using the software Chekcell [35]. The unit cell parameters thus obtained are indicated in Table 2.2, along with two independent results previously reported [16, 34] for the narrow-pore form of MIL-53 (Al).

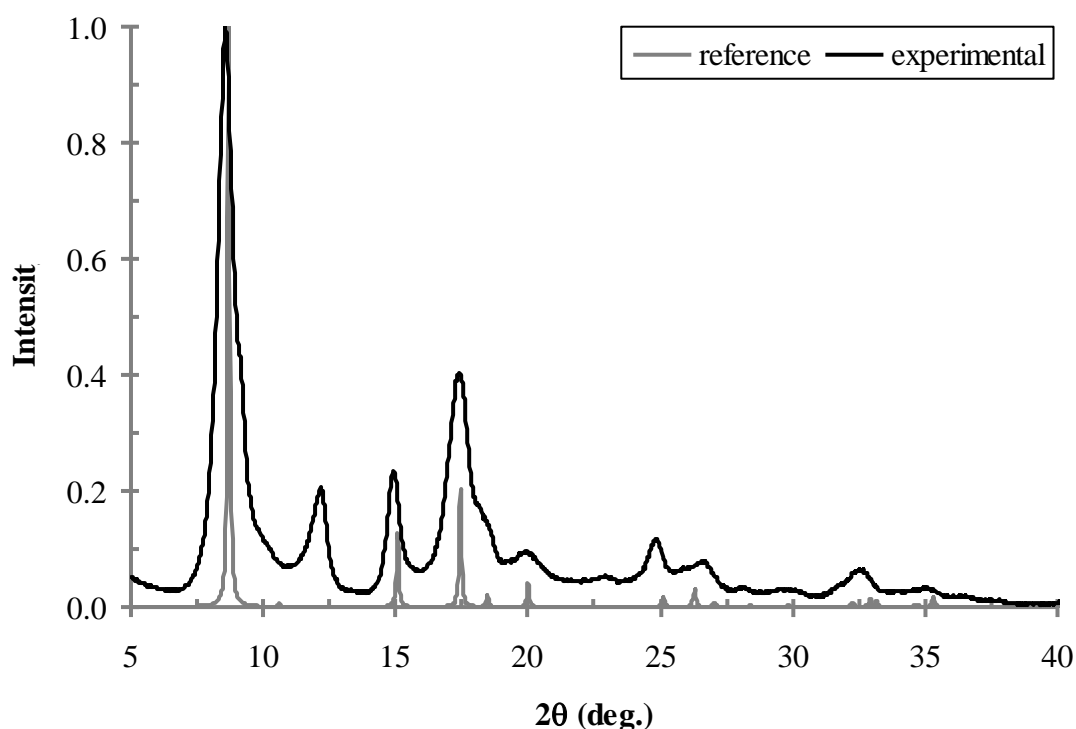


Figure 2.7: Powder XRD spectrum of MIL-53(Al) sample: (blue line) present work, (red line) reference monoclinic unit cell with parameters given in Table 2.2 (obtained using Chekcell), and data from Ref. [1].

2.3.7. Low Temperature Gas Adsorption

The porosity of the dehydrated MIL-53(Al) was measured by means of a gas adsorption isotherm in N_2 at 77 K (Quantachrome Phys-Chemisorption). The analysis through density functional theory (DFT) shows experimental pores between 0.85 and 1.3 nm, which are in accordance with the theoretical value of 0.85 nm. The total BET surface area of the sample is $831 \text{ m}^2/\text{g}$ (Micro: $608 \text{ m}^2/\text{g}$) and the total pore volume is $0.579 \text{ cm}^3/\text{g}$ (Micro: $0.332 \text{ cm}^3/\text{g}$).

The BET surface area of $1100\text{--}1500 \text{ m}^2/\text{g}$ reported by the manufacturer is in agreement with the range of values $1140\text{--}1270 \text{ m}^2/\text{g}$ determined by other authors [16, 18].

Table 2.2. Crystallographic unit cell parameters obtained for MIL-53(Al).

Formula	Al(OH)[O ₂ C-C ₆ H ₄ -CO ₂] \cdot H ₂ O		
Crystal system	Monoclinic		
Space group	Cc		
a (Å)	20.262	(19.513)	(20.756)
b (Å)	7.455	(7.612)	(7.055)
c (Å)	6.787	(6.576)	(6.609)
α (deg.)	90.0	(90.0)	(90.0)
β (deg.)	105.65	(104.24)	(113.58)
γ (deg.)	90.0	(90.0)	(90.0)
V (Å ³)	987.1	(946.8)	(886.9)

*First and second column of values in parenthesis correspond to a low-temperature form of the solid obtained, respectively, by Loiseau et al. [16] and Liu et al. [18].

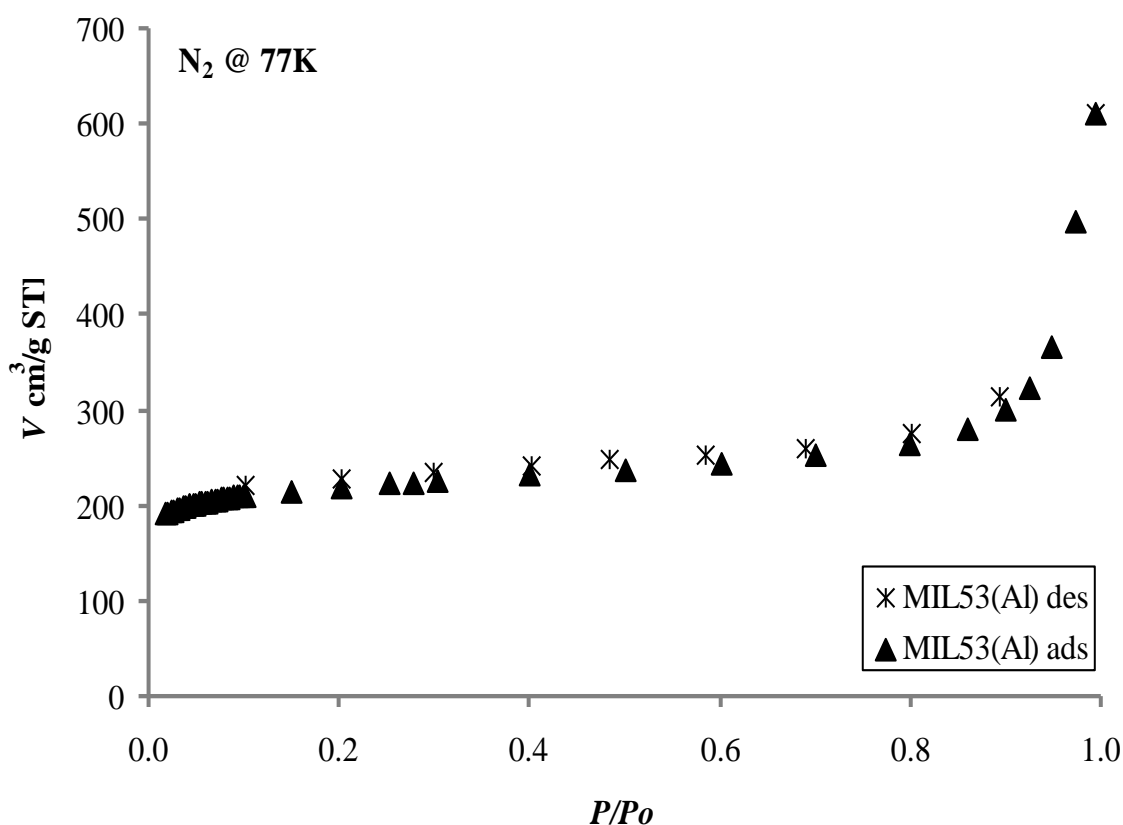


Figure 2.8. Adsorption-desorption of N₂ on MIL-53(Al) The calculated from BET total surface area of the MIL-53(Al) sample is 831 m²/g.

2.5. REFERENCES

- [1] Yaghi, O. M.; O’Keeffe, M.; Ockwig, N. W.; Chae, H. K.; Eddaoudi, M.; Kim, J. *Nature* **2003**, *423*, 705–714.
- [2] Férey, G.; Mellot-Draznieks, C.; Serre, C.; Millange, F. *Acc. chem. Res.* **2005**, *38*, 217–225.
- [3] Bourrelly, S.; Llewellyn, P. L.; Serre, C.; Millange, F.; Loiseau, T.; Férey, G. *J. Am. Chem. Soc.* **2005**, *127*, 13519–13521.
- [4] Liu, B.; Smit, B. *Langmuir* **2009**, *25*, 5918–5926.
- [5] Latroche, M.; Subl’e, S.; Serre, C.; Mellot-Draznieks, C.; Llewellyn, P. L.; Lee, J.-H.; Chang, J.-S.; Jhung, S. H.; Férey, G. *Angew. Chem., Int. Ed.* **2006**, *45*, 8227–8231.
- [6] Furukawa, H.; Miller, M. A.; Yaghi, O. M. *J. Mater. Chem.* **2007**, *17*, 3197–3204.
- [7] Llewellyn, P. L.; Bourrelly, S.; Serre, C.; Vimont, A.; Daturi, M.; Hamon, L.; DeWeireld, G.; Chang, J.-S.; Hong, D.-Y.; Hwang, Y. K.; Jhung, S. H.; Férey, G. *Langmuir* **2008**, *24*, 7245–7250.
- [8] Serre, C.; Millange, F.; Thouvenot, C.; Nogues, M.; Marsolier, G.; Louer, D.; Férey, G. *J. Am. Chem. Soc.* **2002**, *124*, 13519–13526.
- [9] D. Riou and G. Férey, *J. Mater. Chem.*, **1998**, *8*, 2733.
- [10] D. Riou, O. Roubeau, and G. Férey, *Microporous Mesoporous Mater.*, **1998**, *23*, 23.
- [11] D. Riou, C. Serre, and G. Férey, *J. Solid State Chem.*, **1998**, *141*, 89.
- [12] F. Serpaggi and G. Férey, *J. Mater. Chem.*, **1998**, *8*, 2737.
- [13] F. Serpaggi and G. Férey, *J. Mater. Chem.*, **1998**, *8*, 2749.
- [14] F. Serpaggi and G. Férey, *Microporous Mesoporous Mater.*, **1999**, *32*, 311.
- [15] C. Serre, F. Millange, C. Thouvenot, M. Nogues, G. Marsolier, D. Louer, and G. Férey, *J. Am. Chem. Soc.* **2002**, *124*, 13519.
- [16] Loiseau, T.; Serre, C.; Huguenard, C.; Fink, G.; Taulelle, F.; Henry, M.; Bataille, T.; Férey, G. *Chem. Eur. J.* **2004**, *10*, 1373–1382.
- [17] Barthelet, K.; Marrot, J.; Riou, D.; Férey, G. *Angew. Chem., Int. Ed.* **2002**, *41*, 281–284.
- [18] Liu, Y.; Her, J.-H.; Dailly, A.; Ramirez-Cuesta, A. J.; Neumann, D. A.; Brown, C. M. *J. Am. Chem. Soc.* **2008**, *130*, 11813–11818.
- [19] Neimark, A. V.; Coudert, F.-X.; Triguero, C.; Boutin, A.; Fuchs, A. H.; Beurroies, I.; Denoyel, R. *Langmuir* **2011**, *27*, 4734–4741.
- [20] Trung, T. K.; Trens, P.; Tanchoux, N.; Bourrelly, S.; Llewellyn, P. L.; Loera-Serna, S.; Serre, C.; Loiseau, T.; Fajula, F.; Férey, G. *J. Am. Chem. Soc.* **2008**, *130*, 16926–16932.
- [21] Llewellyn, P. L.; Maurin, G.; Devic, T.; Loera-Serna, S.; Rosenbach, N.; Serre, C.; Bourrelly, S.; Horcajada, P.; Filinchuk, Y.; Férey, G. *J. Am. Chem. Soc.* **2008**, *130*, 12808–12814.
- [22] Millange, F.; Serre, C.; Férey, G. *Chem. Commun.* **2002**, *38*, 822–823.
- [23] Barthelet, K.; Marrot, J.; Riou, D.; Férey, G. *Angew. Chem.* **2002**, *114*, 291–294.
- [24] Barthelet, K.; Marrot, J.; Riou, D.; Férey, G. *Angew. Chem. Int. Ed.* **2002**, *41*, 281–284.
- [25] Ramsahye, N. A.; Maurin, G.; Bourrelly, S.; Llewellyn, P. L.; Loiseau, T.; Serre, C.; Férey, G. *Chem. Commun.* **2007**, *43*, 3261–3263.
- [26] Llewellyn, P. L.; Bourrelly, S.; Serre, C.; Filinchuk, Y.; Férey, G. *Angew. Chem., Int. Ed.* **2006**, *46*, 7751–7754.
- [27] Boutin, A.; Springuel-Huet, M.-A.; Nossov, A.; G’ed’eon, A.; Loiseau, T.; Volkringer, C.; Férey, F.; Coudert, F.-X.; Fuchs, A. H. *Angew. Chem., Int. Ed.* **2009**, *48*, 8314–8317.
- [28] Khan, N. A.; Jhung, S. H. *Cryst. Growth Des.* **2010**, *10*, 1860–1865.
- [29] Beurroies, I.; Boulhout, M.; Llewellyn, P. L.; Kuchta, B.; Férey, G.; Serre, C.; Denoyel, R. *Angew. Chem., Int. Ed.* **2010**, *49*, 7526–7529.
- [30] Ramsahye, N. A.; Maurin, G.; Bourrelly, S.; Llewellyn, P.; Loiseau, T.; Férey, G. *Phys. Chem. Chem. Phys.* **2007**, *9*, 1059–1063.
- [31] Liu, Y.; Eubank, J. F.; Cairns, A. J.; Eckert, J.; Kravtsov, V. C.; Luebke, R.; Eddaoudi, M. *Angew. Chem., Int. Ed.* **2007**, *46*, 3278–3283.
- [32] Mayer, R. P.; Stowe, R. A. *J. Colloid Sci.* **1965**, *20*, 893.
- [33] Do, D. D. *Adsorption Analysis: Equilibria and Kinetics*; Imperial College Press: London, UK, 1998. 15
- [34] John Wiley: New York, 1986. <http://www.chem.ucla.edu/~webspectra/irtable.html>.
- [35] Laugier, J.; Bochu, B.: *Chekcell*. <http://www.ccp14.ac.uk/tutorial/lmgp>

CHAPTER 3

EQUILIBRIUM GRAVIMETRIC MEASUREMENTS

3.1.	INTRODUCTION	63
3.2.	EXPERIMENTAL	64
	3.2.1. Gravimetric Technique for Adsorption Measurements	64
	3.2.2. Adsorption Equilibrium Measurements	68
3.4.	CONCLUSION	69
3.5.	REFERENCES	70

3.1 INTRODUCTION

Any application of adsorption requires that the adsorbed amount be quantified accurately and unambiguously. The present work is aiming at the thermodynamic framework investigation for quantifying the adsorption equilibrium. In general, the most common methods used for measuring adsorption, are the volumetric and gravimetric techniques [1].

In volumetric technique a given amount of sorptive gas is expanded into a vessel which includes a sorbent sample and which initially has been evacuated. Upon expansion the sorptive gas is partly adsorbed on the (external and internal) surface of the sorbent material, partly remaining as gas phase around the sorbent. By a mass balance, the amount of gas being adsorbed can be calculated if the void volume of the sorbent, i.e. the volume which cannot be penetrated by the sorptive gas molecules is known at least approximately.

The line diagram of the volumetric setup is shown in (Fig. 3.1).

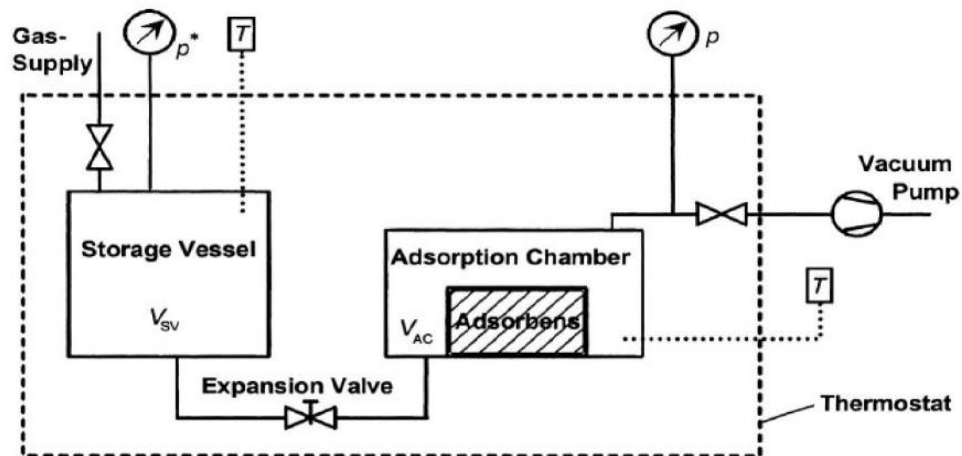


Figure 3.1. Experimental setup for volumetric measurement of pure gas adsorption equilibria.

In the gravimetric method, the weight change of the adsorbent sample in the gravity field due to adsorption from the gas phase is recorded (Fig. 3.2). Various types of sensitive microbalance have been developed for this purpose. A continuous-flow gravimetric technique coupled with wavelet rectification allows for higher precision, especially in the near-critical region.

The gravimetric method measures excess adsorption as the apparent increase in weight of the sample corrected for the buoyancy force exerted by the bulk fluid. The gravimetric methods are typically more accurate for the following reasons:

- Errors associated with volume measurement (loss in transfer, parallax, spillage, over-titration, etc.) are reduced in gravimetric measurements.
- Gravimetric methods are less sensitive to temperature than volumetric methods.
- While both types of methods are subject to sample loss, gravimetric methods are less so.
- A mass is easier to reproducibly determine than a concentration.
- A mass is easier to standardize than a concentration. Again there are errors associated with both, but mass is generally easier to deal with.

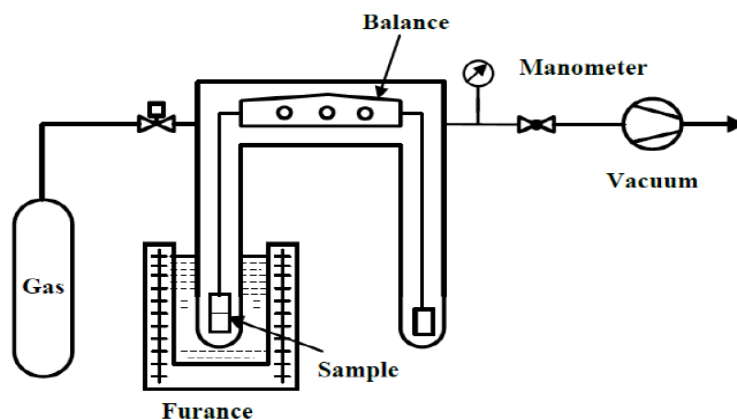


Figure 3.2. Schematic diagram of gravimetric apparatus.

The choice between the volumetric and gravimetric techniques is a matter of convenience but the gravimetric method is more suitable for automation.

3.2. EXPERIMENTAL

3.2.1 Gravimetric Technique for Adsorption Measurements

In the present work, the single-component adsorption isotherm for studied gases was obtained using the standard static gravimetric technique [2, 3].

Briefly, the method consists of progressive addition of gas to the measuring cell containing the MOF sample, followed by equilibration under isothermal conditions in order to generate data points along the adsorption isotherm. Pressure and weight changes are continuously monitored until equilibration, which is assumed to occur when the rate of change of the measured mass approaches zero. The procedure is repeated until enough data points are collected to generate a complete isotherm. The cell is then progressively depressurized and equilibrated to generate further points along the descending path of the isotherm and to check for possible hysteresis effects.

Major advantages of gravimetric method include sensitivity, accuracy, and the possibility of checking the state of activation of an adsorbent sample. However, consideration must be given to buoyancy correction in gravimetric measurement. A counterpart is used for this purpose. The solid sample is placed in a sample holder on one arm of the microbalance while the counterpart is loaded on the other arm. Care must be taken to keep the volume of the sample and the counterpart as close as possible to reduce the buoyancy effect. The system is vacuumed and the balance is zeroed before starting experiments. Buoyancy is measured by introducing helium and pressurizing up to the highest pressure of the experiment. It is assumed that helium does not adsorb and any weight change (ΔW) is due to buoyancy. Knowing the density of helium (ρ_{He}), one can determine the difference in the volume (ΔV) between the sample and the counterpart:

$$\Delta V = \frac{\Delta W}{\rho_{\text{He}}(P, T)} \quad (3.1)$$

The measured weight can be corrected for the buoyancy effect at a specified temperature and pressure:

$$W = W_{\text{exp}} - \Delta V \rho_b(P, T) \quad (3.2)$$

where W_{exp} is the weight reading before correction.

The gravimetric apparatus consists of the balance to measure the adsorption amount and pressure sensor to measure the equilibrium pressure. In the gravimetric method, the weight change of the adsorbent sample in the gravity field due to adsorption from the gas phase is recorded. Various types of sensitive microbalance have been developed for this purpose.

The adsorption measurements of gases on MIL-53(Al) were performed in an ISOSORP 2000 high-pressure magnetic-suspension balance (MSB) from Rubotherm GmbH (Bochum, Germany) with automated online data acquisition of temperature, pressure, and sample weight, by means of an in-house developed software interface (Fig. 3.3) [4]. The adsorption experiments were carried out using both open and closed-loop gravimetry. In the MSB the sample holder is coupled to a suspension magnet, instead of hanging directly at the balance.



Figure 3.3. ISOSORP 2000 high-pressure magnetic-suspension balance (MSB) from Rubotherm GmbH (Bochum, Germany).

Using this freely suspension coupling, the measuring force is transmitted contactlessly from the closed measuring cell to a Sartorius microbalance, located outside under ambient atmosphere. Our MSB apparatus has a resolution of 0.01 mg, an uncertainty $\leq 0.002\%$, and reproducibility $\leq 0.03\text{mg}$ for a maximum load of 25 g. A schematic diagram of the experimental setup is shown in Fig. 3.4.

The advantage of the MSB is the possibility of accurately weighing samples contactlessly under nearly all environments. Instead of hanging directly at the balance, the sample is coupled to a suspension magnet, achieving a constant vertical position in a closed measuring cell.

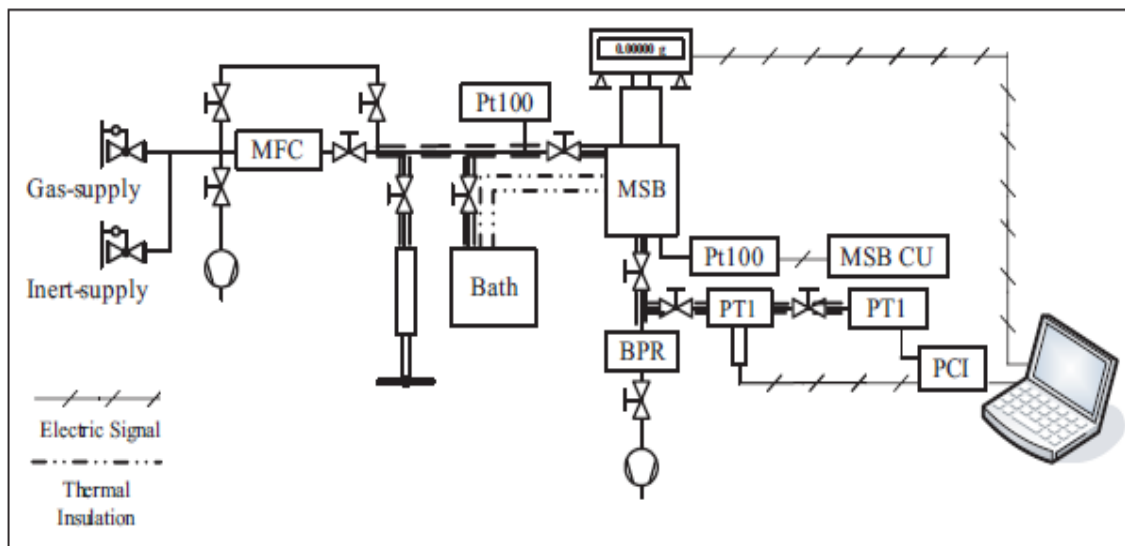


Figure 3.4. Schematic of the experimental set-up used for the adsorption measurements. Labeling is as follows: MSB, magnetic suspension balance; MSB CU, MSB control unit; BPR, back-pressure regulator; MFC, mass-flow controller; PCI, PC interface for data acquisition; PT, pressure transducer; Pt100, thermocouple.

The conditions that can be imposed on the measuring chamber are limited to 100 °C and 150 bar. A mass-flow meter/controller (MFC) from Hastings (0.1–10 slpm N₂), with a 1%FS (full-scale) accuracy, is coupled to the feed line. A pressure generator is used whenever the desired pressure is higher than the available feed pressure. The temperature is measured and controlled using four-wire Pt100 probes and two thermostatic baths from Selecta Ultratherm; the cell temperature is kept within (± 0.1) K of the set-point. A Bronkhorst back-pressure regulator (BPR), with 0.5% FS accuracy, is coupled to the outlet line to control the pressure in the chamber for the continuous flow experiments; the controllable pressure range is 3–16 bar. Five transducers are employed to accurately measure different pressure ranges: Keller AG for 0–0.1MPa with 0.5% FS accuracy; Lukas Schaevitz for UHV–0.5MPa with 0.08% FS accuracy; Lukas Schaevitz for 0–3.5MPa with 0.04% FS accuracy; Omegadyne for 0–20.7MPa with <0.01MPa of error; and Kistler Inst. AG for 0–20MPa with <(± 0.16) % of error. The range of thermodynamic conditions spanned in the experiments reported here is 0–9MPa and 273–325 K.

Buoyancy forces are taken into account to correct the influence of gas density on the measured apparent weight of the sample. The displacements of gas by the sample holder, solid adsorbent, and adsorbed phase, are taken into consideration. The correction due to the sample holder is obtained with blank experiments performed at different pressures with the empty holder. The buoyancy due to the solid matrix of the adsorbent, which results in an apparent weight loss, is estimated as the product of the skeletal volume of the adsorbent and the gas density. Finally, the buoyancy effect exerted on the adsorbed phase is corrected to obtain the absolute adsorption isotherm, $n(P, T)$.

The weight, m , displayed by the balance, results from the net force exerted on the sample (3.3):

$$m = m_h \left(1 - \frac{\rho_g}{\rho_h} \right) + m_s \left(1 - \frac{\rho_g}{\rho_s} + n_{\text{ex}} \right) \quad (3.3)$$

where, m_h and ρ_h are the mass and density of the sample holder, respectively, m_s and ρ_s are the mass and density of the adsorbent sample, respectively, ρ_g is the density of the bulk gas at the equilibrium pressure and temperature, and n_{ex} is the specific excess adsorption (3.4):

$$n_{\text{ex}} = n \left(1 - \frac{\rho_g}{\rho_a} \right) \quad (3.4)$$

where ρ_a is the density of the adsorbed phase; n_{ex} gives the amount adsorbed in excess of the equilibrium gas occupying the same volume, and is the well-defined thermodynamic quantity known as excess adsorption [5].

The blank experiments with an empty holder give the mass and density of the holder from the intercept and slope of the linear decrease of apparent weight with gas density (3.5):

$$m = m_h - \frac{m_h}{\rho_h} \rho_g \quad (3.5)$$

The values of m_h and ρ_h are estimated at different temperatures using N_2 in order to check for the validity of the measurements. Adsorption experiments using a non-adsorbing gas, such as helium at high temperature, provide the mass (m_s) and density (ρ_s) of the MIL-53(Al) sample:

$$m - m_h \left(1 - \frac{\rho_g}{\rho_h} \right) = m_s - \frac{m_s}{\rho_s} \rho_g \quad (3.6)$$

In this work, it is assumed that helium acts as an inert probe that penetrates into all the accessible pore volume of the MIL-53(Al) without being adsorbed. Finally, the experiments with the MIL-53(Al) sample provide the excess adsorption isotherm (3.7):

$$m_s n_{\text{ex}} = m - m_h \left(1 - \frac{\rho_g}{\rho_h} \right) - m_s \left(1 - \frac{\rho_g}{\rho_s} \right) \quad (3.7)$$

which can then be converted into the total adsorption isotherm (3.8):

$$n = \frac{\rho_a}{\rho_a - \rho_g} n_{\text{ex}} \quad (3.8)$$

Alkanes C₁-C₄ and other ancillary gases (He and N₂) were supplied by Air Liquide and Praxair (Portugal); all gases were research grade. Prior to the experiments, the sample was activated at 473 K over night in an muffle (Nabertherm B170 GmbH), transported to the set-up under an inert (helium) atmosphere, and finally degassed in situ under vacuum, at 353.15 K for at least 8 hours; ~0.73 g of MIL-53(Al) powder was employed in the measurements. The alkanes adsorption isotherms were measured at 303.15 K, 323.15 K, and 353.15 K, over a pressure range of ~0.01–5.0 MPa.

3.2.2 Adsorption Equilibrium Measurements

In gravimetric adsorption equilibrium measurements for microporous solids, the thermodynamic property most readily determinable is that which Gumma and Talu [6] denote as *net adsorption*, n_{net} : it is the total amount of gas present in the measuring cell with the adsorbent minus the amount that would be present in the empty cell (without the adsorbent) at the same pressure and temperature. In the case of a gravimetric experiment,

$$n_{net} = \frac{w - m_s + V_h \rho_g}{m_s} \quad (3.9)$$

where n_{net} is expressed per unit mass of adsorbent, W is the apparent weight of the sample measured by the balance, m_s is the mass of sample (measured in vacuum after degassing and thermal pretreatment of the adsorbent), V_h is the volume of all moving parts present in the measuring cell (such as the holding basket) that are subject to the buoyancy force exerted by the gas, and ρ_g is the density of the gas at the pressure and temperature conditions of the experiment.

The advantage of reporting adsorption results in terms of n_{net} is that it completely circumvents the use of probe molecules to fix the reference state of each sample, since the value of V_h is independent of the fluid–adsorbent system. In our apparatus, V_h was determined by calibration with nitrogen and helium at ambient temperature only once without any sample in the system.

Adsorption measurements, however, are invariably reported in terms of excess adsorption, n_{ex} , which is the total amount of gas introduced into the measuring cell minus the amount that remains in the gas phase upon equilibration of the system [7]; in other words, n_{ex} is the amount of gas in excess of the amount that would be present in the same system, at the same pressure and temperature, if the gas did not adsorb. This quantity is related to n_{net} by (3.10):

$$n_{ex} = n_{net} + V_s \rho_g \quad (3.10)$$

where V_s is the specific adsorbent volume impenetrable to the adsorbate. In the case of MIL-53, $V_s = 1/\rho_s$ where ρ_s is the skeletal (or structural) density of the adsorbent.

The relations between absolute adsorption and the other two adsorption quantities are

$$n = n_{ex} + V_p \rho_g = n_{net} + (V_p + V_s) \rho_g \quad (3.11)$$

where V_p is the specific pore volume of the adsorbent.

3.3. CONCLUSIONS

The adsorption of the C₁-C₄ light alkanes on MIL-53(Al) were studied using both open- and closed-loop gravimetry in the pressure and temperature ranges of 0.01–5 MPa and 303–353 K, respectively. The adsorption equilibrium of the components of the natural gas on MIL 53 (Al) have been measured and analyzed, within the scope of developing sustainable strategies for gas separation, recovery and storage.

3.4 REFERENCES

- [1] Talu, O. *Adv. Colloid Interface Sci.* **1998**, 76-77, 227–269
- [2] Esteves, I. A. A. C.; Lopes, M. S. S.; Nunes, P. M. C.; MOTA, J. P. B. *Sep. Purif. Technol.* **2008**, 62, 281–296.
- [3] Cruz, F. J. A. L.; Esteves, I. A. A. C.; Agnihotri, S.; Mota, J. P. B. *J. Phys. Chem. C* **2011**, 115, 2622–2629.
- [4] Coudert, F.-X.; Jeffroy, M.; Fuchs, A. H.; Boutin, A.; Mellot-Draznieks, C. *J. Am. Chem. Soc.* **2008**, 130, 14294–14302.
- [5] Coudert, F.-X.; Mellot-Draznieks, C.; Fuchs, A. H.; Boutin, A. *J. Am. Chem. Soc.* **2009**, 131, 3442–3443.
- [6] Gumma, S; Talu, O. *Langmuir* **2010**, 26, 17013–17023.
- [7] Sircar, S. *J. Chem. Soc., Faraday Trans.* **1985**, 81, 1527–1540.

CHAPTER 4

EXPERIMENTAL AND THEORETICAL STUDIES OF SUPERCRITICAL METHANE ADSORPTION IN THE MIL-53(AI) METAL ORGANIC FRAMEWORK

4.1.	INTRODUCTION	75
4.2.	EXPERIMENTAL	75
4.2.1.	Molecular Model and Simulation Method	75
4.3.	RESULTS AND DISCUSSION	79
4.3.1.	Adsorption Equilibrium Measurements	79
4.3.2.	Data Fitting	87
4.3.3.	Isosteric Heat of the Adsorption	89
4.3.4.	DOE Target Calculations	92
4.4.	CONCLUSION	95
4.5.	REFERENCES	96

4.1 INTRODUCTION

Methane is an important hydrocarbon because it is the major component of natural gas (NG), which is commonly considered as a suitable and nonpolluting energy source for the future [1].

In the present work, the energetics and confinement of supercritical methane in MIL-53p(Al) are studied experimentally via gravimetric adsorption experiments and by Grand Canonical Monte Carlo (GCMC) simulations.

A combined experimental and theoretical study of the adsorption equilibrium properties of supercritical methane in MIL-53(Al) over pressures in the range ~0.01–7 MPa and temperatures in the 303–353 K region is reported here. Overall, it spanned the largest P - T range over which experimental results on methane adsorption in MIL-53(Al) have been reported to date.

Finally, we examine the potential use of MIL-53(Al) as a methane adsorptive storage medium, compare its performance with those of activated carbons, which are the prime contenders in this field, and explore the optimum operating temperature to use MIL-53(Al) in this type of application.

4.2. EXPERIMENTAL

4.2.2. Molecular Model and Simulation Method

Monte Carlo (MC) and molecular dynamics (MD) simulations of adsorption in MOFs have been carried out mostly using classical force fields. The dispersion interactions of the framework atoms in those nanoporous materials have been usually modeled using the UFF [2] or DREIDING [3] force fields, or combinations thereof, with or without refinement of the interaction parameters. This is the case for Cu-BTC [4-7], various types of IRMOFs [8,9], MIL-47(V) [10,11], and several other types of MOFs [5,6,12,13]. In a study on the breathing effect of MIL-53(Al) upon CO₂ adsorption, Ramsahye et al. [14] modeled the interaction between the sorbate and the organic ligand of MIL-53(Al) framework using 12-6 Lennard–Jones (LJ) parameters derived by Shen et al. [15] for the benzene–CO₂ system; the interactions with the inorganic part of MIL-53(Al) were adapted from previous work on aluminosilicalite materials [16]. A more recent work [11] of the same group on the adsorption of light hydrocarbons in MIL-53(Cr) and MIL-47(V) frameworks employed a combination of the UFF [2] or DREIDING [3] force fields.

The porous framework of MIL-53(Al) is dominated by the organic ligand and, since the polarisability of the aluminium atoms is much lower than that of the oxygen atoms [14], as a first approximation the dispersive contribution of the inorganic part of MIL-53(Al) can be attributed only to the oxygens and hydroxyl groups. It is thus likely that a force field whose parameterization is determined from vapor–liquid equilibria, enthalpies of vaporization, and vapor pressures of organic compounds, namely alkylbenzenes with ether or hydroxyl functionalities requires minimum

adjustment of its parameters to provide a reasonably accurate quantitative description of the adsorption of a small, nonpolar molecule, like methane, into the porous framework of MIL-53(AI).

In the present work, the parameterization of solid–fluid dispersive interactions in MIL-53(AI) is based on the TraPPE-UA [17-21] force field to take advantage of the transferability of the parameters built into it. We shall demonstrate that no reparameterization of the dispersive parameters for MIL-53(AI) is necessary if this force field is employed. In TraPPE-UA, non-bonded interactions are governed by a 12-6 LJ plus fixed point charge functional form:

$$U(r_{ij}) = 4\varepsilon_{ij} \left[\left(\frac{\sigma_{ij}}{r_{ij}} \right)^{12} - \left(\frac{\sigma_{ij}}{r_{ij}} \right)^6 \right] + \frac{q_i q_j}{4\pi\varepsilon_0 r_{ij}} \quad (4.1)$$

where r_{ij} , ε_{ij} , σ_{ij} , q_i , and q_j are the bead–bead separation, the LJ well depth, the LJ diameter, and the partial charges on beads i and j , respectively.

The unlike LJ interactions are computed with Lorentz–Berthelot combining rules:

$$\sigma_{ij} = \frac{\sigma_i + \sigma_j}{2} \quad (4.2)$$

$$\varepsilon_{ij} = \sqrt{\varepsilon_i \varepsilon_j} \quad (4.3)$$

In the TraPPE-UA force field, hydrogens are combined with the carbons they are bonded to, forming single pseudo-atoms; hydrogens bonded to heteroatoms, such as oxygen, are represented explicitly with a partial charge. Thus, groups such as CH₄, CH₃, CH₂, CH, and so forth are treated as single interaction sites.

In our molecular simulation work, MIL-53lp(AI) is modeled as a rigid lattice with its constituent atoms at the crystallographic positions reported by Liu et al. [9], which were obtained from the neutron diffraction pattern of the sample upon cooling from 450 K to 295 K; the lattice parameters at ambient temperature are very similar to those at 450 K. The lattice parameters for the MIL-53lp(AI) unit cell are reported as [9] $a = 6.6384(4)$ Å, $b = 16.761(2)$ Å, and $c = 12.839(2)$ Å in the *Imma* space group (orthorhombic); the unit cell volume is $V_c = 1428.5(2)$ Å³.

The crystallographic unit framework of MIL-53lp(AI) is depicted in Fig. 2.1, where, for clarity, the hydrogen atoms are not shown; the unit framework consists of six different types of pseudo-atoms: Al, O(1), O(2), C(1), C(2), and C(3). The crystallographic unit cell is obtained through a series of symmetry operations on the unit framework, resulting in a parallelepipedic box with a total number of pseudo-atoms (after eliminating replicas because of the periodic boundary conditions) [34]; the specific volume of the unit cell is $v_c = 1.033$ cm³/g.

In the parameterization of the solid–fluid dispersive interactions using TraPPE-UA, the LJ parameters for the aromatic CH_(aro) and C_(aro) pseudo-atoms [respectively, C(1) and C(2) in Fig. 2.1]

(the latter for the link to the side chains of the aromatic ring) and for the C(sp²) carbon [C(3) in Fig. 2.1], which links the two oxygens and the C_(aro), were taken from the parameter set for linear and branched alkenes and alkylbenzenes [18]; the values for the hydroxyl OH were adopted from the alcohol parameter set [19], and those for the secondary oxygen [O(2) in Fig. 2.1] were taken from the parameterization of ethers [20]. Methane is treated as a LJ pseudo-atom with parameters taken from the parameterization of linear alkanes [17].

These parameters are listed in Table 4.1. It is worth noting that even though the TraPPE-UA force field assigns partial charges to some of the pseudo-atoms of MIL-53(Al), the charge distribution in the solid does not affect the adsorption of methane because the latter is modeled as a LJ pseudo-atom. Since in our modeling work the solid is assumed to have a rigid lattice, its intramolecular interactions contribute with a constant term to the total internal energy of the system and, hence, can be removed from the calculations. In practice, our MIL-53p(Al)/CH₄ system is modeled through dispersive interactions only.

Table 4.1. Lennard-Jones parameters for dispersive interactions in the CH₄/MIL-53p(Al) system.

Label	Site	σ (Å)	ϵ/k_B (K)	Ref.
Al	Al	0.0	0.0	[14]
O(1)	OH	3.02	93.0	[19]
O(2)	O	2.80	55.0	[20]
C(1)	CH(aro)	3.695	50.5	[18]
C(2)	C(aro)	3.88	21.0	[18]
C(3)	C	3.85	20.0	[21]
	CH ₄	3.73	148.0	[17]

A spherical potential truncation for pairs of methane molecules separated by more than $r_{ff} = 14$ Å was employed, to be consistent with the TraPPE-UA force field, but without analytic tail corrections. Some authors advocate the use of a cut-and-shifted LJ potential, since standard analytical tail corrections do not apply in inhomogeneous systems [22]. However, this would imply a reparameterization of the TraPPE-UA force field, as was done, e.g., by Dubbeldam et al. [23] for adsorption of linear and branched alkanes in zeolites. In the present work the influence of the potential truncation was reduced by extending to 16.5 Å the potential cutoff, r_{sf} , for the solid–fluid interactions.

The simulation boxes in our GCMC simulations were built by replicating the unit cell of MIL-53p(Al) along each of the coordinate directions until a box of the desired size was obtained. The simulation box size depended on the loading of methane molecules and was chosen so that the number of sorbate molecules remained fixed at a number that was computationally tractable and at the same time allowed relevant density fluctuations to occur.

Under no circumstances did any of the simulation boxes fail to completely enclose the sphere for the fluid–fluid potential truncation; this was done for consistency with the minimum image

convention. The dimensions of the smallest simulation box that meets this criterium are $(L_x)_{\min} = 5a = 33.192 \text{ \AA}$, $(L_y)_{\min} = 2b = 33.522 \text{ \AA}$, and $(L_z)_{\min} = 3c = 38.517 \text{ \AA}$.

The potential cutoff for solid–fluid interactions, $r_{\text{sf}} = 16.5 \text{ \AA}$, also happens to satisfy $r_{\text{sf}} < \min\{(L_x)_{\min}, (L_y)_{\min}, (L_z)_{\min}\}/2$; this choice, however, was not dictated by the minimum image convention but rather by computational tractability. Since the pseudo-atoms of the MIL-53 framework are fixed in space in an infinite lattice, r_{sf} can assume any value.

At the lowest methane loadings, one to three extra unit cells were added along each of the principal axes in order to increase the size of the simulation box. Each run was equilibrated for at least 5×10^5 Monte Carlo steps followed by at least 10^6 steps for the production period. On average, 80% of the steps were attempts to translate a randomly selected methane molecule; the remaining 20% of the steps were attempts to insert or remove a methane molecule from the simulation box. The maximum displacement for translation was adjusted during the equilibration phase to give a 50% acceptance rate. Finally, standard deviations of the ensemble averages were computed by breaking the production run into five blocks.

In the grand canonical ensemble, the thermodynamic state of the system is defined by $\beta = 1/(k_B T)$ (or temperature T), where k_B is the Boltzmann's constant, and by $\nu = \beta\mu$ (or μ), where μ is the chemical potential; the extensive variable that is fixed is the volume V_{box} of the simulation system. The imposed effective chemical potential, ν , of the coexisting bulk fluid is related to its fugacity, f , by (4.4)

$$\nu = \nu_{ig}^0 + \ln(\beta f) \quad (4.4)$$

where ν_{ig}^0 is the reference effective chemical potential for the ideal gas (noninteracting particles);

For a structureless molecule, like methane,

$$\nu_{ig}^0 = \ln \Lambda^3 \quad (4.5)$$

where Λ is the thermal de Broglie wavelength [24].

For the P – T range considered in this study, the equation of state of bulk methane is well described by the Virial equation of state truncated at the second term [25]:

$$Z = 1 + B(\beta P) \quad (4.6)$$

where P is the pressure, Z is the compressibility factor, and B is the second Virial coefficient. For this equation of state the fugacity can be expressed as [26]

$$f = P_{\text{exp}} (Z - 1) = \frac{\rho_g / \beta}{1 - \rho_g \beta} \exp\left(\frac{\rho_g \beta}{1 - \rho_g \beta}\right) \quad (4.7)$$

where ρ_g is the number density of the gas.

The value of B for each temperature was evaluated by nonlinear least-squares fitting of Eq 4.6 to simulated values of (μ, ρ_g) obtained from a small series of inexpensive GCMC simulations of the bulk fluid.

4.3 RESULTS AND DISCUSSION

4.3.1 Adsorption Equilibrium Measurements

As noted before, in volumetric or gravimetric adsorption equilibrium measurements of microporous solids, the thermodynamic property most readily determinable from *net adsorption*, n_{net} : it is the total amount of gas present in the measuring cell with the adsorbent minus the amount that would be present in the empty cell (without the adsorbent) at the same pressure and temperature.

The advantage of using n_{net} is that simulation results can be converted into net adsorption for comparison with experiment using the volume of the simulation box [27], V_{box} :

$$n_{net} = \frac{1}{m_s} \left(\frac{\langle N \rangle}{N_{Av}} - V_{box} \rho_g \right) \quad (4.8)$$

This is because parameter V_c (the specific volume of the unit cell of MIL-53) is determined by simulation (4.9):

$$V_p + V_s = V_{box}/m_s = V_c \quad (4.9)$$

where V_c holds true regardless of the means by which V_s (or V_p) is determined by simulation.

We estimated the value of V_p by molecular simulation of the capillary condensation of methane in the pore structure of MIL-53lp(Al) at $0.8T_c$ (152.5 K), where T_c is the critical temperature of methane, and chemical potential $\mu/k_B = -1623$ K (~ 1.37 MPa).

Assuming that near the saturation pressure the entire system is filled with liquid adsorbate, then the amount adsorbed under those conditions, $n^\infty = 0.195(4)$ g/g, when expressed as a volume of liquid by use of the normal liquid density ($\rho_l = 0.346(3)$ g/cm³), should provide an estimate of the specific pore volume [28]; the obtained value is V_p , cm³/g (4.10):

$$V_p = n^\infty / \rho_l = 0.56(2) \quad (4.10)$$

The specific skeletal volume (V_s , cm³/g) which is impenetrable to the adsorbate, is obtained by subtracting V_p from the specific volume of the unit cell of MIL-53lp(Al), V_c , determined by crystallography:

$$V_s = V_c - V_p = 0.47(2) \quad (4.11)$$

where V_s is the specific adsorbent volume impenetrable to the adsorbate. In the case of MIL-53, $V_s = 1/\rho_s$ where ρ_s is the skeletal (or structural) density of the adsorbent.

Molecular simulations, on the other hand, provide absolute adsorption, n , which is directly obtained from

$$n = \frac{1}{m_s} \frac{\langle N \rangle}{N_{Av}} \quad (4.12)$$

where $\langle N \rangle$ is the ensemble average number of adsorbate molecules in the simulation box, m_s is the mass of adsorbent in the simulation, and N_{Av} is the Avogadro's number.

The relations between absolute adsorption and the other two adsorption quantities are:

$$n = n_{ex} + V_p \rho_g = n_{net} + (V_p + V_s) \rho_g \quad (4.13)$$

where V_p is the specific pore volume of the adsorbent.

Figure 4.1 shows a front-view snapshot of the simulation box for the conditions of the numerical experiment described above. On average, there are 304 methane molecules in the system, which is nearly equivalent to 10 molecules per unit cell. Even though the channels are all alike, it is convenient to discriminate between even- and odd-index channels because the horizontal ab -plane (or xy -plane) that divides a channel into two halves is not a plane of reflection symmetry but of rotational symmetry with respect to a 180° rotation. The vertical ac -plane (or xz -plane) that halves the channel through the central aluminium atoms, on the other hand, is a true plane of reflection symmetry. The lack of symmetry with respect to reflection around the middle ab -plane of a channel resides on the relative position of the hydroxyl OH groups that bridge the aluminium atoms: in even-index channels the z -coordinate (aligned with the c -axis) of the OH group is below the two bridged aluminium atoms; in odd-index channels the OH group is above. The relative position of the hydroxyl OH groups is best perceived by reference to Fig. 4.2, which is discussed below. Some authors have suggested different approaches based on molecular simulation to define the dividing surface for excess calculations. For example, Talu and Myers [29] suggest using the simulated slopes of the helium isotherm at zero pressure to determine V_p , whereas Do et al. [30] suggest using a zero-potential hypersurface for the adsorbing molecule to define the surface for excess calculations.

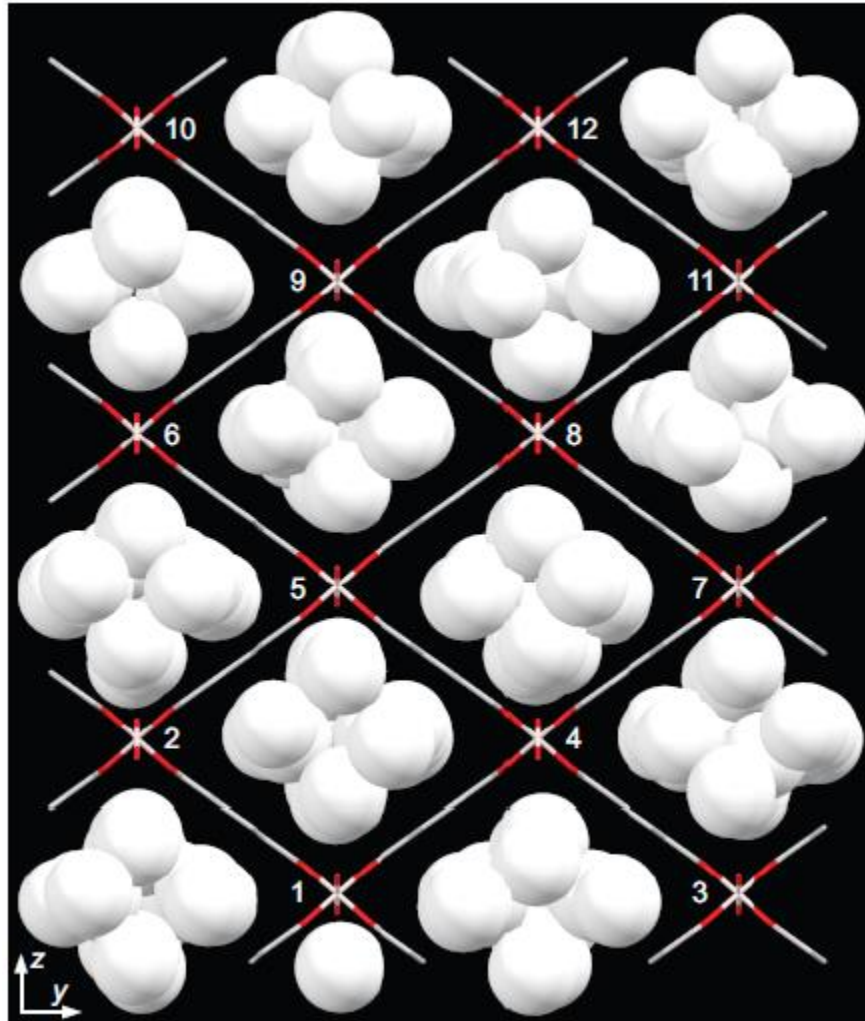


Figure 4.1. Snapshot of the GCMC simulation box with condensed methane molecules inside MIL-53lp(AI) at $T = 152.5$ K and $\mu/k_B = -1623$ K. The atomic structure of odd-index channels is the mirror image, obtained by reflection with respect to the ab plane, of the atomic structure of even-index channels, and vice versa.

We determined by direct Monte Carlo integration the specific volume enclosed by the zero-potential hypersurface:

$$V_{zs} = \frac{V_c}{V_{box}} \int_{V_{box}} [1 - H(V_{sf}(r))] dV, \quad H(x) = \begin{cases} 0, & x < 0 \\ 1, & x \geq 0 \end{cases} \quad (4.14)$$

where $H(x)$ is the Heaviside step function, $u_{sf}(r)$ is the solid–fluid interaction potential for a single molecule, and V_{box} is the volume of the simulation box.

The value of V_{zs} obtained using helium as probe molecule ($\sigma_{ff} = 3.11$ Å, [31]) is $V_{zs}^{He} = 0.2163(5)$ cm³/g; using methane ($\sigma_{ff} = 3.73$ Å), the value reduces to $V_{zs}^{CH_4} = 0.1676(6)$ cm³/g.

Although the adoption of V_{zs} as specific pore volume renders excess adsorption always positive, such approach leads to a pore volume that is considerably smaller than that obtained by simulating the capillary condensation of the same adsorbate probe. However, if v_{zs} is increased by

the volume displaced by a sphere of diameter $\sigma_{ff}/4$ rolling over the outer surface of the zero-potential hypersurface (or a sphere of diameter $\sigma_{ff}/2$ moving its center along the hypersurface), then it approximately matches the value of V_p [32]. We have thus decided to adopt $V_p = 0.56 \text{ cm}^3/\text{g}$ as the best estimate of the specific pore volume of MIL-53lp(Al).

Figure 4.2 shows a 2-D projection of the number density field for condensed methane inside an even-index channel of MIL-53lp(Al); lighter colors represent larger values of the number density. For comparison, we have plotted over the density field the perimeter of the zero-potential hypersurface for different sections of the channel.

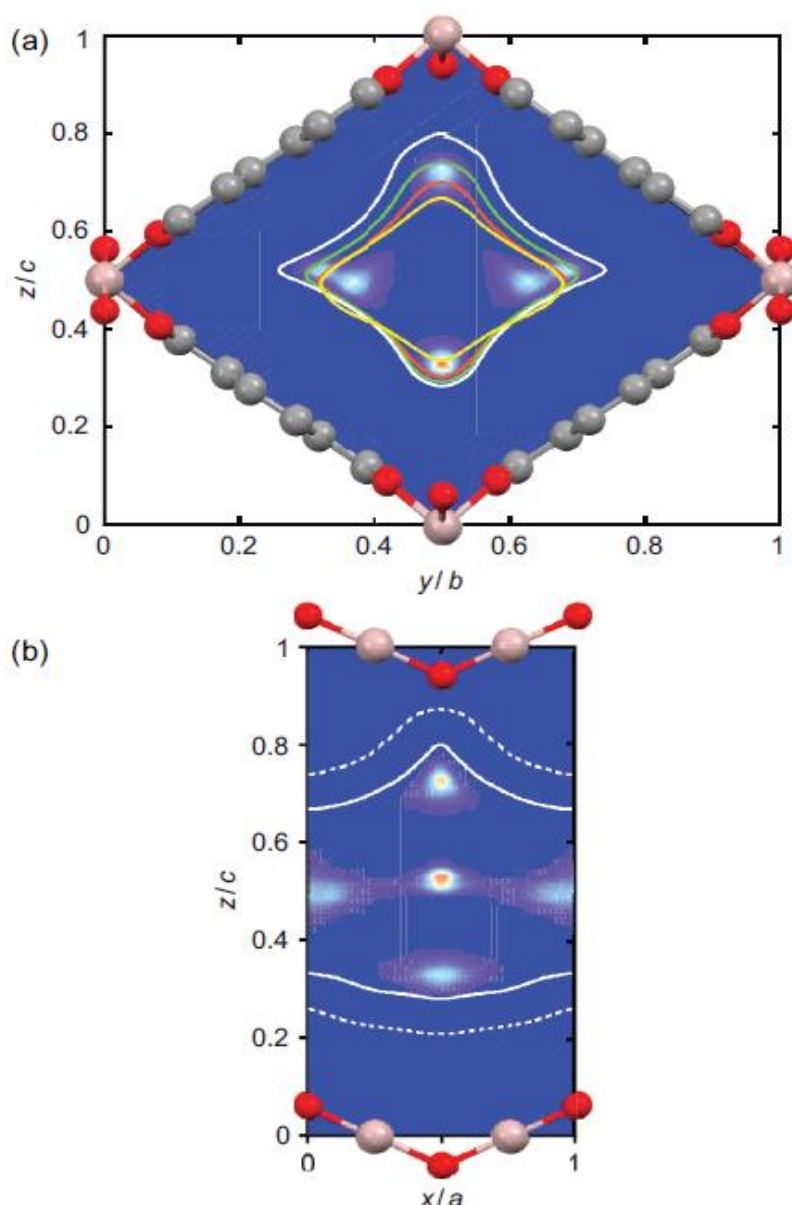


Figure 4.2: Molecular density field (lighter colors represent larger values of ρ) for condensed methane at 152.5 K and $\mu/k_B = -1623$ K inside an even-index, diamond-shaped channel of MIL-53lp(Al) and zero-potential hypersurface (ZPH). (a) Front view of the channel; the colored lines show the perimeter of the ZPH at different axial positions along the channel: $x/a = 0$ (yellow), $x/a = 0.25$ (red), $x/a = 0.375$ (green), and $x/a = 0.5$ (white). (b) Lateral view of the channel; the solid line represents the ZPH for $y/b = 0.5$ and the dashed line shows the hypersurface extended by a sphere of diameter $\sigma_{ff}/4$.

Figure 4.2a shows a cross-sectional view of the diamond-shaped channel. The density field plotted in this figure, $\rho_a(y, z)$, gives the number of methane molecules in a parallelepiped aligned with the x -coordinate, with length a and cross section $dy dz$ centered at (y, z) ; $\rho_a(y, z)$ is related to the true number density, $\rho(\mathbf{r})$, by (4.14):

$$\rho_a(y, z) = \int_0^a \rho(x, y, z) dx \quad (4.15)$$

The colored lines superposed over the density plot show the perimeter of the zero-potential hypersurface on the yz -plane at the following axial positions along the channel: $x/a = 0$ (yellow), $x/a = 0.25$ (red), $x/a = 0.375$ (green), and $x/a = 0.5$ (white).

Figure 4.2b shows a lateral view of the channel extending over the length a of the unit cell. In this case, the contour plot represents a density distribution, $\rho_b(x, z)$, which gives the number of methane molecules in a parallelepiped aligned with the y -coordinate and cross section $dx dz$ centered at (x, z) ; $\rho_b(x, z)$ is defined as:

$$\rho_b(x, z) = \int_0^b \rho(x, y, z) \Theta(y, z) dy \quad (4.16)$$

where $\Theta(y, z) = 1$ if (y, z) is inside the channel and $\Theta(y, z) = 0$ if (y, z) is outside the channel.

The white, solid line plotted over the density field is the perimeter of the zero-potential hypersurface on the xz -plane at $y/b = 0.5$; the dashed line represents the zero-potential hypersurface extended by a sphere of diameter $\sigma_{ff}/4$.

If $\rho_a(y, z)$ and $\rho_b(x, z)$ are integrated over corresponding perpendicular coordinate along the channel, they both give average number of adsorbate molecules $\langle N_{uc} \rangle$, in the unit cell of MIL-53:

$$\langle N_{uc} \rangle = \int_0^b \int_0^c \rho_a(y, z) \Theta(y, z) dy dz = \int_0^a \int_0^c \rho_b(x, z) dx dz \quad (4.17)$$

As discussed above, the solid–fluid interaction potential U_{sf} is symmetric with respect to the vertical ac -plane (or xz -plane) that cuts the cross section of the channel into two halves; because of the position of the bridging OH groups, the symmetry with respect to reflection around the central ab -plane (or xy -plane) that halves the cross section of the channel is broken. This feature propagates to all quantities that depend on the local interaction potential, such as the number density field and the zero-potential hypersurface. In addition, the vertical bc -plane (or yz -plane) located at $x = a/2$ is also a symmetry plane with respect to horizontal reflection (Fig. 4.2b).

Figure 4.3 compares the absolute, excess, and net adsorption isotherms for methane at 303.15 K determined by GCMC simulation up to ~ 7 MPa. Whereas absolute adsorption is a monotonically increasing function of pressure (type I isotherm), the other two functions are concave with respect

to the pressure axis and their maximum value occurs at a pressure that increases with temperature. At pressures below ~ 0.2 MPa, the pore density is much higher than the bulk density of methane and thus the differences between n , n_{ex} , and n_{net} are negligible. At higher pressures, the bulk density increases more rapidly than the pore density and the three measures of adsorption start to deviate from each other. At ~ 7 MPa, the absolute adsorption continues to increase with pressure while the excess adsorption is close to its maximum value and the slope of net adsorption is already negative; the maximum value of n_{net} at 303.15 K occurs at ~ 4 MPa. The thermodynamics of high-pressure, supercritical adsorption is well explained by Myers and Monson [33]. The experimental and simulation equilibrium data of methane adsorption are listed in Tables A1–4 of Annex A

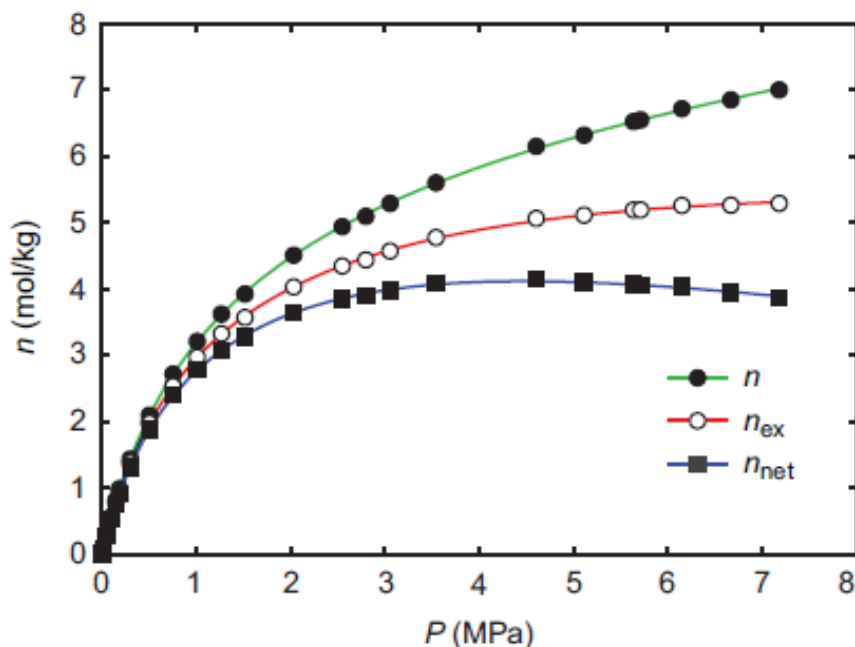


Figure 4.3: Absolute (\bullet), excess (\circ), and net adsorption (\blacksquare) isotherms of methane in MIL-53lp(Al) at 303.15 K determined from GCMC simulations; lines are drawn as a guide to the eye. The reference state corrections used are $V_p = 0.56 \text{ cm}^3/\text{g}$ and $V_s = 0.47 \text{ cm}^3/\text{g}$.

Figure 4.4 compares the three experimental adsorption isotherms with the predictions of our molecular model. The adsorption data are reported in terms of excess isotherms using the reference value of $0.47 \text{ cm}^3/\text{g}$ for the specific skeletal volume (V_s) of MIL-53lp(Al); the reference state for the GCMC excess isotherms is $V_p = 0.56 \text{ cm}^3/\text{g}$. For reference, Figure 4.4 also includes the experimental adsorption data obtained by Bourrelly et al. [34] in a volumetric apparatus at 304 K; these values are expressed in terms of n_{ex} by subtracting $V_p \rho_g$ from the original, absolute values. The quantitative agreement shown in Fig. 4.4 between our adsorption measurements and GCMC simulations confirms previous observations [35] that for methane adsorption at or above ambient temperature the large-pore structure of MIL-53(Al) is thermodynamically favored over the whole pressure range.

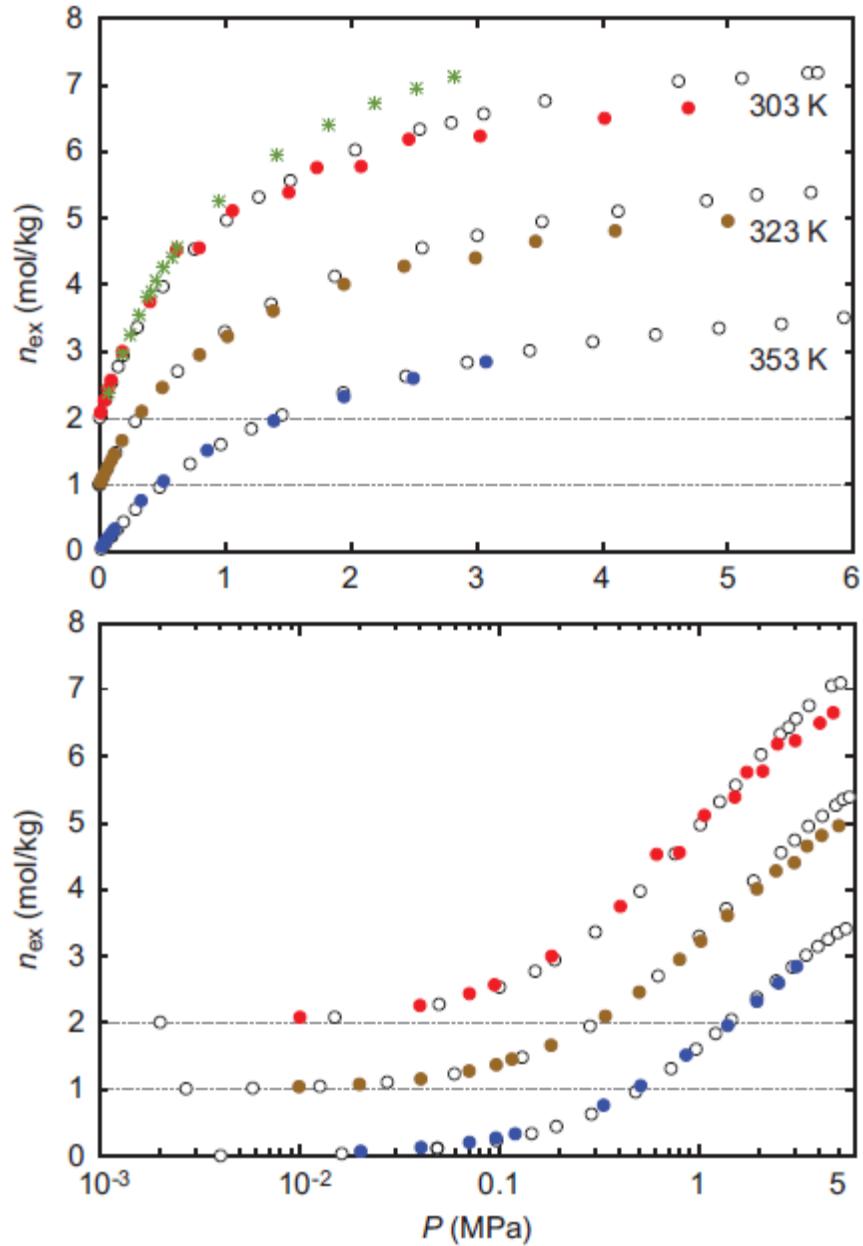


Figure 4.4: Comparison of experimental (filled circles) and simulated (open circles) excess adsorption isotherms of methane in MIL-53p(Al). The reference state corrections used are $V_p = 0.56 \text{ cm}^3/\text{g}$ and $V_s = 0.47 \text{ cm}^3/\text{g}$. The asterisks (*) represent the experimental data obtained by Bourrely et al. [36] in a volumetric apparatus at 304 K, expressed here in terms of n_{ex} by subtracting $v_p \rho_g$ from the original, absolute values. For clarity, the adsorption data at 323 K and 303 K are displaced by 1 mol/kg and 2 mol/kg, respectively.

The second observation regarding Fig. 4.4 is the good agreement between our GCMC predictions and the experimental adsorption data; the agreement is good enough to obviate the need for re-parameterization of the cross-terms of the LJ solid–fluid interaction potential. At pressures below ~ 2 MPa, the GCMC model predicts the experimental loadings with high accuracy at the three different temperatures. At pressures above 2 MPa, the GCMC simulations slightly overpredict the experimental loadings at the two lowest temperatures, but fall on top of the

experimental data obtained at the highest temperature (353.15 K). This suggests that the LJ parameters of the TraPPE-UA force field are indeed transferable to the organic ligand of MIL-53 and possibly to those of other metal-organic frameworks. This corroborates previous claims [37,38] that the good balance between enthalpic and entropic contributions to the free energy in the TraPPE-UA force field makes it transferable to different physical conditions, including those where the “solvent” is a rigid lattice dominated by an organic ligand in which the metal atoms are shielded from the influence of the adsorbate molecules by organic or inorganic groups (in this case the oxygens and hydroxyl groups of the inorganic octahedra). This is a very encouraging result in view of our pursuing work on the adsorption of larger alkanes and alkenes in MIL-53(AI).

The equilibrium data reported by Bourrely et al. [34] are in agreement with our measurements and GCMC results for pressures below ~0.6 MPa. At higher pressures the experimental values reported by these authors are consistently above our measurements; at 3.0 MPa the deviation between the experimental values is ~0.6 mol/kg. We do not have a clear explanation for this discrepancy.

It is worth noting that although the adsorption equilibrium data shown in the comparison plot of Fig. 4.4 are expressed as excess values, the experimental and simulated isotherms could also be compared in terms of absolute or net values. More importantly, however, is that the comparison would be quantitatively the same even though the isotherms would be different.

To see why this would be so, let us compute the error between an experimental excess data point, $(n_{ex})_{exp}$, of Fig. 4.4 and the corresponding simulated value, $(n_{ex})_{sim}$, from Eq 4.13,

$$e_{ex} = (n_{ex})_{exp} - (n_{ex})_{sim} = [(n_{net})_{exp} + v_s \rho_g] - [n_{sim} - v_p \rho_g] = (n_{net})_{exp} - n_{sim} + v_c \rho_g \quad (4.18)$$

where, as stated above, $V_c = V_p + V_s$ is the specific volume of MIL-53's unit cell. If the comparison is made in terms of net values, the result is

$$e_{net} = (n_{net})_{exp} - (n_{net})_{sim} = (n_{net})_{exp} - [n_{sim} - v_c \rho_g] = (n_{net})_{exp} - n_{sim} + v_c \rho_g \quad (4.19)$$

Finally, if the comparison is made in terms of absolute values, the error is

$$e_{ex} = n_{exp} - n_{sim} = [(n_{net})_{exp} + v_c \rho_g] - n_{sim} = (n_{net})_{exp} - n_{sim} + v_c \rho_g \quad (4.20)$$

Thus, the difference between an experimental isotherm data point and its simulated value is the same whether the isotherm is expressed in terms of absolute, excess, or net adsorption.

4.3.2. Data Fitting

The experimental adsorption data were fitted with two commonly employed semi-empirical isotherm models: the Sips and Toth models [50]. The Sips isotherm can be written as

$$n = \frac{n_s (bP)^{1/\eta}}{1 + (bP)^{1/\eta}} \quad (4.21)$$

with

$$b = b_0 \exp\left[\frac{Q}{RT_0} \left(\frac{T_0}{T} - 1\right)\right], \quad \frac{1}{\eta} = \frac{1}{\eta_0} + \alpha \left(1 - \frac{T_0}{T}\right) \quad (4.22)$$

where, n is the adsorbed phase concentration, n_s is the saturation capacity at temperature T , η_0 and η are parameters, b_0 is the adsorption affinity at the reference temperature T_0 , and Q is the isosteric heat of adsorption at half loading; η characterizes the adsorbate–adsorbent interaction, and its magnitude increases with the heterogeneity of the system. Note that if $\eta = 1$ then the Langmuir isotherm model is recovered.

The isosteric heat of adsorption, Q_{st} , obtained by applying the Clapeyron equation to the Sips isotherm model, is

$$Q_{st} = Q - \alpha \eta^2 RT_0 \ln\left(\frac{\theta}{1-\theta}\right) \quad (4.23)$$

where $\theta = n/n_s$ is the fractional loading; Q equals Q_{st} when $\theta = 1/2$.

The Toth isotherm model can be written as

$$n = \frac{n_s bP}{[1 + (bP)^t]^{1/t}}, \quad t = t_0 + \alpha \left(1 - \frac{T_0}{T}\right) \quad (4.24)$$

where parameter b is defined in the same way as for the Sips model; $1/t$ plays a role similar to parameter η of the Sips model.

The isosteric heat of adsorption derived from the Toth isotherm model is given by

$$Q_{st} = Q - \frac{\alpha RT_0}{t} \left[\ln \frac{\theta}{(1-\theta)^{1/t}} - \frac{\ln \theta}{1-\theta^t} \right] \quad (4.25)$$

where the parameter Q equals Q_{st} when the fractional loading is zero.

The fitted parameters of the Sips and Toth isotherm models are listed in Table 4.2. The goodness of the fittings was assessed using standard fitting statistics: standard deviation of measurements, determination coefficient (r^2), regression sum of squares (RSS), fit standard error (FSE), and average relative error (ARE). As the fitting improves, the r^2 values approach unity and the FSE decreases towards zero. The average relative error (ARE), expressed as a percentage, is defined as

$$ARE = \frac{100}{n_p} \sum \frac{|n_{exp} - n_{sim}|}{n_{exp}} \quad (4.26)$$

where n_p is the number of data points, n_{exp} is the set of experimental values, and n_{sim} is the set of values predicted by the isotherm model.

Table 4.2. Parameters obtained from the data fitting with the Sips and Toth models. The parameters listed in the last two columns are the result of fitting the models with $\alpha = 0$, which make parameters η and t temperature independent. In every case $r^2 > 0.998$; FSE is the standard error of the fitting and ARE is the average relative error.

Parameter	Sips	Toth	Sips	Toth
n_s (mol/kg)	8.38	10.15	8.31	9.96
b_0 (bar ⁻¹)	0.054	0.098	0.056	0.097
α	0.096	0.113	0.0	0.0
η_0 or t_0	1.21	0.60	1.2	0.61
Q (kJ/mol)	19.7	20.9	19.9	19.9
T_0 (K)	303.2	303.2	303.2	303.2
FSE	0.086	0.084	0.085	0.083
ARE (%)	8.6	8.7	6.7	6.6

Figure 4.5 compares the global fitting of the Sips isotherm model and the methane adsorption equilibrium data measured at the three temperatures. In the left plot the experimental data are compared to the global fitting of the Sips model in which parameter η is allowed to vary with temperature according to Eq. (4.21); in the right plot, the comparison is made against the global fitting obtained with a constant value of η . Similar plots were obtained for the Toth isotherm model and are not reproduced here.

As observed in Fig. 4.5, the 3D-surfaces derived from the two global fittings of the Sips models are in very good agreement with the experimental data; the determination coefficient r^2 is higher than 0.998 in both cases. Letting the parameter η change with temperature improves only slightly the quality of the fitting; parameter t of the Toth isotherm model follows a similar trend. The discrepancy in the estimated values of n_s by the two isotherm models (Table 4.2) is probably due to the fact that the experimental adsorption data only spanned fractional loadings up of 0.6.

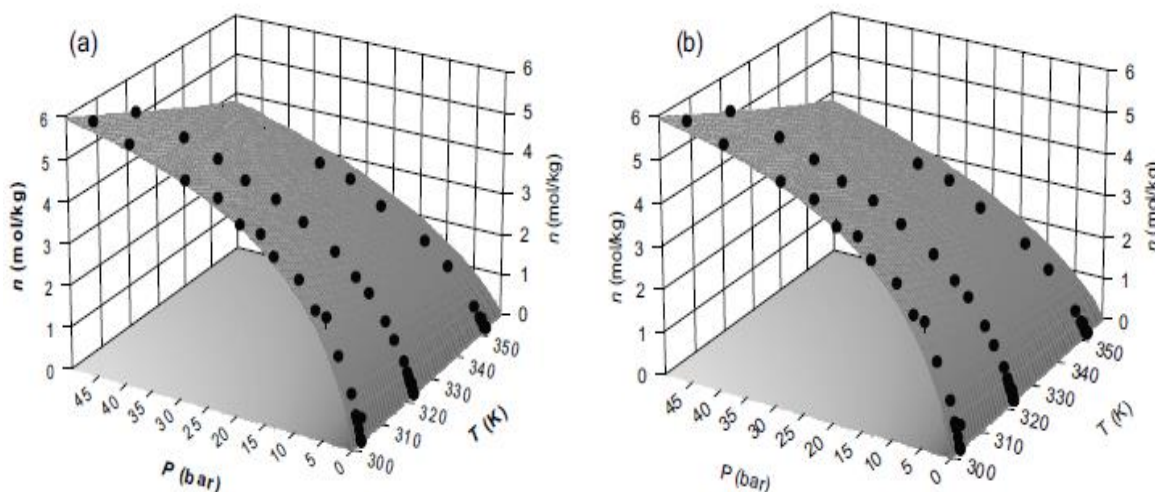


Figure 4.5. Global fitting of the experimental methane adsorption data by the Sips and Toth isotherm models. The fitted parameters are listed in Table 4.2. In the left plot, η is allowed to vary with temperature according to Eq. (4.22); in the right plot, η is a constant ($\alpha = 0$). Symbols represent experimental data and the surface is the isotherm model. The global average relative error (ARE) is 8.6% for 52 experimental data points.

4.3.3. Isosteric Heat of the adsorption

The isosteric heat (or differential enthalpy) of adsorption, Q_{st} , is the amount of heat released when an infinitesimal number of molecules is transferred at constant pressure from the bulk gas phase to the adsorbed phase. This quantity can be calculated from statistical mechanical considerations [31] as

$$Q_{st} = \beta^{-1} - \frac{\varphi(U, N)}{\varphi(N, N)} \quad (4.27)$$

where $\varphi(u, v) = \langle uv \rangle - \langle u \rangle \langle v \rangle$ is the covariance between two properties u and v , $\langle \rangle$ denotes the ensemble average, N is the number of adsorbate molecules in the simulation box, U is the configurational energy of the system, and $\beta = 1/(k_B T)$.

Figure 4.6a shows a plot of the isosteric heat of adsorption as a function of the amount adsorbed. The values of Q_{st} calculated using eq 4.27, which are depicted as open symbols in Fig. 4.6a, show a linear dependence of Q_{st} on the amount adsorbed, but with a mild slope. The isosteric heat at zero loading is ~ 15 kJ/mol; at a loading of 6 mol/kg, $Q_{st} \sim 18$ kJ/mol. The gentle increase of Q_{st} with loading can be explained in terms of the lateral interaction of the adsorbed methane molecules as they become more tightly packed in the pore channels of MIL-53p(AI).

The GCMC results also show that the temperature range of 303–353 K is small enough to justify the assumption that Q_{st} is independent of temperature. In this case it is possible to calculate Q_{st} from the adsorption isotherms obtained experimentally at the three temperatures using the integrated form of the Clapeyron equation (4.28):

$$\ln(p)_n = \text{constant} - \frac{Q_{st}}{RT} \quad (4.28)$$

A plot of $\ln(p)$ versus $1/T$ should yield a linear isostere of slope $-Q_{st}/R$.

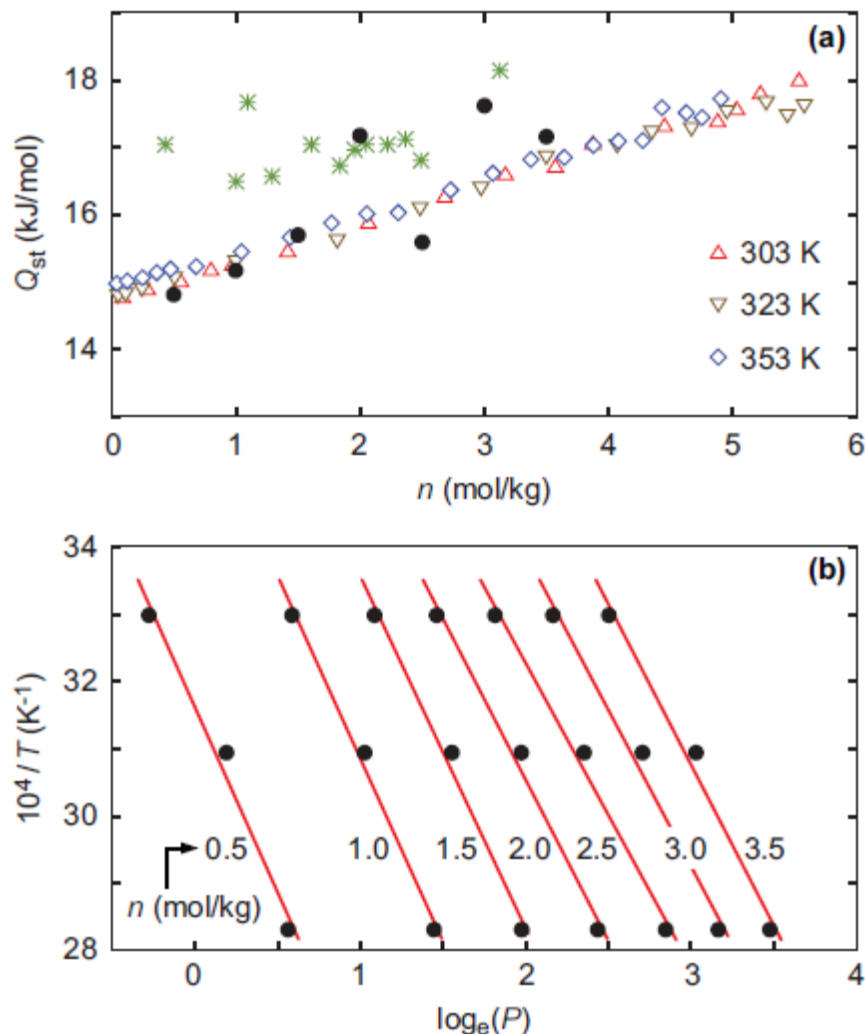


Figure 4.6. (a) Isosteric heat as a function of loading and (b) adsorption isosteres for the $\text{CH}_4/\text{MIL-53p(AI)}$ system at 303–353 K. The open symbols in the top plot are values of Q_{st} obtained from the GCMC simulations by use of the standard fluctuation formula (Eq 4.27), whereas the Q_{st} values represented by the closed circles were calculated from the slope of the linear fitting (lines in bottom graphic) of the isosteric data (closed circles in bottom graphic) derived from the experimental adsorption isotherms; asterisks (*) denote experimental values of Q_{st} collected by microcalorimetry by Bourrely et al. [34] at 304 K.

The experimental isotherms were fitted to third-order polynomials of the form $\ln p = \sum_k n^k$ and then transformed into linear isosteric plots of $\ln p$ against $1/T$ at different loadings and Q_{st} determined from these using Eq (4.28). The isosteres are depicted in Fig. 4.6b; the degree of uncertainty in the Q_{st} values calculated by this method is at least (± 10) per cent. The values of Q_{st} calculated from the isosteric plots are in fairly good agreement with the GCMC results. For the purposes of comparison with our data, we also plot in Fig. 4.6a the experimental values of Q_{st} collected by microcalorimetry by Bourrely et al. [46] at 304 K. The Q_{st} values reported by these authors are independent of loading and their average, ~ 17 kJ/mol, falls on the midrange of our results. The Q_{st} values plotted in Fig. 4.6a are also within the range of isosteric heats reported [40] for methane adsorption on activated carbon at the same temperatures of our study and for

intratubular adsorption of the same adsorbate at room temperature on bundles of single-walled carbon nanotubes with tube diameter of $\sim 15 \text{ \AA}$ [41].

We have also successfully fitted two commonly employed semi-empirical isotherm models the Sips and Toth isotherms models to the experimental methane adsorption data (Table 4.2 and Fig. 4.5.). The isosteric heat of adsorption derived from the two isotherm models is $\sim 20 \text{ kJ/mol}$ (Fig. 4.7 and Table 4.2.), which is roughly 2 kJ/mol higher than the values plotted in Fig. 4.6a. Overall, the Q_{st} trends shown in Fig. 4.6a are consistent with a view that supercritical methane fills the pore channels of MIL-53lp(AI) through a mechanism in which surface heterogeneity plays only a minor role.

Figure 4.7. shows the isosteric heats of adsorption determined from both isotherm models plotted against fractional loading.

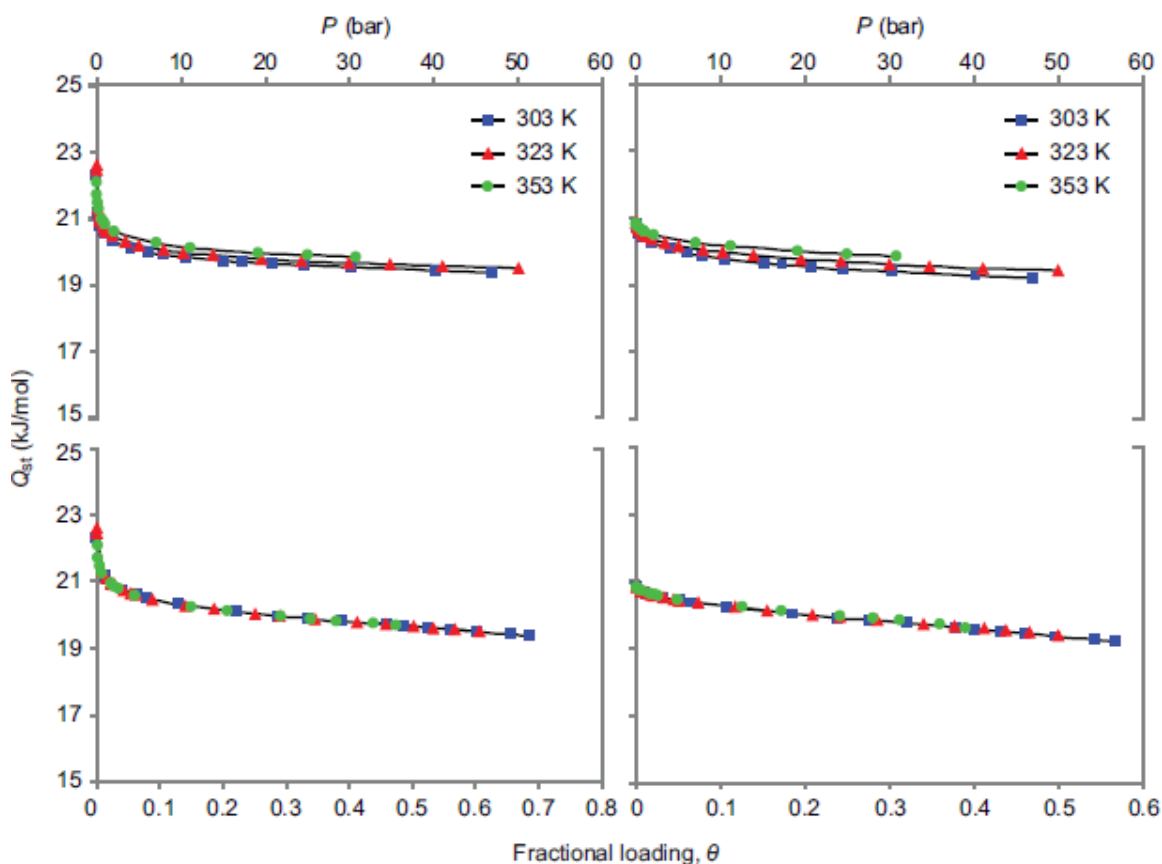


Figure 4.7. Isosteric heats of adsorption derived from the Sips and Toth isotherm models plotted against fractional loading, θ (or pressure, P). Each symbol corresponds to the value of Q_{st} calculated for the pressure and temperature of a point on the experimental adsorption isotherms. The left-hand plots are derived from the Sips isotherm model; the right-hand plots are derived from the Toth isotherm model. In the top plots, η and t are temperature dependent; in the bottom plots, η and t are constants.

The values derived from the two adsorption isotherm models are in close agreement, but the trend with loading goes against the trends of our molecular simulation data and of the values of Q_{st} derived from the slope of the linear fitting of the experimental isosteres. At the higher loadings, the values of Q_{st} derived from the Sips and Toth isotherm models are $\sim 2 \text{ kJ/mol}$ higher than the values plotted in Fig. 4.6.

4.3.4. DOE Target Calculations

It is tempting to compare the methane adsorptive storage capacity of MIL-53(Al) with those of highly porous activated carbons. The comparison is best done on a volumetric basis, because for lightweight vehicles the limiting storage factor is the volume of the tank rather than its weight; for heavyweight vehicles, such as trucks, the limiting storage factor is less clear-cut.

Assuming that MIL-53(Al) is compacted as a monolith or as a close-packed bed inside the storage tank, the isothermal methane storage density (i.e., the loading capacity per storage volume under isothermal conditions) can be expressed as

$$n_v(P, T) = \frac{1-\epsilon}{V_c} n(P, T) + \epsilon \rho_g(P, T) \quad (4.29)$$

where ϵ is the inter-crystal void fraction, P and T are the charge pressure and system temperature, and ρ_g is the molar density of bulk methane at charge conditions.

Usually, the methane storage density is expressed as volumes of stored gas, measured at standard conditions (1 atm and 298.15 K), per storage volume (v/v); the v/v performance indicator and n_v are related by

$$v/v = 23.64 \times 10^{-3} n_v \quad (4.30)$$

where n_v is assumed to be expressed in mol/m^3 .

GCMC calculations carried out by us for $T = 298.15$ K predict that the amount of methane adsorbed in the porous framework of MIL-53lp(Al) at 298.15 K and 3.5 MPa is 5.79(6) mol/kg, which gives a performance indicator of 132.6 v/v for a monolithic block ($\epsilon = 0$) and 107.2 v/v for the theoretical limit ($\epsilon = 0.26$) of a close-packing of uniform spherical particles.

A more realistic performance indicator is the net storage capacity, $(v/v)_{\text{net}}$, which measures the volumes of methane delivered at standard conditions per storage volume; $(v/v)_{\text{net}}$ is more useful in engineering calculations since it measures the actual delivered gas under isothermal operation rather than the stored amount [42]. This performance indicator is given by (4.31):

$$(v/v)_{\text{net}} = 23.64 \times 10^{-3} [n_v(P_H) - n_v(P_L)] \quad (4.31)$$

where P_H and P_L are the charge and exhaustion pressures, respectively; commonly accepted values for the operating pressure range are $P_H = 3.5$ MPa and $P_L = 0.136$ MPa [3,54].

Since our Monte Carlo simulations predict that $n_v(P_L) = 0.811(6)$ mol/kg at 298.15 K, the theoretical net storage capacity provided by MIL-53lp(Al) would be 114.0 $(v/v)_{\text{net}}$ for a monolith and 93.1 $(v/v)_{\text{net}}$ for a close-packed bed.

The theoretical maximum storage capacity for activated carbon predicted by Monte Carlo simulation [43] is 209 v/v for a monolith and 146 v/v for pelletized particles; the corresponding net storage values are 195 (v/v)_{net} and 137 (v/v)_{net}, respectively. Thus, the theoretical methane storage capacities obtained for activated carbon are considerably better than those for MIL-53(Al). The estimations for activated carbon, however, use a highly idealized model in which methane is intercalated between parallel planes of graphite at a slit width of 11.4 Å, optimized for ANG storage. It is highly questionable that a carbon with this particular pore structure can be manufactured. Experimentally, the highest volumetric methane uptakes obtained to date with activated carbons are around 166 v/v and 145 (v/v)_{net} [44]. Based on either the Langmuir or Unilan isotherm models, Bhatia and Myers [45] have shown that the optimum Langmuirian equilibrium constant, K , for maximum isothermal delivery between P_L and P_H at a given temperature T is given by (4.32):

$$K_{opt} = (P_L P_H)^{-1/2} \quad (4.32)$$

Further, $K = \exp(\Delta S^\circ / R) \exp(\bar{Q}_{st} / RT) / P_o$, where ΔS° is the entropy change on adsorption relative to the standard pressure P_o (1 bar), and \bar{Q}_{st} is the average heat of adsorption between P_L and P_H ; for methane, $\Delta S^\circ \approx -9.5R$ for a variety of adsorbents [45]. It then follows that the optimum value of \bar{Q}_{st} for maximum isothermal delivery between P_L and P_H at a given temperature T is given by (4.33):

$$-(\bar{Q}_{st})_{opt} = T\Delta S^\circ + \frac{RT}{2} \ln \left(\frac{P_L P_H}{P_o^2} \right) \quad (4.33)$$

For a delivery cycle at 298 K, insertion of $P_L = 0.136$ MPa and $P_H = 3.5$ MPa into eq 4.30 yields $(\bar{Q}_{st})_{opt} = 18.8$ kJ/mol, which happens to be in good agreement with the values shown in Fig. 4.6b for the highest loadings. Thus, the low net capacity for methane storage exhibited by MIL-53(Al) at ambient temperature cannot be attributed to an inappropriate value of the equilibrium constant, which is related to the heat of adsorption, but rather to a low adsorption capacity at the charge pressure. This is corroborated by further GCMC simulations performed by us for higher pressures at $T = 298$ K, which indicate that the charge pressure must be increased to $P_H \sim 10.9$ MPa for MIL-53(Al) to achieve the DOE target of 150 (v/v)_{net}.

On the other hand, our simulated experiment of methane condensation in MIL-53(Al) at 152.5 K gives a storage capacity of 279 v/v for a monolithic block and 213 v/v for a close packed bed. These values are well above the DOE target of 150 (v/v)_{net}, which suggests that MIL-53(Al) may be an acceptable methane adsorptive storage medium if the system is operated at a suitably low temperature. In view of this, it is of practical interest to determine how low the operating temperature should be; we calculate this temperature by an extrapolation of the available adsorption data.

The partial derivatives of an average quantity $\langle X \rangle$ with respect to the intensive variables that define the ensemble are related to fluctuation formulas that can be conveniently expressed in terms of the covariance φ between X and the intensive variables. For the grand canonical ensemble [46] we have (4.34):

$$\frac{\partial \langle X \rangle}{\partial \nu} = \varphi(X, N), \quad \frac{\partial \langle X \rangle}{\partial \beta} = -\varphi(X, U) \quad (4.34)$$

which allows the differential of $\langle N \rangle$ to be expressed as (4.35):

$$\partial \langle N \rangle = \frac{\partial \langle N \rangle}{\partial \nu} d\nu + \frac{\partial \langle N \rangle}{\partial \beta} d\beta = \varphi(N, N) d\nu - \varphi(N, U) d\beta \quad (4.35)$$

The Gibbs–Duhem equation for a single-component system at constant pressure, applied to the bulk adsorptive, gives (4.36):

$$h_g d\beta = d\nu(\text{const}P) \rightarrow \left(\frac{\partial \nu}{\partial \beta} \right)_P = h_g \quad (4.36)$$

where $h_g = (5/2)\beta^{-1} + h_g^{\text{ex}}$ is the molecular enthalpy of the bulk adsorptive. For the truncated Virial equation of state, eq 4.5, the excess molecular enthalpy is given by $h_g^{\text{ex}} = P[B + \beta(dB/d\beta)]$ [26].

From Eqs 4.35 and 4.36 it is possible to determine the slope of an adsorption isobar from the fluctuation formulas and the value of h_g :

$$\left(\frac{\partial \langle N \rangle}{\partial \beta} \right)_P = h_g \varphi(N, N) - \varphi(N, U) \quad (4.37)$$

Using this formula it is possible to interpolate the GCMC adsorption isotherms at a constant pressure value using cubic Hermite interpolation, which matches both $\langle N \rangle$ and $(\partial \langle N \rangle / \partial \beta)_P$ rather than by simple polynomial interpolation that matches just $\langle N \rangle$ the resulting polynomial provides the adsorption isobar at the selected pressure. Using this procedure it is possible to extrapolate more reliably the adsorption isobar to a temperature outside the range of temperatures of the isotherms that were interpolated to build the isobar.

We have determined the isobars at $P_L = 0.136$ MPa and $P_H = 3.5$ MPa from the GCMC data at 298.15 K, 303.15 K, 323.15 K, and 353.15 K, and extrapolated the isobars to get the temperature at which the net storage capacity of a monolithic block of MIL-53(AI) meets the DOE target of 150 $(\nu/\nu)_{\text{net}}$ (see Fig. 4.8); the predicted temperature is ~253 K. This temperature happens to be a few degrees above the lowest temperature [47] at which there is no occurrence of structural breathing in MIL-53(AI) upon methane adsorption and the open-pore form remains the stable structure over the whole pressure range. The equilibrium loadings at $P_L = 0.136$ MPa and $P_H = 3.5$ MPa calculated by GCMC simulation for $T = 253$ K are 2.03(2) mol/kg and 8.44(7) mol/kg, respectively,

which give a net deliverable capacity of $147 (v/v)_{\text{net}}$. This value is only 2% less than the DOE target of $150 (v/v)_{\text{net}}$, which demonstrates the reliability of our extrapolation procedure.

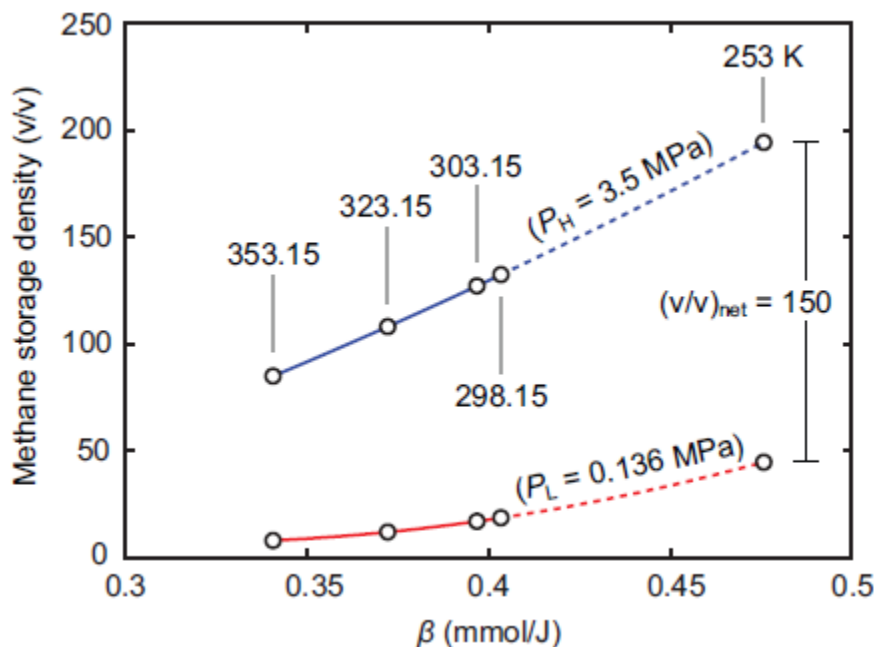


Figure 4.8. Cubic Hermite interpolation (solid lines) of the GCMC adsorption isotherms (open circles) at $P_L = 0.136$ MPa and $P_H = 3.5$ MPa and extrapolation (dashed lines) of the two isobars to the temperature at which $(v/v)_{\text{net}} = 150$.

4.4. CONCLUSIONS

We have reported a combined experimental and theoretical study of the adsorption equilibrium properties of supercritical methane in the large-pore form of MIL-53(AI) over pressures in the range ~ 0.01 –7 MPa and temperatures in the 303–353 K regions. We demonstrated that the use of the TraPPE-UA force-field for modeling the solid–fluid interaction potential of the MIL-53(AI)/CH₄ system provides a good description of the experimental adsorption isotherms and isosteric heats of adsorption. Furthermore, a previously unobserved anisotropic distribution of the confined fluid molecules was interpreted in terms of symmetry annihilation in the pseudo one-dimensional nanopores; this fact arises from anti-parallel alignments of the OH groups in the inorganic octahedra.

Finally, we examined the potential use of MIL-53(AI) as a methane adsorptive storage medium, and compared its performance with those of activated carbons. Our simulations show that a MIL-53(AI) monolith must operate with a charge pressure slightly above 10 MPa to deliver the DOE target of 150 volumes of methane per storage volume in an isothermal cycle operating at 298.15 K and depletion pressure of 0.136 MPa. To achieve the same net storage capacity for the DOE's reference charge pressure of 3.5 MPa, the MIL-53(AI) monolith must operate isothermally at ~ 253 K.

4.5. REFERENCES

- [1] Dell, R. M.; Rand, D. A. J. *Clean Energy*; The Royal Society of Chemistry: Cambridge, U.K., 2004.
- [2] Rappe, A. K.; Casewit, C. J.; Colwell, K. S.; Goddard III, W. A.; Skiff, W. M. *J. Am. Chem. Soc.* **1992**, *114*, 10024–10039.
- [3] Mayo, S. L.; Olafson, B. D.; Goddard III, W. A. *J. Phys. Chem.* **1990**, *94*, 8897–8909.
- [4] Vishnyakov, A.; Ravikovitch, P. I.; Neimark, A. V.; Bullow, M.; Wang, Q. M. *Nano lett.* **2003**, *3*, 713–718.
- [5] Yang, Q.; Zhong, C. *ChemPhysChem* **2006**, *7*, 1417–1421.
- [6] Yang, Q.; Xue, C.; Zhong, C.; Chen, J.-F. *AIChE J.* **2007**, *53*, 2832–2840.
- [7] García-Pérez, E.; Gascón, J.; Morales-Florez, V.; Castillo, J. M.; Kapteijn, F.; Calero, S. *Langmuir* **2009**, *25*, 1725–1731.
- [8] Martín-Calvo, A.; García-Pérez, E.; Castillo, J. M.; Calero, S. *Phys. Chem. Chem. Phys.* **2008**, *10*, 7085–7091.
- [9] Liu, Y.; Her, J.-H.; Dailly, A.; Ramirez-Cuesta, A. J.; Neumann, D. A.; Brown, C. M. *J. Am. Chem. Soc.* **2008**, *130*, 11813–11818.
- [10] Liu, B.; Smit, B. *Langmuir* **2009**, *25*, 5918–5926.
- [11] Rosenbach, N.; Jobic, H.; Ghoufi, A.; Salles, F.; Maurin, G.; Bourrelly, S.; Llewellyn, P. L.; Devic, T.; Serre, C.; Férey, G. *Angew. Chem., Int. Ed.* **2008**, *47*, 6611–6615.
- [12] Yang, Q.; Zhong, C. *J. Phys. Chem. B* **2006**, *110*, 17776–17783.
- [13] Wang, S.; Yang, Q.; Zhong, C. *Sep. Purif. Technol.* **2008**, *60*, 30–35.
- [14] Ramsahye, N. A.; Maurin, G.; Bourrelly, S.; Llewellyn, P. L.; Loiseau, T.; Serre, C.; Férey, G. *Chem. Commun.* **2007**, *43*, 3261–3263.
- [15] Shen, J.-W.; Domański, K. B.; Kitao, O.; Nakanishi, K. *Fluid Phase Equilib.* **1995**, *104*, 375–390.
- [16] Maurin, G.; Llewellyn, P. L.; Bell, R. G. *J. Phys. Chem. B* **2005**, *109*, 16084–16091.
- [17] Martin, M. G.; Siepmann, J. I. *J. Phys. Chem. B* **1998**, *102*, 2569–2577.
- [18] Wick, C. D.; Martin, M. G.; J. I. Siepmann, J. I. *J. Phys. Chem. B* **2000**, *104*, 8008–8016.
- [19] Chen, B.; Potoff, J. J.; Siepmann, J. I. *J. Phys. Chem. B* **2001**, *105*, 3093–3104.
- [20] Stubbs, J. M.; Potoff, J. J.; Siepmann, J. I. *J. Phys. Chem. B* **2004**, *108*, 17596–17605.
- [21] Kamath, G.; Cao, F.; Potoff, J. J. *J. Phys. Chem. B* **2004**, *108*, 14130–14136.
- [22] Macedonia, M. D.; Maginn, E. J. *Mol. Phys.* **1999**, *96*, 1375–1390.
- [23] Dubbeldam, D.; Calero, S.; Vlugt, T. J. H.; Krishna, R.; Maesen, T. L. M.; Smit, B. *J. Phys. Chem. B* **2004**, *108*, 12301–12313.
- [24] Frenkel, D.; Smit, B. *Understanding Molecular Simulation*; 2nd ed., Academic Press: San Diego, 2002.
- [25] Setzmann, U.; Wagner, W. *J. Phys. Chem. Ref. Data* **1991**, *20*, 1061–1155.
- [26] Poling, B. E.; Prausnitz, J. M.; O’Connell, J. P. *The Properties of Gases and Liquids*; 5th ed., McGraw-Hill: New York, 2001.
- [27] Gumma, S.; Talu, O. *Langmuir* **2010**, *26*, 17013–17023.
- [28] Sing, K. S. W.; Everett, D. H.; Haul, R. A. W.; Moscon, L.; Pierotti, R. A.; Rouquerol, J.; Siemieniewaska, T. *Pure Appl. Chem.* **1985**, *57*, 603–619.
- [29] Talu, O.; Myers, A. L. *Colloids Surf., A* **2001**, *187*{188}, 83–93.
- [30] Do, D. D.; Do, H. D.; Nicholson, D. *J. Phys. Chem. B* **2009**, *113*, 1030–1040.
- [31] Nicholson, D.; Parsonage, N. G. *Computer Simulation and the Statistical Mechanics of Adsorption*; Academic Press: London, 1928.
- [32] We conjecture that an even better agreement between the volume of the liquified adsorbate and the volume of the extended hypersurface would be obtained if the diameter of the sphere was a function of its position on the hypersurface to reflect the local structure of the solid–fluid interaction potential. However, this would be a numerically challenging task whose outcome for the purposes of the present work does not seem to outweigh the effort.
- [33] Myers, A. L.; Monson, P. A. *Langmuir* **2002**, *18*, 10261–10273.
- [34] Bourrelly, S.; Llewellyn, P. L.; Serre, C.; Millange, F.; Loiseau, T.; Férey, G. *J. Am. Chem. Soc.* **2005**, *127*, 13519–13521.
- [35] Barthelet, K.; Marrot, J.; Riou, D.; Férey, G. *Angew. Chem.* **2002**, *114*, 291–294.

- [36] Mota, J. P. B. **Rodrigues, A. E.**; Saatchian, E.; Tondeur, D.: *Carbon* **1997**, *35*, 1259–1270.
- [37] Siepmann, J. I.; Karaborni, S.; Smit, B. *Nature* **1993**, *365*, 330–332.
- [38] Martin, M. G.; Siepmann, J. I. *J. Am. Chem. Soc.* **1997**, *119*, 8921–8924.
- [39] Serre, C.; Millange, F.; Thouvenot, C.; Nogues, M.; Marsolier, G.; Louër, D.; Férey, G. *J. Am. Chem. Soc.* **2002**, *124*, 13519–13526.
- [40] Esteves, I. A. A. C.; Lopes, M. S. S.; Nunes, P. M. C.; MOTA, J. P. B. *Sep. Purif. Technol.* **2008**, *62*, 281–296.
- [41] Cruz, F. J. A. L.; Mota, J. P. B. *Phys. Rev. B* **2009**, *79*, 165426-1–14.
- [42] Talu, O.: An Overview of Adsorptive Storage of Natural Gas, in *Fundamental of Adsorption: Proc. IVth Int. Conf. on Fundamentals of Adsorption*; Suzuki, M., Ed.; Elsevier: Amsterdam, Netherlands 1993; pp 655.
- [43] Matranga, K. R.; Myers, A. L.; Glandt, E. D. *Chem. Eng. Sci.* **1992**, *47*, 1569–1579.
- [44] Lozano-Castelló, D.; Alcáñiz-Monge, J.; de la Casa-Lillo, M. A.; D. Cazorla-Amorós, D.; Linares-Solano, A. *Fuel* **2002**, *81*, 1777–1803.
- [45] Bhatia, S. K.; Myers, A. L. *Langmuir* **2006**, *22*, 1688–1700.
- [46] Escobedo, F. *J. Chem. Phys.* **1998**, *108*, 8761–8772.
- [47] Boutin, A.; Coudert, F.-X.; Springuel-Huet, M.-A.; Neimark, A. V.; Férey, G.; Fuchs, A. H.: *J. Phys. Chem. C* **2010**, *114*, 22237–22244.

CHAPTER 5

EXPERIMENTAL AND THEORETICAL STUDIES OF C₂H₆, C₃H₈, C₄H₁₀ ADSORPTION IN THE METAL ORGANIC FRAMEWORK MIL-53(Al)

5.1.	INTRODUCTION	101
5.2.	EXPERIMENTAL	101
	5.2.1. Molecular Model and Simulation Method	101
5.3.	RESULTS AND DISCUSSION	102
	5.3.1. Adsorption Equilibrium Measurements	102
	5.3.1.1. Adsorption isotherms of C ₁ -C ₄ n-alkanes	106
	5.3.1.2. Analysis of the experimental adsorption isotherms	112
	5.3.2. Data Fitting	119
	5.3.3. Evaluation of the MIL 53 (Al) storage capacity towards C ₂ -C ₄ gases	129
5.4.	CONCLUSION	136
5.5.	REFERENCES	137

5.1 INTRODUCTION

Natural gas consists mainly of methane typically with up to 20% associated hydrocarbons primarily ethane, propane and butane that represent a large amount of most crude oils. Before natural gas can be used in any application either as fuel, either for fertilizer production or hydrogen production it must undergo processing to remove almost all substances other than methane. For that purpose, now using two different technologies, *absorption method* which does not allow for ethane recovery and *cryogenic expansion process* which based on condensation processes, [1] allows almost 100% ethane and heavier hydrocarbons recovery but is a very high energy costs technology. Design of new porous materials that are able to selective adsorption of the light hydrocarbons from different gas mixtures or for methane storage is important from an economical point of view [2]. The adsorption/separation of light hydrocarbons have been investigated in several different porous materials such as carbon nanotubes, activated carbons and its modified forms, pillared layered clays and zeolites [3-7].

Over a past decade a new class of structured nanoporous (MOFs) materials gained much attention in adsorption/separation and storage of the light alkanes because of their crystal structures that exhibit unusual flexibility and tuneable host-guest properties [8-11].

In this work, the equilibrium of the C₂-C₄ adsorption in MIL-53(Al) over pressures in the range 0.01-4.5 MPa and temperatures in the 303-353 K regions was studied. Once again, the chosen *P-T* range over which experimental results on C₂-C₄ adsorption in MIL-53(Al) has been reported is the largest span investigated to date.

The potential use of MIL-53(Al) as a C₂-C₄ n-alkanes adsorptive storage media was investigated both, experimentally *via* gravimetric adsorption experiments and theoretically by Grand Canonical Monte Carlo (GCMC) simulations.

5.2. EXPERIMENTAL

5.2.1. Molecular Model and Simulation Method

In our molecular simulation work, MIL-53(Al) is modeled as a rigid lattice with its constituent atoms at the crystallographic positions and the parameterization of solid-fluid dispersive interactions in MIL-53(Al) is based on the TraPPE-UA [12-16] force field to take advantage of the transferability of the parameters built into it. Details of structural model used for MIL-53(Al) are described in Chapter 4.

The parameterization of the solid-fluid dispersive interactions using TraPPE-UA was treated *via* the LJ potential only. The corresponding LJ parameters are summarized in Table 5.1, the location of each atom type on the framework being reported in Fig. 2.1.

Table 5.1. Lennard-Jones parameters for dispersive interactions in the C₂-C₄/MIL-53lp(Al) system.

Label	Site	$\sigma(\text{Å})$	ϵ/k_B (K)	Ref.
Al	Al	0.0	0.0	[25]
O(1)	OH	3.02	93.0	[26]
O(2)	O	2.80	55.0	[27]
C(1)	CH(aro)	3.695	50.5	[28]
C(2)	C(aro)	3.88	21.0	[28]
C(3)	C	3.85	20.0	[29]
	C ₂ H ₆	3.75	98	[30]
	C ₃ H ₈ (CH ₃ CH ₂)	3.84	(93, 60)	[31]
	C ₄ H ₁₀ (CH ₃ CH ₂)	3.96	(85, 52)	[32]

5.3 RESULTS AND DISCUSSION

5.3.1. Adsorption Equilibrium Measurements

As it was noted in the literature review, adsorption of the alkanes in the MIL-53(Al) solid passes through the more complex mechanism comparing to some other MIL materials and zeolites [17,18].

The analysis of the simulated results for ethane adsorption is given below. Figure 5.4 shows the unit cell of MIL-53(Al)lp along the three crystallographic coordinates (a , b , and c); these are aligned with the Cartesian coordinates x , y , and z . For the time being, ignore the slicing of the unit cell along the a -coordinate (top-right image). In the following, a , b , and c also denote the lengths of the three dimensions of the unit cell. From the left image of the Fig. 5.1 it is evident that viewing the cell along the a -axis (or x -axis), the bc cross section or yz cross-section of the unit cell contains the cross sections of two channels of MIL-53. Then, the bc plane, which is represented by the cyan dashed line in the top-right image and cuts the unit cell at $x = a/2$ into two halves, is a plane of reflection symmetry. There also is a rotational symmetry: if the box is rotated by 180° around the line parallel to the a -axis, located by the cyan circle, we get the same configuration (the left image Fig 5.1.). These findings are in agreement with our previous data for the methane simulations (Chapter 4).

Figure 5.2 shows a yz view of the framework atoms in a simulation box with $L_y = 2b$ and $L_z = 2c$.

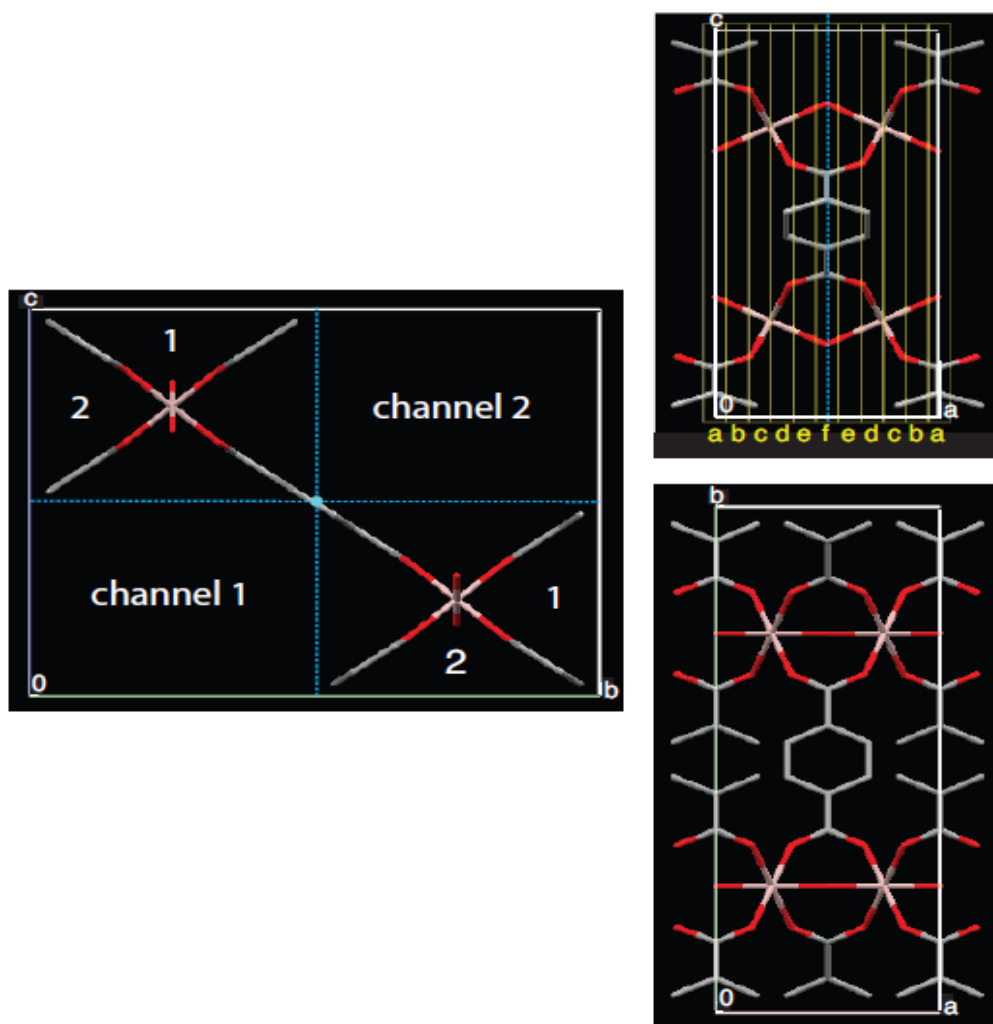


Figure 5.1: Orthographic view of the unit cell along *a* axis (top-left), *b* axis (top-right), and *c* axis (bottom-right).

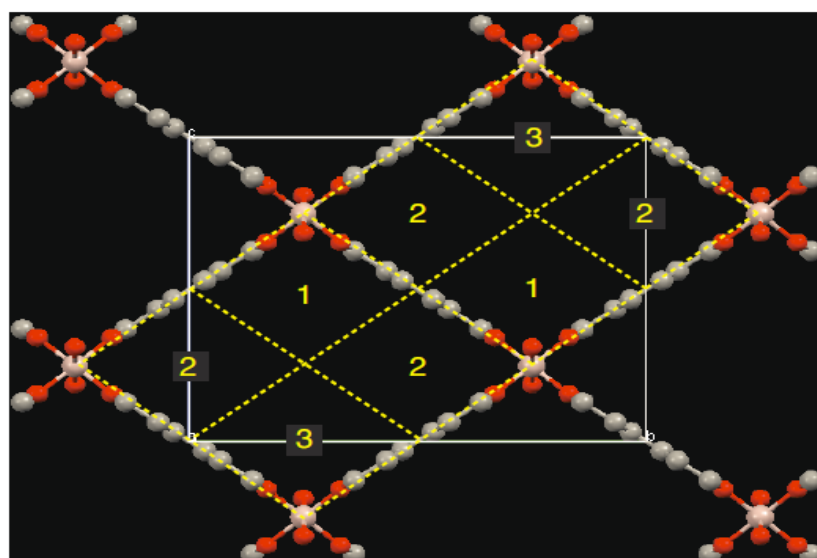


Figure 5.2: Orthographic view of the unit cell along the *a* axis (top-left) and identification of the three types of sub-channel: type 1, type 2, and type 3. Sub-channel 3 is a mirror image of sub-channel 1.

Figure 5.3 shows molecular density profile, $n_a(x)$, along the a -axis of each sub-channel of the unit cell of MIL-53(Al)p for a loading of one and three ethane molecules per unit cell. The j th profile, $n_a^{(j)}(x)$, gives the statistical average of the number of ethane molecules in a slab of the j th sub-channel width dx centered at x .

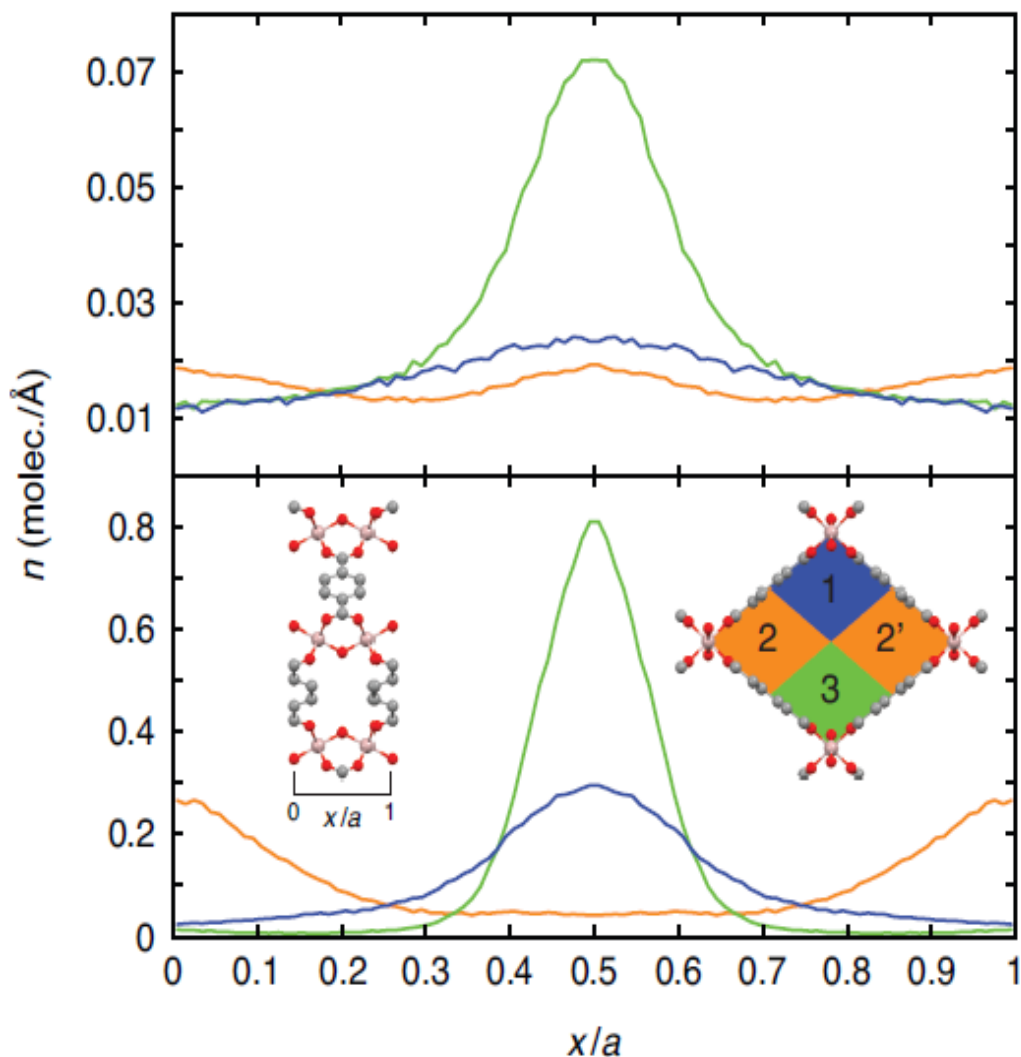


Figure 5.3. Molecular density profile, $n_a(x)$, along the a -axis of each sub-channel of the unit cell of MIL-53(Al)p for a loading of one (top) and three (bottom) ethane molecules per unit cell.

Figures 5.4 and 5.5 show a 2-D projection of the number density field for condensed ethane inside an even-index channel of MIL-53p(Al);), at various positions along the a -axis of the unit cell of MIL-53(Al)p for a loading: (i) Fig 5.4 of one ethane molecule per unit cell (0.5 ethane molecules per channel over a distance of length a); (ii) Fig. 5.5 for a loading of six ethane molecules per unit cell (3 ethane molecules per channel over a distance of length a).

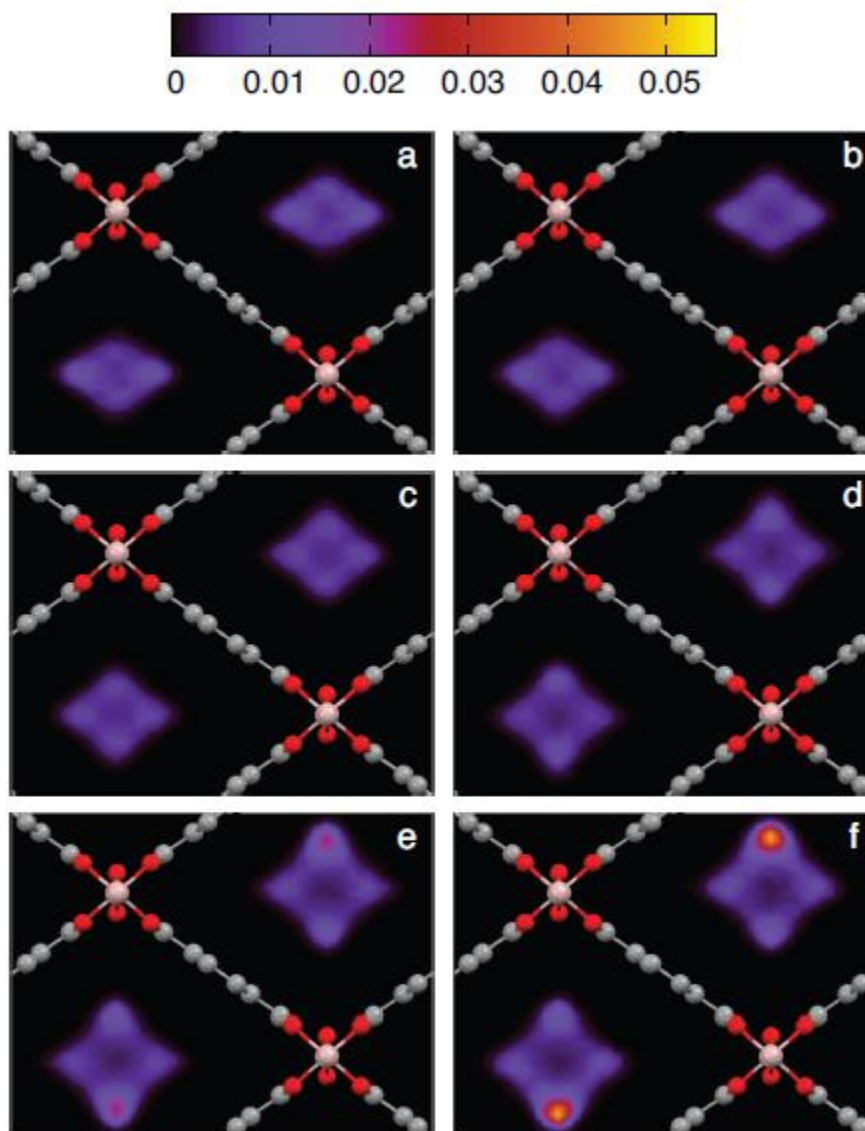


Figure 5.4. Molecular density field, $n_a(x; y)$, at various positions along the a -axis of the unit cell of MIL-53(Al) for a loading of one ethane molecule per unit cell (0.5 ethane molecules per channel over a distance of length a).

The j th field, $n(j) a(x; y)$, gives the statistical average of the number of ethane molecules in a slab of the unit cell of width $dx = a=10$ and cross-sectional area $dx dy$ centered at $(dx j; x; y)$; index j runs from (a) $j = 1$ to (f) $j = 6$.

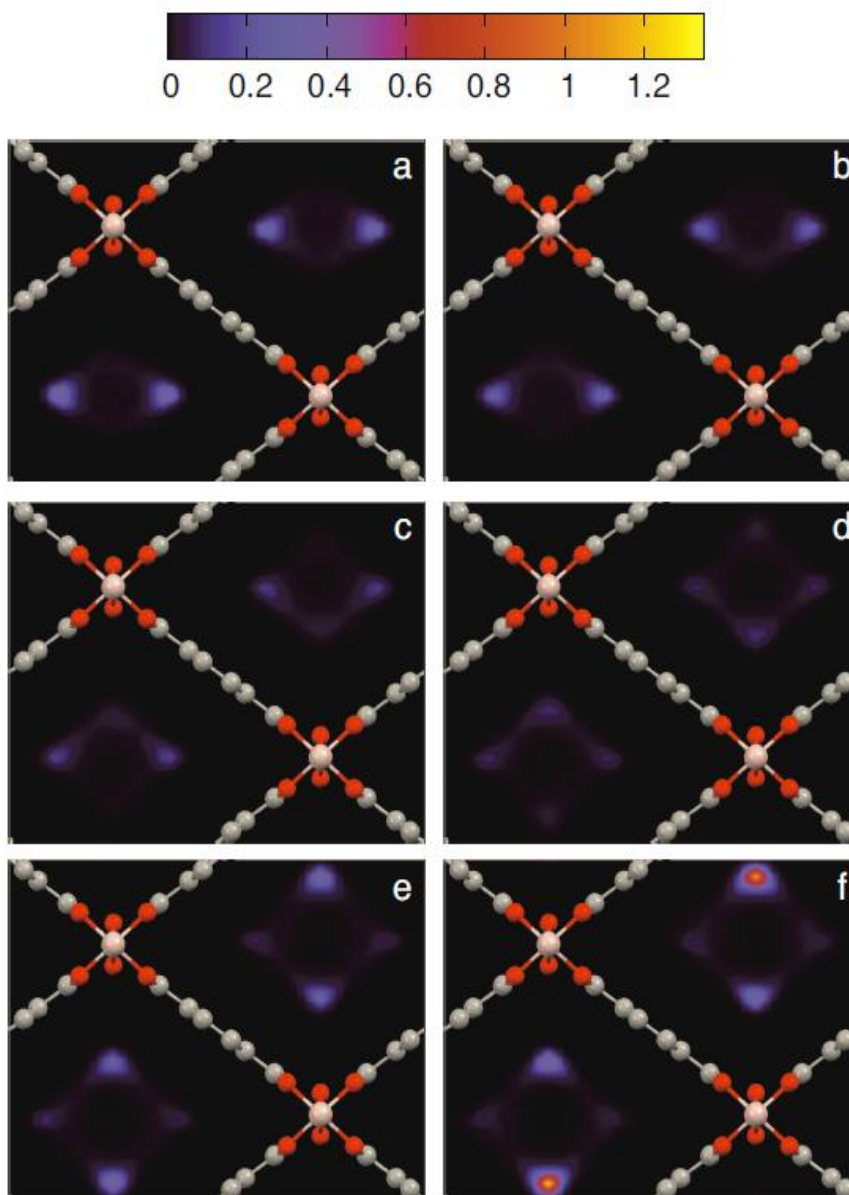


Figure 5.5. Molecular density field, $n_a(x; y)$, at various positions along the a -axis of the unit cell of MIL-53(Al) for a loading of 6 ethane molecules per unit cell (3 ethane molecules per channel over a distance of length a).

The j th field, $n_a^{(j)}(x; y)$, gives the statistical average of the number of ethane molecules in a slab of the unit cell of width $dx = a=10$ and cross-sectional area $dx \cdot dy$ centered at $(dx \cdot j; x; y)$; index j runs from (a) $j = 1$ to (f) $j = 6$.

5.3.1.1. Adsorption Isotherms of C₂-C₄ n-alkanes

Pure component adsorption isotherm of C₂-C₄ n-alkanes on MIL-53(Al) were measured gravimetrically from vacuum up to ~5 MPa under three temperatures 303.15 K, 323.15 K and 353.15 K. In order to better understand the adsorption process results are given together with

methane adsorption data. A comparison of the absolute, excess and net adsorption isotherms for methane, ethane, propane and n-butane adsorption on MIL-53 (AI) are given in Figs. 5.6 -5.9.

It appears that Langmuir isotherms (type I) are obtained. For all investigated gases absolute adsorption is a monotonously increasing function of pressure, the other two functions are concave with respect to the pressure axis and their maximum value occurs at a pressure that increases with temperature.

Methane adsorption isotherms presented on Fig. 5.6. At pressures below ~0.15 MPa, the pore density is much higher than the bulk density of methane and thus the differences between n , n_{ex} , and n_{net} are negligible. At higher pressures, the bulk density increases more rapidly than the pore density and the three measures of adsorption start to deviate from each other. At ~5 MPa, the absolute adsorption continues to increase with pressure while the excess adsorption is close to its maximum value and the slope of net adsorption is already negative; the maximum value of n_{net} under the whole investigated temperatures occurs at ~4 MPa. These relationships corresponds to the whole investigated temperature range (Fig. 5.6 a, b and c) under methane adsorption.

As shown on Fig. 5.7, relations between absolute, excess, and net adsorption isotherms for ethane are corresponds to that once described for methane. For ethane, at pressure below ~0.15 MPa the differences between n , n_{ex} , and n_{net} are negligible. At ~3 MPa, the absolute adsorption continues to increase with pressure while the excess adsorption is close to its maximum value and the slope of net adsorption is already negative; the maximum value of n_{net} under all investigated temperatures occurs at ~1.5 MPa.

With respect to the propane adsorption it is confined by critical conditions. The maximum applicable pressures for propane are ~0.9, ~1.4 and ~2.5 MPa at 303.15 K, 323.15 K and 353.15 K respectively. A comparison of the absolute, excess, and net adsorption isotherms of propane is presented in Fig. 5.8. There is no significant difference between n , n_{ex} , and n_{net} below ~0.15 MPa under all investigated temperature range. Adsorption isotherms at 353.15 K (Fig. 5.8c) shows the most similar behavior to methane and ethane adsorption isotherms. At pressures above ~0.15 MPa the three measures of adsorption start to deviate from each other. At ~2.5 MPa the absolute and excess adsorption continues to increase with pressure while the net adsorption is close to its maximum value. Meanwhile, the three measures of adsorption at 303.15 K and 323.15 K presented in Fig. 5.8a, b are increasing under the whole investigated pressure range. This is due to the fact that the increase of the bulk density relatively to the pore density is limited by critical pressure of propane. The same situation observed for butane adsorption isotherms (Fig. 5.9). The maximum applicable pressures are ~0.25, ~0.45 and ~0.7 MPa at 303.15 K, 323.15 K and 353.15 K respectively. The three measures of adsorption presented on Fig. 5.9a, b and c are monotonously increasing functions of pressure.

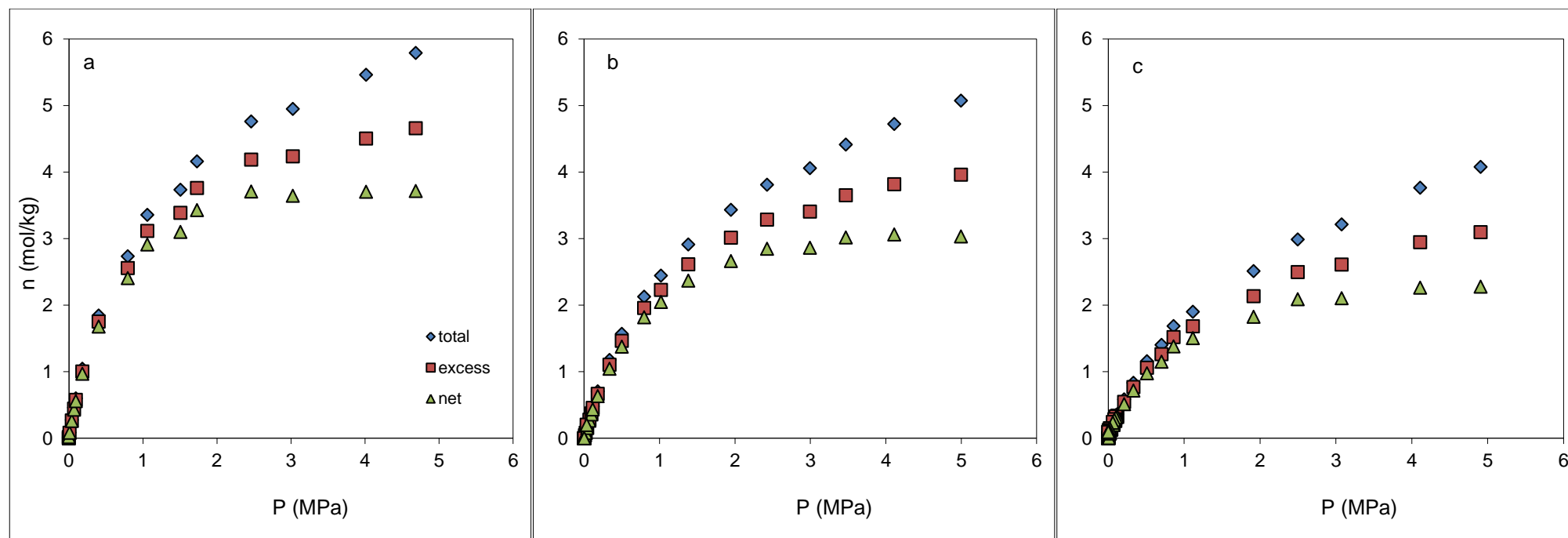


Figure 5.6. Absolute (\diamond), excess (\square), and net (Δ) adsorption isotherms of methane in MIL-53p(AI) at 303.15 K (a), 323.15 K (b) and 353.15 K (c) determined from gravimetric measurements. The reference state corrections ($V_p = 0.56 \text{ cm}^3/\text{g}$ and $V_s = 0.47 \text{ cm}^3/\text{g}$) used for calculations of absolute adsorption values were determined by GCMC simulation.

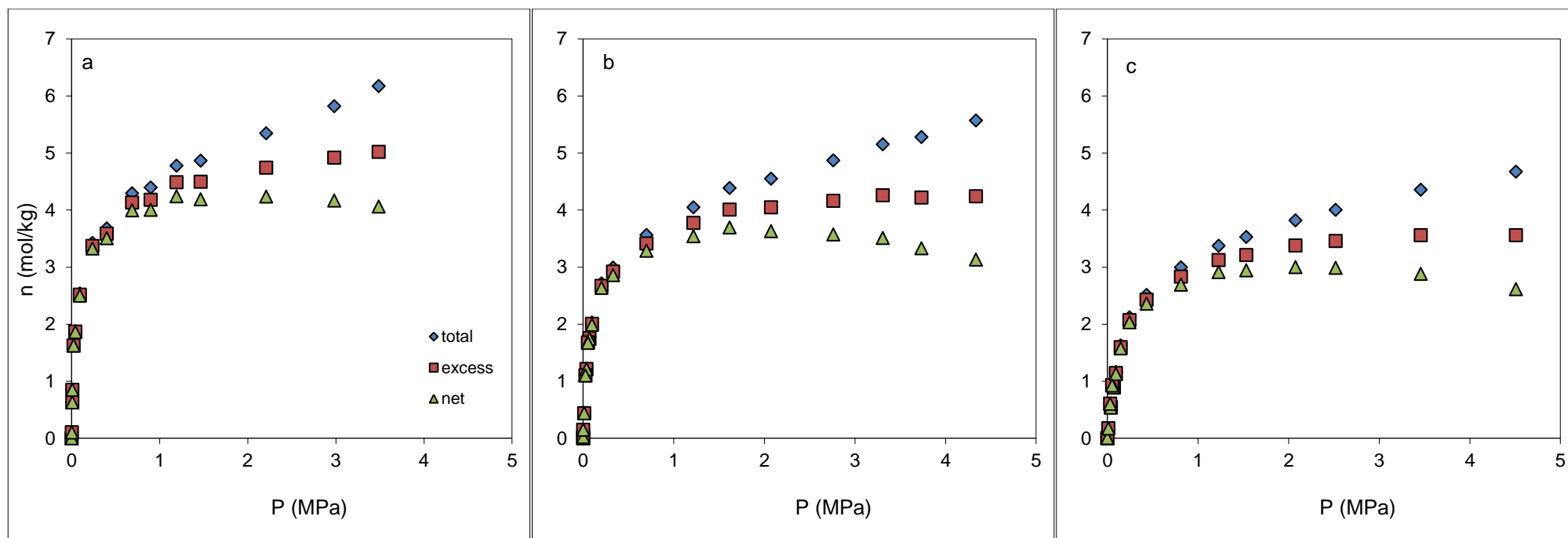


Figure 5.7. Absolute (\diamond), excess (\square), and net (Δ) adsorption isotherms of ethane in MIL-53lp(AI) at 303.15 K (a), 323.15 K (b) and 353.15 K (c) determined from gravimetric measurements. The reference state corrections ($V_p = 0.56 \text{ cm}^3/\text{g}$ and $V_s = 0.47 \text{ cm}^3/\text{g}$) used for calculations of absolute adsorption values were determined by GCMC simulation.

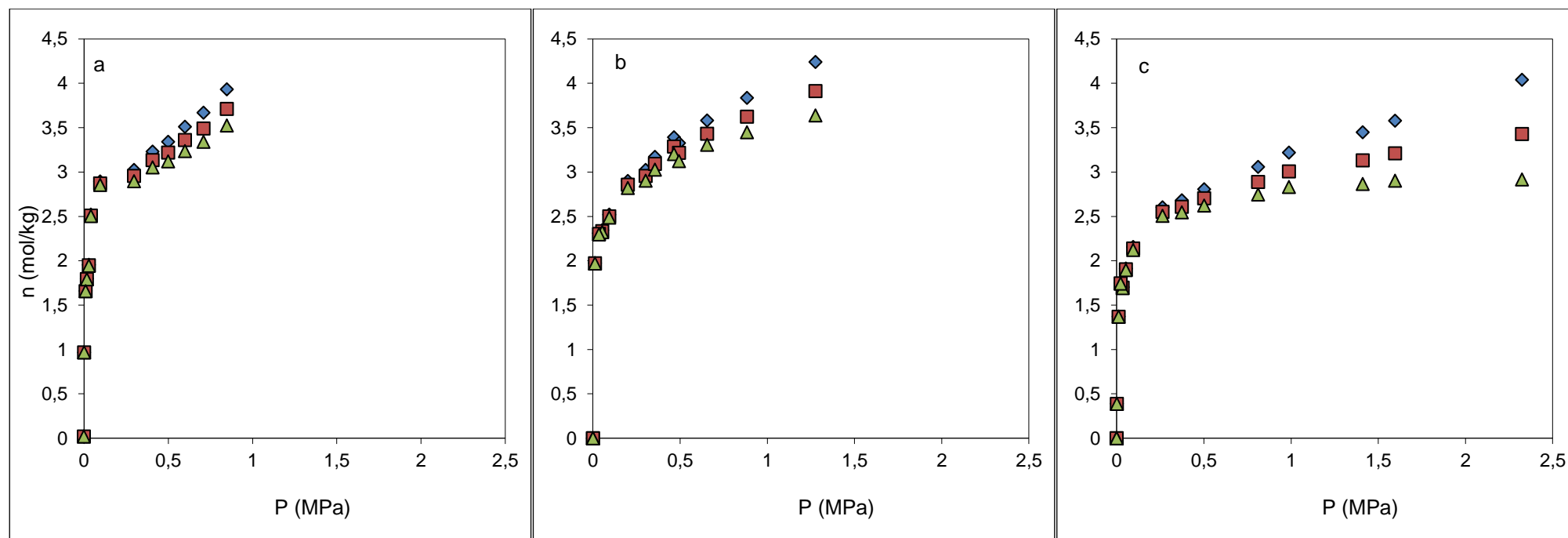


Figure 5.8. Absolute (\diamond), excess (\square), and net (Δ) adsorption isotherms of propane in MIL-53p(AI) at 303.15 K (a), 323.15 K (b) and 353.15 K (c) determined from gravimetric measurements. The reference state corrections ($V_p = 0.56 \text{ cm}^3/\text{g}$ and $V_s = 0.47 \text{ cm}^3/\text{g}$) used for calculations of absolute adsorption values were determined by GCMC simulation.

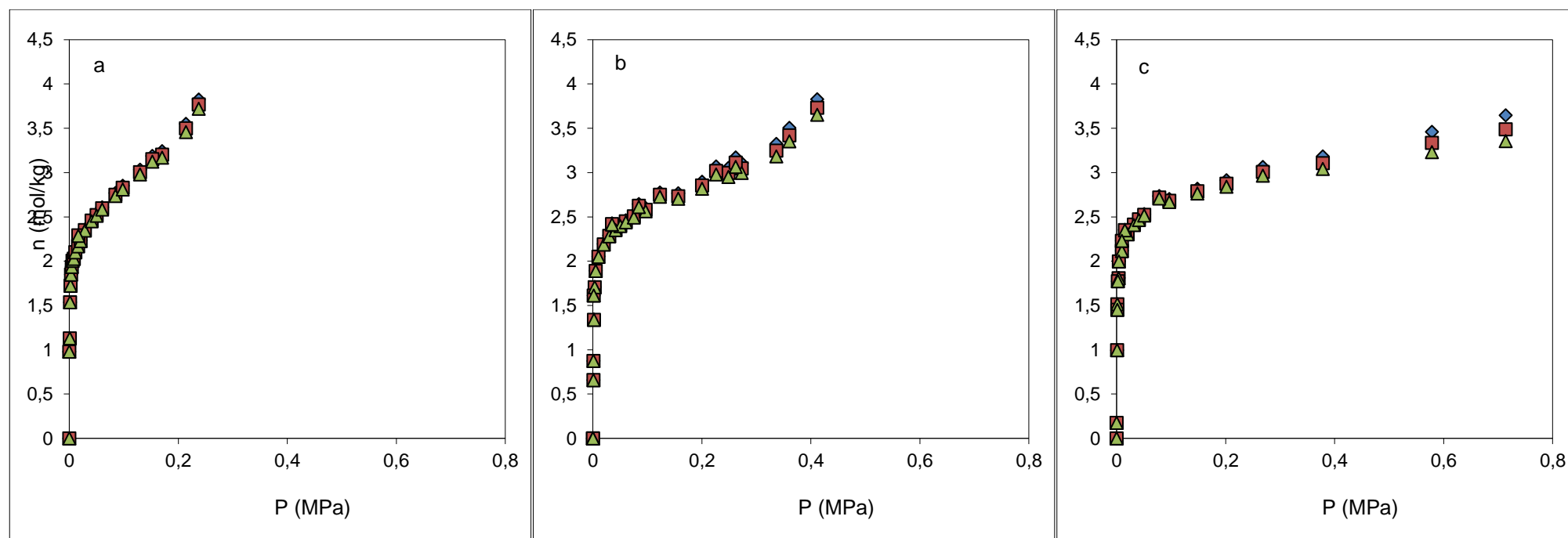


Figure 5.9. Absolute (\diamond), excess (\square), and net (Δ) adsorption isotherms of butane in MIL-53p(AI) at 303.15 K (a), 323.15 K (b) and 353.15 K (c) determined from gravimetric measurements. The reference state corrections ($V_p = 0.56 \text{ cm}^3/\text{g}$ and $V_s = 0.47 \text{ cm}^3/\text{g}$) used for calculations of absolute adsorption values were determined by GCMC simulation.

5.3.1.2. Analysis of the experimental adsorption isotherms

The adsorption isotherms for C₁-C₄ n-alkanes on MIL-53(Al) were measured at 303.15 K, 323.15 K and 353.15 K (Figs 5.10 – 5.12). The isotherms given in Figs 5.10a, 5.11a, 5.12a, are of Langmuir type presented in a standard form of amount adsorbed (mol/kg) versus pressure. As shown on Figs 5.11a–5.12a for the C₁-C₄ gases, the amount of adsorbed fluid increases rapidly with pressure, until reaching an approximately constant plateau and, thus, exhibiting Langmuir type isotherms. The exact location of that plateau depends on the molecular nature of the adsorbate, being reached earlier for the lighter molecules.

However, when plotted as a function of the log of the pressure (Fig. 5.10b), one can distinguish a step in the C₃ and C₄ adsorption isotherms while a convex shape is obtained for the C₂ adsorption. The only a very small concentration of the narrow pore form of MIL-53(Al) in the transition zone could explain such a shape of the isotherm. By contrast, only a concave profile is pointed out for methane which is commonly observed when plotting a Langmuir isotherm for a rigid microporous material. The steps in the propane and butane isotherms are the signature of the breathing of the MIL-53(Al) structure upon adsorption.

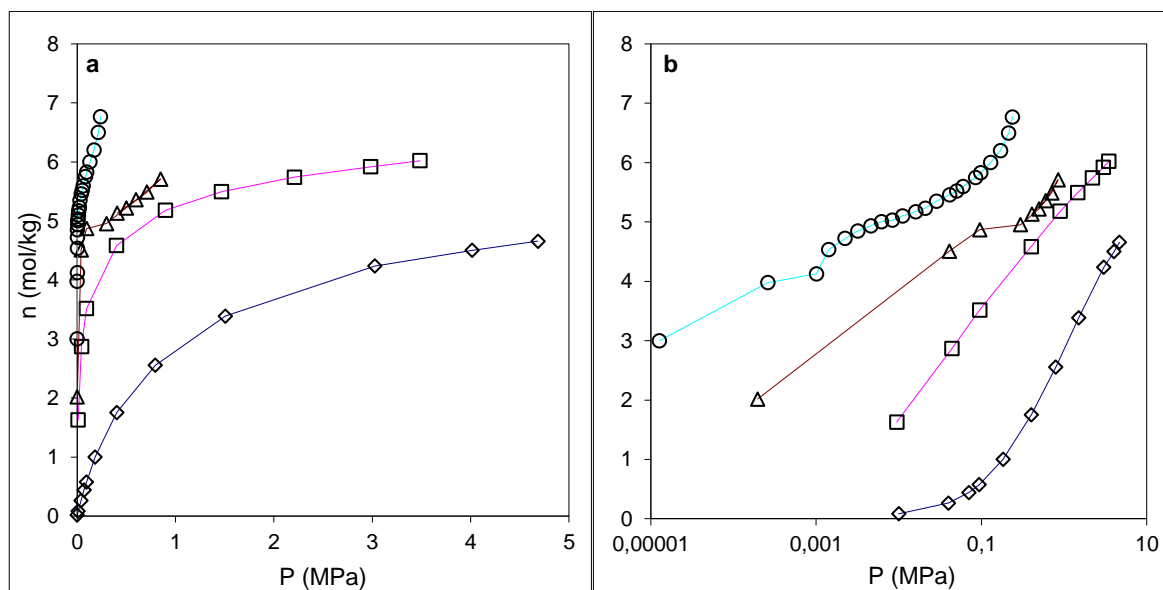


Figure 5.10. Methane (\diamond), ethane (\square), propane (Δ) and butane (\circ) adsorption isotherms on MIL-53(Al) at 303.15K expressed here in terms of n_{ex} lines are drawn as a guide to the eye. Figure represents both standard form, amount adsorbed (mol/kg) versus pressure (a) and the semi-log scale (b) amount adsorbed (mol/kg) versus the log of pressure. The reference state corrections used are $V_p = 0.56 \text{ cm}^3/\text{g}$ and $V_s = 0.47 \text{ cm}^3/\text{g}$. For clarity, the adsorption data for C₄, C₃ and C₂ are displaced by 3 mol/kg, 2 mol/kg, and 1 mol/kg, respectively. The lines are drawn as a guide to the eye.

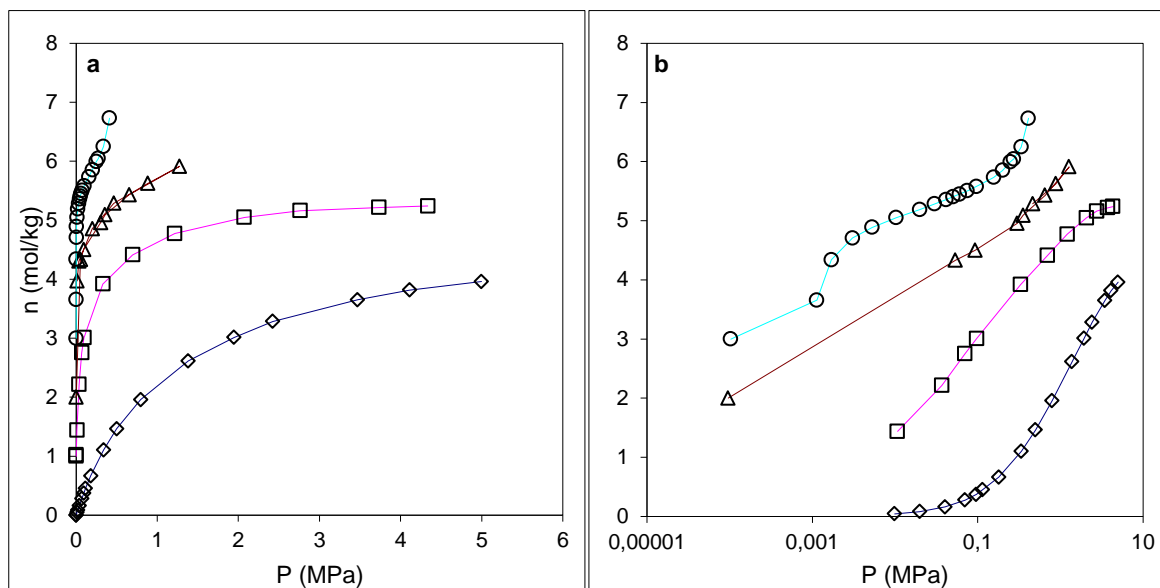


Figure 5.11. Methane (◇), ethane (□), propane (Δ) and butane (○) adsorption isotherms on MIL-53(AI) at 323.15K expressed here in terms of n_{ex} lines are drawn as a guide to the eye. Figure represents both standard form, amount adsorbed (mol/kg) versus pressure (a) and the semi-log scale (b) amount adsorbed (mol/kg) versus the log of pressure. The reference state corrections used are $V_p = 0.56 \text{ cm}^3/\text{g}$ and $V_s = 0.47 \text{ cm}^3/\text{g}$. For clarity, the adsorption data for C₄, C₃ and C₂ are displaced by 3 mol/kg, 2 mol/kg, and 1 mol/kg, respectively. The lines are drawn as a guide to the eye.

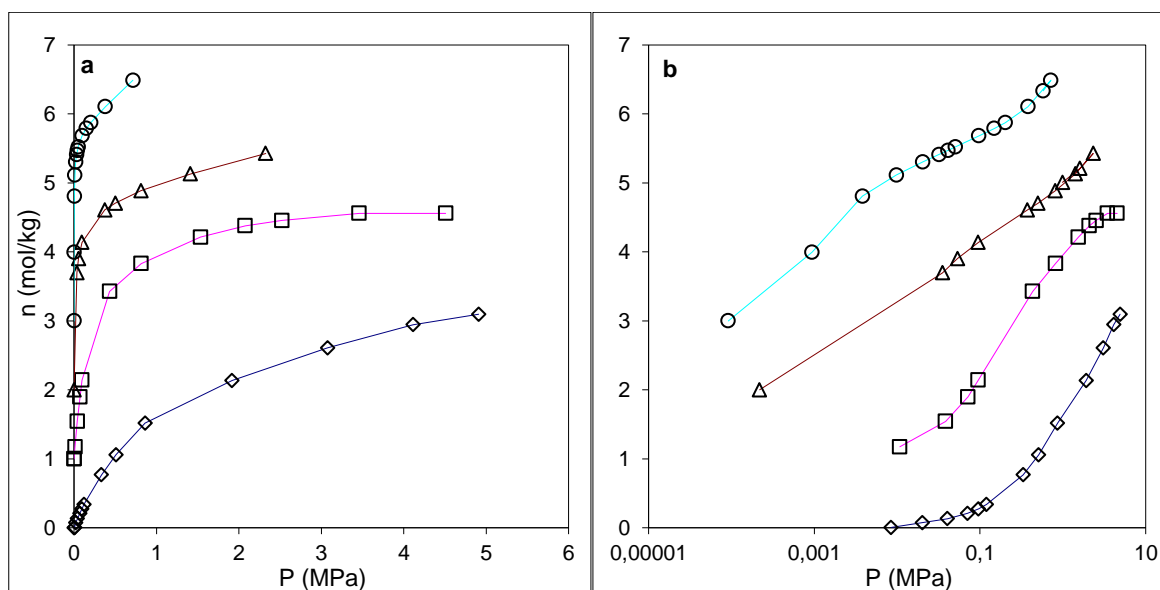


Figure 5.12. Methane (◇), ethane (□), propane (Δ) and butane (○) adsorption isotherms on MIL-53(AI) at 353.15K expressed here in terms of n_{ex} lines are drawn as a guide to the eye. Figure represents both standard form, amount adsorbed (mol/kg) versus pressure (a) and the semi-log scale (b) amount adsorbed (mol/kg) versus the log of pressure. The reference state corrections used are $V_p = 0.56 \text{ cm}^3/\text{g}$ and $V_s = 0.47 \text{ cm}^3/\text{g}$. For clarity, the adsorption data for C₄, C₃ and C₂ are displaced by 3 mol/kg, 2 mol/kg, and 1 mol/kg, respectively. The lines are drawn as a guide to the eye.

Based on the analysis of the experimental data for the C₂-C₄ adsorption isotherms we can conclude the three main effects influent on the structural transitions of MIL-53(Al) (Figs. 5.13-5.15):

There is size effect on the extent of breathing phenomena. The position of the step is a function of pressure. With increase of the alkyl chain length chain the adsorption sub-step appears at a much lower relative pressure (Fig. 5.13) and pressure steps for the *lp-np* and *np-lp* transitions become shorter.

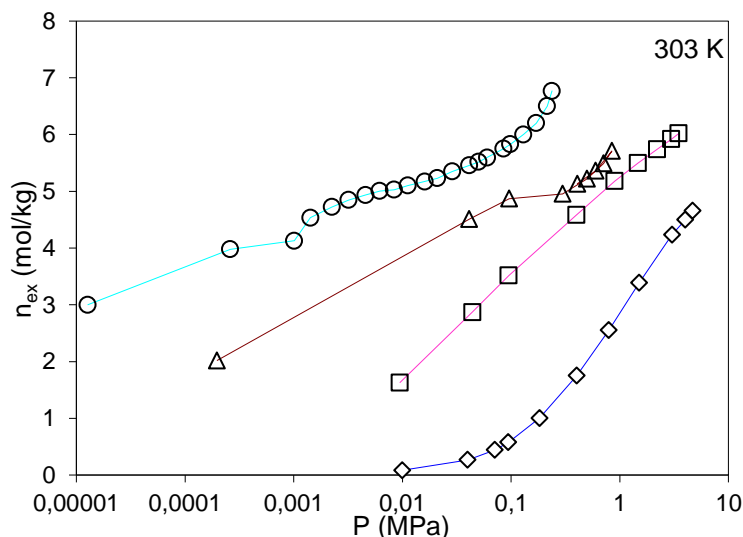


Figure 5.13 Semi-log scale of methane (\diamond), ethane (\square), propane (Δ), and butane (O) adsorption isotherms in MIL-53lp(Al) at 303.15K. For clarity, the adsorption data for C₄, C₃ and C₂ are displaced by 3mol/kg, 2mol/kg, and 1 mol/kg, respectively. The lines are drawn as a guide to the eye.

There is temperature effect on the extent of breathing phenomena. Strongly depending on temperature, with temperature increase this effect becomes already evident for C₂ (Fig. 5.13); and this tendency is even more pronounced for long-chain alkanes (Fig. 5.14).

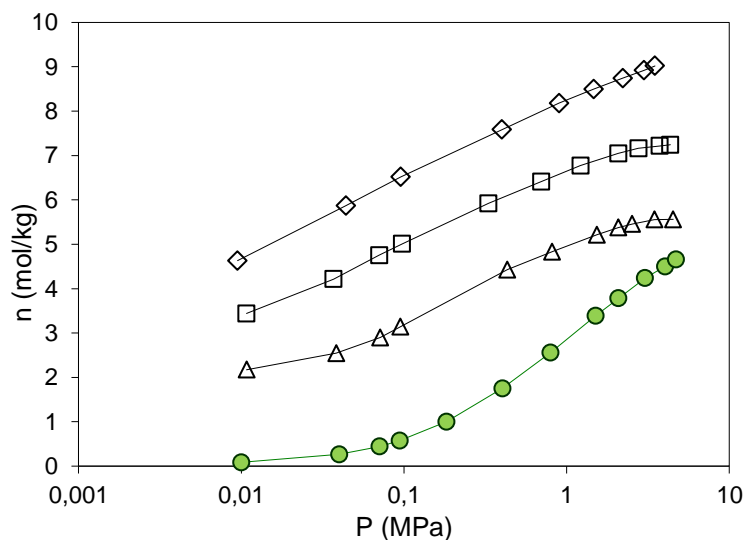


Figure 5.14. Comparison of the experimental isotherms presented in semi-log scale obtained at 303 K (\diamond), 323 K(Δ) and 353 K (\square) during the adsorption of ethane on MIL-53(Al). The green circles represent methane adsorption at 303 K and given as a reference isotherm (no transformation in MIL-53(Al)). For clarity, the adsorption data at 353 K 323 K and 303 K are displaced by 2 mol/kg, 3 mol/kg, and 4 mol/kg, respectively. The lines are drawn as a guide to the eye.

There is size effect on temperature dependence of the breathing phenomena. With temperature increase, the breathing effect becomes to be more evident for the longer alkanes. For instance, example given in Fig. 5.15 for butane proves that with temperature breathing appears at lowest relative pressure and breathing magnitude becomes to be more evident.

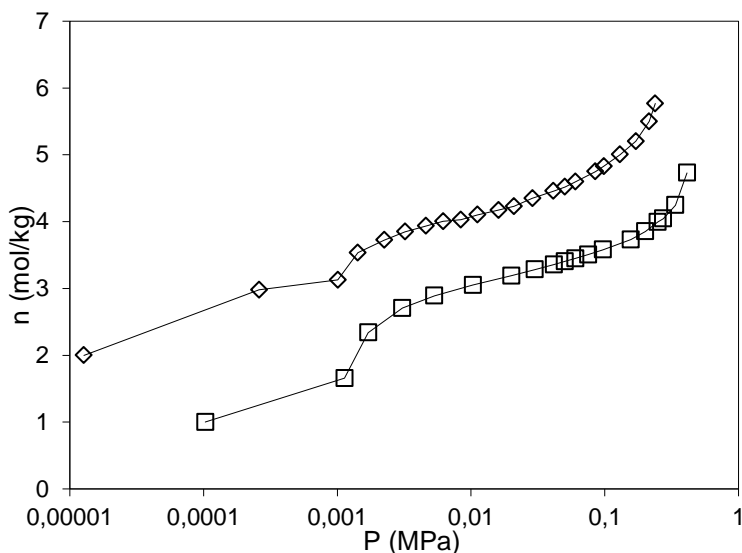


Figure 5.15. Experimental adsorption isotherms of butane on MIL-53(Al) at 303 K (\diamond) and 323 K (\square) presented in semi-log scale. The lines are drawn as a guide to the eye. For clarity, the adsorption data for 303 K and 323 K are displaced by 2 mol/kg, and 1 mol/kg, respectively. The lines are drawn as a guide to the eye

Summary of our findings is given in diagram (Scheme 5.1), which presents guest-induced structural transitions of the MIL-53 (Al) upon C₁-C₄ adsorption and the temperature influence. With increase of the temperature and chain lengths the magnitude of breathing increases.

It should be noted, that our hypothesis is in full agreement with the literature findings known up to date on predicted pressures for the *lp*---*np* and *np*----*lp* transitions for MIL-53 (Cr) [19] given in Table 5.2.

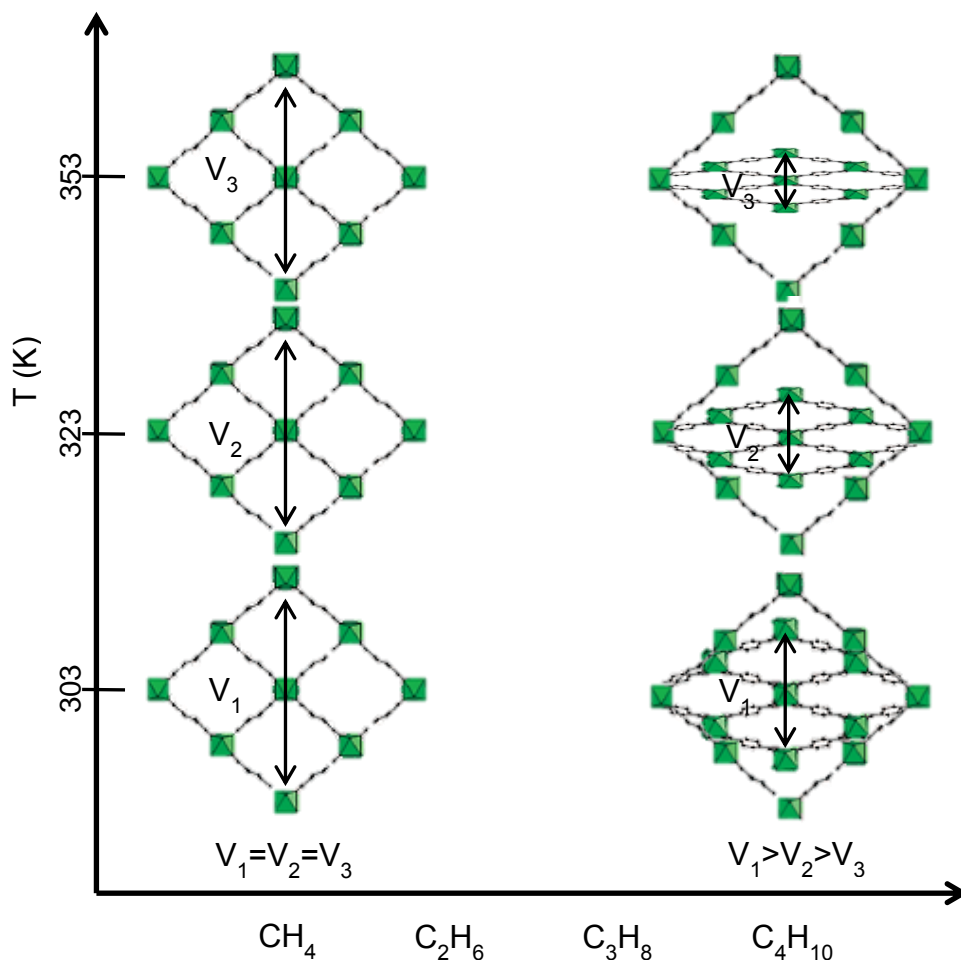
Table 5.2. Predicted pressures for the *lp*-*np* and *np*-*lp* transitions for MIL-53 (Cr)

Guest	CO ₂	C ₂ H ₆	C ₃ H ₈	C ₄ H ₁₀
P (<i>lp</i> - <i>np</i>)	0.3 bar	0.17 bar	30 mbar	9.0 mbar
P (<i>np</i> - <i>lp</i>)	5 bar	3.3 bar	0.45 bar	0.15 bar

More in details the literature finding can be summarized as a followed:

- Contrary to other porous materials, MOFs express, as so called host-guest properties.
- The MOF's guest-responsive behaviors, such a "breathing" and "gate opening", (i.e. (i) progressive swelling or (ii) contraction or ((iii) pore deformation or (iv) amorphous-to-crystal and (v) crystal to-crystal structural transitions) are the main results of such an exceptional guest-responding MOF's behavior upon gas adsorption [20].

- The MIL-53 materials family [21], a particularly eye-catching case of the last category (i.e. (v) crystal to-crystal structural transitions), has attracted a lot of attention due to its large flexibility and the occurrence of a double structural transition upon adsorption of some gases (CO₂, H₂O, C₂H₆, C₃H₈, C₄H₁₀) but not others (H₂, CH₄) [22].



Scheme 5.1. Diagram for the hypothesis of the temperature and chain size effects on “breathing” phenomena in MIL-53 (Al) upon C₁-C₄ adsorption.

Although, both experimental and molecular simulation studies performed so far, mainly focused on MOF’s structural and energetic characterization, a current depiction of the guest-induced structural transitions is lacking a general thermodynamic interpretation of all the results obtained so far. Therefore, the necessity of understanding the thermodynamic conditions for the host-guest interactions which allow the breathing to happen is indeed highlighted in a literature [23].

Recently a generic thermodynamic framework for the understanding of guest-induced structural transitions in flexible nanoporous materials such as MOFs was developed [24], by using the osmotic pseudo-ensemble. For a material that has two possible framework structures and where gas adsorption follows type I isotherms [25], it was proposed a full taxonomy of possible guest-induced structural transitions.

This classification relies only on a few key parameters, namely: the free energy difference, ΔF ,

between the (empty) host structures, their pore volumes, $V_p(i)$, and the adsorption affinities for the guest, K_i .

Indeed, all guest-responsive hybrid materials studied so far exhibit free energy differences between host structures in the range ΔF 2-5 kJ/mol [19]. In the case of materials such as MIL-53, where the large-pore (lp) form is intrinsically more stable than the narrow-pore (np) form at room temperature, our taxonomy predicts either the occurrence of two structural transitions upon gas adsorption or the absence of any transition. This is determined by a balance between intrinsic stability of the crystal structures, adsorption affinities, and accessible volume. In the case of alkanes adsorption in MIL-53, adsorption isotherms from ref [22] show that the variation of pore volume (and adsorbed quantities at saturation) for both phases is small and the main factor is the change in adsorption affinities for different guests.

Within the limits of this model, the presence or absence of structural transitions for a given adsorbate is unambiguously determined by one factor only: the ratio K_{np}/K_{lp} of adsorption affinities in the two structures. A double guest-induced structural transition happens if and only if K_{np}/K_{lp} is large enough so that the following inequality holds [24]:

$$(V_p^{(np)} - V_p^{lp}) \ln \left(\frac{K_{np} / K_{lp} \times V_p^{lp} - V_p^{(np)}}{V_p^{lp} - V_p^{(np)}} \right) + V_p^{lp} \ln \frac{K_{np}}{K_{lp}} \geq \frac{\Delta F}{\rho RT} \quad (5.2)$$

If, on the contrary, K_{np}/K_{lp} is too small, there will be no structural transition at all.

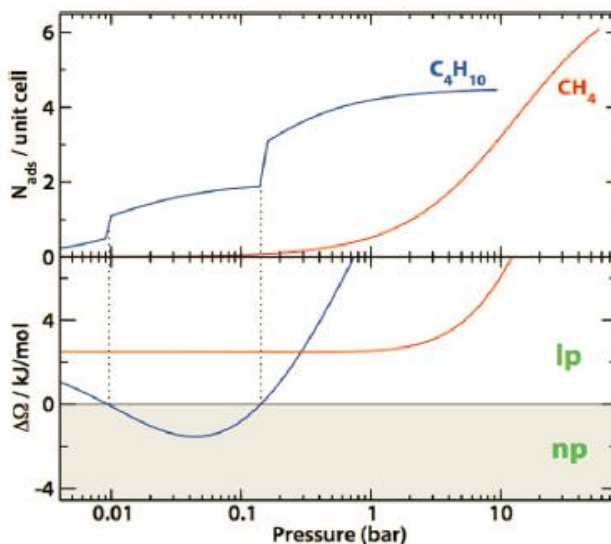


Figure 5.16. Upper panel: adsorption isotherms of CH_4 (in red) and C_4H_{10} (in blue) in MIL-53 (Cr), in a Langmuir model. Lower panel: difference in osmotic potential between lp and np phases, as a function of pressure. Vertical dotted lines correspond to C_4H_{10} -induced structural transition.

By way of illustration, difference in osmotic potential between lp and np phases, as a function of pressure is shown in Fig. 5.16. An example is given for the Langmuir isotherms fitted the C_4H_{10} and CH_4 adsorption in MIL-53 (Cr) at 303 K [22].

For C_4H_{10} , $K_{np}/K_{lp} \approx 4$ and there are two successive structural transitions; this leads to an isotherm where two steps can be clearly seen on a logarithmic pressure scale. Contrarily, for CH_4 ,

$K_{np}/K_{lp} \approx 1$ (Fig.5.17) and the *lp* structure is thermodynamically favored throughout the pressure range; the isotherm, being simply that of CH₄ in MIL-53 *lp*, has no step (Fig.5.16).

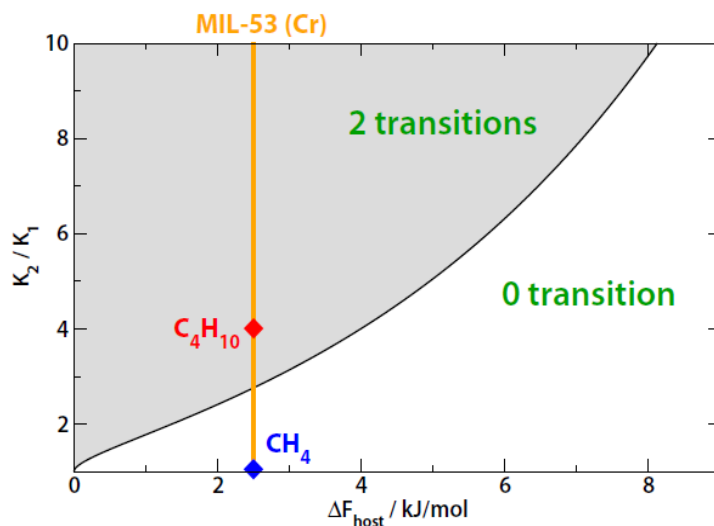


Figure 5.17. Existence of guest-induced structural transitions upon gas adsorption as a function of ΔF_{host} , the free energy difference between empty structures, and the ratio of gas affinities, K_1/K_2 . The orange line corresponds to the adsorption of alkanes in MIL-53(Cr) and the symbols indicate the points of the graph corresponding to CH₄ (in blue) and C₄H₁₀ (in red).

A phase diagram of MIL-53 (Cr) as a function of guest pressure and host-guest affinities, for a series of adsorbates with a constant K_{lp}/K_{np} ratio is presented in Fig. 5.18. There are the points corresponding to the phase transitions induced by C₂H₆, C₃H₈, and C₄H₁₀. It is noteworthy that the pressure domain of the *np* phase, which has a constant width in the logarithmic scale of Fig. 5.18, actually gets smaller in a linear scale for adsorbates with larger affinities for the solid. Therefore, it was demonstrated that the existence of the breathing phenomena in MIL-53 (Cr) is determined by the relative affinities of the sorbate for the *lp* and *np* phases [22].

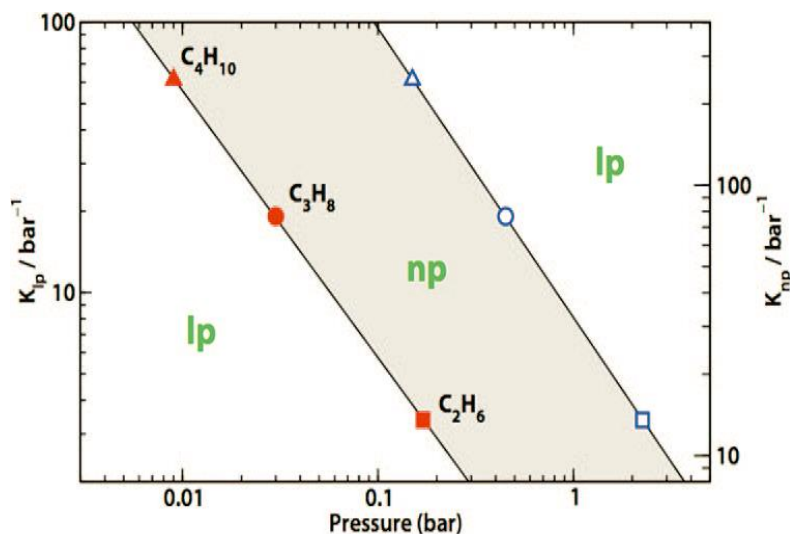


Figure 5.18. Existence domains of the *lp* and *np* phases of MIL-53 upon gas adsorption, with guests of different affinities (K_{lp} and K_{np}). Symbols correspond to *lp*-*np* and *np*-*lp* (respectively, filled and open) transitions for the C₂ to C₄ alkanes.

5.3.2. Data Fitting

We have compare of the experimental isotherms of the C₂-C₄ gases adsorbed on MIL-53(Al) for temperature range 303-353 K to the isotherms simulated by GCMC molecular model (Figure 5.19 -5.20). The adsorption data are reported in terms of excess isotherms using the reference value of 0.47 cm³/g for the specific skeletal volume (V_s) of MIL-53p(Al); the reference state for the GCMC excess isotherms is $V_p = 0.56$ cm³/g.

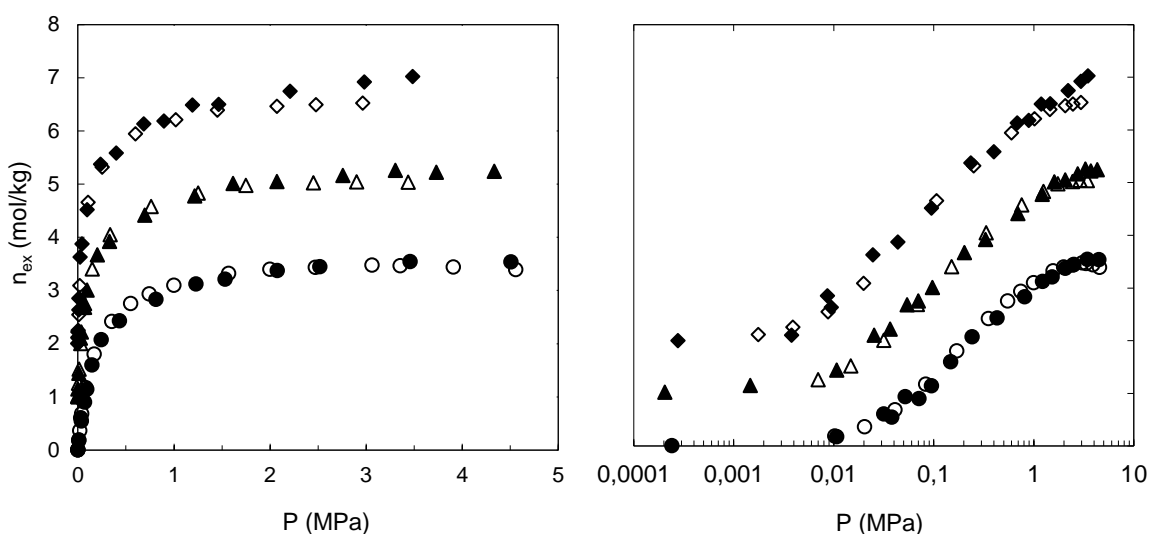


Figure 5.19. Comparison of excess adsorption isotherms of ethane in MIL-53p(Al): gravimetry (solid symbols) and simulation (open symbols). The rhombs, triangles and circles are corresponds to the 303K, 323K and 353K respectively. The reference state corrections used are $v_p = 0.56$ cm³/g and $v_s = 0.47$ cm³/g. For clarity, the adsorption data at 323 K and 303 K are displaced by 1 mol/kg and 2 mol/kg, respectively.

There are different tendencies between our GCMC predictions and the experimental adsorption data obtained. For the ethane adsorption at 303K and 323 K at pressures below ~2 MPa, the GCMC model predicts the experimental data with high accuracy. At pressures above 2 MPa, the GCMC simulation data slightly differ from the experimental ones. While for the 353 K for the ethane adsorption different profiles are observed. The GCMC simulation points are over the experimental values in the pressure range of ~0.02-0.5 MPa. That happens due to the fact that our simulation model is built for the adsorption process into large pore form of MIL-53(Al), thus cannot modeled the adsorption profile in the narrow pore form of MIL-53(Al). In accordance with the results discussed above the breathing magnitude of MIL-53(Al) transformation becomes more evident for the ethane adsorption at 353 K and influences the adsorption process, which is evident from experimental adsorption profile and cannot be seen from the simulated one. However, it should be noted that agreement between GCMC predictions and experimental data is good enough to obviate the need for re-parameterization of the cross-terms of the LJ solid–fluid interaction potential.

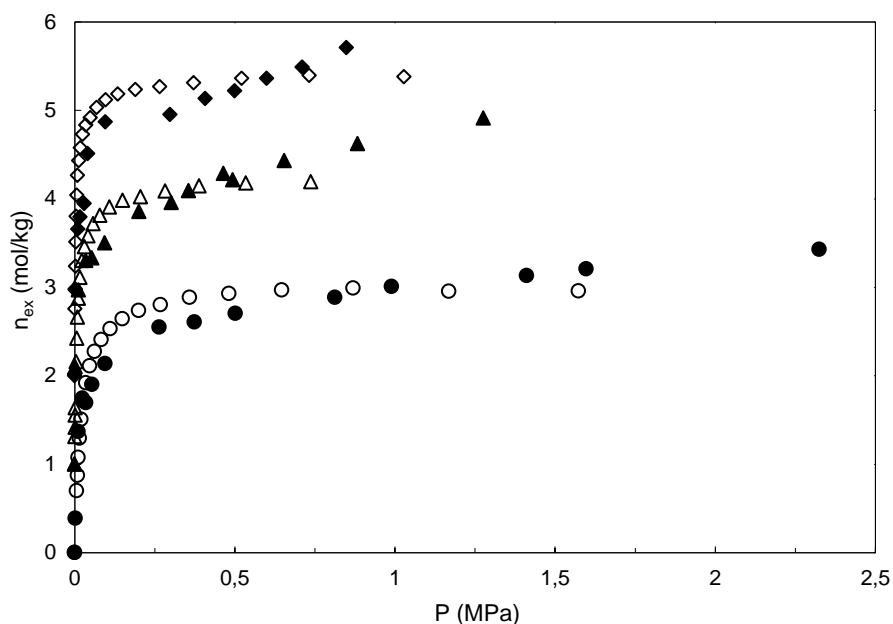


Figure 5.20. Comparison of excess adsorption isotherms of propane in MIL-53p(AI): gravimetry (solid symbols) and simulation (open symbols). The rhombs, triangles and circles correspond to the 303K, 323K and 353K respectively. The reference state corrections used are $v_p = 0.56 \text{ cm}^3/\text{g}$ and $v_s = 0.47 \text{ cm}^3/\text{g}$. For clarity, the adsorption data at 323 K and 303 K are displaced by 1 mol/kg and 2 mol/kg, respectively.

The differences between experimental and simulation data are more pronounced for the propane and butane adsorption. There is data presented for propane only (Fig. 5.20), as far as for the butane adsorption, the simulation does not fit the experimental profile.

The reason for such a deviation is breathing phenomena observed for C₃ and C₄ adsorption on MIL-53(AI). Furthermore, the tendency of deviation between experimental and simulated adsorption profiles with temperature and increase of carbon chain follows the tendency described by diagram 5.1 on the temperature and chain size effects on “breathing” phenomena in MIL-53(AI) upon C₁-C₄ adsorption. Namely, with increase of the temperature and chain lengths the magnitude of breathing increases, and thus deviation between experimental and simulation profiles becomes to be more pronounced.

The SIPS and TOTH models

The experimental adsorption data were fitted with the Sips and Toth semi-empirical isotherm models (Table 5.3., Fig. 5.21-5.23.).

As observed, the models derived from the two global fittings of the Sips and Toth are in very good agreement with the experimental data; the coefficient r^2 is higher than 0.998 in all cases.

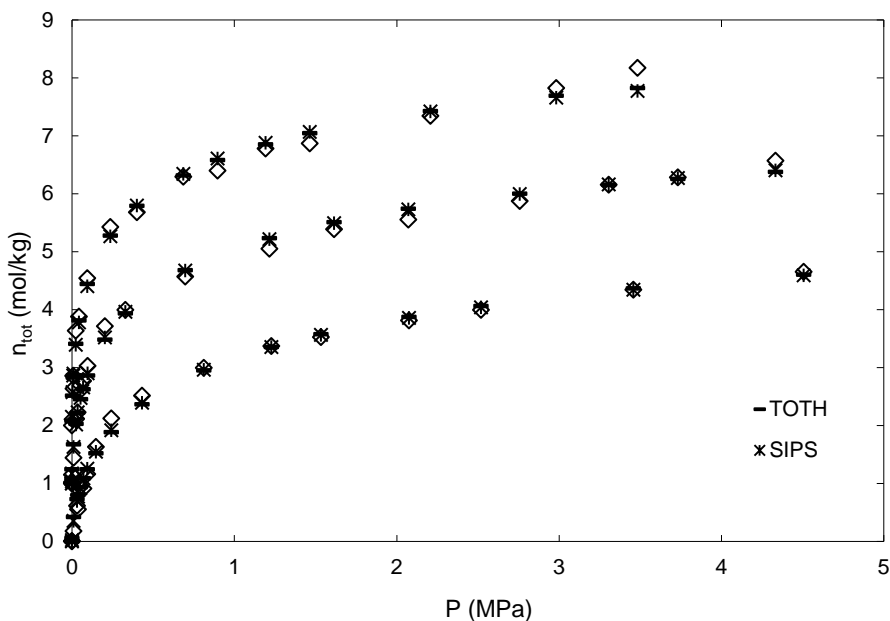


Figure 5.21. Global fitting of the experimental ethane adsorption data by the Sips and Toth isotherm models with the η and t is allowed to vary with temperature. The fitted parameters are listed in Table 5.3. Open symbols represent experimental data, the stars and bars are the Sips and Toth isotherm models. For clarity, the fittings data at 323 K and 303 K are displaced by 1 mol/kg and 2 mol/kg, respectively. The global average relative error (ARE) is 8.7% and 6.8% for 53 experimental data points.

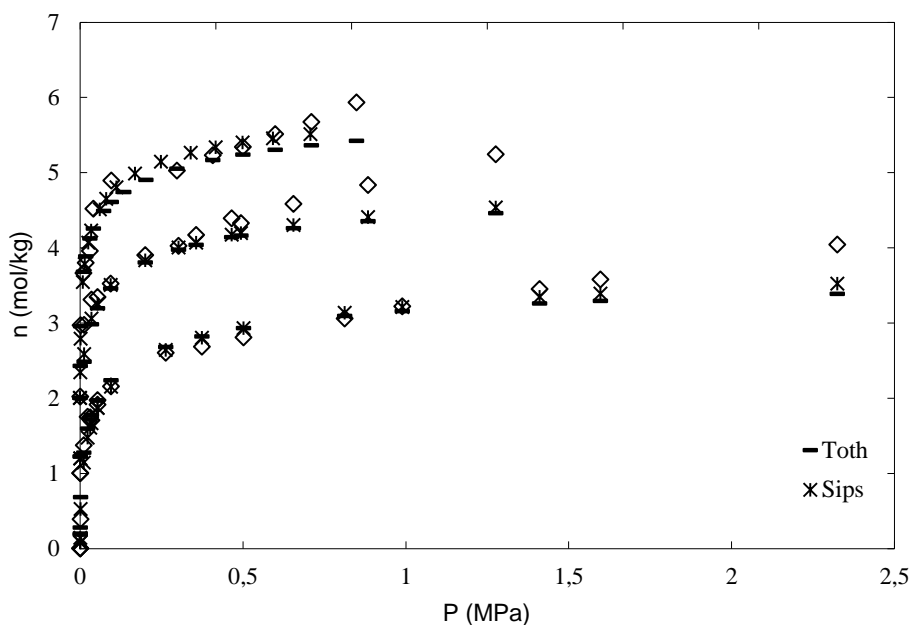


Figure 5.22. Global fitting of the experimental propane adsorption data by the Sips and Toth isotherm models with the η and t is allowed to vary with temperature. The fitted parameters are listed in Table 5.3. Open symbols represent experimental data, the stars and bars are the Sips and Toth isotherm models. For clarity, the fittings data at 323 K and 303 K are displaced by 1 mol/kg and 2 mol/kg, respectively. The global average relative error (ARE) is 7.5% and 6.4% for 48 experimental data points.

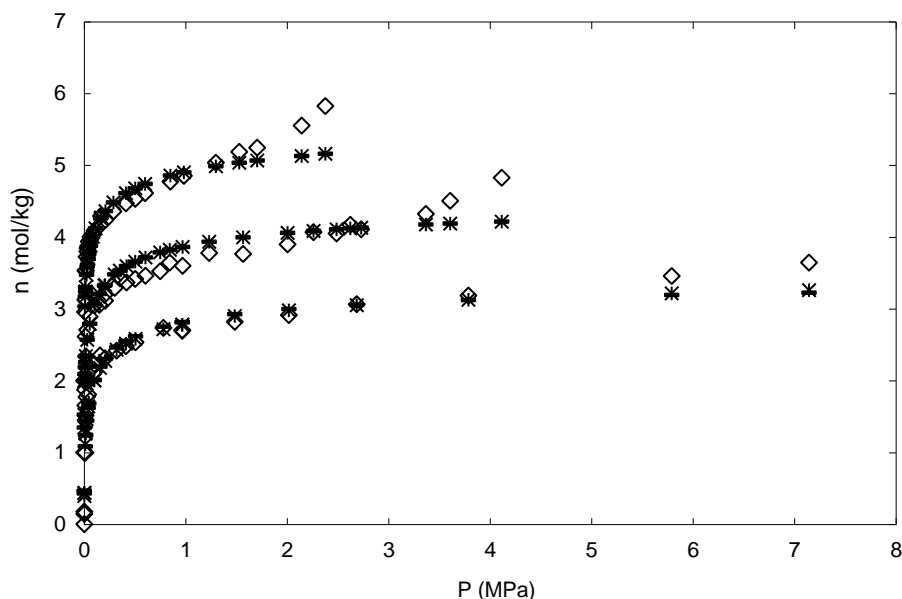


Figure 5.23. Global fitting of the experimental butane adsorption data by the Sips and Toth isotherm models with the η and t s allowed to vary with temperature. The fitted parameters are listed in Table 5.2. Open symbols represent experimental data, the stars and bars are the Sips and Toth isotherm models. For clarity, the fittings data at 323 K and 303 K are displaced by 1 mol/kg and 2 mol/kg, respectively. The global average relative error (ARE) is 7.5% and 6.4% for 48 experimental data points.

According to our previous experience of using Sips and Toth isotherms model to the methane adsorption it was shown that models fit better the experimental data when parameters η and t are temperature depending. Thus, the experimental data of C₂-C₄ adsorption were fitted by the Sips and Toth models in which parameter η and t is allowed to vary with the temperature.

The goodness of the fittings were assessed using standard fitting statistics (Table 5.3): standard deviation of measurements, determination coefficient (r^2), regression sum of squares (RSS) and average relative error (ARE) in percentage are given.

Table 5.3 Parameters obtained from the data fitting for the C₁-C₄ experimental adsorption with the Sips and Toth models. In every case $r^2 > 0.998$.

Parameter	SIPS	TOTH	SIPS	TOTH	SIPS	TOTH	SIPS	TOTH
	CH ₄		C ₂ H ₆		C ₃ H ₈		C ₄ H ₁₀	
T ₀ (K)	303 K							
n _s (mol/kg)	8.3	10.1	7.5	9.5	4.3	5.2	3.9	4.3
T ₀ (K)	323 K							
n _s (mol/kg)	7.9	9.4	7.3	9.2	4.1	5.0	3.8	4.2
T ₀ (K)	353 K							
n _s (mol/kg)	7.6	8.9	7.0	8.8	3.9	4.8	3.6	4.0
b ₀ (bar ⁻¹)	0.05	0.10	0.25	6.4	1.2	6.9	1.4	7.2
α	0.09	0.11	0.19	0.15	0.15	0.54	0.29	0.09
η_0 or t_0	1.2	0.6	1.9	0.3	2.1	0.25	2.4	0.3
ARE (%)	8.6	8.7	8.7	6.8	7.5	6.4	8.5	8.3

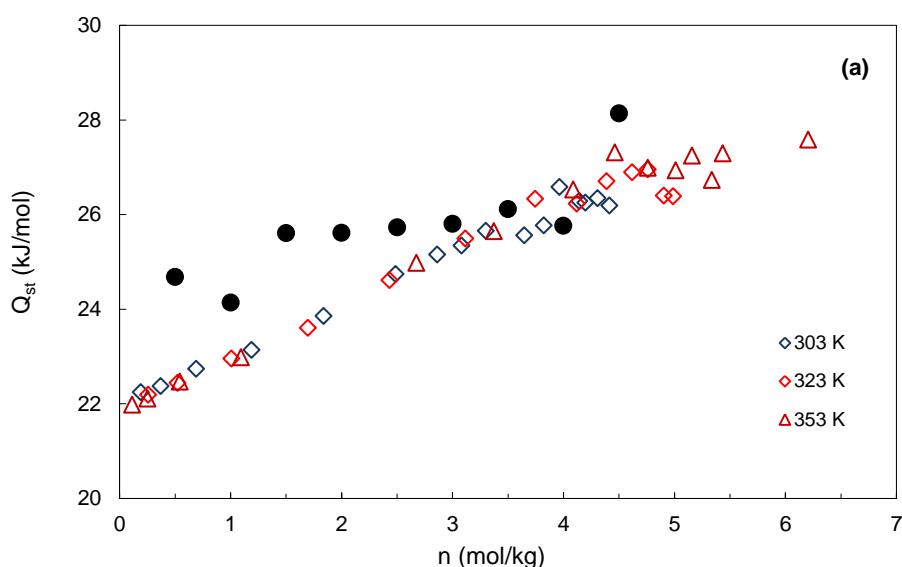
From the analysis of the data obtained it is evident that the adsorption capacity (n_s) decreases with the temperature for all studied gases and decreases with increase of the alkane chain (Table 5.3).

The Isosteric Heat

The isosteric heat (or differential enthalpy) of adsorption, Q_{st} , is the amount of heat released when an infinitesimal number of molecules is transferred at constant pressure from the bulk gas phase to the adsorbed phase. The isosteric heat of adsorption, Q_{st} was estimated both as derived by GCMC molecular simulation using statistical mechanical considerations and from the adsorption isotherms obtained experimentally using the integrated form of the Clapeyron equation; and the Sips and the Toth isotherm models, the values are presented in Table 5.4.

Figures 5.24a, 5.25a and 5.26a show a plot of the isosteric heat of adsorption as a function of the amount adsorbed. Values of Q_{st} presented in these Figures are the comparison of the isosteric heat of adsorption calculated using GCMC simulation, which is depicted as open symbols and values obtained by linear isosteric plots of $\ln p$ against $1/T$ at different loadings and Q_{st} using Clapeyron equation, depicted as solid symbols (isosteres are presented in the Figure 5.24b, 5.25b and 5.26b).

Figures 5.27, 5.28 and 5.29 represent the isosteric heat of adsorption obtained by Sips and Toth isotherms model. The right side of the graph represents the data obtained by Sips model, left one the data obtained by applying Toth model. Top of the graph represents plots of Q_{st} against pressure and the bottom against the fractional loading. One can distinguish that the values of Q_{st} calculated from the isosteric plots are in fairly good agreement with the GCMC results and data obtained by Sips and Toth models but the trend with loading goes against the trends of our molecular simulation data and of the values of Q_{st} derived from the slope of the linear fitting of the experimental isosteres.



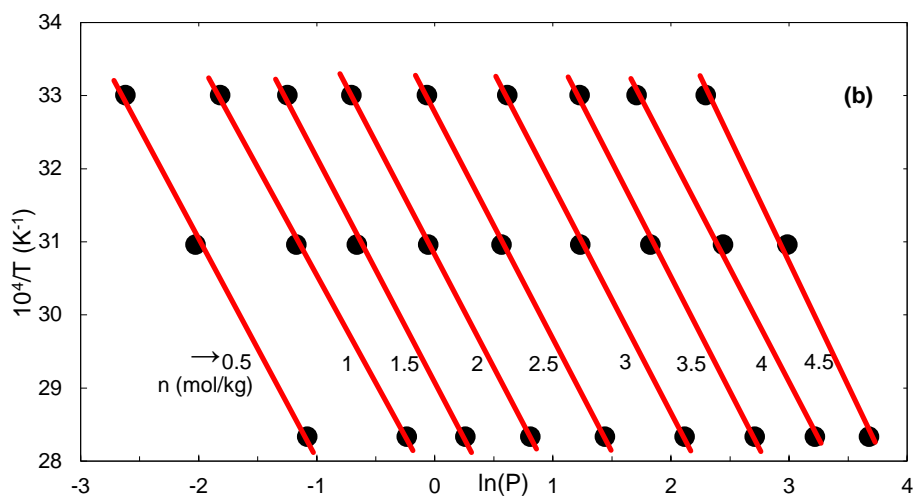


Figure 5.24. (a) Isosteric heat as a function of loading and (b) adsorption isotherms for the C₂H₆/MIL-53p(Al) system at 303–353 K. The open symbols in the top plot are values of Q_{st} obtained from the GCMC simulations by use of the standard fluctuation formula (Eq4.27), whereas the Q_{st} values represented by the closed circles were calculated from the slope of the linear fitting (lines in bottom graphic) of the isosteric data (closed circles in bottom graph) derived from the experimental adsorption isotherms.

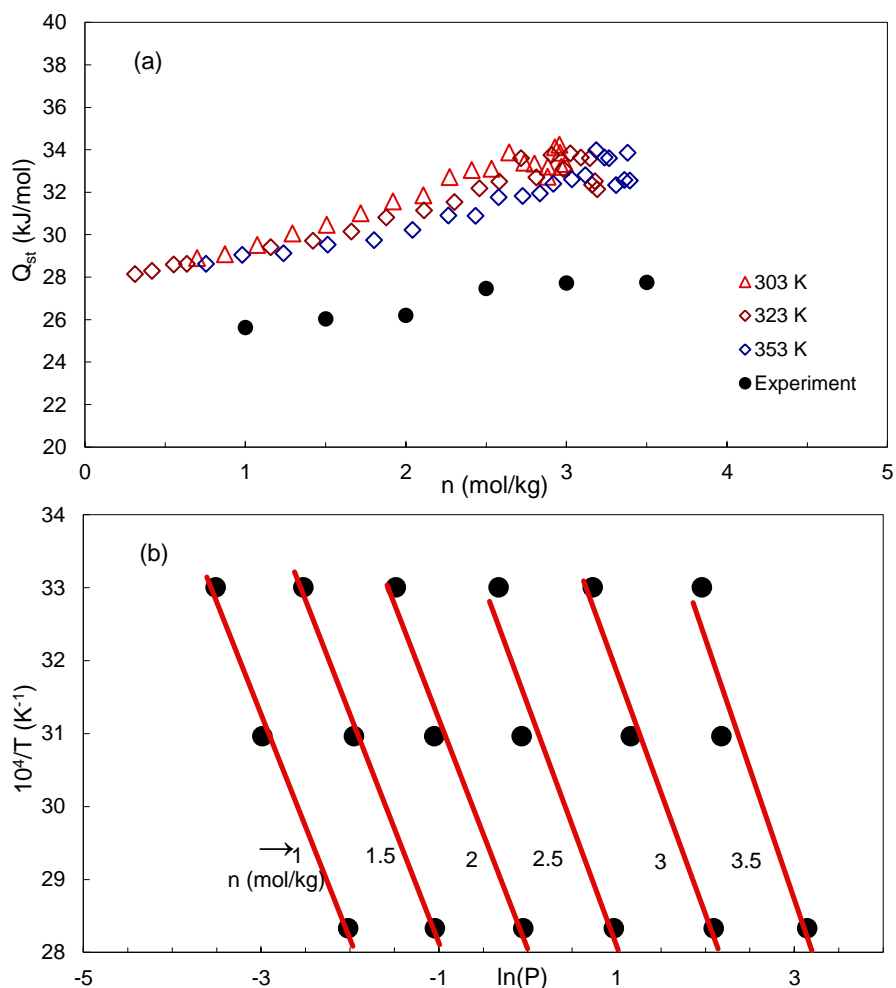


Figure 5.25. (a) Isosteric heat as a function of loading and (b) adsorption isotherms for the C₃H₈/MIL-53p(Al) system at 303–353 K. The open symbols in the top plot are values of Q_{st} obtained from the GCMC simulations, the Q_{st} values represented by the solid circles were calculated from the slope of the linear fitting of the isosteric data (closed circles in bottom graph) derived from the experimental adsorption isotherms.

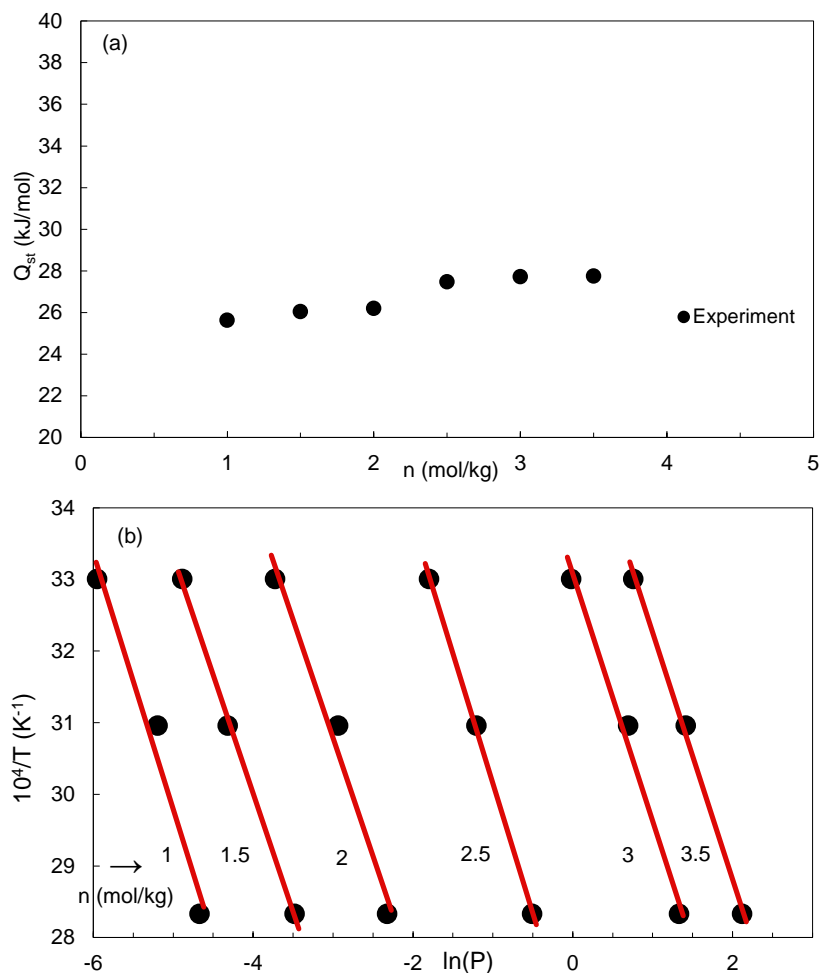


Figure 5.26 (a). Isosteric heat as a function of loading and (b) adsorption isotherms for the C₄H₁₀/MIL-53p(Al) system at 303–353 K. Q_{st} values represented by the solid circles were calculated from the slope of the linear fitting of the isosteric data (closed circles in bottom graph) derived from the experimental adsorption isotherms.

Table 5.4 Isosteric Heat of adsorption determined by GCMC simulation method, integrated form of Clapeyron equation and Sips, Toth isotherms models.

Q_{st} kJ/mol	CH ₄	C ₂ H ₆	C ₃ H ₈	C ₄ H ₁₀
	303 K			
SIPS	19,7	24,3	24,8	26,5
TOTH	19,9	25,9	53,5	28,6
Simulation	16,3	25,5	32,2	-
	323 K			
SIPS	19,4	24,3	25,0	26,4
TOTH	19,5	26,3	53,7	28,2
Simulation	16,0	25,2	31,4	-
	353 K			
SIPS	19,6	24,8	25,0	26,4
TOTH	19,6	27,0	54,0	28,3
Simulation	15,9	24,9	31,6	-
	Temperature dependent			
Clapeyron	16,2	25,8	26,8	28,7

For practical usage of the adsorbents for natural gas storage it should be taken into account

that adsorption is a process which evolves heat.

In general, all the values calculated for heat of the adsorption for all of the gases are in a range of ca. 20-32 kJ/mol (Table 5.4). Overall the shown trend for the Q_{st} values is consistent with a view that at the start of fill cycle there is already a layer of adsorbed gas on the adsorbent. Thus, adsorption at these initial sites tends to produce almost equal and the highest heat of adsorption for all studied gases on MIL-53 (Al).

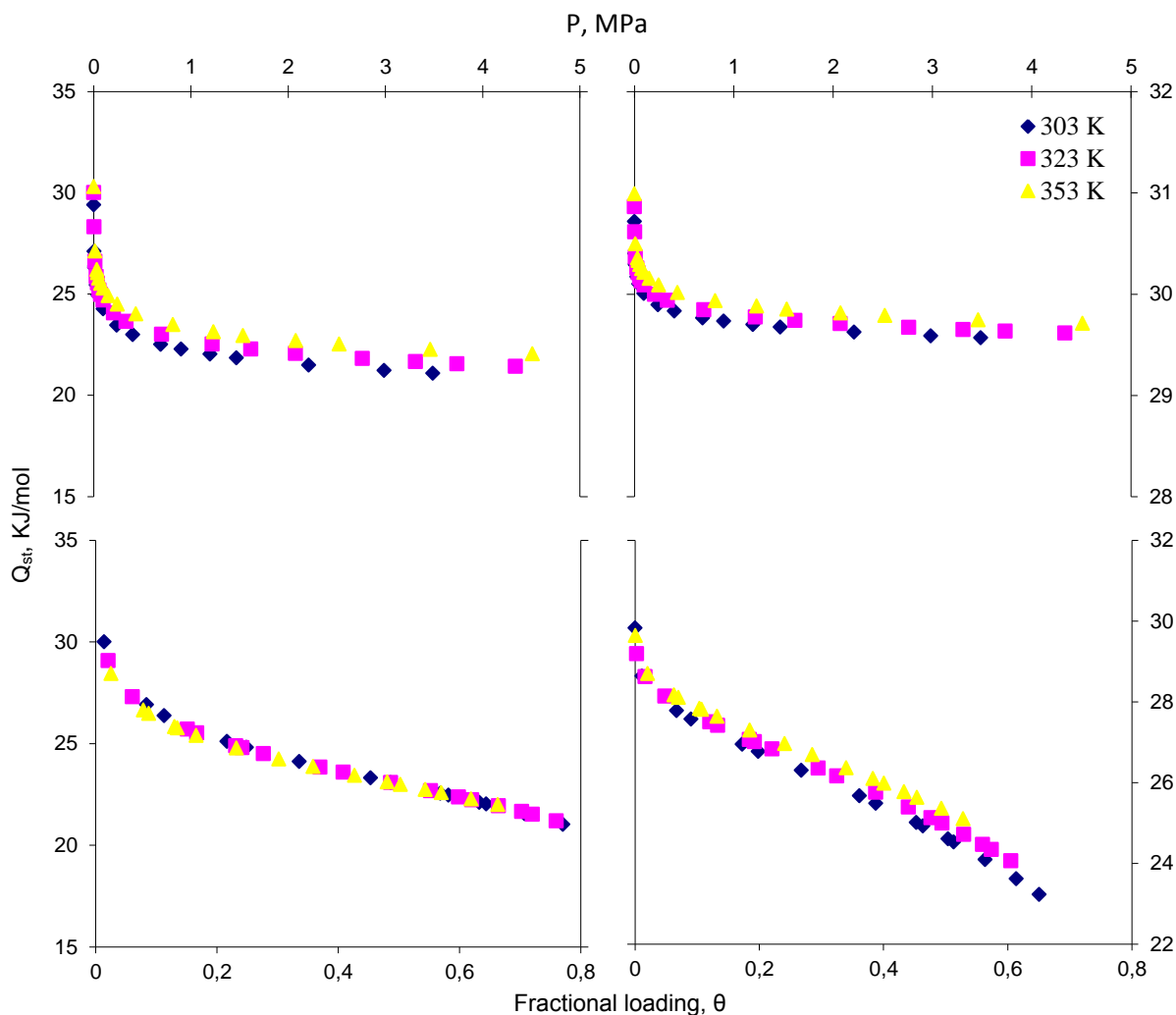


Figure 5.27. Isosteric heats of adsorption of ethane derived from the Sips and Toth isotherm models plotted against fractional loading, θ (or pressure, P). Each symbol corresponds to the value of Q_{st} calculated for the pressure and temperature of a point on the experimental adsorption isotherms. The left-hand plots are derived from the Sips isotherm model; the right-hand plots are derived from the Toth isotherm model. The η and t are temperature dependent.

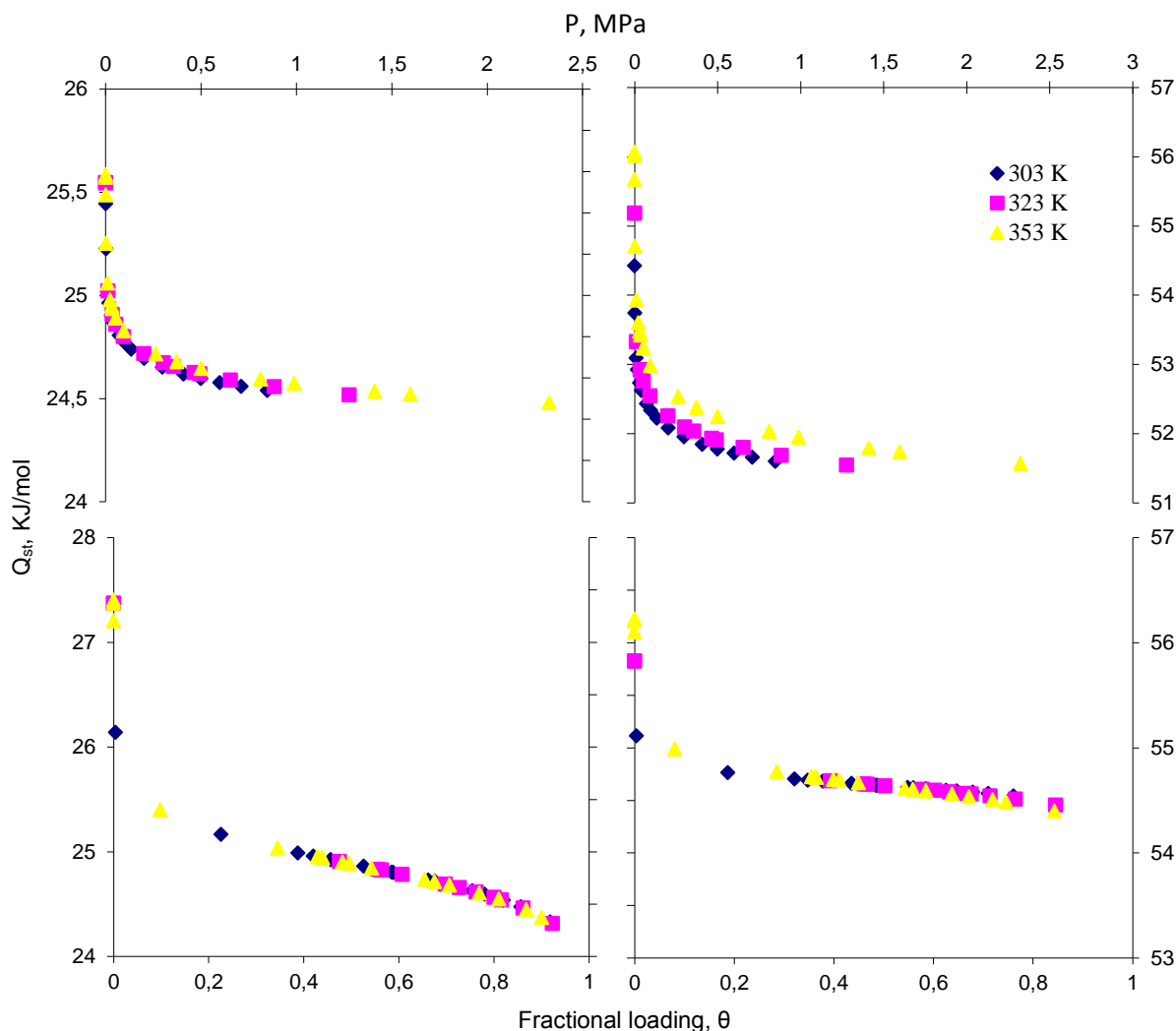


Figure 5.28. Isosteric heats of adsorption of propane derived from the Sips and Toth isotherm models plotted against fractional loading, θ (or pressure, P). Each symbol corresponds to the value of Q_{st} calculated for the pressure and temperature of a point on the experimental adsorption isotherms. The left-hand plots are derived from the Sips isotherm model; the right-hand plots are derived from the Toth isotherm model. The η and t are temperature dependent.

According to the data presented in Table 5.4 for the methane and ethane the isosteric heat values obtained by four different methods are in a good agreement and varies within ~ 2 kJ/mol (around 10%). The values of the Q_{st} obtained by Sips and integrated form of the Clapeyron equation for the propane adsorption is in a good agreement 25.0 and 26.8 kJ/mol respectively. However, deviation is observed for the simulated values of isosteric heat propane adsorption, they are 6-7 kJ/mol higher than experimental values calculated by Sips method and by using the integrated form of the Clapeyron equation. Most probably the deviation occurs due to the limit of chosen molecular simulation model. Moreover, it should be noted that Q_{st} obtained by the Toth model for propane adsorption is about of 54.0 kJ/mol, which is disproportionately high and cannot be explained. Regarding the butane adsorption the values of Q_{st} obtained by Sips, Toth models and Clapeyron equation are in a good agreement, the Q_{st} values are of 26.5, 28.5 and 28.7 kJ/mol, respectively.

It is also known from literature that the double transition is dictated solely by the affinity for the large pore form with a proposed critical adsorption enthalpy of ~20 kJ/mol [22].

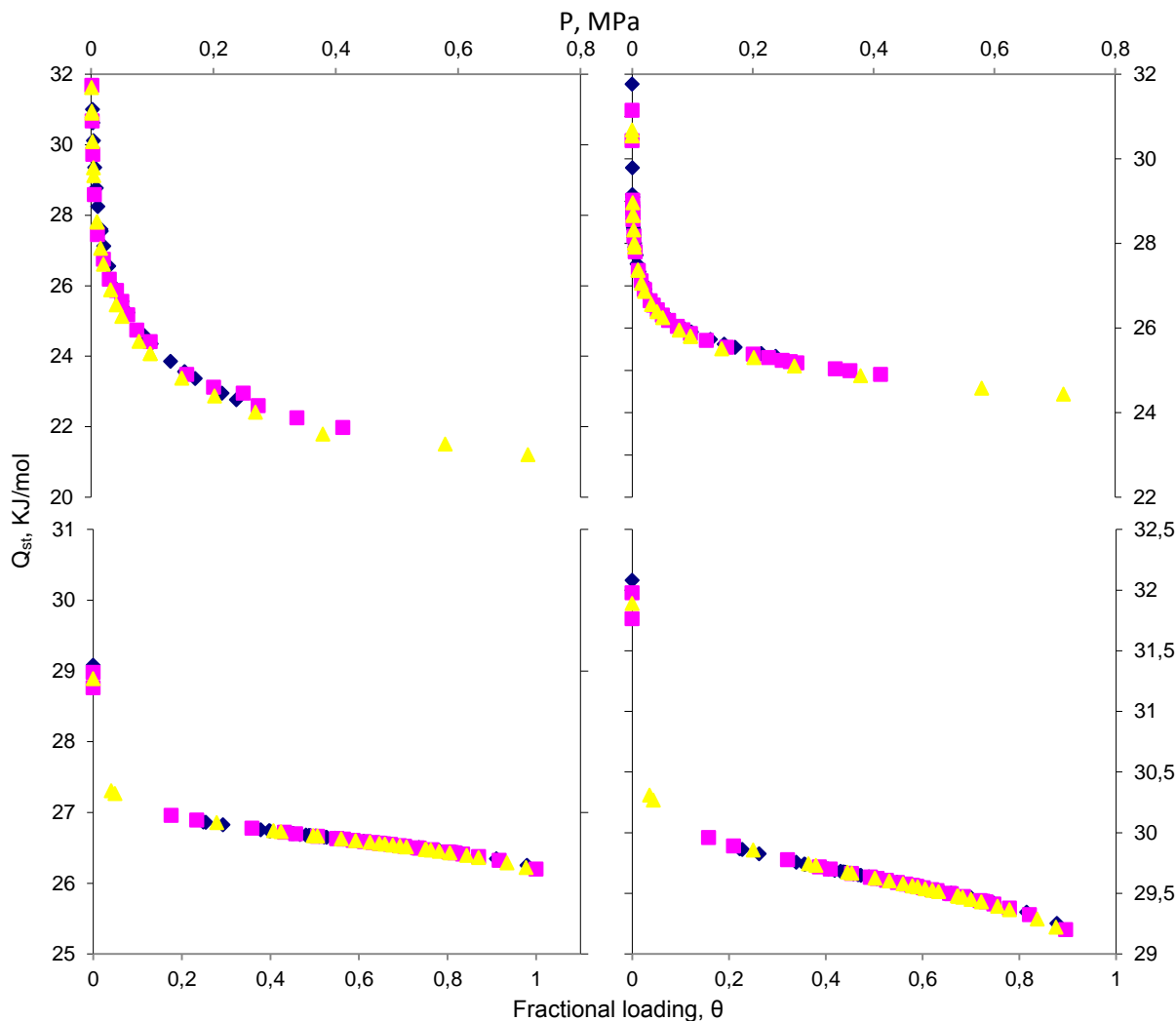


Figure 5.29. Isosteric heats of adsorption derived from the Sips and Toth isotherm models plotted against fractional loading, θ (or pressure, P). Each symbol corresponds to the value of Q_{st} calculated for the pressure and temperature of a point on the experimental adsorption isotherms. The left-hand plots are derived from the Sips isotherm model; the right-hand plots are derived from the Toth isotherm model. The η and t are temperature dependent.

It is worth noting that the overall trend of the isosteric heat of the adsorption for the C₁-C₄ gases adsorption is increasing with the increasing of the chain length. From C₁ to C₂ gases increase in Q_{st} is about 5-8 kJ/mol, and for C₂-C₄ the increase is by 1-2 kJ/mol.

5.5.3. Evaluation of the MIL 53 (Al) storage capacity towards C₂-C₄ gases

In this section, we provide data on usage of the general thermodynamic framework for the net adsorption reference state for an estimation of the storage capacity of MIL-53 (Al) towards C₁-C₄ gases under investigated conditions.

Because net adsorption is measured with a reference based on an empty container (with no solid), it is a direct measure of the additional amount that is stored in the container as a result of adsorption under identical conditions. Net adsorption is thus a direct measure of the density enhancement for storage applications.

As it was discussed above, the net adsorption is concave function with respect to the pressure axis and its maximum value occurs at a pressure that increases with temperature. Decrease with net adsorption value indicates that the amount stored in the container is actually lower than what could be stored in the same container when there is no adsorbent at the same temperature and pressure. This does not indicate the decrease/absence of the adsorption but simply indicates that additional amount present in the container due to adsorption is less than the amount of gas that would be in the space occupied by the solid. For example, if the net adsorption goes to zero at certain pressure, it indicates that there is no advantage in usage of the adsorbent for natural gas storage above this pressure; Thus, it means, that above this pressure, storing the compressed gas in its bulk phase (without the adsorbent in the container) results in a larger storage capacity; while the maximum of the net adsorption indicates the maximal additional storage values.

In practice, the methane and ethane are stored at higher pressure of 25 MPa (so called Compressed Natural Gas (CNG)) and the propane and butane at lower pressure of 1.5-2.0 MPa (so called Liquid Petroleum Gases (LPG)). In current work the adsorption of C₁, C₂ was studied up to 5 MPa, and it was up to 1 MPa for the C₃ and C₄ gases. The net adsorption data were analyzed together with the data on bulk gases compressed under identical conditions which, allows us to estimate the total storage capacity, and gives us a possibility for rough estimation of the MIL 53 role in storage capacity enhancement above critical pressure in the studied systems. The data are presented in Figures 5.32-5.34 and in Table 5.5. For the adsorbent/adsorbate systems, the MIL-53(Al) loadings were fixed at ca. 25-35 vol% in order to disregard the heat release (the heat of the adsorption) influence on the initial experimental conditions [26].

Figure 5.30 (a, b and c) shows the total storage capacity for methane under pressure up to 5 MPa for three different temperatures. For the methane the maximum of net adsorption occurs at pressure close to 4 MPa and then it starts to decrease with pressure increasing. However, the maximum of the total storage capacity is observed at highest investigated pressure (~5 MPa), because of the high bulk density of stored methane. The same situation is observed for the ethane storage (Figure 5.31). The maximum net adsorption is observed at 2 MPa, but highest total storage capacity is at maximal investigated pressure. A bit different situation is observed for propane and butane (Figures 5.32 and 5.33). Since our experimental adsorption isotherms is limited by the critical pressure above which gas becomes liquid, we cannot be sure that the maximum value of

the net adsorption observed at highest values of the applied pressure is the real net adsorption maximum. Moreover, under investigated conditions the compression of butane and propane is negligible. Consequently, the total storage capacity of butane and propane under investigated conditions is almost equal to its net adsorptions.

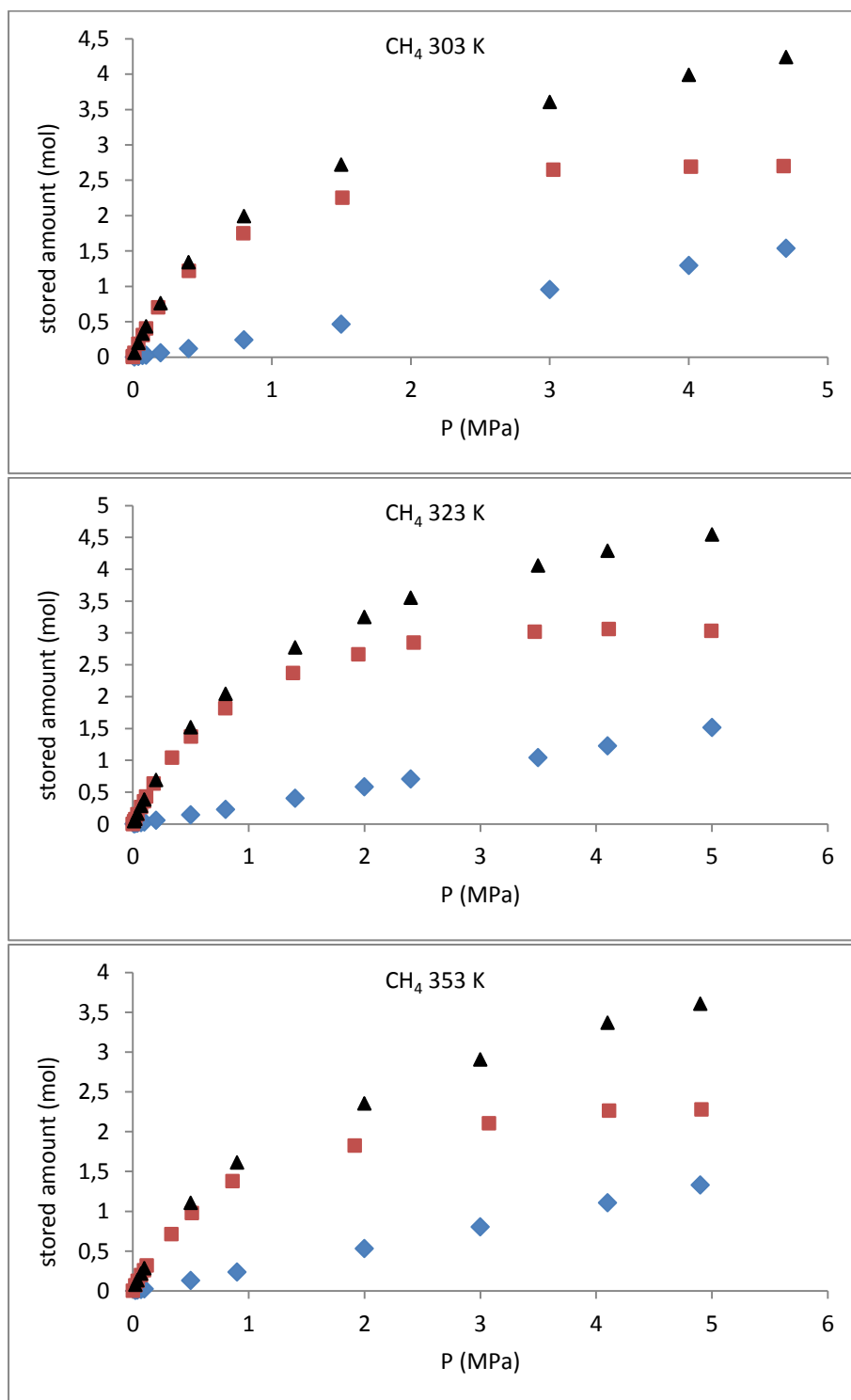


Fig. 5.30. Total storage capacity (black), net adsorption (red) and bulk gas compressed (blue) under identical conditions for the CH₄ adsorption on MIL-53(AI) at 303, 323 and 353 K

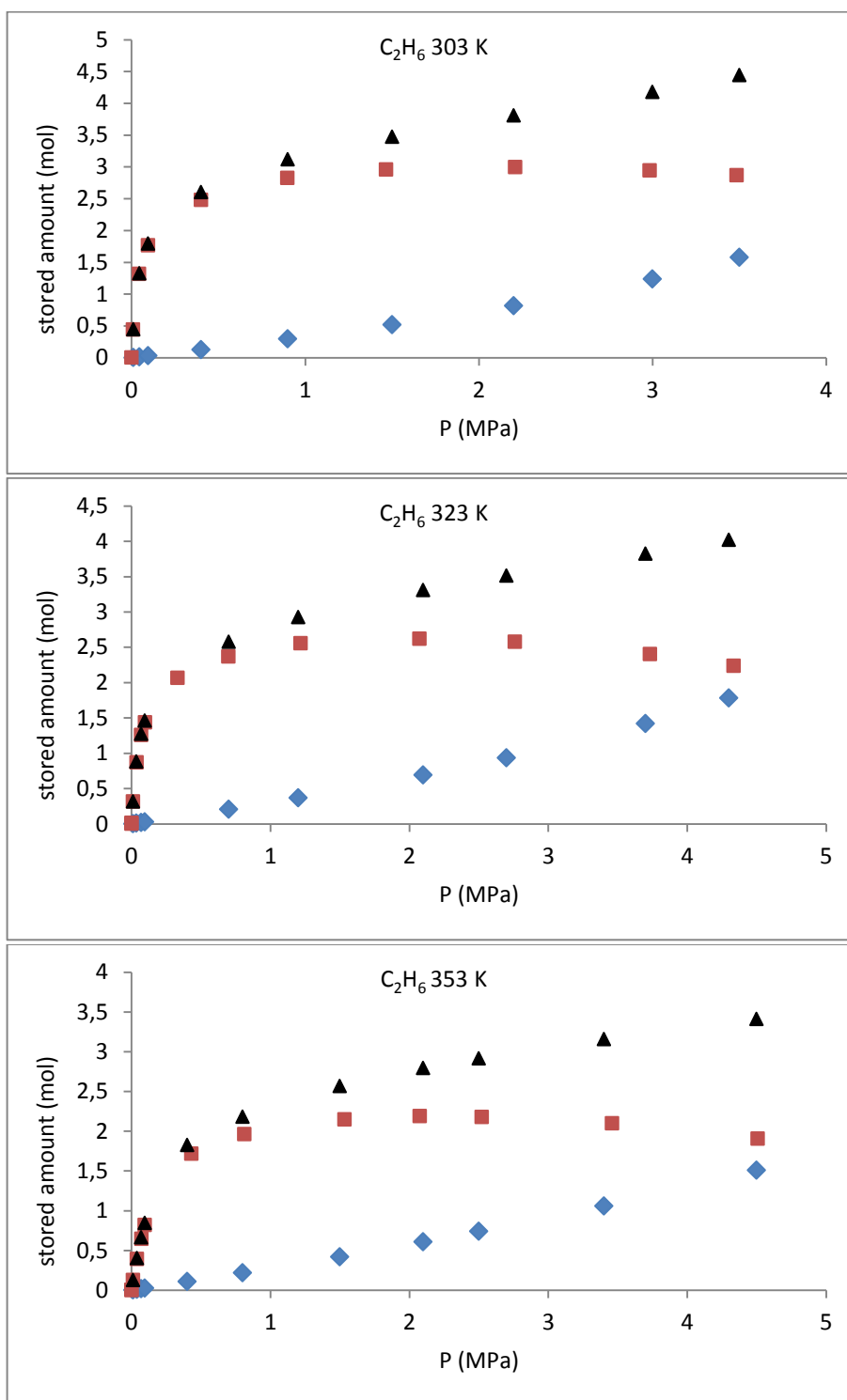


Fig. 5.31. Total storage capacity (black), net adsorption (red) and bulk gas compressed (blue) under identical conditions for the C₂H₆ adsorption on MIL-53(Al) at 303, 323 and 353 K

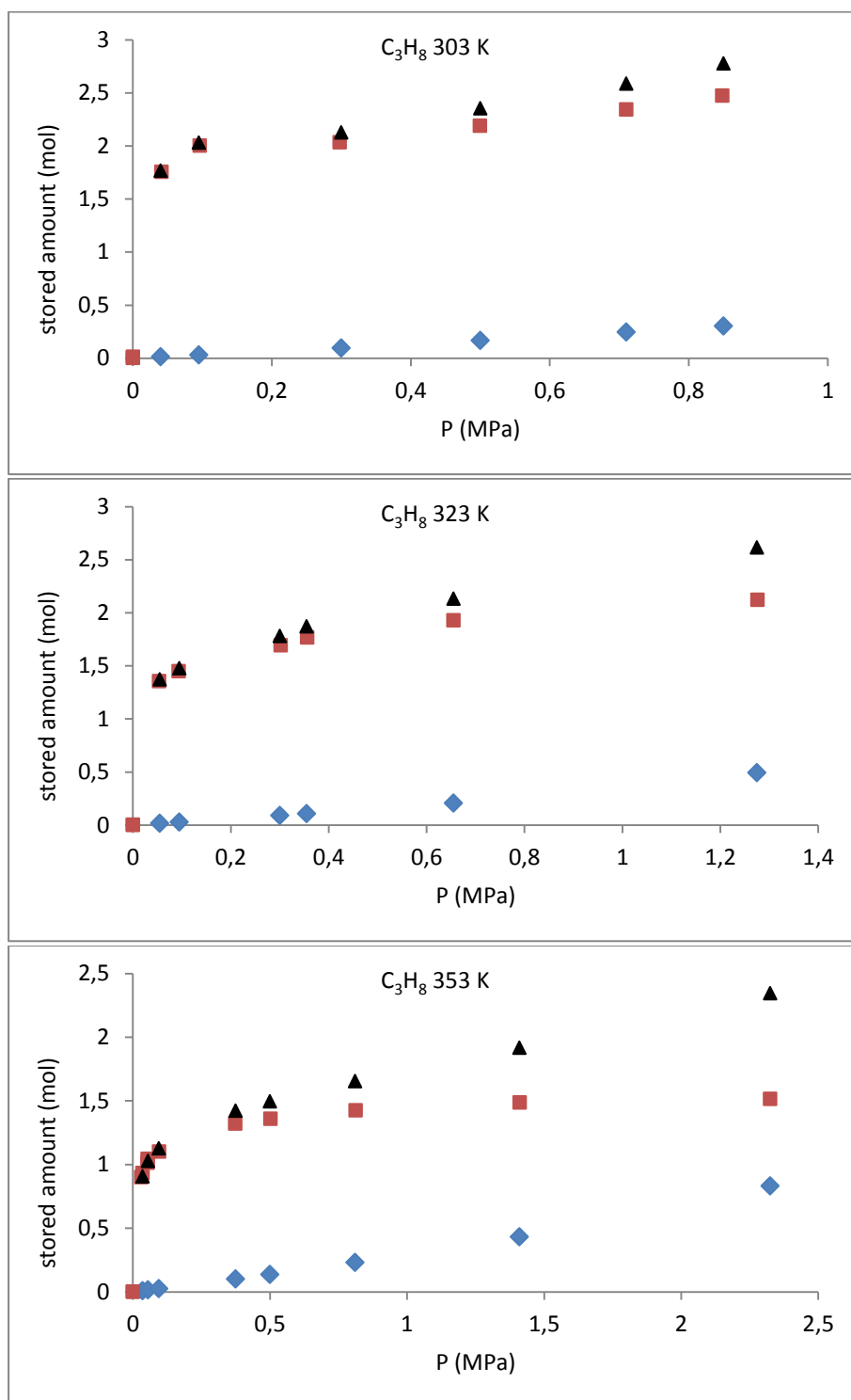


Fig. 5.32. Total storage capacity (black), net adsorption (red) and bulk gas compressed (blue) under identical conditions for the C₃H₈ adsorption on MIL-53(Al) at 303, 323 and 353 K

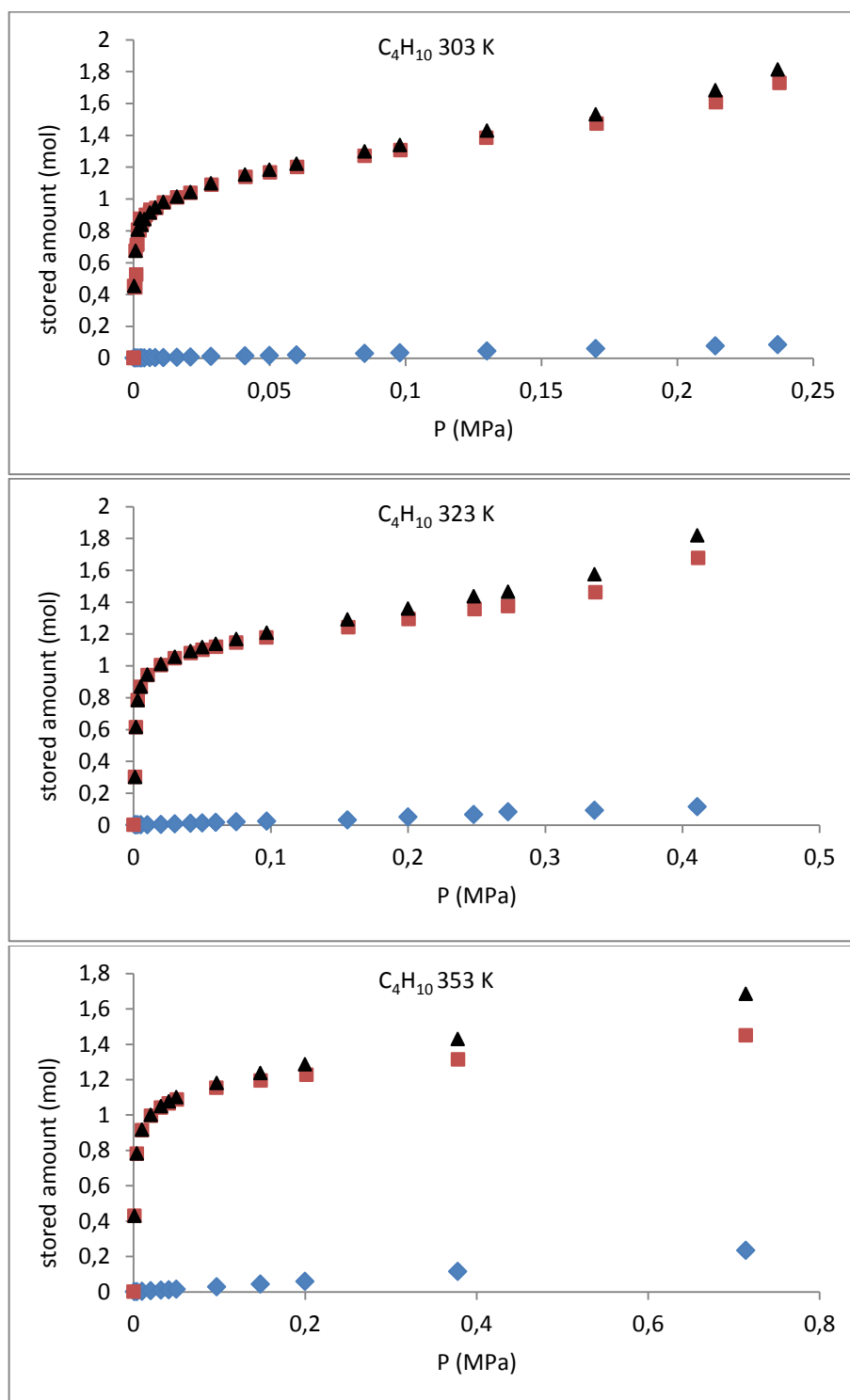


Fig. 5.33 Total storage capacity (black), net adsorption (red) and bulk gas compressed (blue) under identical conditions for the C₄H₁₀ adsorption on MIL-53(Al) at 303, 323 and 353 K

However, to be more realistic we made an attempt to estimate the storage capacity of the MIL-53(Al) for the propane and butane gases under critical conditions. Taking into consideration the following:

- knowing that under critical pressures (for propane they are 1.07, 1.7 and 3.1 MPa, and for butane they are 0.28, 0.49 and 1 MPa at 303, 323 and 353 K, respectively) the density of the liquid gases is almost constant with pressure;
- assuming that maximum of the obtained net adsorption (at pressures for the propane of 0.85, 1.28 and 2.3 MPa, and for the butane of 0.28, 0.4 and 0.71 MPa at 303, 323 and 353 K, respectively) will be the same at critical pressure,

we calculated the additional storage amount provided by the MIL-53(AI) to the liquid propane and butane. The results are also presented in Table 5.5.

Thus, it can be concluded, that for the C₁-C₂ gases on the MIL-53(AI), the highest enhancement of 60-40% above simple gas compression is found at 4.9 and 3.7 MPa, respectively; and for the C₃-C₄ gases, the highest enhancement of the storage capacity due to the adsorption is of 27-20%.

Table 5.5. Storage capacity of propane and butane under critical pressure.

	P _{crit} MPa	Density g/cm ³	Stored amount, mol	n _{net} , mol	Additional storage amount by n _{net} , %	MIL-53(AI) loading, vol%
Propane						
303 K	1,08	0,48	8,41	2,47	29,4	35
323 K	1,71	0,45	7,79	2,12	27,2	
353 K	3,12	0,37	6,49	1,51	23,3	
Butane						
303 K	0,28	0,57	8,14	1,73	21,2	25
323 K	0,49	0,54	7,79	1,68	21,5	
353 K	1,01	0,50	7,19	1,45	20,1	

Practical Benefits for Gas Storage

On January 31, 2007, the European Commission proposed new standards for transport fuels to reduce full life cycle emissions by up to 10 percent between 2011 and 2020. The proposal aims to encourage the development of low-carbon fuels and biofuels, considering reductions in greenhouse gas emissions caused by the production, transport and use of the supplier's fuels.

A low-carbon fuel standard (LCFS) is a rule enacted to reduce carbon intensity in transportation fuels as compared to conventional petroleum fuels, such as gasoline and diesel. The main purpose of a low-carbon fuel standard is to decrease carbon dioxide emissions associated to fuel-powered vehicles considering the entire life cycle ("well to wheels"), in order to reduce the carbon footprint of transportation.

A natural gas vehicle or NGV is an alternative fuel vehicle that uses the most common low-carbon fuels, such a compressed natural gas (CNG) or liquefied natural gas (LNG) as a cleaner alternative to other fossil fuels. Natural gas vehicles should not be confused with vehicles powered by propane (LPG), which is a fuel with a fundamentally different composition. LPG, also known as *autogas*, still a petroleum based gas, is denser as it is a liquid at room temperature, and thus far cheaper tanks (consumer) and fuel compressors (provider), thus it requires far less compression (20% of CNG cost).

Despite its advantages, the use of natural gas vehicles faces several limitations, including fuel storage and infrastructure available for delivery and distribution at fueling stations. For example, CNG must be stored in high pressure cylinders (3000psi to 3600psi operation pressure), and LNG must be stored in cryogenic cylinders (-260F to -200F). These cylinders take up more space than gasoline or diesel tanks that can be molded in intricate shapes to store more fuel and use less on-vehicle space. As with other alternative fuels, other barriers for widespread use of NGVs are natural gas distribution to and at fueling stations as well as the low number of CNG and LNG stations.

In this connection the Adsorbed Natural Gas (ANG) storage technology has some promising advantages over existing gas storage methods, such as

- Store a larger volume of natural gas in the same container, at the same pressure.
- Store the same volume of natural gas in the container at a lower pressure.
- Allows for using of different shapes of containers (not only cylinders)



Fig. 5.34. Non Cylindrical ANG and Cylindrical CNG, LNG, LPG tanks

Despite that, the principles of NG adsorption have been around for the decades; however no one had succeeded to develop commercially viable technology until now.

In this perspective, the accomplished research contributes to Adsorbed Natural Gas storage technology development.

It should be also noted, that gas delivery is very important and it is different from storage capacity aspect which should be taken into consideration when speaking about the ANG. A gas delivery parameter can be estimated for the adsorbent by the desorption run. Experimental desorption run is shown in the Figures 5.35-5.36 for butane at 323 and 353 K and confirm the high gas delivery efficiency of the MIL-53(AI) (as compared to the storage capacity of this material).

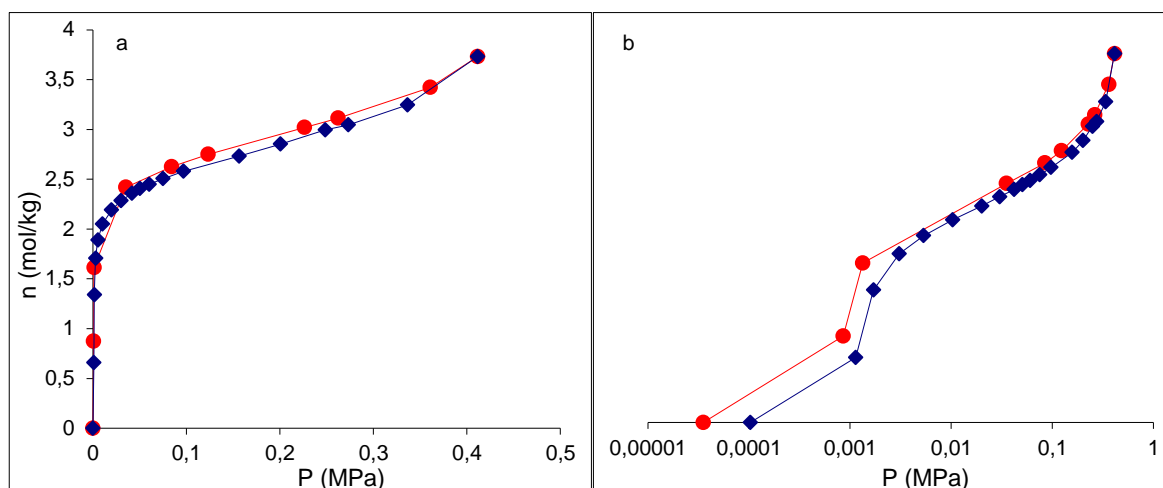


Figure 5.34 Adsorption (blue rhombs) and desorption (red circled) runs for butane in MIL-53(Al) at 323 K and presented a) in a standard form amount adsorbed (mol/kg) versus pressure. b) in semi-logarithmic scale.

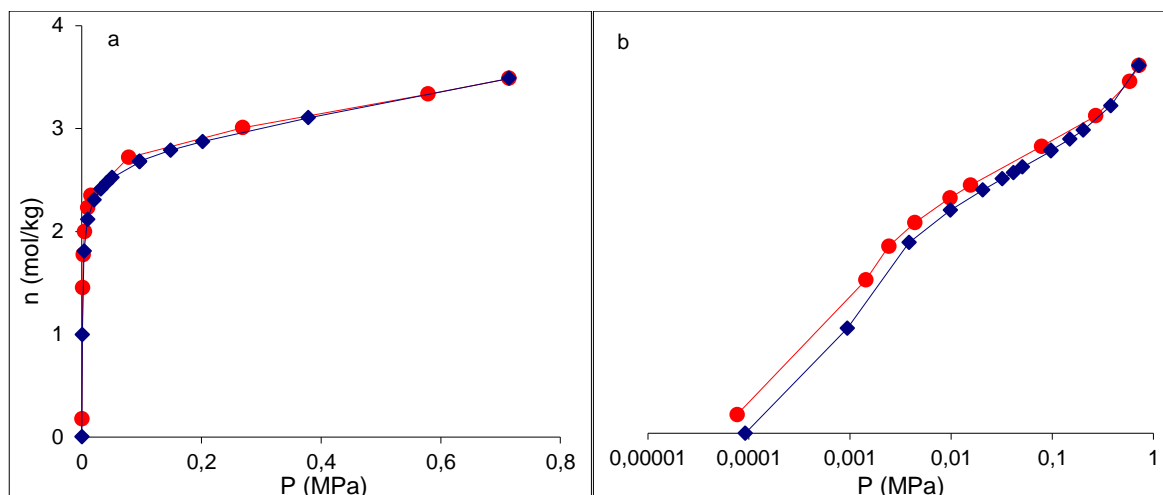


Figure 5.35 Adsorption (blue rhombs) and desorption (red circled) runs for butane in MIL-53(Al) at 323 K and presented a) in a standard form amount adsorbed (mol/kg) versus pressure. b) in semi-logarithmic scale.

5.4. CONCLUSION

It has been reported the experimental and simulated data on the adsorption equilibrium of C₂-C₄ light alkanes on the MIL-53(Al) over pressures range of ~0.01–5 MPa and temperatures of 303–353 K. The obtained data are given in comparison with the data discussed for CH₄ adsorption in Chapter 4. It has been confirmed that the adsorption of the light hydrocarbons on the MIL-53(Al) passed through more complex mechanism. Depending of the guest molecules, the MIL-53(Al) can switch between two structural transition (1p---np---1p forms) during the adsorption run for the C₂-C₄ gases. It was concluded that the effects founded, namely size (the alkyl chain length) and temperature influence on breathing phenomena of the MIL-53 (Al) are in agreement with a generic thermodynamic framework concept of the guest-induced structural transitions in flexible nanoporous materials according to the osmotic pseudo-ensemble approach and with a view that

the double transition is dictated solely by the affinity for the lp form with a proposed critical (threshold) adsorption enthalpy of ~20 kJ/mol.

For useful descriptions of the adsorption equilibrium data at various temperatures, the temperature-dependent form of the Sips and Toth equations were used. It was shown, that the adsorption capacity decrease with the temperature and decrease with increase of the alkane chain.

The isosteric heat of adsorption was estimated from statistical mechanical considerations, by applying the Sips and Toth models and integrated form of the Clapeyron equation. From the obtained data analysis, it was shown the trend for the Q_{st} values, which is consistent with a view that at the start of fill cycle there is initial layer of adsorbed gas on the adsorbent which produces almost equal and the highest heat of adsorption of ca. 25-30 kJ/mol for the C₂-C₄ gases on the MIL-53 (Al), while these values are slightly less than 20 kJ/mol for the methane adsorption.

Three reference states, the net, excess and absolute adsorption, were used to analyses the adsorption process of C₁-C₄ gases at three different temperatures. Without intending to add to the confusion, we believe that net adsorption is best suited by defining adsorption in micropores as the difference between the total amount of gas present in the container minus the amount that would be present if the adsorbent were completely absent.

The net adsorption parameters were analyzed together with data on bulk gases compressed under identical conditions, allowing estimation of the total storage capacity, and like that giving us a possibility for rough estimation of the MIL-53(Al) role in storage capacity enhancement in the studied systems. Gas delivery efficiency for the ANG method using MIL-53(Al) is also discussed, based on analysis of the experimental desorption runs for the studied gases. In this perspective, the research accomplished contributes to the Adsorbed Natural Gas storage technology development.

5.5. REFERENCES

- [1] R. W. Baker, *Membrane Technology and Applications*, John Wiley & Sons, New York, 2nd edition, **2004**.
- [2] R. W. Baker, *Ind. Eng. Chem. Res.*, **2002**, 41, 1393.
- [3] J. W. Jiang, S. I. Sandler, M. Schenk and B. Smit, *Phys. Rev. B: Condens. Matter Mater. Phys.*, **2005**, 72 (4), 045447.
- [4] Yufeng He, Jeong-Ho Yun, and Nigel A. Seaton *Langmuir*, **2004**, 20, 6668.
- [5] Shaheen A. Al-Muhtaseb, Fahmi A. Abu Al-Rub, and Mohamed Al Zarooni *J. Chem. Eng. Data* **2007**, 52, 60
- [6] J. F. A. Denayer, L. Devriese, S. Couck, J. Martens, R. Singh, P. A. Webley and G. V. Baron, *J. Phys. Chem. C*, **2008**, 112 (42), 16593.
- [7] Wen-Zhuo Li, Zi-Yang Liu, Yu-Liang Che and D. Zhang, *J. Colloid Interface Sci.*, **2007**, 312, 179.
- [8] Maji, T. K.; Kitgawa, S. *Pure Appl. Chem.* **2007**, 79 (12), 2155–2177.
- [9] Ferey, G. *Chem. Soc. Rev.* **2008**, 37 (1), 191–214.
- [10] Francois-Xavier Coudert, Anne Boutin, Marie Jeffroy, Caroline Mellot-Draznieks, and Alain H. Fuchs *ChemPhysChem* **2011**, 12, 247 – 258
- [11] Rowsell, J. L. C.; Yaghi, O. M. *Micr. Mes. Mat.* **2004**, 73 (1-2), 3–14.
- [12] Martin, M. G.; Siepmann, J. I. *J. Phys. Chem. B* **1998**, 102, 2569–2577.
- [13] Wick, C. D.; Martin, M. G.; J. I. Siepmann, J. I. *J. Phys. Chem. B* **2000**, 104, 8008–8016.
- [14] Chen, B.; Potoff, J. J.; Siepmann, J. I. *J. Phys. Chem. B* **2001**, 105, 3093–3104.

- [15] Stubbs, J. M.; Potoff, J. J.; Siepmann, J. I. *J. Phys. Chem. B* **2004**, *108*, 17596–17605.
- [16] Kamath, G.; Cao, F.; Potoff, J. J. *J. Phys. Chem. B* **2004**, *108*, 14130–14136.
- [17] N. Rosenbach Jr, A. Ghoufi, I. Deroche, P. L. Llewellyn, T. Devic, S. Bourrelly, C. Serre, G. Férey and G. Maurin *Phys. Chem. Chem. Phys.*, **2010**, *12*, 6428–6437
- [18] Barthelet, K.; Marrot, J.; Riou, D.; Férey, G. *Angew. Chem., Int. Ed.* **2002**, *41*, 281-284
- [19] Coudert, F.-X.; Mellot-Draznieks, C.; Fuchs, A. H.; Boutin, A. *J. Am. Chem. Soc.* **2009**, *131*, 3442–3443.
- [20] Kitagawa, S.; Uemura, K. *Chem. Soc. Rev* **2005**, *34*, 109. Fletcher, A. J.; Thomas, K. M.; Rosseinsky, M. J. *J. Solid State Chem.* **2005**, *178*, 2491. Mellot-Draznieks, C.; Serre, C.; Surble, S.; Audebrand, N.; Férey, G. *J. Am. Chem. Soc.* **2005**, *127*, 16273. Serre, C.; Mellot-Draznieks, C.; Surble, S.; Audebrand, N.; Filinchuk, Y.; Férey, G. *Science* **2007**, *315*, 1828.
- [21] Millange, F.; Serre, C.; Férey, G. *Chem. Commun.* **2002**, 822. Serre, C.; Millange, F.; Thouvenot, C.; Nogues, M.; Marsolier, G.; Louer, D.; Férey, G. *J. Am. Chem. Soc.* **2002**, *124*, 13519. Liu, Y.; Her, J.-H.; Dailly, A.; Ramirez-Cuesta, A. J.; Neumann, D. A.; Brown, C. M. *J. Am. Chem. Soc.* **2008**, *130*, 11813.
- [22] Llewellyn, P. L.; Maurin, G.; Devic, T.; Loera-Serna, S.; Rosenbach, N.; Serre, C.; Bourrelly, S.; Horcajada, P.; Filinchuk, Y.; Férey, G. *J. Am. Chem. Soc.* **2008**, *130*, 12808.
- [23] Alaerts, L.; Maes, M.; Giebeler, L.; Jacobs, P. A.; Martens, J. A.; Denayer, J. F. M.; Kirschhock, C. E. A.; De Vos, D. E. *J. Am. Chem. Soc.* **2008**, *130*, 14170.
- [24] Coudert, F.-X.; Jeffroy, M.; Fuchs, A. H.; Boutin, A.; Mellot-Draznieks, C. *J. Am. Chem. Soc.* **2008**, *130*, 14294.
- [25] Rouquerol, F.; Rouquerol, J.; Sing, K. *Adsorption by Powders and Porous Solids*; Academic Press: New York, 1999.
- [26] R.W. Judd, D.T.M. Gladding, R.C. Hodrien, D. R. Bates, J.P. Ingram, M. Allen, The Use of Adsorbed Natural Gas Technology for Large Scale Storage., *BG Technology, Gas Research and Technology Centre*.

EXPERIMENTAL AND THEORETICAL STUDIES OF C₂H₆, C₃H₈, C₄H₁₀ ADSORPTION IN

CHAPTER 6

CONCLUSIONS

6.1.	METAL ORGANIC FRAMEWORK MIL-53(AI) CHARACTERISTICS	143
6.2.	THERMODYNAMICS OF GAS ADSORPTION ON MIL-53(AI)	144
6.3.	MOLECULAR SIMULATION OF GAS STORAGE ON MIL-53(AI)	146
6.4.	SUGGESTIONS FOR FUTURE RESEARCH	147
6.5.	REFERENCES	149

6. CONCLUSIONS

By analogy with the structure of this thesis, its achievements and conclusions can be divided in three major sections:

- Treatability studies of the MIL-53(Al) using chemical-physical techniques;
- Treatability studies of the thermodynamics of C₁-C₄, adsorption using gravimetric analysis; Theoretical calculations of the gas storage on MIL-53(Al)
- Molecular simulation of the adsorption using the Grand Canonical Monte Carlo (GCMC) method. Theoretical calculations of the gas storage on MIL-53(Al)

6.1 METAL ORGANIC FRAMEWORK MIL-53(Al) CHARACTERISTICS

The detailed characterization of MIL-53(Al) material using advanced physical-chemicals methods constituted the starting point of the research. The characterization of MIL-53(Al) was performed in three different directions, namely

- Structure identification using the elemental analysis, the solid state ¹³C-NMR and the Fourier-transform infrared spectroscopy (FT-IR).
- Chemical-physical properties identification by the mercury porosimetry, the low temperature N₂ adsorption with density functional theory, and the thermogravimetric analysis
- Unit cell parameters Identification by the X-ray powder diffraction.

Identification of MIL-53 (Al) structure.

The elemental analysis was done to ascertain the structure and purity of the adsorbent material. The results are presented in table 2.1. By analysis of the results of the solid state ¹³C-NMR and the Fourier-transform infrared spectroscopy (FT-IR) we have identified the MIL-53(Al) structure.

Identification of the chemical-physical properties of MIL-53 (Al).

Mercury porosimetry was done to obtain the particle size distribution. The value was estimated using the conventional method of Mayer and Stowe [1] applied to low-pressure (0.2–10 MPa) mercury intrusion data. The particle size distribution is well fitted by a log-normal distribution with mean diameter $D_p = 30.0 \mu\text{m}$ and standard deviation $\sigma D_p = 1.7 \mu\text{m}$; our estimate of D_p is in good agreement with the mean value of $32 \mu\text{m}$ value reported by the manufacturer [9]. By low (77 K) temperature N₂ adsorption together with density functional theory the values of, total pore volume, volume of micropores, surface area, surface area of micropores and diameter of pores was estimated. These values are presented in Table 6.1.

Table 6.1 Results of low temperature N₂ adsorption

	S _{BET} , m ² /g	S _{micro} , m ² /g	V _{total} , cm ³ /g	V _{micro} , cm ³ /g	D _{pores} , nm
Experimental	830	610	0,58	0,33	0,85-1,3

According to the TGA analysis performed, the MIL-53(Al) structure is stable up to ca. 773 K, after that it starts to collapse; the profile is in full agreement with similar TGA observations known from the literature [11].

Identification of the unit cell parameters of MIL-53(Al)

The powder X-ray diffraction of the hydrated MIL-53(Al) sample have been done to establish unit cell parameters of MIL-53(Al) in order to use obtained data in Grand Canonical Monte Carlo simulation. Also by X-ray powder diffraction the value of the specific volume of the MIL-53(Al) unit cell ($V = 1.033 \text{ cm}^3/\text{g}$) was obtained and used in our calculations.

Overall assessment of the data obtained shows that they are in good agreement with the literature findings known up to date for the MIL-53(Al) materials characterization.

6.2 THERMODYNAMICS OF GAS ADSORPTION ON MIL-53(Al). EXPERIMENTS AND MODELING

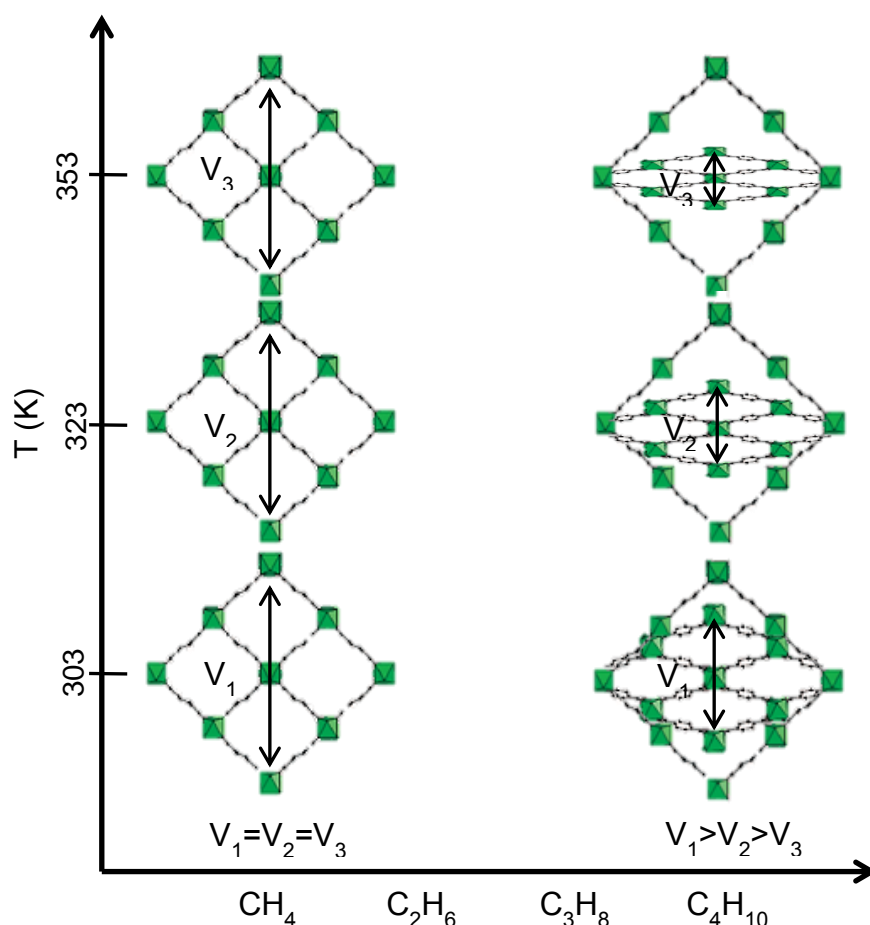
Adsorption of C_1 - C_4 n-alkanes on MIL-53(Al) was done using high-pressure magnetic-suspension balance measurements with automated online data acquisition of temperature, pressure, and sample weight in a wide range of temperature 303-353 K and pressure 0-5 MPa.

The maximum adsorption capacity of the C_1 - C_4 n-alkanes on MIL-53(Al) was calculated using the Sips and Toth isotherms models. The results are presented in Table 6.2.

Table 6.2 Maximal adsorption capacity obtained from the data fitting for the C_1 - C_4 experimental adsorption by the Sips and Toth isotherms models

Parameter	SIPS	TOTH	SIPS	TOTH	SIPS	TOTH	SIPS	TOTH
	CH_4		C_2H_6		C_3H_8		C_4H_{10}	
T_0 (K)	303 K							
n_s (mol/kg)	8.3	10.1	7.5	9.5	4.3	5.2	3.9	4.3
T_0 (K)	323 K							
n_s (mol/kg)	7.9	9.4	7.3	9.2	4.1	5.0	3.8	4.2
T_0 (K)	353 K							
n_s (mol/kg)	7.6	8.9	7.0	8.8	3.9	4.8	3.6	4.0

It was also shown that the adsorption of the C_2 - C_4 n-alkanes has a complex mechanism involving MIL-53(Al) structural transformation during the adsorption. The behavior of the structural transformation, so called “breathing” of MIL-53(Al), was analyzed and a hypothesis of the effect temperature and chain size effects on “breathing” phenomena in MIL-53(Al) upon C_1 - C_4 adsorption was elaborated the results are presented in Scheme 6.1 and earlier in Scheme 5.1.



Scheme 6.1. Diagram for the hypothesis of the temperature and chain size effects on “breathing” phenomena in MIL-53 (Al) upon C_1 - C_4 adsorption

Therefore, upon the adsorption of the ethane, propane and butane, the MIL-53(Al) can switch between two structural transition (lp---np---lp forms) during the adsorption run. It was concluded, that founded effects, namely size (the alkyl chain length) and temperature influence on breathing phenomena of the MIL-53 (Al) are in agreement with a generic thermodynamic framework concept of the guest-induced structural transitions in flexible nanoporous materials according to the osmotic pseudo-ensemble approach and with a view that the double transition is dictated solely by the affinity for the lp form with a proposed critical (threshold) adsorption enthalpy of ~ 20 kJ/mol.

Overall, our findings can be summarized as following:

- *There is size effect on temperature dependence of the breathing phenomena.* With temperature increase, the breathing effect becomes to be more evident for the longer alkanes;
- *There is temperature effect on the extent of breathing phenomena.* Strongly depending on temperature, with temperature increase effect becomes to be already evident;
- *There is size effect on the extent of breathing phenomena.* The position of the step is a function of pressure. With increase of the alkyl chain length chain the adsorption sub-step appears at a much lower relative pressure. This finding is in full agreement with the

literature findings known up to date on predicted pressures for the lp----np and np-----lp transitions for MIL-53(Cr) [2]

In this perspective, this research contributes to a broader interpretation of the generic thermodynamic framework concept, namely to understanding of guest-induced structural transitions in flexible nanoporous materials such as MOFs.

Moreover, in this part of the work, the isosteric heat of the adsorption for the C₁-C₄ n-alkanes in MIL-53(Al) was evaluated using four different approaches, such as the GCMC simulation method, integrated form of Clapeyron equation and Sips, Toth isotherms models. Results are compared in Table 6.3.

In general, the values calculated for heat of the adsorption for all the gases studied are in a range of ca. 20-32 kJ/mol. In principal, they are in good agreement whatever the calculation methods, and just slightly vary from each other (by 2 kJ/mol or ~10%) for methane, ethane and butane. For the propane they vary by 5-6 kJ/mol (i.e. ~20%) between the experimental and simulation values; and they are in a good agreement for the experimental and values from the Sips model.

Table 6.3. Isosteric Heat of adsorption determined by GCMC simulation method, integrated form of Clapeyron equation and Sips, Toth isotherms models.

Q _{st} kJ/mol	CH ₄	C ₂ H ₆	C ₃ H ₈	C ₄ H ₁₀
303 K				
SIPS	19,7	24,3	24,8	26,5
TOTH	19,9	25,9	53,5	28,6
Simulation	16,3	25,5	32,2	-
323 K				
SIPS	19,4	24,3	25,0	26,4
TOTH	19,5	26,3	53,7	28,2
Simulation	16,0	25,2	31,4	-
353 K				
SIPS	19,6	24,8	25,0	26,4
TOTH	19,6	27,0	54,0	28,3
Simulation	15,9	24,9	31,6	-
Temperature dependent				
Clapeyron	16,2	25,8	26,8	28,7

For the detailed analysis of the experimental data, adsorption was calculated using three different reference states; the net adsorption (n_{net}); the excess adsorption (n_{ex}) and the absolute adsorption (n).

The net adsorption together with data on bulk gases compressed under identical conditions were used to estimate the storage capacity of MIL-53(Al). It was concluded, that for the C₁-C₂ gases on MIL-53(Al), the highest enhancement of 60-40% above simple gas compression is found at 4.9 and 3.7 MPa, respectively; and for the liquid C₃-C₄, the highest enhancement of the storage capacity due to the adsorption is of 27-20%.

Gas delivery efficiency for the ANG method using MIL-53(Al) was also discussed, based on analysis of the experimental desorption runs for the studied gases. *In this perspective, the*

accomplished research contributes to the Adsorbed Natural Gas storage technology development.

6.3 MOLECULAR SIMULATION OF THE GAS STORAGE ON MIL-53(Al)

The molecular simulation work was done using the Grand Canonical Monte Carlo simulation model. The parameterization of solid–fluid dispersive interactions in MIL-53(Al) was based on the TraPPE-UA force field. The specific pore volume of the unit cell of MIL-53(Al) of ($V_p = 0.56 \text{ cm}^3/\text{g}$) was estimated by molecular simulation of the capillary condensation of methane in the pore structure of MIL-53lp(Al) at $0.8T_c$ (152.5 K) and chemical potential μ/k_B of -1623 K ($\sim 1.37 \text{ MPa}$). This value was used for the followed calculations of the total amount adsorbed. The molecular simulation was also used to calculate the adsorption isotherms of studied gases in MIL-53(Al) for three different reference states, and the values of the isosteric heat of the adsorption (Table 6.3). The simulation results show a very good agreement with our experimental data.

Moreover, the simulation was used to calculate the DOE target of 150 (v/v) at loading pressure $P_H = 3.5 \text{ MPa}$, delivery pressure $P_L = 0.136 \text{ MPa}$ and 298 K for the methane storage on the MIL-53(Al). Calculations were done for two possible modes of the MIL-53(Al) packaging inside the storage tank as a monolith or as a close-packed bed. The theoretical net storage capacity provided by MIL-53lp(Al) was estimated as 114.0 (v/v)_{net} for a monolith and 93.1 (v/v)_{net} for a close-packed bed. It was concluded, that for a monolith block to achieve the goal of 150 (v/v)_{net} storage capacity by methane in MIL-53(Al), the charge pressure must be either increased to $P_H \sim 10.9 \text{ MPa}$, or the monolith must operate isothermally at $\sim 253 \text{ K}$. For a delivery cycle at 298 K, insertion of $P_L = 0.136 \text{ MPa}$ and $P_H = 3.5 \text{ MPa}$, the isosteric heat value ($Q_{st, \text{opt}} = 18.8 \text{ kJ/mol}$) was also calculated, which happens to be in good agreement with the values shown in Table 6.3.

Furthermore, methane condensation in MIL-53l(Al) at 152.5 K was also simulated, and gave the storage capacity values of 279 (v/v) for a monolithic block and of 213 (v/v) for a close packed bed. These values are well above the DOE target of 150 (v/v)_{net}, thus suggesting that MIL-53(Al) could be an acceptable methane adsorptive storage medium if the system is operated at a suitably low temperature.

6.4 SUGGESTIONS FOR FUTURE RESEARCH

The adsorption of short linear alkanes has been explored in the highly flexible MIL-53(Al) porous metal–organic framework by means of molecular simulations based on Grand Canonical Monte Carlo and by gravimetric experiments. The unusual shape of the adsorption isotherms with the existence of steps has been successfully evaluated by creating a (narrow pore, large pore) phase mixture domain, the composition of which varies with pressure, size of the alkane chain and temperature.

A further step consisted of combining our computational approach and gravimetry studies with several experimental tools including microcalorimetry and *in situ* X-ray diffraction, to fully

characterize the adsorption behavior of the rigid MIL-53(Al), i.e. the preferential arrangement of each type of alkane inside the pores and the resulting interaction energy. Finally, relationships should be established between the adsorption enthalpies and alkyl chain length that can be further utilized to predict the energetics of the adsorption process for longer alkane chains.

Adsorption Microcalorimetry.

The adsorption of the various alkanes should be carried out at 303 K using a manometric adsorption apparatus coupled with a Tian-Calvet type microcalorimeter. This experimental device measures the isotherm and the enthalpy of adsorption simultaneously using a point by point introduction of gas to the sample.

Energetics Parameters Estimation

The relationships should be evaluated between the adsorption enthalpies and carbon number of the alkanes that can further provide an estimation of the energetics of the adsorption process for longer alkane chains.

In situ X-ray Diffraction.

In situ synchrotron X-ray diffraction experiments should be performed using advanced experimental setup which allows the XR powder data collection under controlled gas pressure to estimate quantitative parameters for the breathing phenomena upon C₂-C₄ adsorption.

Alkanes Mixture Adsorption

While the adsorption of alkane mixtures is still under investigation, finally this type of studies will be extremely useful for the components of natural gas separation application.

6.5 REFERENCES

- [1] Mayer, R. P.; Stowe, R. A. *J. Colloid Sci.* **1965**, *20*, 893. Nakamoto, K.: *Infrared and Raman Spectra of Inorganic and Coordination Compounds*;
- [2] Coudert, F.-X.; Mellot-Draznieks, C.; Fuchs, A. H.; Boutin, A. *J. Am. Chem. Soc.* **2009**, *131*, 3442–3443.

ANNEX A

GAS STORAGE IN METAL ORGANIC FRAMEWORK MIL-53(Al) EXPERIMENT AND SIMULATION

The methane adsorption isotherms were measured both experimentally and theoretically. For the experimental work were used the standard static gravimetric technique. The adsorption isotherms were measured at 303.15 K, 323.15 K, and 353.15 K, over a pressure range of ~0.01–5.0 MPa. For the theoretical work was used Grand Canonical Monte Carlo simulation method. The experimental and simulated adsorption (large pore form only) equilibrium data are listed in Tables A 1-12. Each data point is reported as net (n_{net}), excess (n_{ex}), and total adsorption (n); the reference state corrections for calculating n_{ex} and n are $v_p = 0.564 \text{ cm}^3/\text{g}$ and $v_s = 0.470 \text{ cm}^3/\text{g}$.

Table A.1: Experimental and Simulated methane adsorption equilibrium data at 303.15 K. The reference state corrections are $v_p = 0.564 \text{ cm}^3/\text{g}$ and $v_s = 0.470 \text{ cm}^3/\text{g}$.

Experimental data				Simulated data			
P (MPa)	n_{net} (mol/kg)	n_{ex} (mol/kg)	n (mol/kg)	P (MPa)	n_{net} (mol/kg)	n_{ex} (mol/kg)	n (mol/kg)
0.00000	0.00000	0.00000	0.00000	0.00200	0.01227	0.01183	0.01146
0.00021	0.01759	0.01754	0.01750	0.01497	0.09167	0.08835	0.08557
0.01001	0.08578	0.08354	0.08167	0.04991	0.29482	0.28366	0.27436
0.03996	0.27497	0.26602	0.25856	0.10002	0.56235	0.53987	0.52114
0.07074	0.45839	0.44255	0.42934	0.15068	0.80964	0.77567	0.74735
0.09432	0.59753	0.57640	0.55879	0.18902	0.98575	0.94304	0.90744
0.18264	1.04306	1.00207	0.96792	0.30161	1.43470	1.36622	1.30914
0.40220	1.84266	1.75208	1.67660	0.50464	2.09284	1.97758	1.88153
0.79430	2.73476	2.55472	2.40469	0.75656	2.71237	2.53869	2.39396
1.50666	3.73329	3.38778	3.09989	1.01255	3.20765	2.97430	2.77983
3.02667	4.94690	4.23552	3.64276	1.26754	3.61489	3.32185	3.07764
4.01606	5.46046	4.50151	3.70246	1.51924	3.91951	3.56735	3.27388
4.68406	5.78804	4.65728	3.71507	2.03446	4.50300	4.02933	3.63460
1.06106	3.35562	3.11406	2.91277	2.54794	4.93512	4.33981	3.84369
1.72928	4.15817	3.76018	3.42854	2.79933	5.08958	4.43453	3.88864
2.46220	4.75876	4.18530	3.70746	3.05499	5.28350	4.56761	3.97101

Table A.2: Experimental and Simulated methane adsorption equilibrium data at 323.15 K. The reference state corrections are $v_p = 0.564 \text{ cm}^3/\text{g}$ and $v_s = 0.470 \text{ cm}^3/\text{g}$.

Experimental data				Simulated data			
P (MPa)	n_{net} (mol/kg)	n_{ex} (mol/kg)	n (mol/kg)	P (MPa)	n_{net} (mol/kg)	n_{ex} (mol/kg)	n (mol/kg)
0.00000	0.00331	0.00331	0.00331	0.00058	0.00248	0.00236	0.00226
0.00019	0.00015	0.00011	0.00008	0.00269	0.01153	0.01097	0.01050
0.00991	0.04617	0.04409	0.04236	0.00582	0.02496	0.02375	0.02274
0.01991	0.08623	0.08205	0.07857	0.01261	0.05435	0.05173	0.04954
0.04033	0.16909	0.16062	0.15357	0.02738	0.11555	0.10984	0.10508
0.07043	0.29193	0.27714	0.26481	0.05958	0.24841	0.23595	0.22556
0.09610	0.39367	0.37348	0.35666	0.12993	0.51289	0.48558	0.46282
0.11525	0.47805	0.45381	0.43362	0.28399	1.01436	0.95427	0.90420
0.18069	0.70356	0.66555	0.63389	0.62213	1.83816	1.70543	1.59480
0.33812	1.17488	1.10360	1.04421	0.99700	2.51278	2.29880	2.12047
0.50072	1.56927	1.46349	1.37536	1.36595	3.00806	2.71363	2.46827
0.79690	2.12580	1.95688	1.81613	1.87212	3.53938	3.13400	2.79616
1.38198	2.91018	2.61488	2.36883	2.56678	4.11601	3.55749	3.09205
1.94577	3.43119	3.01263	2.66387	3.00591	4.39951	3.74379	3.19732
2.42413	3.80871	3.28380	2.84642	3.52049	4.72215	3.95216	3.31048
3.46965	4.41203	3.65169	3.01813	4.12352	5.01063	4.10633	3.35271
4.11000	4.72335	3.81716	3.06208	4.83029	5.33070	4.26847	3.38324
4.99567	5.07424	3.95986	3.03129	5.22806	5.50300	4.35168	3.39221
0.00000	0.00000	0.00000	0.00000	5.65871	5.64046	4.39253	3.35255
0.00012	0.00039	0.00037	0.00035				
2.99207	4.05821	3.40651	2.86348				
1.01872	2.44303	2.22642	2.04592				
0.03316	0.21056	0.20360	0.19780				

Table A.3: Experimental and Simulated methane adsorption equilibrium data at 353.15 K. The reference state corrections are $v_p = 0.564 \text{ cm}^3/\text{g}$ and $v_s = 0.470 \text{ cm}^3/\text{g}$.

Experimental data				Simulated data			
P (MPa)	n_{net} (mol/kg)	n_{ex} (mol/kg)	n (mol/kg)	P (MPa)	n_{net} (mol/kg)	n_{ex} (mol/kg)	n (mol/kg)
0.00000	0.00000	0.00000	0.00000	0.00401	0.01048	0.00971	0.00906
0.02016	0.07799	0.07412	0.07089	0.01620	0.04362	0.04052	0.03793
0.04048	0.14095	0.13317	0.12669	0.04872	0.12920	0.11987	0.11210
0.07066	0.22211	0.20853	0.19721	0.09674	0.25215	0.23362	0.21817
0.09599	0.29373	0.27527	0.25990	0.14448	0.36892	0.34120	0.31810
0.11975	0.36162	0.33860	0.31942	0.19270	0.48121	0.44420	0.41336
0.33195	0.83149	0.76753	0.71424	0.28835	0.69020	0.63472	0.58848
0.50960	1.15717	1.05884	0.97690	0.48039	1.05869	0.96600	0.88875
0.86149	1.68412	1.51737	1.37842	0.72276	1.45423	1.31439	1.19785
0.00846	0.00600	0.00438	0.00303	0.96431	1.79166	1.60468	1.44885
3.07568	3.21455	2.60844	2.10340	1.20799	2.07911	1.84446	1.64890
1.91568	2.50950	2.13550	1.82387	1.45364	2.33516	2.05234	1.81665
4.11340	3.76177	2.94468	2.26384	1.94212	2.76128	2.38244	2.06672
4.90949	4.07676	3.09619	2.27912	2.43548	3.10571	2.62960	2.23281
2.49706	2.98585	2.49603	2.08789	2.92480	3.41445	2.84162	2.36424
1.11532	1.89893	1.68264	1.50242	3.42237	3.68628	3.01491	2.45540
0.70332	1.40037	1.26446	1.15121	3.92438	3.92380	3.15281	2.51029
0.21068	0.58511	0.54455	0.51075	4.42253	4.12750	3.25750	2.53247
0.10089	0.34659	0.32718	0.31101	4.92655	4.32572	3.35539	2.54674
0.08243	0.30204	0.28622	0.27303	5.42471	4.48223	3.41260	2.52120
0.06065	0.25439	0.24273	0.23301	5.92147	4.67976	3.51098	2.53695
0.02039	0.15370	0.14978	0.14652				
0.01007	0.12580	0.12386	0.12225				
0.00426	0.10622	0.10540	0.10472				
0.00120	0.09538	0.09515	0.09496				

Table A.4: Experimental and Simulated ethane adsorption equilibrium data at 303.15 K. The reference state corrections are $v_p = 0.564 \text{ cm}^3/\text{g}$ and $v_s = 0.470 \text{ cm}^3/\text{g}$.

Experimental data				Simulated data			
P (MPa)	n_{net} (mol/kg)	n_{ex} (mol/kg)	n (mol/kg)	P (MPa)	n_{net} (mol/kg)	n_{ex} (mol/kg)	n (mol/kg)
0.00028	0.00023	0.00017	0.00012	3.54946	5.43572	4.44261	3.61497
0.00947	0.63140	0.62928	0.62751	2.96534	5.33636	4.52074	3.84102
0.04403	1.87908	1.86919	1.86095	2.47856	5.15822	4.48766	3.92882
0.09524	2.53744	2.51598	2.49810	2.07270	5.01098	4.45908	3.99914
0.40023	3.67651	3.58430	3.50748	1.45161	4.76059	4.38554	4.07299
0.89702	4.39622	4.18111	4.00187	1.01863	4.46215	4.20620	3.99289
1.46606	4.86554	4.49557	4.18728	0.60098	4.08769	3.94222	3.82099
2.20948	5.34375	4.74072	4.23825	0.25188	3.37360	3.31565	3.26736
2.98343	5.82108	4.91807	4.16564	0.10687	2.67547	2.65176	2.63200
3.48518	6.17222	5.02060	4.06101	0.01996	1.09243	1.08813	1.08455
1.19303	4.77985	4.48628	4.24167	0.00879	0.54386	0.54196	0.54037
0.68634	4.29245	4.13069	3.99590	0.00391	0.25081	0.24995	0.24922
0.23617	3.42371	3.36995	3.32516	0.00177	0.11387	0.11347	0.11313
0.02475	1.63272	1.62718	1.62255				
0.00867	0.85214	0.85019	0.84858				
0.00380	0.10355	0.10270	0.10199				

Table A.5: Experimental and Simulated ethane adsorption equilibrium data at 323.15 K. The reference state corrections are $v_p = 0.564 \text{ cm}^3/\text{g}$ and $v_s = 0.470 \text{ cm}^3/\text{g}$.

Experimental data				Simulated data			
P (MPa)	n_{net} (mol/kg)	n_{ex} (mol/kg)	n (mol/kg)	P (MPa)	n_{net} (mol/kg)	n_{ex} (mol/kg)	n (mol/kg)
0.00000	0.00000	0.00000	0.00000	4.07797	4.98918	3.94224	3.06976
0.00021	0.02172	0.02167	0.02164	3.43965	4.90337	4.03555	3.31232
0.01075	0.44185	0.43959	0.43771	2.90291	4.76008	4.03983	3.43959
0.03686	1.22323	1.21548	1.20902	2.45133	4.61935	4.02084	3.52206
0.07032	1.76863	1.75380	1.74145	1.75100	4.38905	3.97423	3.62853
0.09732	2.02741	2.00686	1.98974	1.25362	4.11910	3.83017	3.58938
0.33071	2.99088	2.92006	2.86105	0.76270	3.74498	3.57546	3.43419
0.69825	3.56547	3.41246	3.28496	0.33701	3.11635	3.04490	2.98536
1.21640	4.04875	3.77290	3.54305	0.15106	2.43247	2.40140	2.37552
2.07292	4.54866	4.04752	3.62994	0.06869	1.69533	1.68140	1.66980
2.75987	4.87099	4.16265	3.57242	0.03169	1.00810	1.00166	0.99629
3.73304	5.28129	4.21733	3.33078	0.01483	0.52301	0.51994	0.51738
4.33428	5.56898	4.24026	3.13311	0.00704	0.25629	0.25478	0.25352
3.30686	5.15231	4.25708	3.51113				
1.61583	4.38728	4.00986	3.69538				
0.20362	2.71321	2.66994	2.63389				
0.05436	1.69214	1.68069	1.67115				
0.02542	1.10689	1.10155	1.09710				
0.00147	0.14851	0.14820	0.14795				

Table A.6: Experimental and Simulated ethane adsorption equilibrium data at 353.15 K. The reference state corrections are $v_p = 0.564 \text{ cm}^3/\text{g}$ and $v_s = 0.470 \text{ cm}^3/\text{g}$.

Experimental data				Simulated data			
P (MPa)	n_{net} (mol/kg)	n_{ex} (mol/kg)	n (mol/kg)	P (MPa)	n_{net} (mol/kg)	n_{ex} (mol/kg)	n (mol/kg)
0.00000	0.00000	0.00000	0.00000	4.55894	4.41547	3.39087	2.53699
0.00024	0.00306	0.00301	0.00297	3.91007	4.30821	3.43979	2.71608
0.01078	0.17574	0.17366	0.17190	3.35493	4.19649	3.45984	2.84594
0.03832	0.55126	0.54389	0.53761	3.06103	4.14244	3.47478	2.91838
0.07147	0.91133	0.89755	0.88581	2.47295	3.96533	3.43396	2.99114
0.09493	1.15913	1.14083	1.12523	1.99946	3.82186	3.39828	3.04528
0.43197	2.51296	2.42835	2.35623	1.56982	3.64750	3.31996	3.04700
0.81328	2.99395	2.83190	2.69379	1.00021	3.29998	3.09658	2.92708
1.53429	3.52999	3.21329	2.94336	0.74212	3.08220	2.93355	2.80966
2.07596	3.81936	3.37824	3.00227	0.55153	2.86082	2.75181	2.66097
2.52082	4.00451	3.45581	2.98814	0.35445	2.48635	2.41749	2.36010
3.45898	4.35467	3.55825	2.87946	0.17104	1.83662	1.80406	1.77692
4.50865	4.67047	3.55897	2.61162	0.08338	1.18766	1.17194	1.15884
1.22899	3.37543	3.12543	2.91235	0.04107	0.69073	0.68299	0.67654
0.24316	2.11848	2.07127	2.03104	0.02044	0.36854	0.36465	0.36140
0.05210	0.94173	0.93170	0.92315	0.01028	0.18926	0.18726	0.18559
0.14788	1.62594	1.59743	1.57312				
0.03173	0.61171	0.60563	0.60044				

Table A.7: Experimental and Simulated propane adsorption equilibrium data at 303.15 K. The reference state corrections are $v_p = 0.564 \text{ cm}^3/\text{g}$ and $v_s = 0.470 \text{ cm}^3/\text{g}$.

Experimental data				Simulated data			
P (MPa)	n_{net} (mol/kg)	n_{ex} (mol/kg)	n (mol/kg)	P (MPa)	n_{net} (mol/kg)	n_{ex} (mol/kg)	n (mol/kg)
0.00000	0.00000	0.00000	0.00000	0.00126	0.75550	0.75522	0.75499
0.00020	0.01786	0.01781	0.01778	0.00175	0.97961	0.97923	0.97890
0.04109	2.51884	2.50960	2.50189	0.00244	1.23865	1.23811	1.23766
0.09604	2.89275	2.87095	2.85278	0.00340	1.51251	1.51176	1.51113
0.29761	3.02443	2.95458	2.89638	0.00474	1.80367	1.80262	1.80174
0.49945	3.34151	3.22006	3.11887	0.00661	2.04256	2.04108	2.03985
0.71021	3.66979	3.48944	3.33917	0.00923	2.26617	2.26410	2.26238
0.84819	3.93235	3.71015	3.52500	0.01289	2.43573	2.43282	2.43041
0.40763	3.23048	3.13299	3.05175	0.01801	2.58126	2.57718	2.57378
0.20204	2.83320	2.78654	2.74767	0.02517	2.73262	2.72689	2.72211
0.07202	2.25203	2.23574	2.22216	0.03519	2.84177	2.83371	2.82699
0.02971	1.95406	1.94738	1.94181	0.04923	2.92963	2.91828	2.90882
0.01687	1.79788	1.79410	1.79094	0.06889	3.04942	3.03342	3.02008
0.01024	1.66036	1.65806	1.65615	0.09644	3.14038	3.11780	3.09899
0.13411	2.50403	2.47339	2.44786	0.13506	3.21675	3.18487	3.15830
0.59903	3.50923	3.36059	3.23673	0.18924	3.28162	3.23656	3.19901
0.00149	0.96817	0.96784	0.96756	0.26525	3.32984	3.26610	3.21298
0.00000	0.00000	0.00000	0.00000	0.37195	3.39969	3.30943	3.23422
				0.52178	3.48824	3.36033	3.25373
				0.73229	3.57542	3.39397	3.24276
				1.02813	3.63789	3.38026	3.16557

Table A.8: Experimental and Simulated propane adsorption equilibrium data at 323.15 K. The reference state corrections are $v_p = 0.564 \text{ cm}^3/\text{g}$ and $v_s = 0.470 \text{ cm}^3/\text{g}$.

Experimental data				Simulated data			
P (MPa)	n_{net} (mol/kg)	n_{ex} (mol/kg)	n (mol/kg)	P (MPa)	n_{net} (mol/kg)	n_{ex} (mol/kg)	n (mol/kg)
0.00010	0.00008	0.00006	0.00005	0.00099	0.31196	0.31176	0.31158
0.05373	2.34345	2.33210	2.32264	0.00135	0.41733	0.41705	0.41682
0.09359	2.52136	2.50149	2.48493	0.00184	0.55390	0.55352	0.55320
0.30191	3.02280	2.95694	2.90206	0.00215	0.63614	0.63570	0.63532
0.35591	3.17029	3.09199	3.02675	0.00468	1.15933	1.15835	1.15754
0.65476	3.58081	3.43047	3.30520	0.00640	1.42260	1.42127	1.42015
1.27610	4.24072	3.91241	3.63884	0.00874	1.66159	1.65976	1.65824
0.88348	3.83469	3.62416	3.44873	0.01196	1.87935	1.87684	1.87475
0.46494	3.39076	3.28696	3.20047	0.01636	2.11532	2.11187	2.10900
0.20040	2.89911	2.85598	2.82005	0.02240	2.30787	2.30313	2.29918
0.03494	2.31076	2.30339	2.29726	0.03069	2.46353	2.45700	2.45156
0.01214	1.97348	1.97093	1.96880	0.04207	2.58967	2.58067	2.57318
0.00010	0.00009	0.00007	0.00005	0.05770	2.73005	2.71764	2.70731
0.49344	3.32566	3.21504	3.12287	0.07918	2.82907	2.81194	2.79767
				0.10872	2.92963	2.90597	2.88624
				0.14936	3.01510	2.98235	2.95507
				0.20530	3.06881	3.02346	2.98567
				0.28236	3.15222	3.08934	3.03695
				0.38856	3.23202	3.14476	3.07204
				0.53499	3.29929	3.17806	3.07703
				0.73703	3.36090	3.19231	3.05180
				1.19300	3.43573	3.15868	2.92780

Table A.9: Experimental and Simulated propane adsorption equilibrium data at 353.15 K. The reference state corrections are $v_p = 0.564 \text{ cm}^3/\text{g}$ and $v_s = 0.470 \text{ cm}^3/\text{g}$.

Experimental data				Simulated data			
P (MPa)	n_{net} (mol/kg)	n_{ex} (mol/kg)	n (mol/kg)	P (MPa)	n_{net} (mol/kg)	n_{ex} (mol/kg)	n (mol/kg)
0.00022	0.00018	0.00014	0.00010	0.00623	0.69947	0.69830	0.69732
0.03526	1.70246	1.69566	1.69000	0.00829	0.87318	0.87161	0.87031
0.05367	1.91252	1.90216	1.89352	0.01103	1.07652	1.07444	1.07270
0.00009	0.00008	0.00006	0.00005	0.01469	1.29543	1.29265	1.29033
0.03118	1.74292	1.73692	1.73191	0.01958	1.50990	1.50618	1.50307
0.05372	1.97113	1.96076	1.95212	0.02611	1.72267	1.71768	1.71352
0.09516	2.15534	2.13690	2.12154	0.03484	1.92620	1.91951	1.91394
0.37367	2.68133	2.60694	2.54496	0.04653	2.11858	2.10960	2.10211
0.50157	2.80591	2.70474	2.62044	0.06217	2.28505	2.27297	2.26290
0.81218	3.05713	2.88759	2.74632	0.08313	2.42577	2.40951	2.39595
1.41075	3.44813	3.13063	2.86607	0.11122	2.55466	2.53273	2.51445
2.32487	4.04016	3.42771	2.91738	0.14890	2.67376	2.64416	2.61949
1.59706	3.57869	3.20965	2.90215	0.19947	2.77776	2.73775	2.70442
0.98915	3.21849	3.00760	2.83187	0.26739	2.85515	2.80103	2.75592
0.26337	2.60156	2.54970	2.50649	0.35867	2.95795	2.88462	2.82351
0.02359	1.74906	1.74452	1.74074	0.48142	3.02866	2.92918	2.84629
0.01127	1.37181	1.36964	1.36784	0.64660	3.10365	2.96855	2.85595
0.00193	0.38842	0.38805	0.38774	0.86901	3.17624	2.99251	2.83940
0.00010	0.00009	0.00007	0.00005	1.16868	3.20611	2.95593	2.74744
				1.57269	3.30067	2.95959	2.67535
				2.11774	3.34889	2.88331	2.49530

Table A.10: Experimental and Simulated butane adsorption equilibrium data at 303.15 K. The reference state corrections are $v_p = 0.564 \text{ cm}^3/\text{g}$ and $v_s = 0.470 \text{ cm}^3/\text{g}$.

Experimental data				Simulated data			
P (MPa)	n_{net} (mol/kg)	n_{ex} (mol/kg)	n (mol/kg)	P (MPa)	n_{net} (mol/kg)	n_{ex} (mol/kg)	n (mol/kg)
0.00001	0.00001	0.00001	0.00001				
0.00026	0.97840	0.97834	0.97829				
0.00076	1.45544	1.45527	1.45513				
0.00167	1.74089	1.74052	1.74021				
0.00242	1.88995	1.88940	1.88895				
0.00000	0.00000	0.00000	0.00000				
0.00101	1.12723	1.12701	1.12682				
0.00142	1.53510	1.53478	1.53452				
0.00299	1.79805	1.79738	1.79682				
0.00396	1.87449	1.87361	1.87287				
0.00607	1.96249	1.96113	1.96000				
0.00839	2.02958	2.02770	2.02613				
0.01120	2.10377	2.10126	2.09916				
0.01605	2.17418	2.17057	2.16757				
0.02095	2.23461	2.22989	2.22597				
0.00000	0.00000	0.00000	0.00000				
0.00069	0.95498	0.95482	0.95470				
0.00123	1.52872	1.52845	1.52822				
0.00224	1.72342	1.72292	1.72250				
0.00321	1.84904	1.84832	1.84772				
0.00459	1.93606	1.93503	1.93417				
0.00618	2.00567	2.00429	2.00313				
0.02876	2.35596	2.34947	2.34406				
0.04121	2.46641	2.45709	2.44932				
0.05025	2.53118	2.51978	2.51028				
0.06014	2.60869	2.59499	2.58358				
0.08498	2.76927	2.74979	2.73355				
0.09821	2.85065	2.82803	2.80919				
0.12979	3.03249	3.00232	2.97718				
0.17032	3.24245	3.20237	3.16897				
0.21419	3.55061	3.49948	3.45687				
0.23764	3.82425	3.76705	3.71939				
0.15263	3.18720	3.15148	3.12172				
0.01658	2.29337	2.28964	2.28653				

Table A.11: Experimental and Simulated butane adsorption equilibrium data at 323.15 K. The reference state corrections are $v_p = 0.564 \text{ cm}^3/\text{g}$ and $v_s = 0.470 \text{ cm}^3/\text{g}$.

Experimental data				Simulated data			
P (MPa)	n_{net} (mol/kg)	n_{ex} (mol/kg)	n (mol/kg)	P (MPa)	n_{net} (mol/kg)	n_{ex} (mol/kg)	n (mol/kg)
0.00010	0.00011	0.00009	0.00007				
0.00113	0.65741	0.65717	0.65697				
0.00170	1.33893	1.33857	1.33827				
0.00306	1.70708	1.70644	1.70590				
0.00532	1.89079	1.88967	1.88874				
0.01032	2.05266	2.05049	2.04868				
0.02000	2.19421	2.19000	2.18649				
0.03001	2.29022	2.28388	2.27859				
0.04166	2.36535	2.35653	2.34917				
0.05031	2.41627	2.40559	2.39668				
0.06021	2.46143	2.44862	2.43794				
0.07498	2.52157	2.50556	2.49222				
0.09686	2.60006	2.57928	2.56196				
0.15657	2.76547	2.73139	2.70299				
0.20050	2.89664	2.85251	2.81574				
0.24860	3.05099	2.99555	2.94935				
0.27306	3.10608	3.04486	2.99385				
0.33657	3.32319	3.24633	3.18229				
0.41154	3.82673	3.73062	3.65053				
0.36063	3.50345	3.42056	3.35150				
0.26213	3.17069	3.11206	3.06322				
0.22608	3.06915	3.01907	2.97734				
0.12312	2.77521	2.74864	2.72649				
0.08428	2.64319	2.62516	2.61013				
0.03511	2.42612	2.41867	2.41246				
0.00004	0.00004	0.00003	0.00002				
0.00086	0.87398	0.87380	0.87365				
0.02046	2.11227	2.10795	2.10434				
0.01483	2.05591	2.05279	2.05018				
0.00133	1.61249	1.61221	1.61198				

Table A.12: Experimental and Simulated butane adsorption equilibrium data at 353.15 K. The reference state corrections are $v_p = 0.564 \text{ cm}^3/\text{g}$ and $v_s = 0.470 \text{ cm}^3/\text{g}$.

Experimental data				Simulated data			
P (MPa)	n_{net} (mol/kg)	n_{ex} (mol/kg)	n (mol/kg)	P (MPa)	n_{net} (mol/kg)	n_{ex} (mol/kg)	n (mol/kg)
0.00009	0.00009	0.00007	0.00006				
0.00094	0.99536	0.99518	0.99503				
0.00381	1.80857	1.80784	1.80722				
0.00981	2.11686	2.11498	2.11340				
0.02044	2.30910	2.30516	2.30188				
0.03193	2.41805	2.41189	2.40675				
0.04123	2.47854	2.47057	2.46393				
0.05053	2.53249	2.52270	2.51455				
0.09668	2.69406	2.67520	2.65949				
0.09661	2.70137	2.68251	2.66680				
0.14836	2.81708	2.78786	2.76350				
0.20166	2.91301	2.87292	2.83951				
0.37852	3.18241	3.10459	3.03974				
0.71412	3.64525	3.48697	3.35508				
0.57877	3.45816	3.33394	3.23044				
0.26865	3.06199	3.00790	2.96283				
0.07809	2.73381	2.71862	2.70596				
0.01545	2.35255	2.34957	2.34709				
0.00972	2.23148	2.22961	2.22805				
0.00437	1.99829	1.99745	1.99675				
0.00242	1.77322	1.77276	1.77237				
0.00143	1.45187	1.45160	1.45137				
0.00008	0.17578	0.17576	0.17575				
0.00009	0.14499	0.14497	0.14496				
0.00147	1.51234	1.51205	1.51182				

